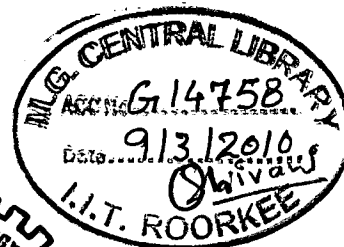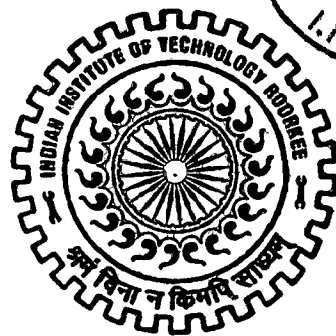# DEVELOPMENT OF ANODIZED Al-OXIDE WITH CNT/CNF IN NANOPORES AND ITS TRIBOLOGICAL BEHAVIOUR

A THESIS

Submitted in partial fulfilment of the
requirements for the award of the degree
of
DOCTOR OF PHILOSOPHY
in
METALLURGICAL AND MATERIALS ENGINEERING

by
MANOJ KUMAR KUSHWAHA

DEPARTMENT OF METALLURGICAL AND MATERIALS ENGINEERING
INDIAN INSTITUTE OF TECHNOLOGY ROORKEE
ROORKEE - 247 667 (INDIA)
JULY, 2009

INDIAN INSTITUTE OF TECHNOLOGY ROORKEE
ROORKEE

CANDIDATE'S DECLARATION

I hereby certify that the work which is being presented in the thesis entitled **DEVELOPMENT OF ANODIZED Al-OXIDE WITH CNT/CNF IN NANOPORES AND ITS TRIBOLOGICAL BEHAVIOUR** in partial fulfilment of the requirements for the award of the degree of Doctor of Philosophy and submitted in the Department of Metallurgical and Materials Engineering of the Indian Institute of Technology Roorkee, Roorkee is an authentic record of my own work carried out during a period from July, 2004 to July, 2009 under the supervision of Dr. A. Sil, Associate Professor and Dr. S. Ray, Professor, Department of Metallurgical and Materials Engineering, Indian Institute of Technology Roorkee, Roorkee.

The matter presented in the thesis has not been submitted by me for the award of any other degree of this or any other Institute.

(MANOJ KUMAR KUSHWAHA)

This is to certify that the above statement made by the candidate is correct to the best of our knowledge.

(S. Ray)
Supervisor

(Anjan Sil)
Supervisor

Date: 22/7/09

The Ph.D. Viva-Voice Examination of Mr. **MANOJ KUMAR KUSHWAHA**, Research Scholar, has been held on _____

Signature of Supervisors

Signature of External Examiner

ABSTRACT

The replacement of materials in conventional components by lightweight aluminium, its alloys and composites based on these matrices has lead to significant weight saving and consequently, improved fuel economy especially in space, aerospace, automotives and marine industries. In view of depleting fossil oil and its increasing cost, there is a need to pursue the objective of weight saving more aggressively by the materials and design engineers. Aluminium and its alloys have been extensively investigated because of their high strength to weight ratio, good corrosion resistance, and high thermal conductivity. However, these materials have shortcomings including low hardness, high friction coefficient, tendency of galling and difficulty in lubrication, which limit their extended applications. These shortcomings may be overcome by developing self-lubricated, hard and wear resistant coatings of nano-composites which has opened up new possibilities in extending material properties.

The basic idea of the present work is to develop an oxide layer over the surface of aluminium of different levels of purity by anodizing process, a traditional and relatively simple way to impart hardness and thus improve wear and corrosion resistance of aluminium and its alloys. But the hard anodic oxide film surface does not provide a low friction lubricating surface. It is fortunate that the anodized surface has porosity and it is possible to generate self organized pores in this oxide layer by appropriate control of the anodization process. The porous anodic alumina films are potentially advantageous as lubricant reservoirs, although they have received only limited preliminary attention in tribology. The pores in the anodic aluminium layer could be impregnated by the lubricant (either in the liquid or solid state or both) and there will be slow dispensing of the lubricant on the sliding surface from the pores, which have very high aspect ratio (depth divided by diameter).

Invention of Carbon nanotubes (CNTs) in the early nineties has provided the possibility of a graphene based structure which may fit in the pores of anodized alumina. Two step anodization process developed in the mid nineties has resulted in near perfect hexagonally ordered nano-sized pores in anodic alumina layer. These mono-disperse nano-pores could act as templates for aligned growth of CNTs. Thermal chemical vapour deposition (CVD) process is widely used for the growth of CNTs/ Carbon nanofibers (CNFs). These CNTs and/or CNFs have shown low friction because of their graphitic structure and peculiar geometry. However, tribological applications of CNTs are still in its infancy. A few research groups have reported the tribological application of CNTs/CNFs which are limited to low loads primarily for MEMS and NEMS. No studies, to the best of my knowledge, have examined such tailored surface of anodized alumina layers containing CNTs/CNFs in the nano-sized pores for engineering applications at higher loads.

In view of the above, the present study involves study of two stage anodization process of pure and commercially pure aluminium for developing self organized nano-sized pores in the porous anodic aluminium oxide (PAAO). CNTs/CNFs have been grown in the pores of these PAAO substrates to result in alumina based composite. The tribological performance of the composite surface of porous anodic aluminium oxide (PAAO) having CNTs/CNFs embedded in it, has been studied under dry sliding condition and also, in presence of lubricant oil with the objectives to develop a low friction wear resistant surface. The effect of process parameters on the outcome has also been investigated for the different stages of the overall process, viz. (i) anodization (formation of porous anodic alumina substrates) and (ii) growth of CNTs/CNFs in the pores of the substrates by thermal CVD.

The work in the thesis has been divided in the following seven chapters.

Chapter 1 (*Introduction*) presents a brief overview on the role of aluminium and its alloys in transportation, aerospace sectors and light weight structural components. It

also provides a brief introduction to the importance of various aluminium based self-lubricating wear resistant coatings including porous anodized aluminium oxide layer embedded with CNTs/CNFs in the pores by CVD. The tribological behaviour of these surfaces has been discussed.

Chapter 2 (*Literature Review*) presents a review of the literature pertinent to all sections of the thesis work. Summaries of the research findings reported by various research groups world wide are presented. This chapter has been subdivided into three sections. Section **2.1** describes the various aspects on preparation of Porous Anodic Aluminium Oxide (PAAO) template as it has been used in the present study to grow Carbon Nanotubes (CNTs) and Carbon Nanofibres (CNFs) in the pores. Major emphasis has been given on the optimization of PAAO growth as tribological performance of the coating developed, depends upon the morphology and structure of PAAO. Various aspects of anodization process, including pre-treatments and post-treatments applied have been discussed. Two-step anodization, an effective way for obtaining well ordered porous structure has been described in detail. An overview on effects of various process parameters of anodization on the resulting pore structure, morphology and material properties has been presented.

In section **2.2**, growth of CNTs/CNFs in PAAO has been discussed. Since present study deals with the cost-effective thermal chemical vapour deposition method to grow CNTs/CNFs, therefore major emphasis has been given to develop self-lubricating coating by this method only. However, other methods for CNT/CNF syntheses have also been discussed in brief. The effect of CVD parameters on the resulting CNTs/CNFs structures has also been discussed.

Section **2.3** describes tribological studies on the CNTs/CNFs embedded PAAO. It is to mention that very few research results are available in the open literature.

Chapter 3 (*Experimental*) describes experimental procedures used in the present work for developing CNTs/CNFs embedded self-lubricated porous anodic aluminium oxide (PAAO) nano composite surfaces. Details of testing equipments and testing/characterization methods used for the preparation of composite surfaces

and their tribological testing are presented. Since morphology and chemical composition play a crucial role in the performance of the nano sized materials, Field Emission Scanning Electron Microscopy (FESEM) coupled with EDAX is used to examine the morphology of the surfaces at all the three stages i.e. development of (i) PAAO layer, (ii) CNT/CNF and (iii) tribo surface characteristics. This chapter has been divided into three different sections. Section **3.1** describes the anodization and pore structure characterization of PAAO developed. Section **3.2** deals with the experimental method (thermal CVD) to grow CNTs/CNFs within the pores of AAO. The CNTs have been characterized by Raman spectroscopy and TEM Section **3.3** describes the tribological testing procedures and associated characterization techniques used in this study.

Chapter 4 (*Results and discussion: Anodization*) outlines the results of the anodization and their explanation. This chapter has been further subdivided into various sections, the results of initial steps, which are common to all processes for anodization, have been presented. The effect of pre-treatment of as-received substrate on the morphology of resultant anodized alumina film and the improvement in the ordering of porous structure in two step anodization compared to one step anodization are reported. The surface roughness of the substrates as estimated by optical profilometer and Atomic Force Microscope (AFM), decreases significantly in pure as well as in commercial aluminium samples by electropolishing. Pore ordering has been found to improve if samples are pretreated by annealing than electropolishing. However, the samples with joint electropolishing and annealing show still better ordering.

The current density through the sample increases exponentially with voltage applied. The porosity that develops in the PAAO decreases as the anodization voltage increases. The effects of process variables such as applied voltage, current, temperature, concentration and pH of the electrolyte, on the resulting anodized alumina structure for acid electrolytes, are presented in this chapter. The results of anodization i.e. ordering and uniformity of the porous

structure obtained by phosphoric acid, oxalic acid, chromic acid and sulphuric acid electrolytes are presented, which have further been subdivided into two sections in which the structural features of the grown anodized layer of pure aluminium and commercial aluminium samples have been reported.

'Self ordering regime', is a set of anodization parameters for a given electrolyte, which provides well–ordered porous structure. Such regime has also been established for phosphoric and oxalic acid electrolytes in the present study. The time duration in the first step of anodization also plays a key role in the degree of ordering. Longer the time duration, more is the degree of ordering. On the basis of characteristics of the porous alumina films, it can be concluded that

1. The pore diameter and interpore distance are linearly dependent on the applied voltage.

2. The degree of ordering of the porous film morphology is a function of time duration of anodization in the first step of the standard 'two-step anodization process'.

3 The self-ordering voltage varies with the electrolyte used. Electrolytes which have higher dissolution ability of aluminum have lower self-ordering voltage.

4. There is no significant change in the results of anodization on pure aluminium and commercially pure aluminium substrates. However, pure aluminium is slightly better in terms of regularity and ordering of porous structure.

Chapter 5 (*Results and discussion: CNTs/CNFs growth within porous Alumina*) provides the results of the experiments carried out to establish influence of PAAO templates and that of CVD process parameters on the growth and morphology of resulting CNTs/CNFs embedded PAAO. This chapter has been divided in six sections. Section **5.1** provides common findings of growth evidence of CNTs/CNFs in the pores through cross sectional view of CNT embedded samples and EDAX analysis for a few representative samples. Section **5.2** provides influence of pore diameter of the PAAO template on the diameter of the CNTs/CNFs produced by CVD. Section **5.3** describes effects of

catalyst and the catalyst deposition process on the resulting morphology and structure of the CNTs/CNFs developed. Three subsections of 5.3.1, 5.3.2 and 5.3.3 explain the influences of catalyst deposition process, the type of the catalyst and PAAO template acting as catalyst, respectively on the morphology of CNTs/CNFs. Sections **5.4** and **5.5** provide results of influence of time and decomposition temperature of CVD on CNTs/CNFs structure and morphology.

On the basis of the results obtained, following inferences have been drawn.

(a)   The diameter of the PAAO template plays a major role on the growth of CNTs/CNFs within the pores, especially from the bottom of the pores.

(b)   For pore size less than 100 nm, CNTs/CNFs grow from the top of the PAAO, rather than from the pore bottom.

(c)   Catalyst deposition is an important step in the synthesis process as improper deposition conditions lead to defective structures in CNTs / CNFs.

(d)   Type of the catalyst influences the growth, structure and morphology of the CNTs/CNFs. When cobalt is used as catalyst, a good yield of tubular structures is obtained. CNTs/CNFs are found to grow from the bottom of the pores and such growth scheme is found applicable in majority of the pores.

(e)   The CNTs characterization by Raman spectroscopy shows that CNTs with highest degree of graphitization can be obtained using Lithium compound catalyst used. The catalysts Cobalt, Nickel and Nickel-Cobalt compound used result in decreasing order of graphitization in the CNTs developed.

(f)   CNTs growth on PAAO substrate mainly from the top surfaces has been observed without any catalyst used, however the growth in this case is non-uniform and sparsely distributed.

(g)   The optimum time required for the growth of CNTs at 650 °C is 10 minutes. The carbon structures other than tubular structure (CNTs and CNFs) are found to develop for growth time more than 10 mins.

(h)   When CVD temperature is kept at 500° C, no growth of CNTs has been observed except at few points.

(i)   The average diameter of the CNTs/CNFs has been found to increase exponentially up to a certain limit of temperature.

(j)   There are other factors which also affect growth of CNTs/CNFs by CVD in PAAO and therefore the synthesis is a complex process.

The chapter ends with a discussion on all of the above mentioned results.

Chapter 6 (*Results and discussion: Dry and lubricated friction and wear*) presents the results of tribological studies on the composite surface of PAAO embedded with CNTs/CNFs. Dry sliding friction and wear behaviour have been studied in a pin on disc set-up against the counterface of hardened steel under different normal loads and fixed sliding speed. The results have been compared with that of the PAAO alone without any CNTs/ CNFs in the pores. In addition, wear tests on the composite surface has been carried out in presence of lubricating oil and the results have been compared with the corresponding results for dry sliding. The pores in PAAO surface have been sealed and subjected to wear tests both under dry and lubricated conditions, for comparison. The following are the findings:

(i)   CNTs/CNFs embedded PAAO results in reduction in both wear rate and friction forces compared to that of PAAO alone, tested under dry sliding condition.

(ii)   The wear and friction on the surface of PAAO alone and that with CNTs/CNFs embedded in pores decrease markedly in presence of lubricating oil over those observed under dry sliding condition.

(iii)   Wear resistance of PAAO surface anodized in oxalic acid is generally more than that of the surface anodized in phosphoric acid bath. However, the friction coefficient is significantly lower on the surface anodized in phosphoric acid bath as compared to that on the surface anodized in the oxalic acid bath but there is a trend reversal for friction in presence of lubricating oil i.e. friction is less on surface anodized in oxalic acid bath compared to that anodized in phosphoric acid bath.

These results are followed by discussion.

Chapter 7 *(Conclusions)* presents the major conclusions

ACKNOWLEDGEMENTS

periods. Above all, I am highly indebted to the almighty God, who blessed me with spiritual support and fortitude at each and every stage of my work.

CONTENTS

LIST OF FIGURES

of the as-received pure aluminium sample with rolling marks/ scratches and minor pits visible (d).

Electron) emission mode images of the PA sample on the right side (b), anodized in 0.5 M Phosphoric acid at 150 V at room temperature

anodization in the first step and 0.5 hour in the second step and inset shows its FFT.

figure.

xxx

sliding wear test. (c) EDS of the surface before dry sliding and (d)
EDS of the surface after dry sliding

Oxalic acid electrolyte

LIST OF TABLES

LIST OF PUBLICATIONS

1. Kushwaha M.K., Sil Anjan and Ray S. *"Journal of Nanoscience and nanotechnology"*, vol. 8, no. 8, pp 4152-4158 (2008). American Scientific Publishers, USA, titled "Carbon nanotube/nanofiber embedded nanoporous Anodized aluminium oxide surface and its tribological properties."

2. Kushwaha M.K., Sil Anjan and Ray S. (2007) Poster presentation titled "Carbon nanotube/nanofiber embedded in nanopores of Anodic aluminium oxide (AAO) surface." and abstract published in the proceedings of the *International conference ANM-2007, held at I.I.T. Bombay, Mumbai,* India, 8-11 Jan. 2007.

3. Kushwaha M.K., Sil Anjan and Ray S. (2007) Preparation of Anodic Aluminium Oxide (AAO) surface and its pore distribution characteristics published in the proceedings of the *International conference CPIE-2007, held on 22-24 march 2007 at Dr. B R Ambedkar National Institute of Technology Jalandhar* (India).

4 Kushwaha, M.K., Sil. Anjan and Ray S. (2008) Pore distributions in porous anodic aluminium oxide (PAAO) surfaces of pure and commercial grade aluminium substrates, (communicated to Thin solid films)

The replacement of materials in conventional components by lightweight aluminium, its alloys and composites based on these matrices has led to significant weight saving and consequently, improved fuel economy especially in space, aerospace, automotives and marine industries. In view of depleting fossil oil and its increasing cost, there is a need to pursue the objective of weight saving more aggressively by the materials and design engineers. With an annual consumption of 25 million metric tons, aluminium is one of the world's most commonly used metals. Its lightness coupled with its strength, conductivity, barrier properties and its excellent corrosion resistance have all been and continue to be its most important advantages and the main reasons for the continued growth in its use. Due to these advantages, aluminium and its alloys have been extensively investigated; however, these materials have shortcomings including low hardness, high friction coefficient, tendency of galling and difficulty in lubrication, which limit their extended applications. These shortcomings may be overcome by (i) developing self-lubricated, hard and wear resistant coatings of nano-composites, (ii) using surface engineered aluminium based components, which have opened up new possibilities in extending material properties. 'Various surface treatments such as physical vapour deposition (PVD), laser irradiation have been applied to aluminium-matrix materials to improve their generally poor tribological properties.

Anodic oxidation or anodizing process is a traditional and relatively simple way to impart hardness and thus improve wear and corrosion resistance of aluminium. It is economical than either vacuum-based techniques, such as ion implantation, sputtering deposition, and ion plating, or chemical vapour deposition. However, anodic oxide film surface is hard and has high friction coefficient when sliding against metal and consequently make high friction sliding pair with metals. The bulk of the anodic oxide consists of nonporous (barrier layer) and porous layers. It is possible to generate the pores in the porous layers self organized by appropriate control of the anodization

process. There are several parameters such as voltage, temperature, bath concentration etc., which cont rol the anodization process. The porous anodic alumina films are potentially advantageous as lubricant reservoirs, although they have received only limited preliminary attention in tribology. The pores in the anodic aluminium layer could be impregnated by the lubricant (either in the liquid or solid state or both) and there will be slow dispensing of the lubricant on the sliding surface from the pores, which have very high aspect ratio (depth divided by diameter). The friction coefficient of the anodic oxide film thus can be effectively reduced and its lubricating performance improves by the lubricating phase impregnation. While oils or low molecular weight polymers are used as liquid lubricant, in many situations, a solid lubricant especially MoS_2, which outperforms oils and greases, particularly with respect to load-carrying capacity, temperature range of application, vacuum/environment compatibility, etc. is preferred. However, such solid lubricant may suffer from the problem of surface retention as in majority of the cases the lubricant is applied to the surface externally. Solid lubricant polytetrafluoroethylene (PTFE) is also used in many situations. Considering the facts that the temperature of the contacting surfaces may rise to as high as 90°C during the use and a define limitation of surface retention, therefore development of alternative materials and processing by way of nanocomposite self-lubricated surfaces have made in-road in the recent years by the researchers.

Invention of carbon nanotubes (CNTs) in the early nineties has provided the possibility of a graphene based structure which may fit in the pores of anodized alumina. Two step anodization process developed in the mid nineties has resulted in near perfect hexagonally ordered nano-sized pores in anodic alumina layer. These mono-disperse nano-pores could act as templates for aligned growth of CNTs. Thermal chemical vapour deposition (CVD) process is widely used for the growth of CNTs/CNFs. These CNTs and/or carbon nanofibers (CNFs) also have shown low friction coefficient because of their graphitic structure and peculiar geometry. However, tribological applications of CNTs are still in its infancy. A few research groups have reported the application of CNTs/CNFs which are limited to low loads primarily for micro-electro mechanical system (MEMS) and nano-electro mechanical system NEMS. No studies, to the best of my knowledge, have examined

2

such tailored surface of anodized alumina layers containing CNTs/CNFs in the nano-sized pores for engineering applications at higher loads.

In view of the above, the present study involves study of two step anodization process of pure and commercial pure aluminium for developing self organized nano-sized pores in the porous anodized aluminium oxide (PAAO). CNTs/CNFs have been grown in the pores of these PAAO substrates to result in alumina based composite. The tribological performance of the composite surface of porous anodic aluminium oxide (PAAO) having CNTs/CNFs embedded in it, has been studied under dry sliding condition and also, in presence of lubricant oil with the objectives to develop a low friction wear resistant surface. The effect of process parameters on the outcome has also been investigated for the different stages of the overall process, viz. (i) anodization (formation of porous anodic alumina substrates) and (ii) growth of CNTs/CNFs in the pores of the substrates by thermal CVD.

LITERATURE REVIEW

The literature survey has been focused on fabrication of Porous Anodic Aluminium Oxide (PAAO) template as it has been used in the present study to grow carbon nanotubes (CNTs) and carbon nanofibres (CNFs) in the pores. The knowledge as available on the growth of CNTs/CNFs has been reviewed with special emphasis on chemical vapour deposition (CVD) method, which has been used in the present study. The surface so tailored on the nanometer scale has been investigated for tribological behaviour and so, the prior knowledge in the tribology of ceramic matrix nano-composites has also been covered in this chapter. The concluding section poses the problem investigated in this study.

2.1 FORMATION OF NANOPOROUS ALUMINA BY ANODIZATION

The overall process for the formation of PAAO surface has been categorized into three major steps of (a) pretreatment (b) anodization and (c) post-treatment. The following subsections review the status of these procedures.

2.1.1 Pre-treatments

The response of a substrate towards anodization depends importantly on the history of the materials preparation, its composition and processing route (Fratila et al, 2002). In order to make the substrate favourable for anodization with an expected well-ordered hexagonal nano-porous alumina structure over larger domains, pretreatment is an important step prior to actual anodizing operation (Wu et al, 2002). The pretreatment involves the following steps: (a) mechanical polishing, (b) annealing, (c) degreasing and (d) electro-polishing. However, it is not always necessary to follow all the steps as observed from the literature, because ideally hexagonal ordered or very well–ordered porous structure is desired only in some special applications.

Mechanical polishing is needed if the substrate surface is very rough, so that it becomes relatively smooth and flat. However, the mechanical polishing has a drawback as large amount of stress develops on the surface as well as subsurface due to the polishing operation, which leads to disordered pore structure (Wu et al, 2002 and

Bocchetta et al, 2003). Hence the polishing step is followed by annealing to relieve these stresses before electro-polishing treatment is carried out.

Annealing of the aluminium substrate in the presence of inert gas atmosphere of N_2/Ar is commonly performed in order to increase grain size, reduce dislocation density, eliminate residual stresses present, if any, during rolling and mechanical polishing and thus obtains uniform conditions for pore growth over large area of the sample surface (Jessensky et al, 1998(a)). However, pores can also be obtained without annealing treatment, but their ordering in that case is generally limited to small domains as it is clear that the correlation of self-organization is at least disturbed by a large number of grain boundaries in the non-annealed aluminum foils having smaller grain size (Chic and Xu, 2004). Annealing in some cases is done to facilitate deformation to indent the substrate surface for ordered pre-texturing the sample for anodization using a hardened master in the imprinting process. These well-ordered indents then act as ordered pore initiation sites and on subjecting them to anodization result in well-ordered porous anodic alumina formation. A large number of studies that have been conducted to show the effect of annealing parameters on the final (PAAO) film morphology, have reported a common finding that ordered arrays of PAAO over large domains (up to 3 mm size) can be obtained with high purity aluminium annealed properly (Jessensky et al, 1998(a) and Masuda. et al, 1995). However, a few studies (Lu Bin 2000 and Kaatz et al 2003) also reported that the annealing has no significant effect on improvement of pore ordering.

. In some recent works, the researchers studied the effect of variation of time and temperature parameters of the annealing process and their observations are summarized below. The ordered domain size increases with increasing annealing time. The increase in annealing temperature also results in increased ordered region of nanopores (Yu. et al, 2006). The overall view from the literature shows that the purity of the aluminium plays major role on pore ordering. However, the electro-polishing and annealing help to further improve the ordering, though the annealing step has a better influence than electro-polishing (Lo at al, 2007).

Degreasing is generally carried out to make aluminium surface free from any dirt or grease present on the surface (Montero et al, 2007). There are different types of degreasing methods available and these methods generally refer to degreasing aluminium samples with acetone in an ultrasonic bath, followed by rinsing the samples in methanol and isopropanol solutions.

Electro-polishing is defined by ASTM as the improvement of surface finish of a metal affected by making it anodic in an appropriate solution (Annual book of ASTM Standards, 1979). This process, very common in aluminium finishing industries, selectively removes high points on metal surfaces and provides the surface a high luster with reduced surface roughness (R_a) (Landolt, 1987). The R_a has a direct influence on the tribological properties of the sliding surfaces, which is an important aspect of the present investigation. It has been found that the degree of surface finish of the substrate remains almost same after anodization (Skoneczny et al, 2004), hence good surface finish is required prior to the anodization step. A flat etching front obtained by polishing is also required for ordered pore formation during anodization. (Wu et al, 2004 and Jessensky et al, 1998 (b)). The high Ra causes quick formation of barrier oxide and pores at depressions in the surface compared to other smoother locations. The pores that nucleated at such depressions in an early stage will grow sooner than at other sites. The roughness is thus transferred to the anodization front, at the interface between the aluminium and the oxide layer, and prevents self-organization. (Chic and Xu (2004). Chi k and Xu (2004) also confirmed t hat pre-annealing of the aluminium substrate can increase the grain size, while stirring of the electrolyte during oxidation, and using smooth electropolished aluminium surfaces are all necessary for obtaining ordered hexagonal structures with typical long range ordering of 100 μm^2. Due to the amphoteric nature, aluminium can be electropolished in both acid and alkaline electrolytes; however, a smooth surface finish is usually obtained when polishing is performed in concentrated acid-type solutions. In addition, many researchers, including Yu et al (2007) observed that the topographies of electropolished Al sheets depend on the surface crystalline orientation, while there are some contradictory reports also (Lu et al, 2000). The mean roughness of the polished surface was measured by atomic force microscopy and the value is to be 3 nm over a 3 mm sq scan area (Li et al (1998).

Montero et al (2007(a)) mainly focused on two pretreatment steps i.e. electropolishing and acid etching, as well as the intermediate stripping step. The pretreatment procedure was optimized by accounting for the chemical nature of the substrate, with the results indicating that additional pretreatment steps enhanced the self-ordered porous arrangement. Yu et al (2007) in a very systematic investigation, have observed the influences of electropolishing variables, such as agitation rate,

solution temperature, applied potential, electropolishing time, and the volume percentage of perchloric acid in ethanol–perchloric acid solutions, on the surface roughness of the industrially pure aluminum sheets (Al-1050, 99.5%) using fractional factorial design (FFD).

2.1.2 Anodization

(a) **Introduction:** When a fresh oxide-free aluminium surface is exposed to air at room temperature, an oxide layer (native oxide film) forms immediately because of the high affinity of the aluminium surfaces to oxygen. This oxide film protects the surface from further oxidation and therefore is called self-protecting native film. The thickness of such native film is only about 15 to 18 nm, which is susceptible to breakage and hence it could be artificially increased by anodization (Keller et al, 1953).

Anodization is defined as a process to produce an oxide film or coating on metals and alloys by electrolysis. The metal to be treated is made the anode in an electrolytic cell and its surface is electrochemically oxidized. Anodization of metals, especially aluminium has received a lot of attention since the beginning of the last century, due to its variety of applications, e.g. protective, decorative coatings and dielectrics (Diggle et al, 1969). It has also found applications also in micro filters and catalytic membrane reactors (CMRs) (Bocchetta et al, 2003). Thin film deposition and anodization are used for manufacturing embedded capacitors (Samudrala and Bandyopadhyay, 2009). Nowadays, PAAO film is used as one of the most prominent templates for synthesis of nanowires and nanotubes with monodisperse controllable diameter and high aspect ratio. (Montero et al, 2007a, Sarkar et al, 2007 and Piao et al, 2005). Moreover, PAAO can also be used as two dimensional photonic crystals (Choi et al, 2003a), and humidity sensors, (Pal et al, 2006). Porous anodic alumina template has the necessary multitude and diversity of attributes to play a crucial role in the future of nanotechnology.

(b) **Experimental procedure:** The detailed experimental procedure has been described in chapter-3. A brief introduction and a schematic diagram of the anodization cell is shown below in Fig. 2.1
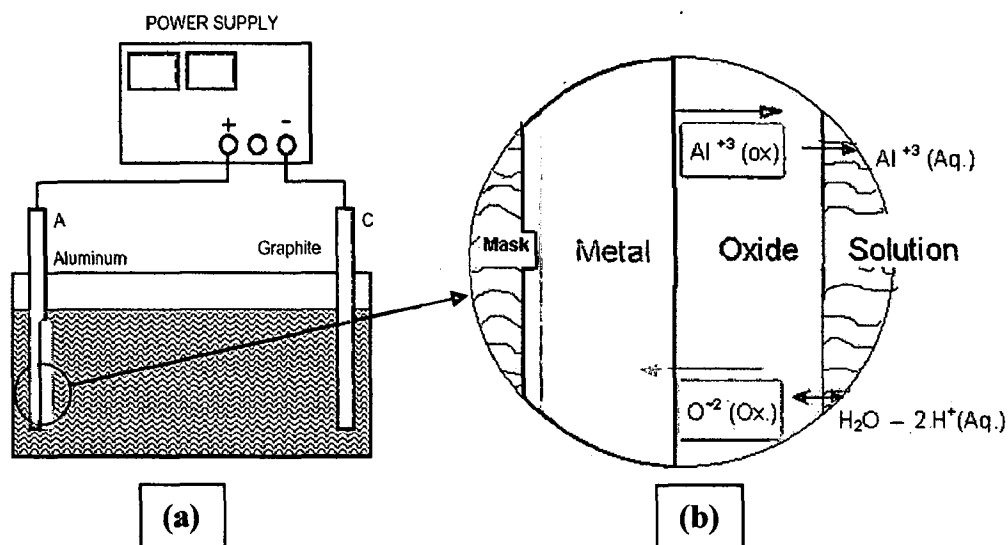
Fig. 2.1: Schematic diagram of (a) anodization cell and (b) magnified view of encircled portion of the oxidized anode.

The aluminium sample (shown in dark blue colour, Fig. 2.1) to be anodized is connected to the positive terminal A (anode) of the electrolytic cell. Cathode 'C' is made of any electrically conducting material. Direct current (d.c.) is passed through the cell under 'constant cell potential' or 'constant current density' mode. The current density / potential ranges, specific to the type of acid solution (electrolyte), is applied for a fixed time period at a fixed temperature of bath which kept constant by using thermostatic controlled arrangement.

(c)   Types of anodic oxide films, their structure and properties

Two types of anodic oxide films viz. (1) barrier or non-porous oxide film and (2) porous or duplex film are formed depending on the type of the electrolyte and its pH value. Barrier films are used as dielectric material in capacitors while porous films have numerous applications. Formation and morphology of porous films are extensively researched these days, due to its extra-ordinary ability to attain well-ordered, hexagonal (also as triangular lattice) porous morphology under some recipes of anodization parameters, termed as 'self-ordering regime'. This film has got very high potential for many industrial applications and its use as a template

in fabrication of many nano-devices e.g. synthesis of magnetic, superconducting and semiconducting nano-structures (Martin et al, 1994 and Saito et al, 1994).

Anodization of aluminium in a neutral or weak acidic solution, such as neutral boric acid, ammonium-borate, tartrate, and ammonium tetraborate in ethylene glycol (pH 5-7) leads to formation of a flat nonporous aluminium oxide film; commonly called a barrier-type film whose thickness depends on voltage (~1.4 nm/V) and maximum thickness is limited to few microns only. These films are limited by the film breakdown voltage of about 500-700 V (Keller et al 1953). A thicker but porous layer of aluminium oxide (up to 200 microns) can be formed by anodization of aluminium in a dilute acidic electrolyte (such as sulphuric, oxalic, chromic or phosphoric acids) in which alumina is partially soluble, due to a competing mechanism of oxide growth and partial dissolution of the aluminium oxide by the hydrogen ions (Thomson et al, 1997). The formation of self-organized porous structure using neutral electrolytes containing fluoride has been reported only recently. The thickness of the porous layer depends on the charge density. Fig 2.2 shows a schematic representation of the two types of anodic layers discussed.

(a)
compact barrier layer

Aluminium substrate

(b)

thin barrier layer

Aluminium
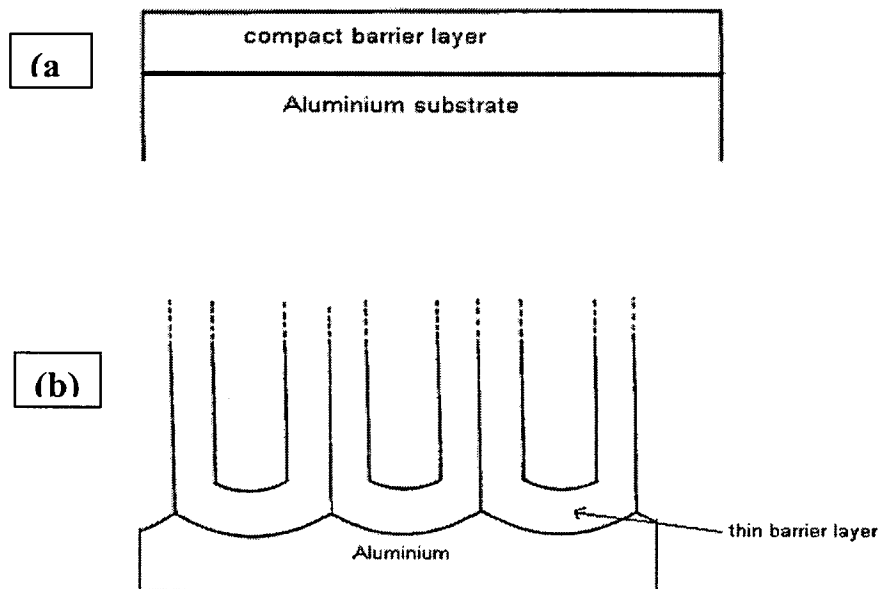
Fig. 2.2: A schematic of the (a) barrier and (b) porous types of films (Thomson et al 1997).

The reactions involved during anodization are as follows:

10

Anode	$2Al(s) + 3H_2O(l) = Al_2O_3(s) + 6H^+(l) + 6e^-$	(2.1)
	$Al(s) = Al^{3+}(l) + 3e^-.$	(2.2)
Cathode	$3H^+(l) + 3e^- = 3/2\ H_2(g)$	(2.3)
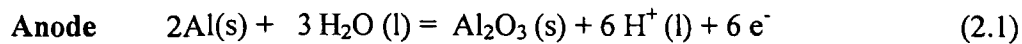
In case of barrier type oxide film formation, electrochemical oxidization of Al takes place by reaction (2.1) and negligible amount of aluminium dissolution into the solution is given by the reaction (2.2). However, for porous oxide films, both of the reactions, viz., (2.1) and (2.2) take place simultaneously. The hydrogen evolution reaction at the cathode (2.3) is common to both types of films formation.

The sealing reaction is as follows:

$$Al_2O_3 + 3H_2O = 2AlO\,(OH).H_2O \quad (Boehmite) \qquad (2.4)$$
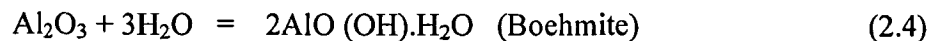
The anodic oxide films are described by different names by different researchers, however the present thesis will confine to PAAO for 'Porous Anodic Aluminium Oxide' and AAO for 'Anodic Aluminium Oxide'. The structure of PAAO is a close-packed array of columnar cells each containing a central pore of which the size and interval can be controlled by changing the forming conditions viz. voltage, current density, acid concentration etc. Both interfaces of the barrier layer have a characteristic scalloped shape. Fig. 2.3 depicts a schematic of ideal PAAO. Fig. 2.3 (a) shows its top view, while (b) shows cross-sectional view, which is generally obtained by intersecting the samples along pore lengths by a diamond knife (ultramicrtomy) (Shimizu et al, 1998). However there are many reports, including present work, in which cross-sectional views have been obtained by fracturing the brittle porous oxide layer along the length of the pores.
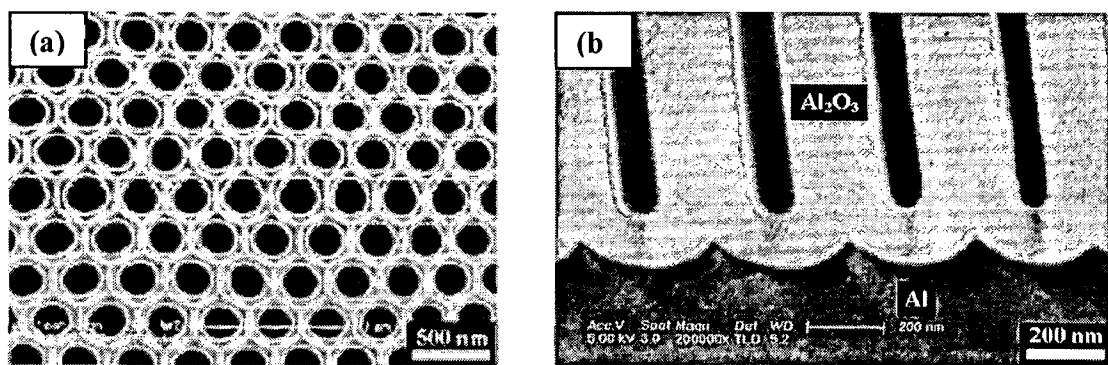
Fig. 2.3: Different views of PAAO showing its structural features; (a) top view and (b) cross-sectional view showing pore depth and barrier layer thickness (Li, Yanbo et al, 2006).

(d)   Voltage and current transients

AAO and PAAO of both barrier and porous type can be formed at constant voltage or constant current density mode. The shapes of the current-time and voltage-time transient curves are well established (Diggle et al, 1969) and can provide insight into the growth mechanisms and kinetics. Typical transients are shown in Fig. 2.4. Generally, both of these transients can be divided into two main regions, initial unsteady state and final steady state.

(a)   (b)
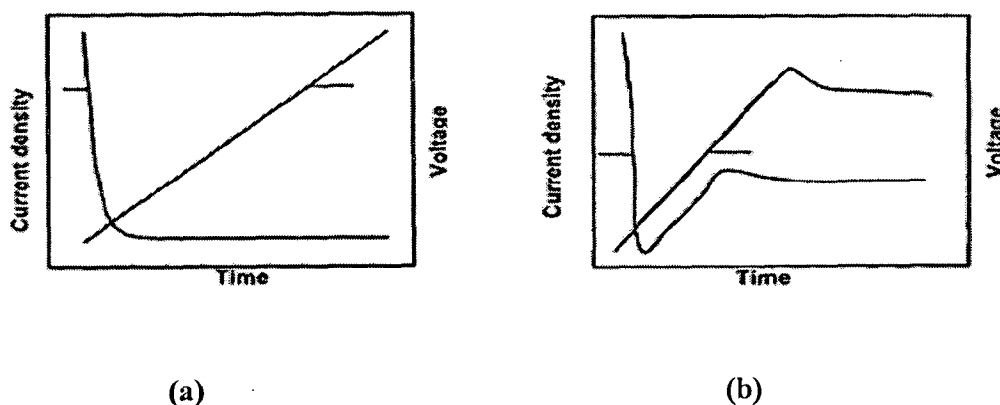
Fig. 2.4:   Voltage - current density transients in (a) barrier AAO and (b) porous layer PAAO formation.

Moreover, five different types of voltage-time and current-time transients have been classified by Tajima et al (1970) based on physical phenomenon that takes place during oxide growth.

1. **Barrier-type films:** At constant current, the voltage increases linearly with time due to a linear growth rate of the oxide until the potential is reached to the breakdown level. At constant voltage, the current decreases exponentially with time to low leakage current values due to the increasing resistance to migration and diffusion of anions and cations through the oxide, which is then maintained almost constant (Fig. 2.4a).

2. **Porous-type films:** At constant current, the voltage increases linearly with time until a critical value is reached when transition from barrier to porous type films occurs. The voltage decreases slightly, due to pore formation, and then reaches a steady state whose characteristics depend on the pH and the applied current

12

density. At constant voltage, the current decreases rapidly over a short period of time due to a sharp increase in barrier layer thickness and just after the initiation of pore formation, the current increases and reaches steady values after a long time. However, it is very often observed that during the steady state growth, the current density continues to decrease slightly. This is due to diffusion limits in the long pore channels. The decrease in voltage and the increase in current after pore formation are related to the increase in the active surface area due to the pores (Fig. 2.4 b). Parkhutic et al (1992) have explained these processes in four stages (I to IV) by the following sketch (Fig. 2.5), in which, the status of electrical transients as well as physical changes that occurs in the PAAO during anodization are depicted. The four stages of porous structure growth are shown in the lower diagram.

I. Barrier layer formation.

II. Pore-initiation.

III. Pore growth and

IV. Steady state pore growth.
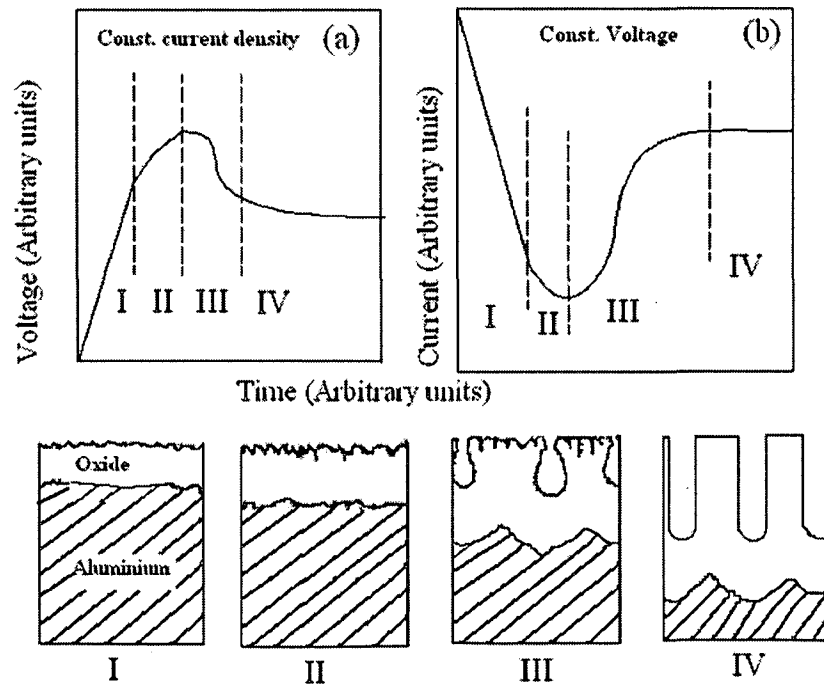
Fig. 2.5:   Schematic diagram of the kinetics of porous oxide growth on aluminium in Galvanostatic (Constant current) and (b) potentiostatic (Constant voltage) regimes (Parkhutic et al, 1992).

3. **Pitting:** At constant current, the voltage increases to a maximum value and decreases gradually with time to low values. At constant voltage, the current decreases sharply over a small time period reaching a minimum and then further increases slowly over time.

4. **Electropolishing:** At constant current, in strong acids, the voltage fluctuates periodically or remains steady at low values.

5. **Crystallographic chemical etching:** In very strong acids where chemical etching of oxide occurs, any oxide formed is etched chemically by the electrolyte instantaneously and the voltage stays at very low values.

For both types of oxide layers, Shimizu et al (1992) have calculated the current efficiency, by applying faraday's law, for oxide formation by measuring the rate of voltage rise and the amount of charge passed if the electric field is known. The maximum thickness of the barrier oxide is restricted by the oxide breakdown at high voltages typically around 500-700 V. In the case of porous type films, pores grow at a steady finite current or voltage (Fig. 2.4 and Fig. 2.5). The thickness of the porous layer is dependent on the anodization time, current density, electric field and temperature. At low temperatures (0-2 °C) porous films are compact and hard; however at high temperatures (>60 °C), thin and soft oxide films are formed due to high dissolution rates of aluminium ions/oxide into solution, sometimes, even leading to electropolishing or complete dissolution of the oxide films (Diggle et al, 1969).

(e)   Structure of porous anodic films:

As-prepared porous anodic aluminium oxide membranes are amorphous (Li et al, 2007) and its typical XRD pattern is depicted in Fig. 2.6. Thompson et al (1997) suggested that chemical composition of PAAO is not stoichiometric Al_2O_3, but incorporates a variable quantity of anion impurities and hydroxyl groups incorporated from the electrolyte into the alumina structure or bound to the alumina surface. They also suggested that aluminum oxides may consist of nano crystallites, hydrated alumina, anions, and water molecules.
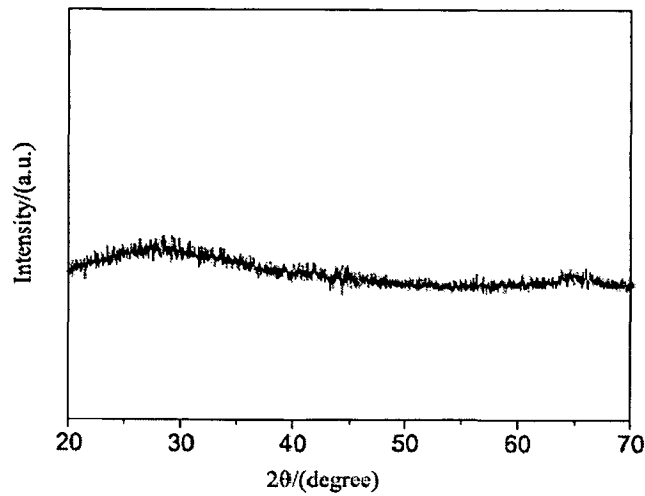
Fig. 2.6: The XRD pattern of the anodized sample (Li et al, 2007).

The high-temperature properties of the PAAO membranes were investigated by Kirchner et al (2007) using thermal analysis, mass spectrometry, X-ray diffraction and solid-state nuclear magnetic resonance. At 970 °C the amorphous alumina crystallizes to γ-Al_2O_3 with the release of SO_2 and O_2. Finally at 1228 °C the alumina converts into the thermodynamically preferred phase, corundum. The pore structure of the oxide membrane was found to be very stable at elevated temperatures, suggesting applications in materials synthesis, catalysis and gas separation (Kirchner et al 2007). A typical example to show the crystallization of amorphous alumina by heating is shown in Fig. 2.7.
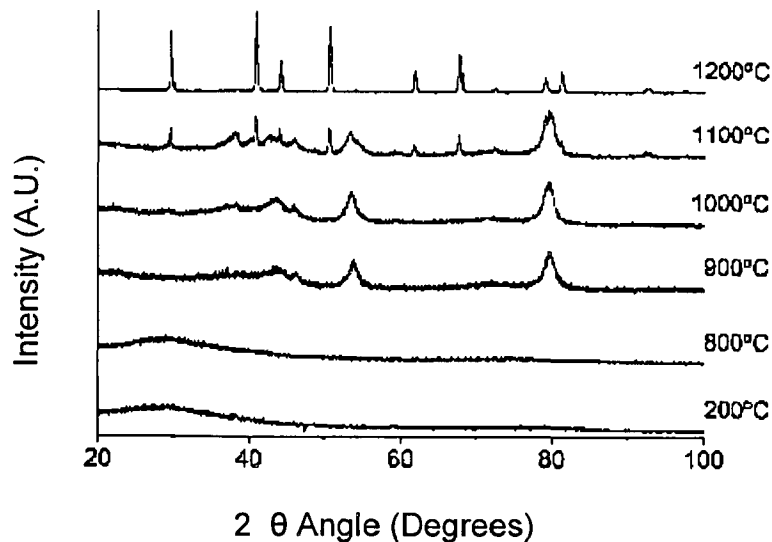
Fig. 2.7: Co-Kα radiation XRD powder diffraction patterns of PAAO heated in steps to various temperatures (Kirchner et al, 2007).

(f) Formation and ordering mechanisms of PAAO films: The high potential of hexagonally well-ordered PAAO films in nanotechnology applications have fuelled in a lot of research work related to the formation and ordering of porous alumina since last decade (Martin et al, 1994 and Saito et al, 1994). The synthesis of porous alumina with self-organized pore size, spacing (tailor-made) and ordering by various techniques became possible recently due to advent of scanning probe lithography (Shingubara et al, 2003), focussed-ion beam (Liu et al, 2003), electron beam lithography (Li et al, 2000) and direct writing laser (DWL) lithography (Stasi et al, 2007). The porous alumina formation has been studied extensively by many researchers in the past 50 years, but till date, there is no consensus opinion about the mechanism, which can conclusively explain pore formation. However, control of the pore size, shape and ordering has been made possible from the work initiated by Masuda and coworkers (Masuda et al, 1996) using two-step anodization.

The electric field applied during the anodization causes the thickening of the native oxide layer (barrier layer) in the beginning followed by on dissolution of this pre-formed barrier oxide layer at some weak points such as at grain boundaries (Bandyopadhyay et al, 1996), at the site of accumulated impurities, at the site where oxide thickness is minimum, or the site at which the surface is concave shaped. Electric field gets concentrated at these sites (Sullivan et al, 1970) resulting in initiation and growth of the pores due to self-perpetuating mechanism or due to positive feedback mechanism (Bandyopadhyay et al, 1996). In the beginning, dissolution occurs at a single point. At this single point, the oxide thickness is reduced and current flows to repair the damage to the oxide layer (oxide formation). This increases the electrolyte temperature at this point, and more rapid dissolution of oxide occurs at the same point. Therefore, both the oxide formation and dissolution are assisted by electric field. This mechanism would perpetuate a pore once it is formed. As the current continues to flow through the single pore, additional oxide forms such that an oxide cell is created. Because the voltage and current fields originated from a point tend to be spherical, the advancing front of the oxide cell would be spherical. Because the pore is of finite size, the cell front will have the shape of spherical section somewhat less than a hemisphere (Keller et al, 1953).

In the stage/process of PAAO formation, due to the competition that prevails among the growing pores, all pores can not grow to the same extent due to different degrees of heterogeneity in the metal just below the growing pores. A few of the pores stop growing while others will continue to grow. A dynamic equilibrium is established between oxide formation at the metal /oxide interface and field-enhanced dissolution of the oxide at the electrolyte/oxide interface. Oxidation occurs at the metal/oxide interface by the migration of O^{2-} or OH^- from the electrolyte as per the reaction (Eq. 2.1) (Uchi et al, 2001). Dissolution of the oxide layer is caused mainly by the hydration reaction of the formed oxide layer as shown below (Shimizu et al, 1992).

Figure 2.8 shows the schematic diagram of pore formation and movement of ions through the barrier layer
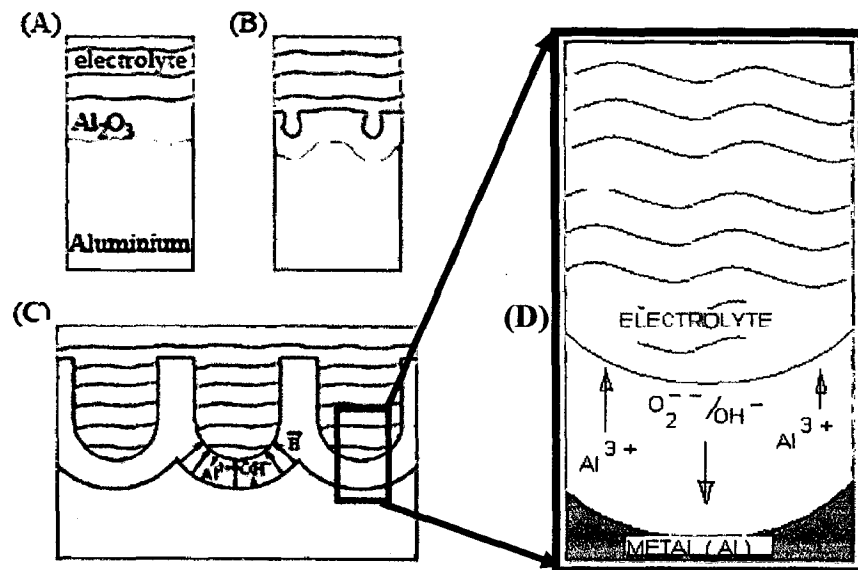
Fig. 2.8: Schematic showing (a-c) pore formation stages (d) enlarged image of the rectangular marked portion of (c) in showing movement of ions through the barrier layer

A great deal of understanding the morphology, ion transport and the initial stages of pore formation was put forward by Thompson et al (1987), Shimizu et al (1991,1992), who performed a variety of studies using marker and tracer along with transmission and scanning electron microscopic analysis. The classic work by Sullivan et al (1970) in the research of porous alumina which was explained by their TEM studies is the basis of the present understanding of the pore formation and its kinetics.

The sectional view of TEM images showed that the scallopes in the aluminium surface formed simultaneously with the formation of the pores. The pores and the spherical scalloped regions increase in their size (diameter) resulting in pear drop shaped pores. The scallop size increased with time until they merged with other scalloped regions, thus resulting in porous alumina with uniform size at steady state. Sullivan et al (1970) also measured the barrier layer thickness, pore size, spacing and established a direct relationship of these parameters with the applied voltage. They have also explained the field-assisted dissolution mechanism. The electric field polarizes the aluminium-oxygen bond, causing stretching and breaking of the aluminium-oxygen bonds and lowers the effective activation energy for dissolution (Fig. 2.9). This in turn leads to field assisted and thermally enhanced dissolution at the bottom of the pores.
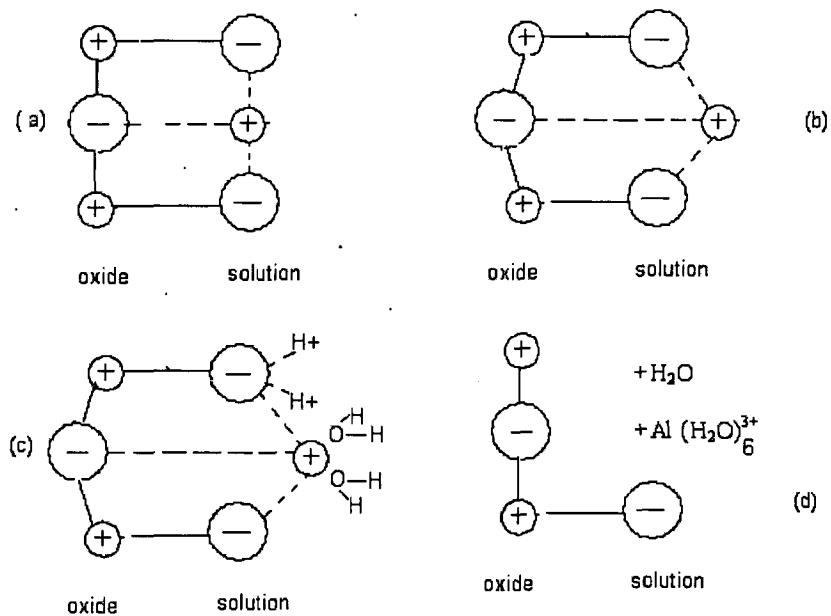
Fig. 2.9: Schematic representation of the field-assisted dissolution of Al_2O_3 (a) before polarization, (b) after polarization, (c) removal of Al^{3+} and O^{2-} ions, and (d) the remaining oxide. (Sullivan et al, 1970).

The field assisted dissolution rate, first proposed by Hoar et al (1959) depends on the pore geometry and therefore, it is not possible to quantify the dissolution through a simple model. Shimizu et al (1992) concluded that the buildup of tensile stress in the oxide contributed to local cracking of the film above pre-existing metal ridges (from electropolishing) on the metal surface. They also suggested that cracked regions are repaired by oxidation processes; however this leads to non-uniform film growth. The locally thinner regions then become preferred regions for pore development (Fig 2.10).
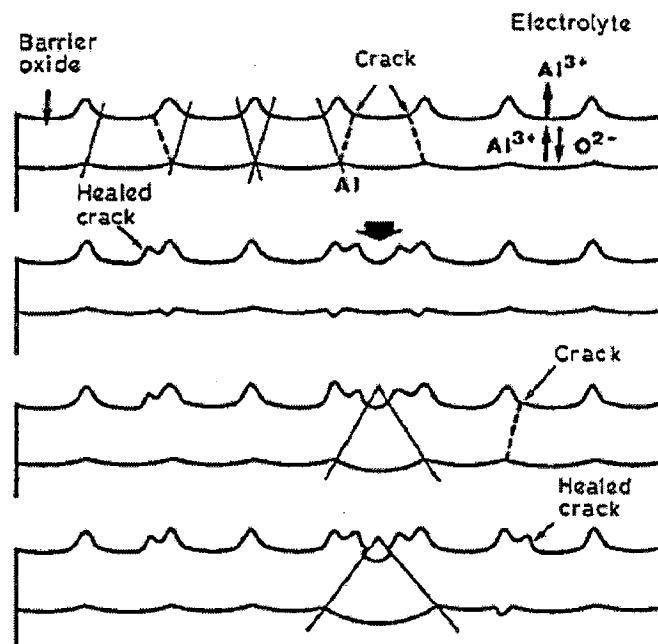
Fig. 2.10:   Schematic diagram showing pore development during anodizing of aluminium, oxide cracking and healing process that occur due to tensile stress in oxide during porous alumina formation as explained by Shimizu et al (1992).

However, they neither confirmed the presence of stress by experimental measurements nor explained the mechanism of formation of pores with a characteristic spacing dependent on the applied voltage / current, pH and temperature.

(g)   Theoretical modeling of porous oxide formation: Though there were several experimental studies reported to understand pore ordering mechanism in the anodization process and to have a control on the process parameters to result in a desired pore structure, there has been no consensus view towards controlling the parameters for obtaining pore ordering. However, in most of the cases the pore ordering was achievable, but the control strategies vary from each other. Therefore, researchers attempted to put forward theoretical models to support the experimental results. These models are attractive for testing pore formation mechanisms, because they can predict the evolution of the film to the steady-state morphology, and evaluate the consistency of a mechanism with observed steady-state film geometries. Few models for PAAO have been developed based on descriptions of ion transport and interfacial reactions (Parkhutik et al, 1992 and Thamida et al, 2002) and on the coupling of interfacial reactions and transport with elastic stress and surface energy (Singh et al, 2005). These models were based on the potential distribution in the film, which determines the rates of metal oxidation at the metal/film interface, and transfer of oxygen and aluminum ions at the film/solution interface. The interfacial reaction rates dictate the rates of interface motion, and hence the evolution of film geometry.

(h)   Ordered pore formation: The formation of disordered or poorly ordered PAAO by the anodization of aluminium has been widely studied (Edwards et al, 1941 and Edwards et al, 1944). Many researchers like Keller et al (1953) have reported on the structural features, factors affecting the formation of PAAO, direct observation of barrier layers, nucleation and growth. However, the pore structures obtained in their studies were either poorly ordered or disordered. Later, many researchers have reported well ordered pore formation. A simple line diagram of the ordered PAAO film is shown in the Fig. 2.11 below.
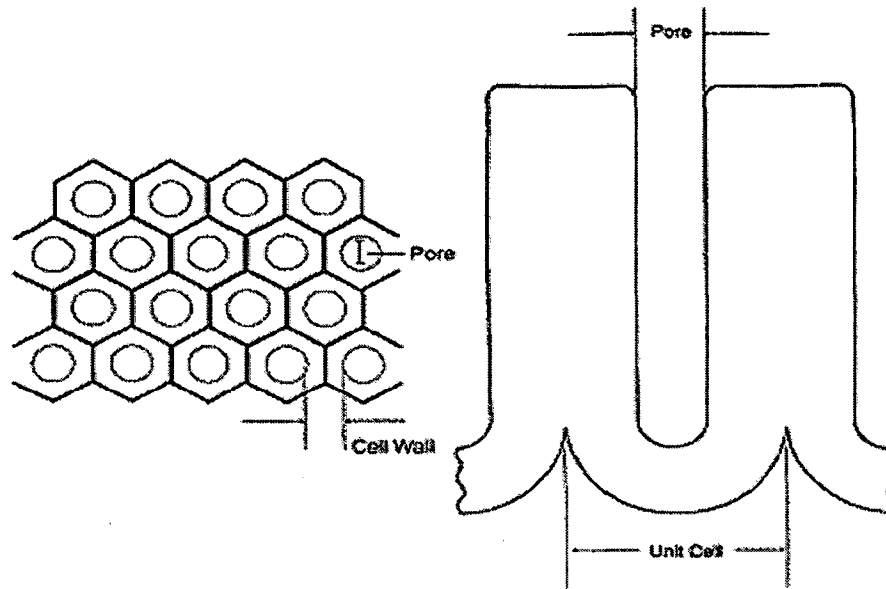
Fig.: 2.11: Schematic depiction of the hexagonally ordered porous anodic aluminium oxide film that forms on the surface of aluminium upon anodization. Both the top view (left) and the sectional side view (right) of a pore are given (Bandyopadhyay et al, 1996).

(i)   Short range and long range ordering

In recent years, it has been noticed that a close packed hexagonal nanochannel array can be formed by a self-organization process during anodization of aluminium under controlled conditions (Ba et al, 2000). The oxide formed is amorphous alumina with long and columnar nanopores with approximately hexagonal ordering and is also termed commercially as 'alumite' (Metzger, et al, 2000). However, the well known honeycomb-like structure of PAAO fil ms features short-distance ordering (ranging from several tens of nanometers to a few microns). To achieve a highly ordered pore arrangement over larger areas in mm range, several patterning techniques have been studied (Stasi et al, 2007). The long-range ordered structure is achieved by minimizing the formation of defects across the entire PAAO layer (Montero et al, 2007(a)). The following methods viz. nano-indentation (Masuda et al, 1997), focussed ion beam techniques (Liu et al, 2003) and the two-step anodizing procedure (Masuda et al, 1996), pre-patterning by optical diffraction grating (Mikulskas et al, 2001), holographic lithography, atomic force microscopy (Masuda et al, 2002), scanning probe

lithography (Shingubara et al, 2003), electron beam lithography (Li et al, 2000) and direct writing laser (DWL) lithography which is latest (Stasi et al, 2007), have also been attempted. The common aim of these procedures is to imprint/indent the aluminum surface with a regular pattern, since this pattern acts as a seed for the growth of alumina pores when subjected to anodization. Out of these, the lithographic methods have many practical limitations, e.g. high cost of the equipment, low throughput (Masuda and Satoh, 1996 and Lo and Budiman, 2007).

Hence conventional non-lithographic methods (two step anodization) is considered more suitable for making ordered nanomaterials because conventional fine line lithography (electron beam, focussed ion beam, X-ray, STM/AFM etc.) has at least one of two major shortcomings: (i) process related damages incurred through exposure to high-energy beams during pattern delineation (writing) or through reactive ion etching (pattern transfer), and (ii) slow throughput associated with direct-write lithography where each wafer is patterned serially one at a time (Bandyopadhyay et al, 1996).

A few recent studies (Li et al, 2006) reported that simple and cost-effective method using stable high-field anodization in ethanol added electrolyte leading to high current densities, results in desired ordered structure, however it has been established that there are some range of process parameters (called as self-ordering regime) within which self ordering may be achieved in only one step of anodization. A brief summary is presented in the next paragraph.

(i) Self ordering regime: Following are few references wherein the self-ordering regimes have been used to obtain ordered porous structure. Asoh et al (2001) have reported that the long-range ordering has been observed to occur under limited voltage conditions that were specific to the solution used for anodization, that is, long-range ordering takes place at 25 V in sulfuric acid solution, (Masuda et al, 1997 (b)) at 40 V in oxalic acid solution, (Masuda and Fukuda (1995); Masuda. and Satoh (1996) and at 195 V in phosphoric acid solution, (Masuda et al, 1998) corresponding to cell sizes of 63, 100, and 500 nm, respectively. Several groups have also reported similar results concerning the long-range ordering conditions for anodic porous alumina (Shingubara et al, (1997) and (2004); Jessensky et al, 1998(b); Li et al, (1998(b)); Neilsh et al, (2002)).

(ii) Mechanisms of self-ordering: A mechanical stress mechanism has been proposed to explain the self-ordering of anodic alumina (Jessensky et al, 1998 a and b). It was suggested by them that the repulsive forces between neighboring pores caused by mechanical stress at the metal/oxide interface, promote the formation of hexagonally ordered pore arrangements. According to this hypothesis, under the usual experimental conditions, the associated volume expansion of the aluminum oxidation gives rise to the mechanical stress. (Li et al, 1998(a)) performed anodization in phosphoric, oxalic and sulphuric acid solutions and reported volume expansion of about 1.4 time for all of the self-ordered regimes. The estimated stress (compressive) in alumina was found as 4 GPa. However, they pointed out that experimental values of the stress in barrier type films reported by Bradhurst et al (1966) do not match the calculated values. Furthermore, their explanation for the cracks observed at high voltages near breakdown based on high compressive stress is questionable as compressive stress generally lead to buckling of films. However, it may be true also that as the adhesion between oxide film and the substrate is strong, so at some points only, the breakage of the film due to buckling, may relieve the built up high compressive residual stress and that may result in overall well ordered structure with some peeled off parts of the coating at some discrete areas as can be easily seen in the top view of the films, Nielsch et al (2002) measured the porosity under conditions of ordering and found that the porosity was equal to ~ 10 % for various self-ordering voltages and concentrations which corresponded to a volume expansion of about 1.2 time. They explained the results based on the theory proposed by Jessensky et al (1998). The model proposed by Jessensky et al (1998 (b)) raises several serious questions. First, the simple argument based on the PBR (Pilling Bed worth Ratio) or volume expansion has been shown in many other experimental systems to be invalid. The measured stresses are in fact tensile with most of the stress present in the aluminium beneath the oxide. This is clearly in contradiction with the proposed model by Jessensky, based on pore repulsion due to compressive stress. While, Asoh et al (2001) reported that although a detailed mechanism which explains the dependence of the ordering on the applied voltage is not clear at present, strain-free cell growth is thought to take place under the most appropriate condition.

Ba et al (2000) have shown that there is a continuous symmetry change of pore distribution depending on the anodizing temperature and the average ordered pore

domain size increases with the increase of acid concentration (0.3 M, 2 μm, 0.6 M, 5 μm). With a decreased anodizing temperature, the flat rear side surface can also be observed by comparing with the rough rear side surface etching at room temperature. According to the experimental results for anodic alumina etched under various conditions (Jessensky O, et al 1998), there is a certain expanding ratio of alumina for the formation of regular pores, but Ba et al (2000) found from their results that, a higher anodizing temperature causes a higher reaction rate at certain acid concentrations and applied voltages, and a higher reaction rate leads to more disorder of pore distribution across the alumina surface. If the local stress level that dominates the formation of regular pores is kept rigid, a higher reaction rate would increase the expanding ratio, and hence increase the local stress.

When current density is high, rapid oxide growth induces a compressive force at the barrier layer between each cell boundary. Therefore, the bottom of cells grown at the barrier layer under a high field must be pressed against each other, so that the self-ordering proceeds with the growth of porous film. Ono et al (2005) has described model of the self-organization of the cell arrangement under a high-current density, i.e., a high electric field compared with the case of a low electric field. Therefore, the bottom of cells grown at the barrier layer under a high field must be pressed against each other, so that the self-ordering proceeds with the growth of porous film.

Cai et al (2002) reported that the formation of hexagonally ordered pore arrays inside each domain can be explained by topological requirements for space filling in a 2D system. On the other hand, the domain growth with anodization time can be explained by the kinetics of pores moving and/or merging (Li et al, 1998 b and Jessensky et al, 1998 b), which is similar to grain growth in metals and alloys. As pores move and merge along the dislocation line at boundaries, the orientations of adjacent domains could change gradually to match each other.

Nielsch et al (2002) reported that transmission electron microscopy analysis of self-ordered porous alumina obtained by electrochemical anodization shows that self-ordering requires a porosity of 10%, independent of the specific anodization conditions. This corresponds to a volume expansion of alumina to aluminum of about 1.2. Self-ordering of porous alumina with any interpore distance is possible if the applied

potential, which mainly determines the interpore distance, and the pH value of the electrolyte, which mainly defines the pore radius, match the 10% porosity rule.

Recently, Ono and coworkers (2004) performed anodization in various electrolytes and reported the porosity as a function of applied voltage. They observed that the porosity value approaches 10% at high voltages close to the breakdown potential. Self-ordering was also observed under these conditions and suggested that the high current density or high electric field strength is the key controlling factor for self-ordering. However, it is unclear whether the porosity value of 10 % is the lowest value observed before breakdown as in oxalic acid solution, breakdown does not occur even up to 80 V while self-ordering is observed at 40 V.

Ono et al (2005) reported that the self-ordering of arbitrary pore intervals can be realized by choosing an adequate electrolyte and electrolytic conditions at the appropriate formation voltage required for maintaining a high-current condition, i.e., a high electric field, as they had suggested in their previous papers.

(j) Two-Step Anodization

Masuda et al (1996) reported that a highly ordered nanoholes array could be obtained by two-step anodization of high purity aluminum using a 0.3 M oxalic acid solution under a constant voltage of 40V at 0°C. The first step anodization is carried out for 76 hours. Although cell arrangement at the surface is not so regular, nanoholes regularity improves with increasing film thickness. Excellent regularity can be achieved at the hole bottom after a long anodization period as shown in Fig. 2.12 a). Then the first anodic alumina film is selectively etched away by a mixture of 35 ml/l 85% H_3PO_4 and 20 g/l CrO_3 at 80° C as established by Schwartz and Platter (1975). The etched surface has a periodic surface roughness, as evidenced by a highly regular array of nanohole bottoms (Fig 2.12 (b). Consequently, the nanohole array formed by the second anodic oxidation exhibits excellent regularity as a result of the initial surface Fig. 2.12(c).

(a)   **(b)**   **(c)**
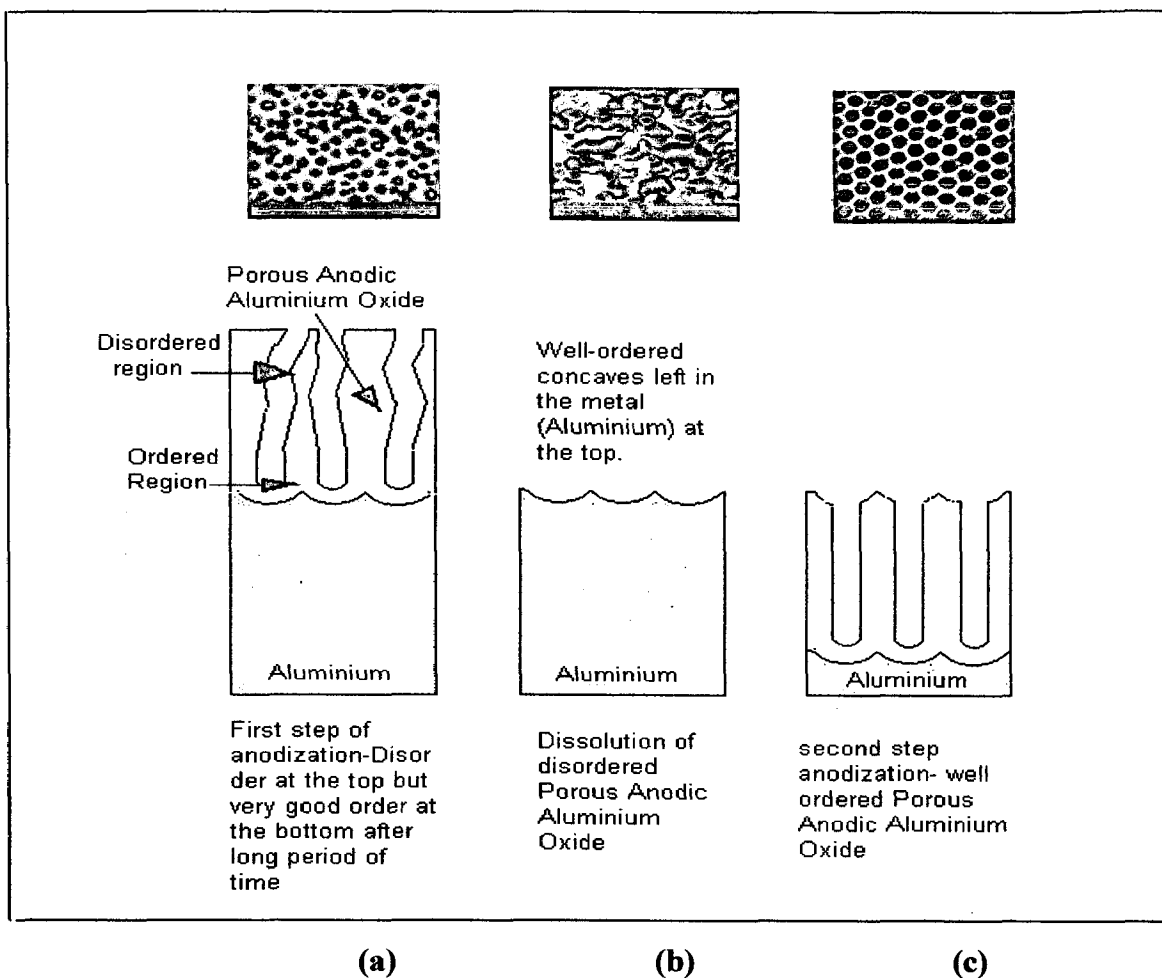
Fig. 2.12:   Mechanism of two step anodization; (a) First step of anodization forms disordered region of PAAO at the top surface and ordered region at the bottom, (b) The oxide part (yellow coloured) is etched away and metal part (light grey is left having concave shaped impressions (well-ordered)

Hence by this technique, one can obtain a highly ordered PAAO, which is characterized by a long anodizing period. There are some reports of multi-step anodization, where three or more steps of anodization have been conducted (Sulka et al (2002); Zhou et al (2006), Li et al (1998(b)); and Zhang, (1998), but the improvement in ordering as well as size of well ordered domains is not significant after the second step.

However recently some researcher have successfully fabricated ideally ordered nanoporous alumina films by high-field anodization realizing the need to produce

26

highly ordered porous anodic alumina film with low cost and by a simple process on a large scale.

(k)   Influence of anodization parameters on PAAO morphology, structure and properties and their interdependence

One of the attractive features of PAAO films is the flexibility of the properties, structure and morphology (pore size may vary from 10 nm to some 100 nm, pore depth from 1 µm to 300 µm, and pore density from 10^9 to 10^{11} pores per square cm (Jessensky et al ,1998(b)), which can be tailored by varying anodization parameters viz. (i) applied voltage or (ii) current density; (iii) pH, (iv) type and (v) temperature of the electrolyte (Hunter and Fowle,1954 a). In contrast to the formation of the alumina which is an electrochemical process, the dissolution of the top alumina layer is a chemical process. Though there are several other parameters also, not discussed here which influence anodization process, however, the present section reviews only the important parameters so that the desired PAAO on aluminium substrate may be developed from the understanding developed by reviewing the existing literature, which should be appropriate for CNTs/CNFs growth within the pores and subsequent use as a self-lubricating wear resistant coating.

(i)   Effect of applied voltage: Voltage is perhaps one of the most established process variables in the analysis of oxide layers formed by anodization. Researchers established the facts that there is direct increase in pore diameter, barrier layer thickness and interpore distance with the increase in voltage (Sullivan et al 1970 and Ono et al, 2003). A typical variation of pore diameter (also called hole diameter) and interpore distance (also called cell diameter) with voltage has been reported by (Shingubara et al, 1997) and is shown in Fig. 2.13 below.
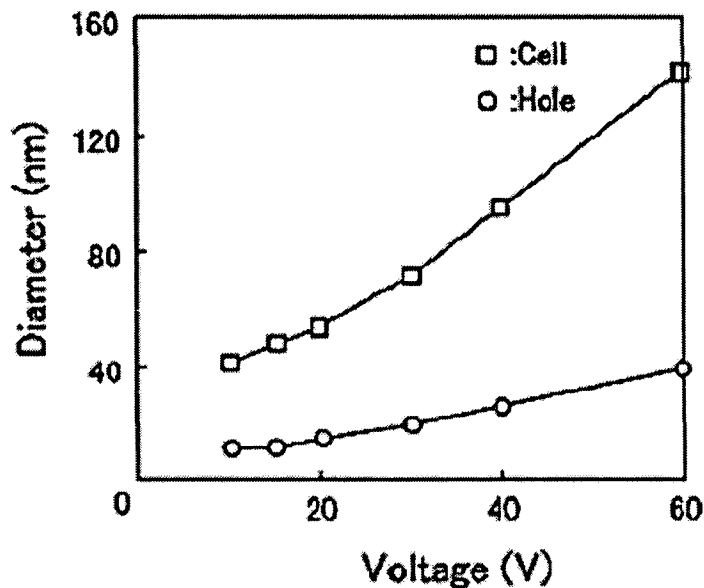
Fig. 2.13: Voltage dependence of pore (hole) diameter and interpore distance (cell diameter), formed by anodization (Shingubara et al, 1997).

Since the conductivity and pH values of different electrolytes are different and are influenced by the concentration, ranges of anodization voltage are also different for different electrolytes (Sarkar et al, 2007). However, the term "*self-ordering regime*" is more common which has already been described in detail earlier in this chapter under the sub-secton of "ordered pore formation", sec 2.1.1 (i), page no. 26. It is set of selected operating parameters within a narrow range for a given electrolyte to get ordered pore formation. Thus it has been very well established that voltage plays an important role in ordered pore formation as its variation and corresponding effects are simple to control and analyze. The self-ordering voltages reported until now and the corresponding cell diameters using various electrolytes were summarized by Ono et al, (2005) and have been presented in Fig. 2.14.
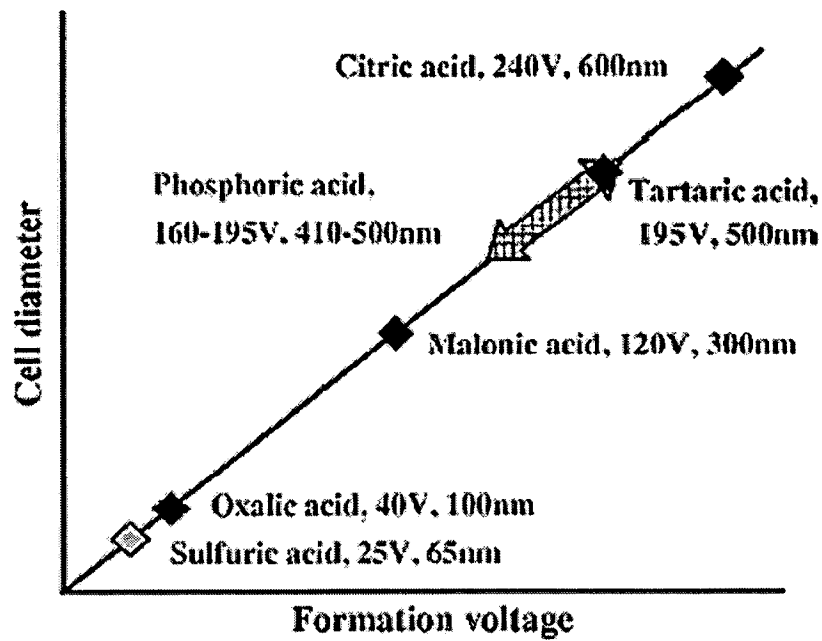
Fig. 2.14: Formation voltage dependence of interpore distance (cell diameter) for various electrolytes (Ono et al, 2005).

Sulka et al (2002) have also tabulated anodization parameters like temperature, acid concentration, cell voltage, duration and resulting thickness of oxide layer.

(ii) *Effect of voltage on porosity:* Porosity of the anodic alumina is an important factor describing the structural features of the film and depends on the applied anodizing potential. According to Keller et al (1953), the porosity (α) of the hexagonal structure can be written as

$$\alpha = \frac{\pi}{2\sqrt{3}} \left(\frac{d}{L_p} \right)^2 \qquad (2.5)$$

where

α - porosity

d is pore diameter and L_p is interpore distance.
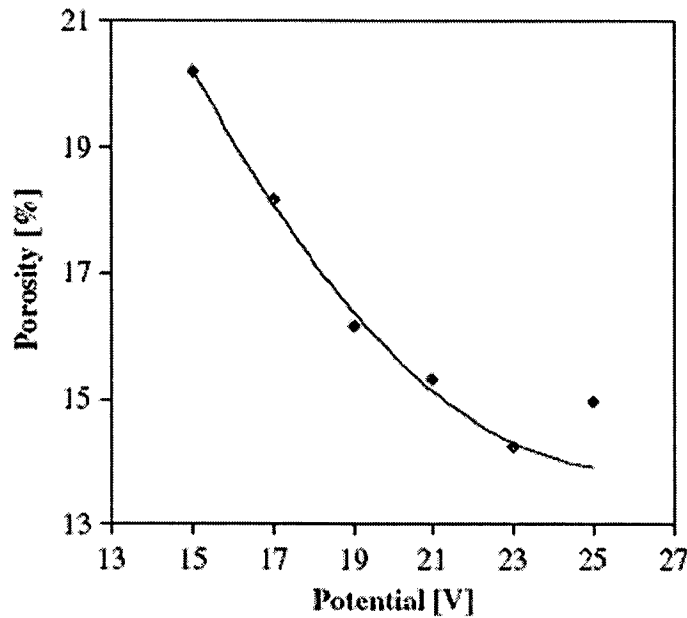
Fig. 2.15: Formation potential (V) dependence of porosity

From Fig. 2.15 it can be seen that porosity of anodized aluminium gradually decreases with increasing anodizing potential. The so called 'pore-filling method' is very commonly used to estimate porosity (Takahashi and Nagayama, 1978).

(iii) Effect of electrolyte bath temperature: Temperature is one of the key factors in determining the pore structure as it governs chemical reactions. As per Bocchetta et al, (2003), increasing temperature is equivalent to increasing aggressiveness of the electrolyte. Reaction rate increases with increase in temperature following Arrhenius equation.

$$K = A.e^{-\frac{E_a}{RT}}$$
(2.6)

where K is rate constant, A is pre-exponential constant, E_a is activation energy necessary to create the transition state, R is gas constant and T is temperature (in K).

Self-organized porous structure is obtained by keeping the electrolytic bath at very low temperature due to low growth rates (Jessensky et al, 1998(b)). Dissolution ability of the electrolyte reduces and hence thicker films are obtained. For instance, anodization in oxalic acid at 40 V is performed at 5 -18 °C and at 0- 2 °C in the case of anodization at 195 V in phosphoric acid. A second reason to keep the temperature

as low as possible is to avoid a local heating at the bottom of the pores during the course of anodization. The local heat causes an inhomogeneous electric field distribution at the bottom, leading to local electrical breakdown of the oxide. In fact, cracks and bursts of the oxide film are generated if porous alumina is formed without temperature control and improper stirring. If the temperature is too low (just below zero degree) and diluted electrolytes are used, the electrolyte may freeze. In addition, the speed of the growth of porous alumina is affected by the temperature. The lower the temperature, the lower is the growth rate. Kashi et al (2005) found that the optimum temperature for self-organization of pore oxidation changes in accordance with the concentration of electrolyte. Current density also increases with increasing temperature,. The current densities reported during the porous oxide film growth using 15% wt/vol.H_2SO_4 with bath temperatures of 20 °C, 25 °C and 30 °C are 5, 15 and 35 mA/cm^2, respectively (Patermarakis and Papandreadis 1993) as shown in Fig. 2.16. Temperature influence on well-ordered nanopore structures grown by anodization have also been reported by Sulka et al, (2007).
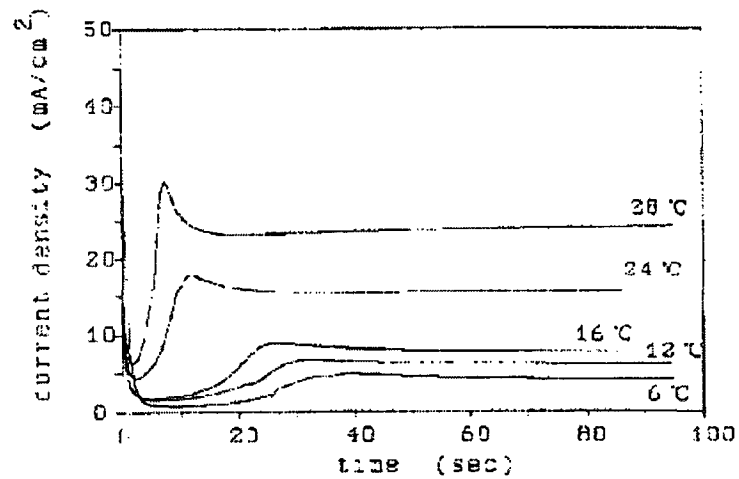
Fig 2.16: Current density-time curves recorded during anodization with constant voltage (18V) and for different temperatures (Source – Debuyck et al, 1994).

Increasing temperature is equivalent to increasing the aggressiveness or decreasing pH in most cases (Bocchetta et al, 2003). However, the anionic impurity content decreases with increasing temperature due to the tendency for the oxide to grow crystalline at higher temperature (Sullivan et al, 1970).

Li et al (2006) reported that by adding ethanol to the electrolyte, the bath temperature could be reduced up to -10 °C and thus high current densities (maximum up to 4000 A/m^2) at the self-ordering voltage of 195 V, using phosphoric acid electrolyte, could be used. This results in growth rate of the film as high as 10 μm min^{-1}, which is about 100 times higher than that of ordinary low-current-density anodization.

(iv) Effect of current densit: According to Ono et al, 2004(b) the condition of high current density is the key factor that determines the self-ordering of the pore arrangement. In the initial stages of anodic oxidation, constant voltage and current measurements lead to very different results as at fixed current density, the electric field at the barrier oxide is a constant, while at fixed potential, the electric field decreases with time. Porous growth at later stages is however similar for both cases of constant voltage and current. Hence, trends in the dependence of pore spacing, diameter and current efficiency observed for constant voltage and constant current cases are also similar. Li Yanbo et al (2006) found that inter-pore distance is not solely dependent on the anodizing voltage but is also influenced by the anodizing current density, which is different from the empirical relationship L_p = 2.5 V first reported by Keller et al (1953) for ordinary anodization. Current density-time curve for different voltages shown Fig. 2.17.
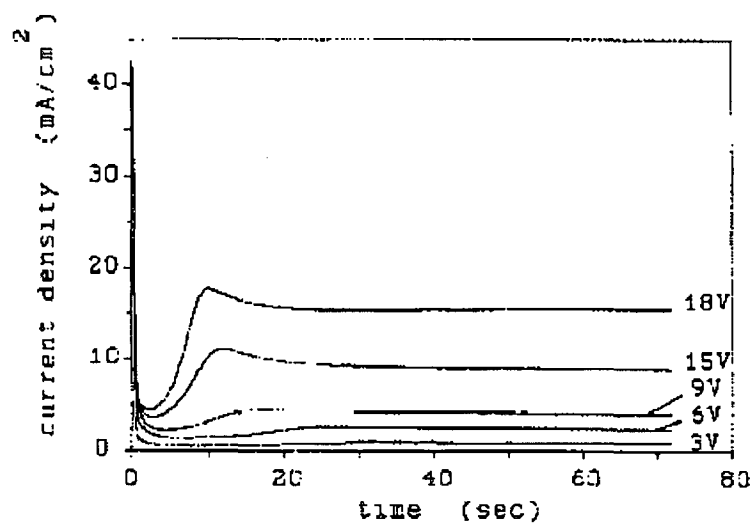
Fig. 2.17: Cur rent density-time curves recorded during anodization with constant temperature (24°C) and for different voltages. (Source – Debuyck et al, 1994)

The authors reported that, at low current densities, porous oxide is formed, while higher current densities promote barrier type oxide formation. The anodic oxides formed in these solutions are amorphous and contain a mixture of AlO_4 tetrahedral and AlO_6 octahedral.

(v)   Effect of pH / concentration of electrolyte: Jia et al (2006) studied the effects of the concentrations of phosphoric acid, oxalic acid and hypo-phosphorous acid on the morphologies of the anodic films. Their results showed that the pore diameter ranged from 250 to 500 nm, and increased with increasing the concentration of phosphoric acid, oxalic acid and hypo phosphorous acid. The pore geometry could change from round to hexagonal, which was related to the electrolyte components and their concentrations. It may be.clearly observed from their results that porosity increases by increasing electrolyte concentration. It is reported that the pore diameter, is affected strongly by dissolution velocity of alumina that is determined by the pH value in the solution. The lower the pH, the lower the potential threshold for field-enhanced dissolution at the pore tips. Depending on the potential, the shape and the diameter of the pore are defined. The smallest pores can be obtained in the lowest pH value, i.e., in the strongest acid (Nielsch et al, 2002).

The effect of pH on anodization at constant voltage is different from that at constant current density and hence both the cases have been discussed separately.

(a)   Effect of pH at constant current density and temperature

In the anodization at constant current density, the increase in pH of the electrolyte decreases the salvation rate and hence increases the barrier layer thickness (Sullivan, 1970). To maintain this value of constant current, steady-state voltage will be increased. As the inter-pore distance is strongly dependent on the voltage, a strong effect of pH on pore spacing is observed. Pore size also increases but with a weaker dependence on pH (Sullivan, 1970). T he electric field (V/cm) increases slightly with increasing pH at constant current density. Increasing pH increases the electrical field (V/cm) at constant current. The porosity decreases with an increase in pH and at constant current density due

to a stronger increase in inter-pore distance than pore diameter as discussed above. Pore density decreases due to increase in pore spacing with increasing pH. As the dissolution rate is decreased, the current efficiency for oxidation increases with increasing pH. However according to Vrublevsky et al (2003) and Vrublevsky. et al (2004), the oxide growth rate does not depend on pH. Their explanation of this observation is based on their argument that the oxide growth occurs at the metal-oxide interface only, the oxidation current density and hence the oxide growth rate is independent of pH.

(b)   Effect of pH at constant voltage and temperature

In anodization at constant voltage, the increase in pH decreases the dissolution current density. But, to maintain constant voltage, the oxidation current density must also decrease and hence, the total steady state current density decreases with pH. According to Thomson and Wood (1983), increasing the pH decreases the electric field (V/cm) due to reduced dissolving power of the electrolyte and that leads to an increase in barrier layer thickness. The increase in pore size and interpore distance and decrease in pore density with pH is much weaker compared to the constant current density case. The anionic impurities content decreases due to an increase in pH and decrease in electric field. Sullivan et al (1970) reported a slight decrease in porosity. However, inconsistencies in their pore size measurements from top view (plan view) and cross-sectional images as well as lack of other experimental data in the literature limits further understanding and more systematic work in this direction is needed.

(vi)   Effect of type of electrolyte bath (acid and its composition):   The morphology and structure of formed oxide film mainly depends on the type of the electrolyte used as have already been discussed in section 2.1.2 d. Barrier and porous type films may form depending on the type of electrolyte used, keeping process parameters unchanged. Since the conductivity and pH values of different electrolytes are different and are influenced by the concentration, ranges of anodization voltage are also different for different electrolytes.   The Table 2.1   illustrates the details of

electrolytes in use commonly as well as the optimum parameters for ordered pore formation.

Table 2.1: Details of anodization process parameters.

S.N.	Electrolyte	Voltage(V)	Temp (°C)	Remarks
1	Sulphuric Acid 15 wt.% per litre.	15-25	20	Optimum Voltage Is 18 V, 63 nm pore interval (for 0.3mol Per litre pH is 0.1)
2	Oxalic Acid 3 wt.% per litre.	35-45	30	Optimum Voltage is 40 V, 100 nm pore interval (pH is 1.2)
3	Chromic Acid 3 wt% per litre.	35-45	40	Optimum Voltage Is 40 V
4	Phosphoric Acid 5 wt% per litre.	100-220	25	Optimum Voltage Is 195 V, 500 nm pore interval (pH is 2.3)

As the size of the pore directly depends on voltage and voltage ranges are dependent on type of acids and hence it can be concluded that type of acid is an important variable. The pore forming electrolytes are dibasic or tribasic acids (Sullivan et al 1970). Normally, three kinds of acid solutions are used for the anodization of the alumina membranes: sulfuric, oxalic, and phosphoric acid solutions. The sulfuric acid solution is suitable for the preparation of alumina membranes with small pores that are in the range of about 10–30 nm. The oxalic acid solution is suitable for the preparation of alumina membranes with medium-sized pores (about 30–80 nm) while the phosphoric acid solution is used for the preparation of large-pore membranes, i.e. larger than 80 nm (Lei et al, 2007).

(vii) *Effect of thickness and time:* Regularity of pores increase with extended time of anodization. Ordering of pores is found better at the bottom portion of oxide compared to the top surface. Extent or degree of pore ordering at the bottom of the pores increases with anodization time for a given condition of process. PAAO thickness is also approximately directly proportional to the process time for a given current density (Stein et al, 2002.), hence when thicker oxide films are formed, ordering automatically improves at both places, top and bottom, as the self-ordering mechanism gets more time for improvement in the ordering of pores and the system tries to attain more stable state, minimizing free energy.

(viii) *Effect of anode material (pure metal/ alloy):* Generally ultra high purity aluminium is taken as anode material in anodization because presence of impurities may affect the ordered pore formation (Yu et al, 2006). Elements like silicon, copper etc are generally found as impurities. Atoms of these elements have different diameter and hence they increase or decrease the stress field in the aluminium lattice, leading to defects in the ordering process. Sarkar et al (2007) have also supported this opinion that high purity Al foil (99·999% purity) is used for obtaining an ordered porous oxide film on aluminium by anodization, because of the fact that the impurity atoms having different size and volume may induce internal stresses during anodization, which can lead to the formation of defective structures in porous alumina template during anodization. Lo et al (2007) have reported that ordering is better in pure aluminium compared to impure aluminium. High purity metal was also preferred by Bocchetta et al, (2003) in order to minimize breakdown phenomena and the formation of flaws or cracks in the porous matrix. However there have been many reports on anodization of aluminium alloys substrates (Fratila et al, 2002 and 2006), because aluminium alloys have high specific strength and hence they find numerous applications in aerospace and transportation. In the 1960s it was reported that different intermetallics show different oxidation rates relative to the aluminum solid solution (Guminski et al, 1968). More recent results (Thompson et al, 1999; Brown et al. 1998; Habazaki et al, 1997 and Paez et al, 2000) on dilute aluminum binary alloys and barrier oxide layers revealed enrichments at the metal/oxide interface of certain alloying elements from the solid solution (e.g. Ti, Cu, Mo), oxygen generation (e.g. Cu, Fe, Cr), void formation and film detachment (e.g. Li, Mg). When a ternary element is present in the composition, the behavior towards anodic oxidation may differ from the binary composition not necessarily through the specific response of the added alloying element

but also through the possible local interactive effects between the alloying elements, second phases and the surrounding solid solution. Presently, these complex effects are not yet fully identified and understood.

(ix) *Effect of stirring:* There are mixed reports about effects of stirring or agitation on the morphology of the PAAO, Burgos et al (2003) consider it as an important factor for the formation of uniform and porous alumina at higher efficiencies (Patermarakis and Papandreadis, 1993). Moreover, the temperature control obtained with agitation prevents a potential runaway and its consequences on porosity (Shawaqfeh and Baltus, 1998). Fratila et al (2006) used wall jet reactor forced and free convection stirring for three different cast aluminum substrates (i.e. Al 99.80 wt.%, Al-10 wt.% Si, Al-10 wt.% Si-3 wt.% Cu) The forced convection regime determined a significant decrease in electrode temperature and an increase in oxide layer thickness and anodizing voltage for all three compositions investigated. Rehim et al (2002) reported that when stirring was done, no pores were obtained, while without stirring, porous structure was obtained in case of chromic acid electrolyte.

(l) *Mechanical properties of anodic alumina:* As the label of porosity in the PAAO structure has got a bearing with the technological application of the structure, therefore the knowledge of porosity development in the anodization process is important. The usual ways of measuring properties like modulus and the hardness are done using nanoindentation method. Ko et al (2006) measured the mechanical properties, such as the modulus, hardness, of PAAO structures, using the nano-indentation method. Relationship between the mechanical properties and the porosity change is also investigated by them. Their results show that the indentation modulus and hardness of the PAAO structure decreases monotonically as the size of the holes increases. They found that there exists residual tensile stress in the specimen structures. Earlier Xia et al (2004) had also added knowledge in this regard.

2.1.3 Post Treatments

After two step anodization following post treatments are generally carried out, viz.

(i) Pore- widening

(ii) Barrier layer thinning and

(iii) Sealing of pores.

(i) Pore widening treatment: After anodization at a given voltage, values of pore diameter (d) and inter pore distance(s) are found corresponding to the voltage value (V) following the relation given in chapter 2, Sec. ......

d = 1.29 nm/V, t = 1.04 nm/V and   s = 2.77 nm/V)   (Sullivan et al, 1970)

Hence the size of the pores is limited by the limit of the maximum voltage value. To increase the pore diameter and depth, without increasing the interpore distance, the sample is to be dipped in mixed solution of phosphoric acid and chromic acid. The first acid, dissolves the oxide layer while the second one, chromic acid, works as an inhibitor to prevent attack of the base metal (Debuyck et al 1994). The Schematic diagram of pore widening mechanism is shown in Fig. 2.18.

1. anodization   **2. optional pore widening**

aluminum film   achievable pore diameter:
                     from 4 nm   to 250 nm
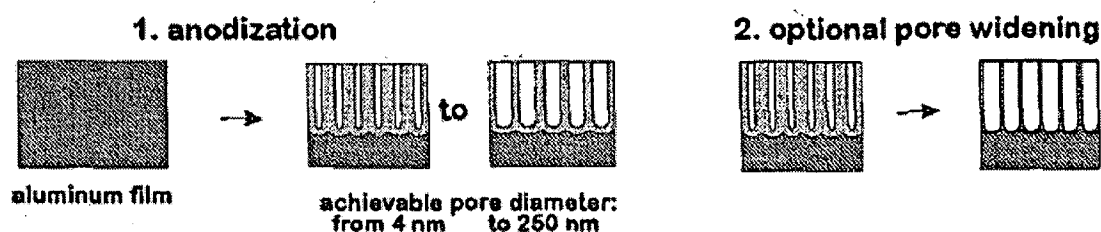
Fig. 2.18:   Schematic of optional pore-widening method (Routkevitch et al, 1996).

Typically, 1 M H_3PO_4 at 30 °C is used for pore widening. Under these conditions, the rate of pore widening is approximately 110 nm /h. Slightly wider pore diameter also helps in easy entrance to ions during catalyst deposition.

(ii) Barrier layer thinning: Since the thickness of the barrier oxide (t_b) is proportional to the potential applied for aluminum anodization (t_b = 1.2 nm/V x applied potential, (Sullivan et al, 1970)), the thick barrier film formed at high voltages (up to 200 V for phosphoric acid) is a big obstacle for a subsequent electrochemical deposition of the catalyst in the pores. Small fluctuations in the barrier oxide thickness lead to large current fluctuations and thus very inhomogeneous filling. Therefore, a well-controlled process for homogeneously thinning the barrier layer is vital for achieving a degree of nearly 100% filling with metals (catalysts deposition in present context) by electrochemical deposition and secondly even low deposition voltages may be used.

It has been reported that high potentials are required for the tunneling of the electrons through this thick barrier layer. Electrodeposition by direct current (DC) is

very unstable and uniform filling of the pores cannot be achieved due to a cathodic side reaction, which leads to a partial removal of the barrier oxide, formation of holes in the barrier layer, and local deposition in single pores. Hence they followed a method to thin the barrier layer during or at the end of the second step of anodization. They increased the pore diameter and reduced barrier layer thickness by isotropicically etching the anodized samples and transferred the samples to an oxalic acid bath, where voltage was continuously decreased as shown as shown in Fig. 2.19.
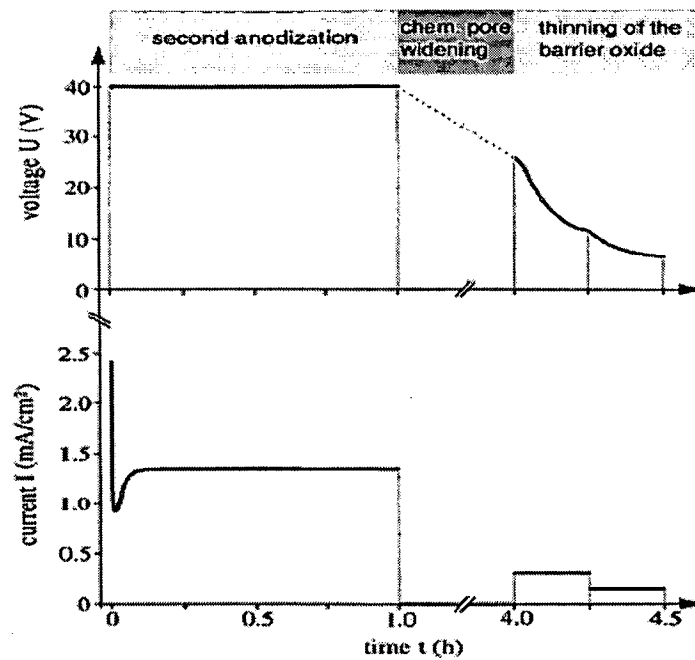
Fig. 2.19: Voltage-time and current-time curves for the second anodization (T = 2 ° C), Chemical pore widening (T = 30 ° C), and the thinning of the barrier layer (T = 2 ° C) in 0.3 M oxalic acid (Nielsch et al, 2000).
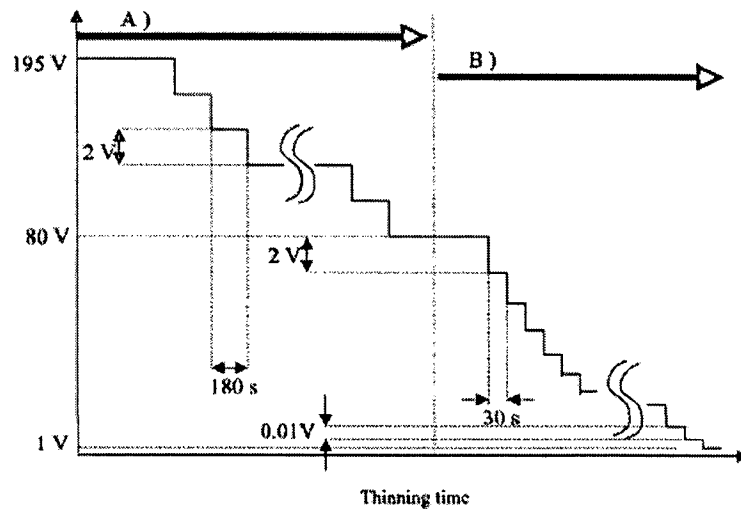
Fig. 2.20: Schematic diagram of the thinning process, which is divided into two parts: (A) Constant potential 2 V lower than that in the former step is applied for 180 s in 0.1 M phosphoric acid during each step. (B) Potential step with exponentially decaying difference is applied for 30 s in 0.3 M oxalic acid Choi et al (2003 b).

For thinning the thick barrier layer by more than 100 nm, Choi et al (2003 b) has developed a modified thinning process to that used by Nielsch et al (2000). It involves two different electrolytes: phosphoric acid is used for the thinning process from 195 V down to 80 V and oxalic acid from 80 V down to 1 V (Fig. 2.20).

(iii) *Sealing of pores:* In the past, the industrial use of porous anodic oxide films was restricted to those films which were sealed. This process of sealing of the porous films involves immersing the films in hot water, usually purified water, or in aqueous solutions of certain salts above 90°. The process involves the closure of the porous structure to form a compact nonporous film, whose thickness is many orders higher than those attainable in barrier-type electrolytes. The chemical process, which is believed to be occurring, is the formation of boehmite by partial hydration of alumina.

$$Al_2O_3 + H_2O = 2AlO\,(OH) \hspace{3cm} 2.7$$
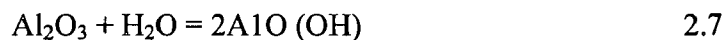
During sealing in certain salts, e.g., nickel acetate and potassium dichromate, sealing also produces the precipitation or incorporation of these salts within the sealed film. While there is some reduction in hardness this is often only around 10 to 15 %, but in

40

some environments sealed hard coatings have outperformed unsealed hard anodic coatings.

(vi)   Catalyst deposition in the pores: Electrochemical methods have been found suitable and used by almost all researchers for catalyst deposition in the bottom of the pores of PAAO, to grow CNTs/CNFs. The thickness of the barrier layer imposes a limitation on the use of d.c. electrodeposition to fill the pores. However the inherent rectifying properties of the barrier layer allow the pores to be filled uniformly by a.c. electrolysis without simultaneously depositing material on the surface or into the macroscopic defects of the film (Routkevitch et al, 1996). It is easy to electrodeposit, using alternating current (AC), various metals into the pores of Al_2O_3 (Routkevitch et al, 1996). For instance, Co c an be electrodeposited by using a sulfate electrolyte $(CoSO_4 /H_3 BO_4)$, and 20 V rms at 200 Hz. Homogeneous nucleation at high current density can be favored by applying a short initial pulse (40–50 V for 1s), promoting homogenenous growth of nanowires. Filling of the nanometric pores can also be initiated by sonication. Alternating current is needed either because of the rectifying nature of the Al metal/oxide junction, or because of diffusion barriers with the deep nanopores.

2.1.3.1 Characterization of PAAO

Various types of techniques have been used to characterize coatings on aluminium substrates (Han et al, 2008). PAAO have generally been characterized by SEM, TEM and nano-indentation for assessing mechanical properties.
Cantrell et al (1990) have assessed the ability of scanning electron acoustic microscopy (SEAM) to characterize ceramic materials. Nowadays AFM is also being used effectively to characterize nanosized objects (Bera et al, 2008). Shukla, et al (2002) have used HR-TEM to study nanoparticles.

2.2   CARBON NANOTUBES/CARBON NANOFIBRES (CNTs/CNFs)
2.2.1 Introduction

As the objective of the thesis work is to develop PAAO nano-composite surface with carbon nanotube/carbon nanofibre (CNT/CNF) in the pores and to

examine its tribological (self-lubrication and wear resistance) behaviour, the related literature has been reviewed exhaustively.

Carbon has a variety of stable forms like diamond, graphite and nanotubes (**Ranjan et al, 2005**). Due to their peculiar mechanical and electrical properties carbon nanotubes have shown tremendous contribution in the advancement of nanotechnology. Chemical vapour deposition (CVD) technique is most commonly used to produce CNTs. Various types of graphitic nano-structures, e.g. fullerenes, carbon nanotubes, carbon nanofibres, nano onions, nano coils, nano belts, nano cones and nano polyhedra etc., which have been reported to form as a result of thermal CVD, are potential candidates as solid lubricants for tribological applications. The icosahedral 60-atom carbon clusters popularly known as bucky balls, have been subjected to much investigation for the past two decades (**Kaur et al, 2008**). However, formation of CNTs over others is more desirable in tribological applications due to two reasons. Firstly, CNTs, due to their graphitic structure, nanoscale dimensions and unique mechanical properties, can be used directly as solid lubricants by growing them in the pores of PAAO and extending above the PAAO surface. Secondly, the grown/embedded CNTs, due to their hollow tubular structure, can further act as a reservoir of liquid lubricants (Xia, 2008), such as hydrocarbon oils to supplement the solid lubrication. The lubricating oil may easily be sucked into CNTs due to strong capillary action as reported in the literature (sun et al, 1999). These embedded CNTs can slowly dispense the lubricant on to the surface during use in tribological applications.

An intense research work is currently ongoing all over the world to improve quantity and quality of CNTs/CNFs. Development of new nano-composites, by using these light weight and high strength nanofibres as reinforcing materials with all types of conventional matrix materials, like polymers, ceramics and metals is an area of a very intense research (Harris, 2004). Nanocomposites represent the current trend in novel nanostructured materials (Samudrala and Bandyopadhyay, 2009). Nano-structured materials have attracted great attention in recent years because of their unique physical properties and applications (Yadav et al, 2008). Several milestones have already been achieved and many more are expected to be reached very soon, as this field of research is growing in an exponential manner. In this context the relevant part of the literature survey on these nanofibres (CNTs/CNFs) covering various related aspects, like, their synthesis methods in use, different types of them, factors affecting their formation,

growth mechanism and basic characterizations, etc, are presented. Special emphasis has been given to literature pertaining to development of self-lubricating PAAO surfaces obtained by embedding CNTs/CNFs within the pores which is prospective candidate material to be used as nano-composite, suitable for tribological applications (Tu et al, 2004; 2005) and is also the main objective of the present work.

The properties and applications of CNTs/ CNFs depend significantly on their structures (Salvetat et al, 2006). One of the minor objectives of this study has been aimed at tailoring the CNTs /CNFs synthesis (within optimally prepared PAAO), produced in sufficient/optimum quantity and having reasonably good quality, are nucleated in and emerge from the majority of the PAAO, and have a minimum of material nucleated on the template surface. These are all desirable properties for tribological applications (Tu, J.P., 2005). Hence, literature survey has been thoroughly conducted, focusing on this comparatively new area and to develop know-how so that proper steps may be taken to realize and also optimize this novel material combination. A review of the literature by Sklar et al, (2005), suggests that these attributes may be difficult to achieve. But number of researchers is working on this area and hence many improvements are being made.

Carbon products in tubular form, called carbon filaments, were first observed when electron microscopes came into wide use around 1950 (Tibbetts, 1984). In the early 90s, such filaments were observed with a diameter in the range order of the nanometer (Iijima, 1991) and have then been called carbon nanotubes (CNTs).

2.2.2 Types of carbon nanotubes (CNTs)

CNTs are generally of two types, viz. (a) single walled CNTs and (b) multi-walled CNTs (Dai, 2001). Each of them has been described separately in the next paragraphs.

(a) **Single walled carbon nanotubes (SWCNT)**

A single walled carbon nanotube (SWCNT) may be considered as an elongated fullerene. Alternately it may be defined as a graphite sheet (sometimes called graphene) rolled up into a cylinder with a typical diameter ranging from 0.3 nm to 2 nm, though the diameter is typically of 1.4 nm (Zhao et al, 2004). Graphene consists of a two-dimensional hexagonal array lattice structure of carbon atoms, and have an appearance like chikenwire and is depicted in Fig. 2.21, left side.
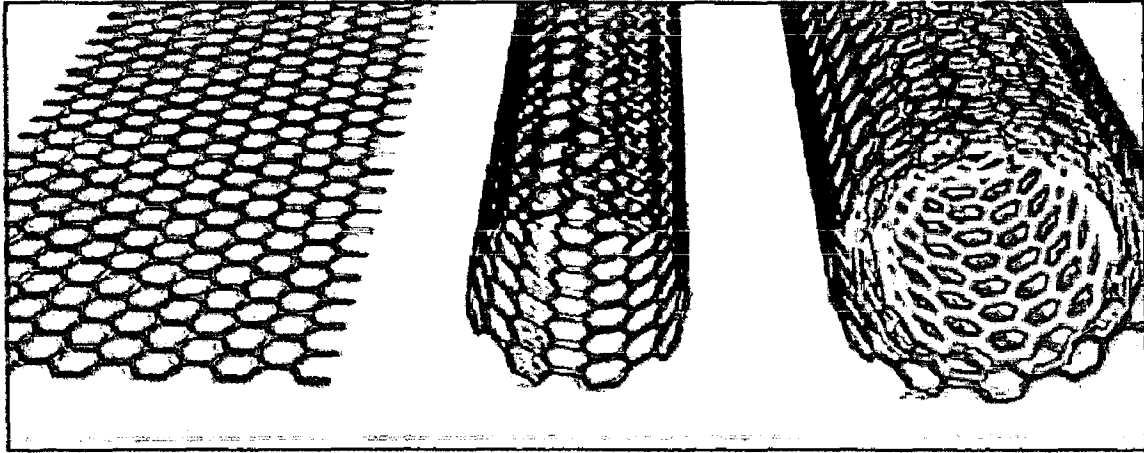
Fig.2.21: Left- graphene, center- SWCNT, right-MWCNT (Graham et al, 2005).

Their lengths of the nanotubes are generally 200 nanometer. The sidewall of SWCNTs consists of sp^2 hybridized carbon atoms that exhibit similar bonding and structure as graphite.

(b)   Multi walled carbon nanotubes (MWCNT)

A multi-walled carbon nanotube (MWNT) consists of concentric cylindrical layers of graphite sheets. The diameter varies from 2 to 100 nm, with their lengths from 5 to 100 µm (Rodriguez, 1993). In the present thesis, MWCNTs are preferred, because of parallel graphitic walls, which are analogous to self-lubricating van der Waals-bonded graphite, having layered structure (Cumings and Zetti, 2000). There are few reports that multiwalled tubes may be used as nano-bearings, because, the walls of the MWCNT can have relative rotational and translational motion between them (Kroto et al, 1985; Cumings and Zetti, 2000).

Figure 2.21 (a) shows images of a SWCNT, while Fig. 2.21 (b) to (e) shows MWCNTs with different number of layers under High Resolution Transmission Electron Microscopy (HRTEM) as reported by Ebbesen et al (1996).
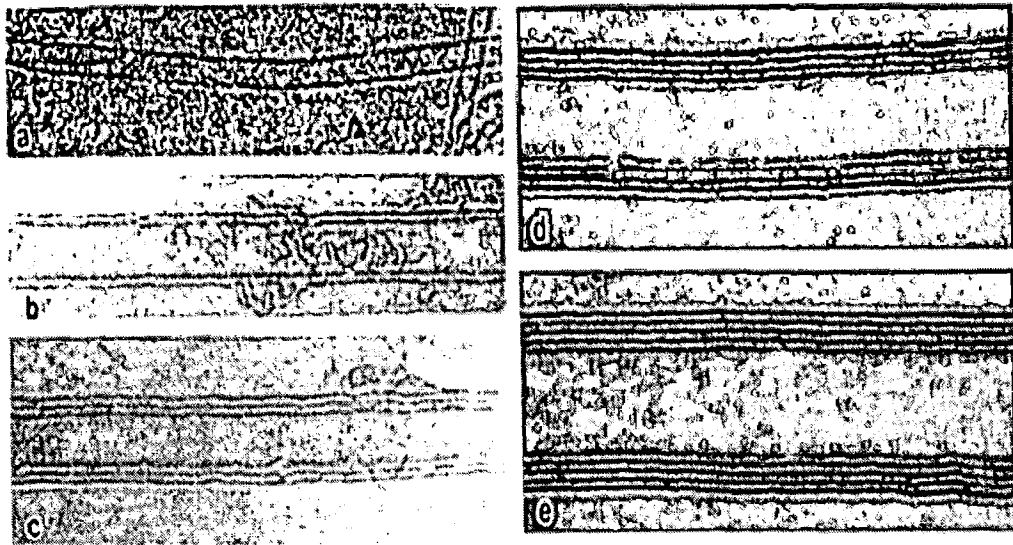
Fig.2.22: HRTEM images of CNTs showing increasing number of oncentric tubes from one to five through diagrams (a) to (e). (Ebbesen et al, 1996)

Figure 2.22 shows the HR-TEM images of MWCNTs. In MWCNTs or nanofibres, the interlayer distance is approximately 0.34 nm, close to the interlayer distance in graphite (0.335nm). In addition to the cylindrical CNTs, there are also other types of CNTs, in which the arrangement of graphite sheets is different. In a platelet nanofibre the graphite sheets are perpendicular to the fibre axis. In a fishbone nanofibre the graphite sheets are stacked with an angle of 25 ° to 45 ° to the fibre axis (Kvande et al, 2006) shown in Fig. 2.23.
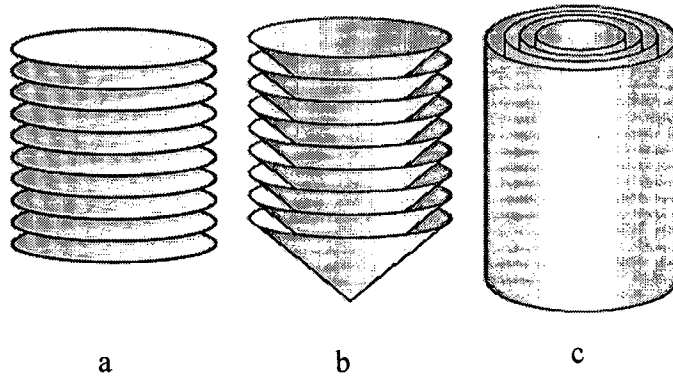
Fig.2.23: Schematic of carbon nanostructures: (a) platelet nanofibres, (b) Herringbone nanofibres and (c) multi-walled nanotubes (McCaldin et al, 2006).

There are no standards for classification and naming these nanostructures and hence few anomalies are found in the literature. One typical classification criterion is shown in Fig. 2.24 below, wherein these nanostructures have been referred as nanofibres only.
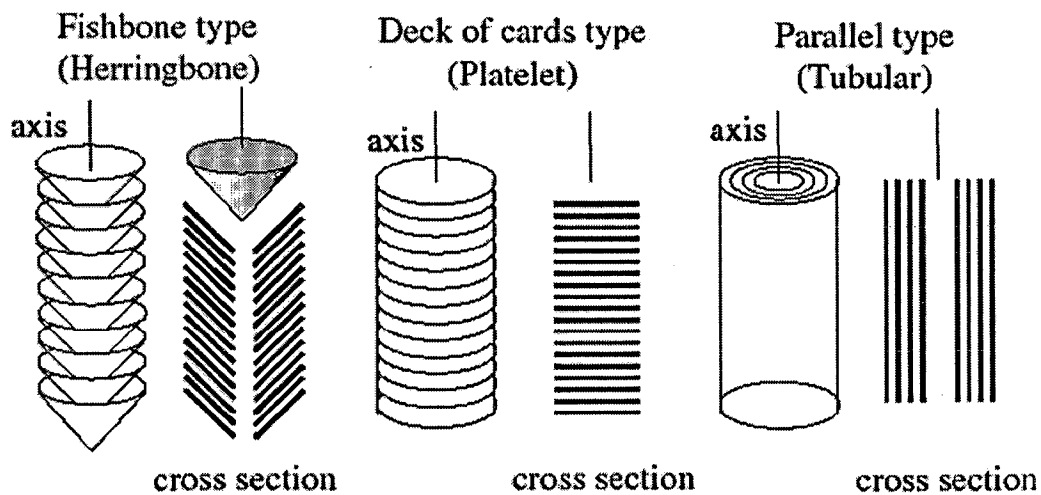
Fig. 2.24: Schematic representation of three types of CNFs (Ismagilov et al, (2005).

Many others have also used similar terminology or slightly different like, Lucas (1998) has termed CNTs as hollow carbon fibres. Toebes et al (2002) reported that the two most encountered forms of CNFs are the fishbone and the parallel type (also called multiwalled carbon nanotubes. As per Li et al (1998), CNTs were earlier called as filamentous carbon. Yacaman et al (1993) has termed CNTs as carbon microtubules with fullerene structure (buckytubes). However in the present thesis, the have been followed as shown in Fig. 2.24, which is also the most commonly used method for this purpose.

2.2.3 Synthesis methods

Carbon nanostructures can be synthesized by various methods, but the important three processes are:

(1) Arc-discharge(AD),

(2) Laser ablation (LA) and

(3) Chemical vapor deposition (CVD)

Some more methods are in use like, Flame method (Hu et al, 2001), High pressure Carbon monoxide disproportionation, i.e. HiPCO and Microwave synthesis (Lee et al, 2005). However, in the present work, chemical vapour deposition technique has been used, which is the only method that can give higher yields of CNTs/CNFs economically with comparatively good quality (Mukhopadhyay et al, 1999) at moderate temperatures and therefore, has been discussed in detail in the following paragraphs.

2.2.3.1 Chemical Vapour Deposition (CVD) method.

The schematic diagram of CVD for synthesis of CNTs shown in Fig. 2.25. CVD is a synthesis process in which the chemical constituents react in the vapor phase near or on a heated substrate to form a solid deposit. CVD is a very old process. Its first practical use was developed in 1880s in the production of incandescent lamps to improve the strength of the filaments. There are many variants of this process and nowadays it is used in combination with PVD (physical vapor deposition) processes, e.g. CVD now makes extensive use of plasma (physical phenomenon) and reactive PVD (evaporation or sputtering) occurs in a chemical environment.

In the present method, PAAO samples, having catalyst deposited in their pores are placed in a ceramic boat, which is then placed inside a tube furnace. First ammonia gas is supplied at high temperatures (about 500° C) to reduce the catalysts. Later on carbon precursor gas (acetylene) is also supplied when the temperature reaches at about 650 °C. After approximately 10 minutes, gas supply is stopped. Furnace is allowed to cool and finally samples bearing CNTs are withdrawn from the furnace when it is cooled. The details of the experimental work are given in Chapter-3.
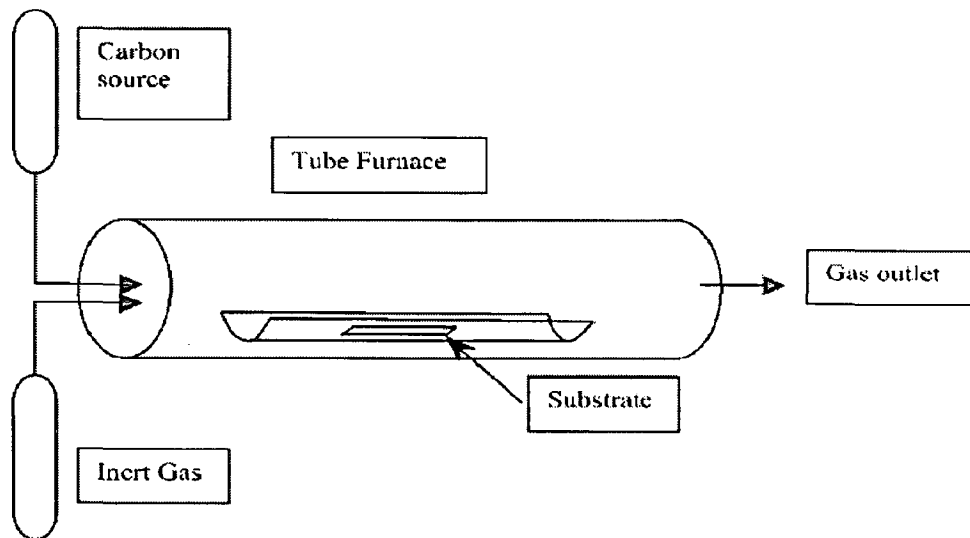
Fig. 2.25: Schematic representations of the CNTs synthesis apparatus. (Öncel et al, 2006).

CVD is widely used because the installation and recurring cost of the CVD equipment is lower in comparison with that of other methods. The overall energy expended to the system to grow CNTs is lower than in the case of laser ablation or arc discharge techniques. For this reason, the reaction needs to be catalyzed by metallic particles (usually Fe, Ni or Co) which decompose the carbon source gas at their surface (Boskovic et al, 2002) and therefore, sometimes this process is referred to as catalytic chemical vapor deposition (CCVD). The earlier mentioned methods (viz. laser ablation and arc discharge) do not necessarily need catalyst, unlike CVD. A relatively high product purity and large scale production can be obtained by CVD method (Maruyama

et al, 2002). The entire thermal or catalytic CVD process, generally, consists of two steps, namely, catalyst preparation and CNT deposition or growth. Catalyst may be prepared and placed in many ways. In t he present thesis work, catalyst has been deposited at the bottom of the pores using A.C. electro deposition method, as explained in chapter-3. The growth process involves heating the catalyst loaded PAAO substrate to moderate temperatures in the range of 550° to 650 °C in the furnace. The upper limit of temperature is due to melting point 660 °C of underlying aluminium metal. However using plasma enhanced CVD or using metallo-organic CVD, the results, which are obtained at such high temperatures in conventional CVDs, can also be obtained at about 200 °C. Carbon is deposited on the catalyst surfaces, which on precipitation develops CNTs/ CNFs. All kinds of carbon nanostructures can be synthesized by this method.

2.2.3.2 Advantages of CVD over AD and LA

The first two methods viz., arc-discharge and laser ablation although produce high-quality and nearly perfect nanotube structures, but large amounts of byproducts are also formed. CVD is the only process with which CNT can be produced with high yields, high purity, while tuning of physico-chemical properties like surface structure, diameter and morphology is possible (Toebes et al, 2002). Cassell et al (1999) have obtained kilogram scale perfect SWCNT materials via simple CVD routes. Many researchers have produced MWCNTs in moderate amounts by CVD using hydrocarbons (CH_4, C_2H_2, C_2H_4, C_3H_6 etc.) or CO as feedstock and Fe, Ni or Co as catalysts. Large-scale synthesis of CNTs (MWCNTs) by CVD has been developed in recent years (Couteau et al, 2003)

Brukh and Mitra (2006) reported that CVD is the only process that permits self-assembly on specific surfaces and substrates. The fibres can be grown into organized predefined patterns because the catalyst particles can be patterned prior to carbon deposition (Ajayan, 2000). In other words, direct synthesis of nanotubes at desirable sites of a sample seems preferable by CVD in comparison with deposition of preliminary prepared nanotubes at these sites. As per Park and Sudershan, (2001), films can be deposited on elaborately shaped parts, including the insides and outsides of features, and that high-aspect ratio holes and other features can be completely filled by CVD. In other words, two advantages of CVD methods are the ability to controllably create films of widely varying stoichiometry and to uniformly deposit thin films of

49

materials, even onto non-uniform shapes (Alsyouri et al, 2003). Due to these advantages, this method was selected for CNTs growth in PAAO in the present study. Thus a possible and very important application of this concept (CNTs/CNFs embedded PAAO surface) could be cylinder liners/sleeves which are currently made of grey cast iron, which is quite heavier than aluminium.

2.2.3.3 Advantages of TCVD over PECVD

Depending on the final application, thermal CVD could be even more desirable than plasma enhanced CVD because thermal CVD processes are more economical (Choi et al, 2001), suitable for large-area, irregular-shaped substrates, and multiple-substrate coatings. Additionally, no radical species are generated during thermal CVD processes that may result in the formation of different side products of carbon. Thus, in absence of those highly reactive species, the employed carbonaceous precursors exclusively interact with the catalytic nanoparticles that subsequently will promote the CNTs growth. Therefore, a vast variety of substrates of any size and shape that are compatible with the furnace dimensions, growth temperature and gas environment can be coated with CNTs (Terrado et al, 2006). CNTs produced by PECVD are having many defects, because the catalyst particles are etched away constantly by the plasma during the growth so that the nanotube shape was core-like (Zhu et al, 2002). For applications in tribology, a large amount of CNFs or CNTs is necessary, which may form a smudged, low-friction transfer layer of graphitic materials after initial run-in period, and thus thermal chemical vapour deposition technique, due to its above-mentioned advantages mainly high yield at low cost, has been followed in the present study.

2.2.3.4 Drawbacks of CVD

Nanotubes obtained by CVD are longer than those obtained by arc-discharge method; however, the tubes synthesized by CVD are not well crystallized and contain high density of defects (Marangoni et al, 2001). The defective nature of CVD grown MWCNTs may be due to the relatively low growth temperature, i.e., in the range of 550 to 1000 °C, which does not provide sufficient thermal energy to anneal nanotubes into perfectly crystalline structures. Though in the context of the present thesis CNTs/CNFs produced from CVD may serve the lubrication purpose, i.e. may act either

as good solid lubricant itself due to nanometeric dimensions, reasonably good degree of crystallinity or as a lubricant reservoir, as already envisioned in earlier few reports (Tu et al, 2004; 2005) and recently Xia, (2008).
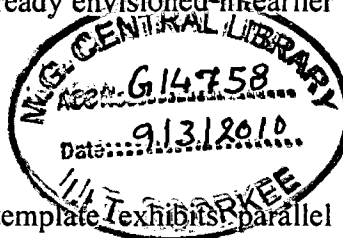
2.2.4 Growth of CNTs in PAAO

Since the morphology of PAAO template exhibits parallel pores growing perpendicular to the surface with a narrow distribution of diameter, PAAO template as a medium is widely used for the fabrication of one-dimensional nanomaterials in recent years (Maschmann et al, 2006). The size, interpore spacing and depth of the pores can be tailor-made as per the requirement by varying anodization process parameters, which offers a lot of flexibility in manufacturing diverse types of nanostructures in confined pores of PAAO (Piao et al, 2005). This method is also called as 'template-modulated method' (yen et al, 2005). Secondly for many electronics applications CNTs are connected to some silicon based structure, if grown separately. Because of the small sizes of CNTs, it is difficult to handle them (Iwasaki et al, 1999) and hence they may be directly grown within aligned pores of PAAO having direct connection with silicon based substrates (Yin et al, 2006 and Hu et al, 2001). These uniformly sized and spaced arrays of vertically aligned CNTs are highly desirable for many applications, including field-emission, microelectronics, electrochemical probes, molecular interfaces, and microfluidic devices (Yin et al, 2006). This nanocomposite is very suitably used for sensing gases (Chen et al, 2005), Since the sensitivity is essentially governed by the specific surface area of the sensor material, the improvement of gas sensitivity is simply achieved using nanosized materials due to their high surface-to-volume ratio (Biswas and Pramanik, 2008) and hence this aligned growth of CNTs in PAAO is being extensively studied due to its great potential.

(a) CNTs in AAO without CVD

CNTs with uniform and controllable dimensions can also be produced by the PAAO template without CVD. Hulteen et al (1997) have prepared arrays of CNTs, capped nanotubes and nanofibrils with a nominal outer diameter of 200 nm and length of 60 µm by polymerization of acrylonitrile within the pores of aluminum oxide membranes. After polymerization, a series of heat treating conditions were used by them, which converted the polymer structure into a quasi-graphitic structure. The CNTs have also been generated by similar method by Parthasarathy et al (1995). Kyotani et al

(1996) and Fuertes et al (2002) have also reported growth of CNTs by pyrolyzing a thin layer of furfuryl alcohol which was previously coated on the surface of the pores in the templates.

(b)   CNTs in PAAO WITH CVD

CVD of materials in porous alumina nanoholes is a challenging topic for researchers. Since porous alumina contains extremely high aspect ratio (ratio of depth to diameter) pores, it is of great interest to discover how high aspect ratio of pores can be filled by CVD and CNTs/CNFs are produced from within the pores having reasonably good quality and sufficient quantity. Li J. et al (1999) first provided the demonstration of CNTs synthesis in porous alumina. Though CVD process was already used for CNT production but without using PAAO as early as 1993 (Jose-Yacaman et al, 1993). Though there are various reports that quality of CNTs grown by this method is poor as compared to growth without PAAO. The strain induced by the channel wall of the PAAO due to the lattice mismatch between alumina and carbon species makes the wall of CNTs disordered. Without PAAO template, well-graphitized CNTs could be synthesized under the same experimental condition (Yang et al, 2003)

Figure 2.26 (a) shows the schematic of the process while Fig. 2.26 (b) shows SEM micrograph of a well-ordered array of CNT grown on PAAO.
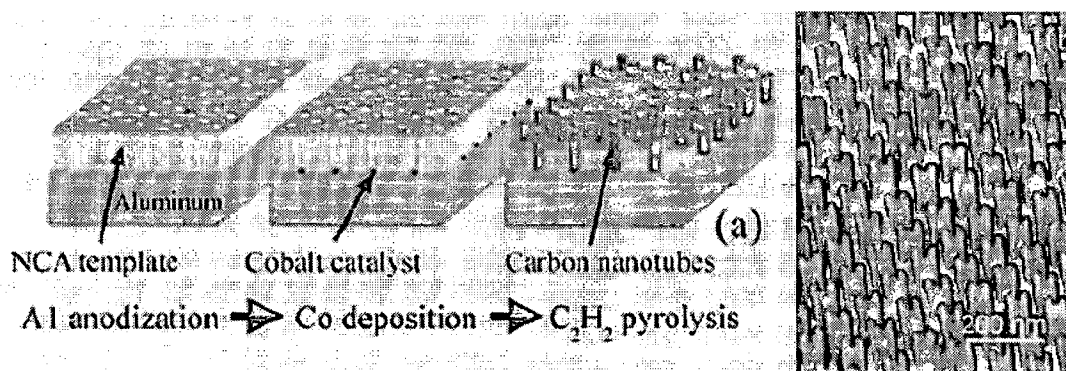
Fig.2.26: Schematic of growth of Carbon nanotubes/fibres in porous alumina (referred as NCA template here) by CVD method (a) and SEM image of arrays of carbon Nanotubes fabricated using this method (b) (Li et. al., 1999).

There are many variants of this process and hence comparison of the various reports from literature is an extremely difficult task. However, there have been few efforts to review this specific and important area. Sklar et al (2005) have summarized some experimental data from literature in a tabular form, including the details of the carbon precursor / dilution gas for all those cases where MWCNTs grew beyond the pore confines. The tube wall of these CNTs from the template-modulated synthesis, such as in PAAO, can be composed of a graphitic multi-walled structure (Kim, 2003), stacked flakes of carbon layers (Kyotani et al, 1996) or an amorphous structure (Tsai, 2000). However tube formation is favored over other forms of carbon such as graphitic sheets with open edges. This is because a tube contains no dangling bonds and therefore is in a low energy form (Dai, 2001). Both types of CNTs, viz. SWCNTs and MWCNTs are reported to have been produced by this method depending on the conditions. Li et al (1998) concluded that the tubes are multi-walled with at least 10 graphitic layers. A similar approach has also been used by Suh et al (1999), who also reported formation of MWCNTs. Further, there are numerous publications pertaining to growth of CNTs by PAAO, e.g. (Gao, 2003; Che et al, 1998, Li et al, 1999, Iwasaki et al., 1999; Sung et al, 1999; Sui et al, 2002; Hu et al, 2001; 2002 and Wang et al, 2002) after the pioneer work of Li (1999) and Li and Papadopoulos (1999). The main objective of all these researchers generally was to get field emission from these aligned CNTs and other electronic applications besides sensors. There are comparatively a few reports which have studied / targeted tribological applications of these composite nanostructures. Even these studies were conducted under very low loads (Tu, J.P. et al, 2004; 2005), probably to explore their potential use in MEMS (micro-electro-mechanical systems) and NEMS (nano-electro-mechanical systems). Literature related to exploration and exploitation of this novel, high potential material under tribological applications in many conventional and emerging engineering and technological areas is very rare. The available literature has been presented in the third section of this chapter, under the title 'Tribology of CNTs/CNFs'.

2.2.5 Growth mechanisms

The way in which CNTs are formed is still not known. The growth mechanism is still a subject of contradiction and more than one mechanisms might be operative during their growth. Following are the theories commonly considered for their growth, viz.:

(i)   V-L-S (Vapour-Liquid-Solid) theory (Kukovitsky et al, 2000)

(ii)   V-S (Vapour-solid) theory (Harris et al, 2007)

The synthesis or growth of CNTs/CNFs by CVD involves the decomposition of a carbon precursor g as over the nanosized catalyst surfaces. When the catalyst is situated in the pores of PAAO, growth mechanism may be slightly different from all other commonly used and general cases where growth takes place outside the pores or on the nanometer sized catalysts placed either on flat substrates or on patterned supports using CVD. A lot of literature review is available on the role of catalysts and their associated factors on the mechanism of CNTs/CNFs growth.Review paper by Dupuis (2005) clearly broadens the knowledge available for the role of catalyst in forming CNTs using CCVD method. All the associated aspects have been discussed in detail. In the next paragraphs available literature for both cases have been presented and discussed.

2.2.5.1 Growth modes

The growth of CNTs by catalytic decomposition of precursor vapors has been postulated as either base or tip growth (Baker, 1989). Generally the reason for this difference has been stated as under. If the adhesion between the substrate and catalyst is stronger, base growth is observed (Song et al, 2004 and Bower et al, 2000b). Tip growth is observed in two cases. First, if the adhesion is less or secondly if part of the catalyst gets broken and remains at the top, encapsulated by the tip of the growing tube, which is also growing vertically upwards. SEM studies indicate residual Co-Fe catalyst in the base of the tubes, indicating a tip growth mechanism could be responsible for the tube growth. (Fan et al, 2003) demonstrated that the nucleation pathway for SWCNTs on a metal surface is by a series of total energy calculations using density functional theory. Incorporation of pentagons at an early stage of nucleation is energetically favorable as they reduce the number of dangling bonds and facilitate curvature of the structure and bonding to the metal. In the presence of the metal surface, nucleation of a closed cap or a capped single-wall carbon nanotube is overwhelmingly favored compared to any structure with dangling bonds or to a fullerene. A more detailed overview of various growth methods can be found in the book by Dai, (2001). These growth modes of nanotubes in CVD are shown schematically in Fig. 2.27.
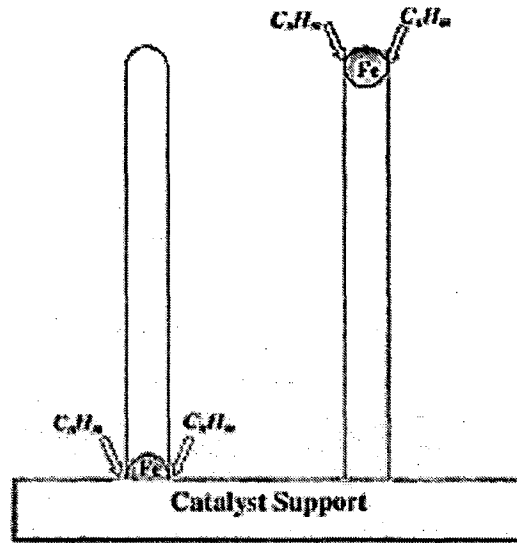
Fig.2.27: Two general growth modes of nanotubes in chemical vapour deposition.: base growth in the left;: tip growth in the right (Dai, 2001)

Both types of mechanisms have been reported in literature, in case of templated growth, while tip growth dominates over base growth.

(a)   Tip growth

Model has been proposed by Baker and others (Baker et al, 1978; Charlier and Iijima, 2001; Dai, 2001) for the so-called tip growth mode. The catalytic particles of some transition metal elements or alloys (e.g., Ni, Co, and Fe) frequently are represented as an inverted truncated cone, out of which the nanotube grows. Carbon must be supplied at the top surface from some carbon-containing gas that is 'cracked' at the surface. It is convenient to consider the schematic diagram (Fig.2.8) reported by Pannala and Wood, (2004), as being divided into three regions. Region 1, which is not explicitly shown on the figure, eventually incorporates a description of the gas-phase reactions just above the catalytic particle.
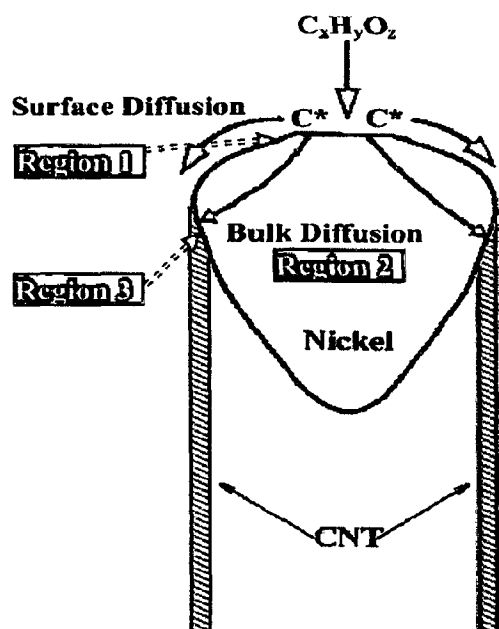
Fig. 2.28: Tip growth mechanism (Pannala and Wood, 2004).

Region 2 contains the catalytic particle itself, whereas region 3 contains the interfacial region between the catalyst and the growing CNT (Toebes et al, 2002; Terrado et al, 2006). This reveals that the MWCNTs were produced by the so-called tip growth mechanism, since the Co catalyst nanoparticles are encapsulated on the nanotube closed tip. The research paper by Pannala and Wood (2004) reports the theoretical modeling of the growth mechanism. Zhu et al (2002) reported that the CNTs growing under tip growth mode starts bending if they are grown for longer durations, due to the weight of the catalyst at the top. To avoid this problem, the substrate is kept inverted so that growth direction is along gravity (downwards), so that bending of CNTs may be avoided. All these structural aspects may affect tribological properties of the resulting CNTs. Only tip growth is possible growth mode within PAAO. With regard to the base growth, the precursor gases must continuously transport to the Co catalyst at pore bottom. If the gas diffusion is blocked, the catalytic growth of CNTs will be terminated. However, under the experimental condition, the nanopores are compactly filled with multiwalled CNTs and, moreover, the tubes have a closed end. The encapsulated Co nanoparticles at their tips can block the gas diffusion implying that the base growth is unfavorable. In the tip growth, the gas diffusion will not be obstructed because the CNT growing site is at the tip of the tubes. Xu J., (2005) has also reported tip growth. .

(b) **Base growth or root growth.**

There are various reports (Zhu et al, 2006) indicating that CNTs have grown in base growth or root growth mode. The base growth mode of SWCNTs formation shown in Fig. 2.29.
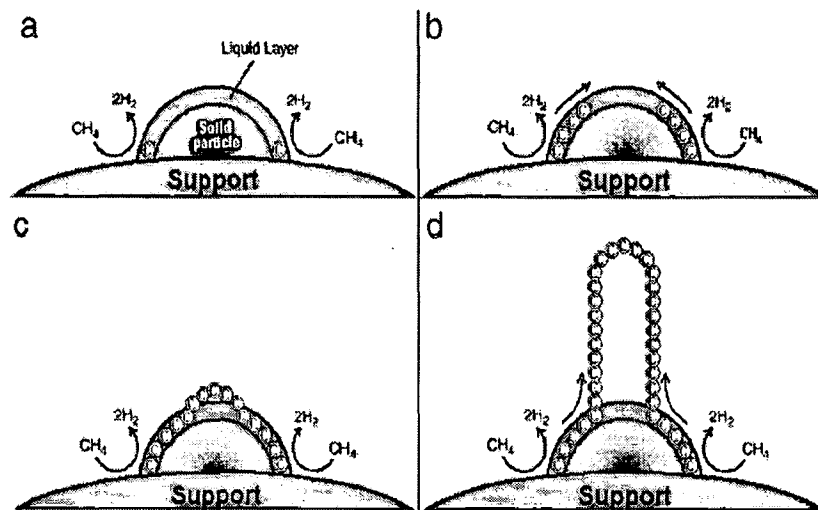
Fig.2.29: Schematic view of the nucleation of a cap and a SWNT. (a) Hydrocarbon decomposition. (b) Carbon diffusion in the surface layer. (c) Super-saturation of the surface and formation of the cap. (d) Growth of a SWNT (Nagy et al, 2004).

2.2.5.2 Mechanism of CNF growth

Toebes et al, (2002) have described growth mechanism of CNF as shown in the Fig 2.30.
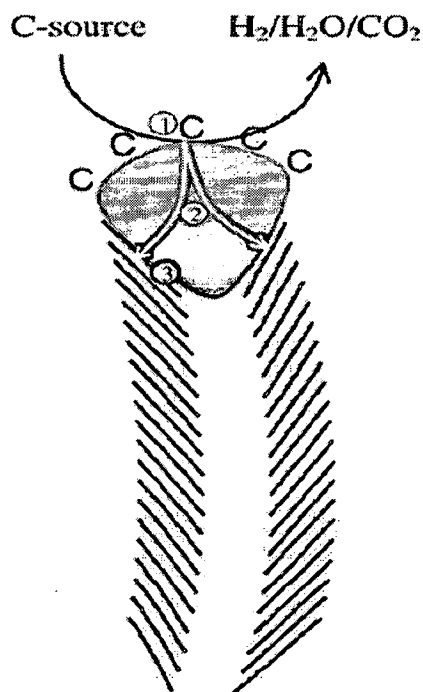
. **Fig. 2.30:** Schematic representation of the catalytic growth of a CNF using a gaseous carbon-containing gas. Step1: decomposition of carbon-containing gases on the metal surface. Step 2: carbon atoms dissolve in and diffuse through the metal. Step 3 : carbon precipitates on the form of CNFs or CNTs at the other side of the metal particle. (Toebes et al, 2002).

2.2.6 Growth in PAAO

PAAO templates have been extensively used to grow CNTs using chemical vapor deposition (CVD) of hydrocarbons (Kyotani et al, 1996); Hornyak GL et al (1999); Li, J. (1998); Li, J. (1999); Papadopoulos C, (1999)). Previous reports can be classified into two categories.

(i) PAAO template itself as catalyst: Hydrocarbon is deposited on the pore surface of an PAAO template and in this case, the carbon tubes were formed by the mild catalytic action of an PAAO template itself (Kyotani et al 1996). However, these carbon tubes showed high crystallinity only after they were annealed at 2800 °C. Similarly, Hornyak and coworkers (1999) produced carbon tubes in the pores of an PAAO membrane by decomposing propylene at 500-1000 ° C and showed that crystalline domains of graphitic layers were localized only in nanometer size. The strain induced by the pore

wall due to the lattice mismatch between alumina and carbon species makes the wall of CNTs disordered. CNTs grown within the templates such as PAAO, would have poorly graphitized structure due to the same reason as mentioned above, unless lattice mismatch between the template and the CNT is minimum.

(ii) Metallic catalyst: The other approach is that hydrocarbon is deposited on the PAAO template embedded with transition metal catalyst such as Co (Li et al, 1998). Li, J.(1999b) fabricated arrays of carbon tubes by pyrolysis of acetylene at 650–700 °C, followed by annealing at 700 °C. This method has been widely adopted by other investigators in order to grow CNTs (Papadopoulos C, (1999); Sui et al, (2001); Zhang et al, (2001); Yuan ZH, (2001)). All these studies reported good quality CNTs in the presence of catalyst.

However, Sui et al. (2001) showed that CNTs synthesized by the pyrolysis of C_2H_2 at 650 °C in an PAAO template with or without Co catalysts had the same tube wall structures consisting of numerous stacked carbon flakes, instead of straight coaxial cylindrical graphitic units. Without PAAO template, well-graphitized CNTs could be synthesized under the same experimental condition (Kibria et al, 2002).

2.2.7 Factors affecting CNTs/CNFs formation in PAAO using CVD

There have been many works carried out to systematically investigate the effect of various important factors on the resulting morphology and properties of the CNTs/CNFs, (Öncel and yürüm, (2006) and Kvande et al (2006)). They reported that although higher yields of fishbone CNFs can be obtained by changing the gas precursor, there is always a trade off between quality and yield with respect to the application. In general, the CNFs synthesized with a low growth rate have good crystallinity. There are o many conflicting reports, considering various factors and their role on morphology, structure, yield etc. Available literature has been categorized and an effort has been made to develop an understanding so that decisions regarding optimized growth of CNTs/CNFs within PAAO may be taken. The effect of each individual factor has been described separately in the next paragraphs.

(a)   Effect of carbon precursor type

Various types of carbon precursor gases have been used by researchers such as CO and short-chain hydrocarbons like, methane (Toebes et al, 2002), ethylene (Fan et

al, 1999 and Pan et al, 2004), acetylene (Pan et al, 2004), propylene (Kyotani et al, 1996) etc. Systematic studies of the relationship between the nature of the carbon-containing gas and the structure of the resulting CNTs/CNFs are very scarce. The intrinsic activity of the gases of course determines the CNTs/CNF growth rate over different catalysts. Some typical studies in this regard are briefly reviewed here in the following paragraphs.

Sklar et al, (2005) has summarized the PAAO-templated MWCNT growth, reported in the literature, where the tubes grow beyond the pore confines. Hernadi et al (2000) observed that over supported Fe or Co catalysts, the activity of acetylene is higher than that of ethylene and propylene, which are in turn higher than methane. For MWCNT growth, most of the CVD methods employ ethylene or acetylene as the carbon feedstock and the growth temperature is typically in the range of 550–750°C while for SWCNT growth, methane (CH_4) is often used at very high temperatures (up to 1200° C) as single walled tubes have smaller diameter and thus higher curvature, hence posses more strain energy and hence their energy for formation is also higher compared to multiwalled tubes. Secondly, CH_4 is stable at higher temperatures and hence preferred for SWCNTs (Dai, 2001). However there are few exceptional reports also, refuting this hypothesis/understanding.

Pan et al (2004) reported that C_2H_4 normally requires 100 °C higher temperature for pyrolysis than for C_2H_2 under identical conditions. Some researchers used a mixture gas of acetylene (C_2H_2) and ammonia (NH_3) in the reaction tube at a total flow rate of 100 sccm with a volume ratio of 1:9 respectively, for 20 min to grow CNTs within the PAAO pores by pyrolysis of acetylene at 600 °C, without using any additional catalyst. Lee (2001) used acetylene with iron catalyst whileYuan et al (2001) used ethylene with an ethylene-argon mixture of 20:40 sccm.

(b)   Effect of catalyst type, its size, support and reaction conditions

It is well known fact that CNT growth by CVD needs catalysis for thermal decomposition of precursors. It has been widely reported that the most effective catalysts for the CVD growth of CNTs are Fe, Co, and Ni (Terrado, 2006). The rationale for choosing these metals as catalyst for CVD growth of nanotubes lies in the phase diagrams for the metals and carbon. At high temperatures, carbon has definite solubility in these metals, which leads to the formation of metal-carbon solid solutions. As temperature lowers, solubility limit decreases and precipitation starts and therefore

the aforementioned growth takes place (Sinnott et al, 1999). In other words, these transition elements are preferred due to their peculiar ability for the decomposition of the carbon feedstock (typically a hydrocarbon), the formation of meta-stable carbides, the carbon diffusion, and the formation of graphitic sheets (Andriotti et al, 2000). As per oncel et al, (2006), widely used catalyst materials in CNTs synthesis are Co, Fe, Ti, Ni, a couple of zeolites and combinations of these metals and/or oxides. The use of bimetallic or trimetallic mixtures of Fe, Co, and Ni with elements such as Y, Mo, Ru and Pt has led to massive increase in yield under certain conditions (Cassell et al, 1999). It is also reported widely that catalyst support manner also affects the growth and in this regard, Nagy and his coworkers have documented reports quite extensively (Nagaraju et al, 2002, Hernadi et al, 2002 (a) and Hernadi, (2002 b). Interestingly, for acetylene and methyl acetylene decomposition on supported Ni, Co, or Fe catalysts, Hernadi,(2002) disclosed that the catalyst supports have more influence on CNTs selectivity than the metallic itself. A porous support exhibiting non-continuous surface can contribute significantly to particle stabilization by preventing sintering, and produce a fine dispersion of well-defined metal particles (Veziri et al, 2009). In addition, the large surface area and high adsorption capacity of porous supports, in contrast to dense substrates, drastically increase the number of dispersed particles, thus increasing nucleation sites, which is advantageous for high yield carbon growth. Examples of porous supports that have been used for catalytic growth of carbon nanostructures include activated carbon, magnesia, alumina, and zeolites (Veziri et al, 2009). PAAO has also become very common these days due to hexagonally ordered nanopores. The numerous studies carried out to study the growth process have shown that the diameter of the CNT is determined by the size of the catalytic particle (Ren, et al 1998, Bower et al (2000), Wei, at al (2001)). For SWCNTs synthesis, very small size catalyst particle is a prerequisite. Li et al (1999a, b) used electrodeposited CO as a precursor, while Iwasaki et al (1999) used Nb located beneath the aluminum layer as a precursor. Wang X.H. et al (2000) reported low-temperature deposition of CNTs at around 520 °C by microwave plasma assisted CVD. Nagaraju et al (2002) compared catalytic activity of Fe, Co and Fe/Co supported on alumina or silica. They showed that a best yield of MWCNTs resulted at 700 °C on hydrated alumina prepared from aluminium iso-propoxide and containing a mixture of Fe and Co in it. Some authors have compared the catalytic activity of Fe, Co, or Ni as the catalyst and laser treated vanadium plates having high surface area as the catalyst support in the decomposition

of acetylene at 720 °C under CVD conditions. Best quality CNTs were obtained over the Fe catalyst with high density and small diameter (10–15 nm) CNTs. Over Ni and Co catalysts, the carbon source was mainly converted to amorphous or fibre-like material (Seo et al, 2004). Lee et al. (2002 a) showed that CNTs can be produced effectively with tungsten-based catalysts. The resulted CNTs were well-aligned, multi-walled structure and highly pure. Lee et al. (2002 b) studied the effect of selected catalysts (Ni, Fe and Co) on the synthesis of CNTs. Soneda et al, 2002, used MgO support and found that Co is the most effective catalyst for MWCNT synthesis, because of a significantly high production rate and high quality tubes with a narrow diameter distribution. Huang et al (2002) used TiO_2 support and concluded that Ni is the best catalyst for the growth of aligned CNTs. The choice of the catalyst and support material may be a determining factor in the SWNT synthesis . Observation of Dupais (2005), that Co is best in terms of quality product is also an additional confirmation to the earlier works, which has found the same result.

Sun et al (1999) reported catalytic synthesis of a large amount of straight carbon nanotubes using a transition-metal cobalt–nickel/zeolite catalyst. It is well known that when a single crystal of metal is used as a catalyst, different crystal planes have different catalytic performance. As for the growth of carbon nanotubes in previous reports, when just one transition metal is used as a catalyst, due to different catalytic activity on the surface of the nanoparticles, (Amelinckx, et al., (1994)). The growth rate along the circumference is not uniform; and this causes the nanotube to curve towards the lower growth rate side. As a matter of fact, the transmission electron microscopy image in their paper reveals that Co–Ni alloy nanoparticles are very much like spheres. This regularity in morphology indicates the surface of the Co–Ni alloy is nearly uniform. In the case of a Co or Ni single metal catalyst, TEM examination indicates that Co or Ni metal nanoparticles are nearly polygonal. In addition, when they used a Ni or Co single metal catalyst to grow carbon nanotubes in the same condition as that of the Co–Ni alloy, no similar results can be obtained, even when they adjusted the growth conditions. Therefore, they speculated that in their experimental condition the catalytic activity on the surface of the Co-Ni alloy is nearly uniform, which results in a uniform growth rate along the circumference. This might be the reason how straight nanotubes are grown.

A study was performed by Deck and Vecchio (2006) of the respective metal–carbon binary phase diagrams to understand why the catalytic ability of different

elements varied. Successful catalysts had carbon solubility limits of 0.5 wt.% to 1.5 wt.% carbon, followed closely by nanotube growth through graphite precipitation. Unsuccessful catalysts were found to have either nearly zero carbon solubility, or to form numerous intermediate carbides, making it difficult for the diffusion required for graphite precipitation to occur.

(c)   **Effect of precursor gas (acetylene), dilution / etchant gas (ammonia)**

As already have been discussed that various types of hydrocarbon gases and dilution or etchent gases are used in the CVD-CNT synthesis. Systematic studies of the relationship between the nature of the carbon-containing gas and the structure of the resulting CNTs/CNFs are very scarce. The intrinsic activity of the gases of course determines the CNF growth rate over different catalysts. Hence this part of the review includes only those observations, which are important and pertinent to this study. The large supply of hydrocarbons to grow CNTs can poison the active catalyst center.

When the concentration of acetylene in the feed gas is high, deactivation of the Co catalyst is fast and the catalytic role of alumina becomes dominant (Jeong et al, 2001).

Researchers have reported the use of ammonia (NH_3) in thermal CVD of carbon nanotubes (Wei et al, 2005; Heer et al, 1995; Li et al, 1996, Terrones et al, 1997; Lee et al, 2000; Lee et al 1999 and Jung et al, 2004). NH_3 is believed to keep catalysts (Fe, Co, Ni, etc.) from being passivated by amorphous carbon, an undesirable product generated from decomposition of hydrocarbons (methane, ethylene, acetylene, etc.). By varying the flow rates of ammonia and hydrocarbon, the density and morphologies of as-grown CNTs can be controlled (Wei et al, 2005). The precursor for carbon nanotubes is fed into the system in the gaseous state at some specific conditions. To avoid oxidation of the carbon, the chamber is kept free of oxygen during the production process. Generally continuous inert gas (e.g.N_2 and Ar) flow is supplied to the reaction chamber. N_2 and Ar are the most extensively used inert gases Öncel et al (2006).

(d)   **Effect of Temperature of CVD reactor**   A systematic study on the growth of CNTs has been carried out by Lee et al (2001) and found that as the growth temperature increases from 750°C to 950°C, the CNTs growth rate increases by four times and the average diameter also increases by from 30 nm to 130 nm and the best crystallinity is obtained at the highest temperature of 950 ° C. Terrado, et al (2006) also observed somewhat similar results. They found that average diameter of MCWNT increases from

30 nm at 750 °C to 100 nm at 900 °C. The growth temperature not only affects the MWCNT diameter, but also its morphology. MWCNTs grown at 750 °C and 800 °C are straighter and aligned than those grown at higher temperatures. However there is a limiting value of temperature, below which no growth is possible. As per Sui et al (2002), carbon nanotubes or nanofibres can be formed only when the deposition temperature is above 550 ° C. They observed that no CNTs could be obtained at 500 ° C. Results of Huh et al (2003) demonstrate that the controlled growth of CNTs can be effectively realized by adjusting Co nanoparticles and growth temperature. MWCNTs have uniform diameters of about 40, 30, and 25 nm at 950°, 850° and 750 ° C, respectively. Fishbone CNFs are most often synthesized on supported Ni catalysts. Typically, MWCNTs are obtained at higher temperatures (700–1000 °C), while CNFs are obtained at lower temperatures (400 – 700 ° C) (Kvande et al, 2006). Hoa et al, (2007) also found that crystallinity improves with temperature. Ducati et al., 2006 synthesized randomly oriented and aligned carbon nanotubes by chemical vapor deposition at temperatures 550 ° C, 700 ° C, 850 ° C. The diameter of the tubes and the degree of crystallization of the graphitic walls are determined by the temperature. The diameter of tubes increase with reation temperature as shown in Fig.2.31.
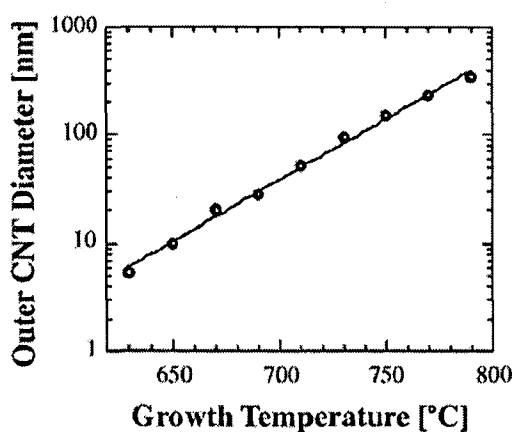
Fig. 2.31: Outer CNT diameters as a function of growth temperature (Kaatz, et al., 2003)

The temperature appears to influence the CNT yield differently depending on the specific reaction system. Kukovecz et al. 2000 reported that the amount of CNTs increases with increasing temperature from acetylene decomposition. It is also reported that the CNF yield decreases with increasing temperature from methane decomposition.

The CNT yield might also decrease with temperature due to catalyst particle sintering at high temperatures. The effect of temperature on the structures of CNTs has been investigated on Fe/SiO_2 by acetylene decomposition from 600 to 1050°C and gas pressure of 0.6 and 760 Torr. At low gas pressure, the CNTs are completely hollow at low temperature and bamboo-like at high temperature. While at 760 Torr, all the CNTs are bamboo like structure regardless of temperature. Therefore, the effect of temperature on carbon structures depends on the gas pressure. Takenaka et al. 2000 reported fishbone CNFs at 500°C but MWNT at 700°C from methane decomposition on Ni/SiO_2. Finally, the reaction temperature influences the graphitic order of CNFs. It has normally been found carbon fibres with more ordered or more disordered carbon after growth at high and low temperatures, respectively.

(e) *Effect of Pressure:*   Studies of the effect of gas pressure on the production of CNTs and CNFs are less performed. Higher pressures will normally increase the carbon yield but decrease the CNT selectivity. From acetylene decomposition over supported Fe and Co catalyst, Hernadi et al. 2000 reported that carbon deposit increases with higher pressure, but leads to worse selectivity and many other kinds of carbon structures. Some studies have observed an optimum partial pressure. Li et al.2005 found that the yields of CNTs increase significantly with the gas pressure from acetylene decomposition over Fe/SiO_2 catalyst, reached 600% at 600 Torr and then decreases with further increase of gas pressure. Li et al. 2006 also observed a change in the internal structures completely hollow structure at low pressure but bamboo structure at high pressure.

(f) *Effect of reducing/dilution gas:*
The gases which are used in CVD along with the carbon precursor gas for reduction of the deposited amorphous carbon species on the catalyst are known by many names, e.g. reducing gases, dilution gases, etchent gases or carrier gases. Use of many types of reducing gases has been reported in the literature and only few important ones have been presented here. Ammonia gas is one of the best choices for this purpose and thus has been used. Ammonia gas dissociates as follows

$2\,NH_3 = N_2 + 3\,H_2$ (Y. Lakhtin, Mir Publishers, Moscow.1998).
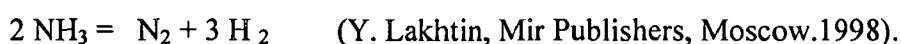
The hydrogen and nitrogen have their individual roles in the growth of CNTs/CNFs. The role of hydrogen has been described quite extensively in both the vapour grown carbon fibre (VGCF) and CNTs literature. Hydrogen is known to either

accelerate or suppress the formation of CNTs. The most significant effect of hydrogen is to change the orientation of the graphite sheets, which has been illustrated nicely by Jiao and Nolan.2000. Jiao et al 2003 found that when no hydrogen was present, only closed forms of carbon deposits such as MWCNTs were produced from CO. As the hydrogen partial pressures increased to 0.1 vol%, the filament with open edges was observed. The number of open edges and the angle between the graphite sheets and the axis increased with increasing H_2 concentration.

(g)   Effect of anodized template:

PAAO template causes significant effect on the morphology and growth of the CNTs/CNFs. There is consensus view that CNTs diameter is almost same as that of the diameter of the pores   Xu J., 2005; Jeong et al, 2001 and Yanagishita (2004) reported that CNTs take the diameter of the PAA pore walls from which they originate. They found diameter of CNTs in the range of 30–50 nm. Similarly Che, G. et al, 1998; Kyotani et al, 1996; Parthasarathy et al, 1995 and Fuertes, 2002, have also obtained diameter of CNTs from these PAAO template, depending on the original pore size in the template in the range of 30–300 nm. There are few reports mentioning that pore diameter may be measured by measuring diameter of the CNTs when separated from PAAO. Wang et al (2000) also reported that diameter and length of CNTs are equal to diameter and depth of pores of PAAO. As per report by Sigurdson et al. 2009, if pore diameter of PAAO is more than 60 nm, open ended CNTs are formed, otherwise close ended CNTs are formed. These open ended tubes are better option for lubrication with oil for tribological applications as in the present case.

2.2.8 Anodic alumina as a catalyst

There are many reports wherein PAAO has been used successfully as catalyst in the absence of other transition metal elements or compounds. The diameter, length, arrangement, and packing density of aligned nanotubes can faithfully replicate the pattern of the PAAO nanopore structure. However, the obtained tubes are very poor in graphitization (Kyotani et al, 1996; Sui et al, 2001). There are some more reports where the same route has been followed (Kim, 2003; Che, 1998; Tsai, 2000 and Sui, 2002). With the metallic catalyst particles, the CNT synthesis usually occurs randomly on a part of the particles, and it further grows out of the pores (Jeong et al, 2003 and Sklar et al, 2005). This morphology has no advantages for using the regularity of the nano structure

involved in the PAAO template. Therefore, many researchers employed the synthesis without the catalysts (Hoa et al, 2007). Flaked graphite sheets of MWNTs are pyrolytically deposited on PAAO, conforming to the surface geometry of the nanopores (Cho et al, 2005). Bamboo shaped CNTs formation mechanism has been reported by Zhao et al (2007). PAAO acts as catalyst

PAAO, which has been known to consist of crystalline γ or γ'-Al_2O_3 (Li et al, 1999(a)) and Sui et al,(2001) was reported to exert a significantly higher dehydrative catalytic activity than that of the chemically prepared γ-Al_2O_3 for dehydrogenation of 2-propanol and decomposition of HCOOH.

2.2.9 Miscellaneous factors affecting CNT growth through PAAO using CVD

Reynolds number i.e. whether the flow is laminar or turbulent in cvd reactor (Sun et al 1999). Additionally, the cracks and warps which are caused by the differences in the thermal expansion coefficients of the AAO template and the aluminum substrate could be avoided by raising the furnace temperature at slowly 5 °C / min up to 650 °C (Sklar et al, 2005). If catalyst deposition process parameters are not controlled properly, growth of CNTs may start at the top of the pores which may block the passage of carbon precursor gas to the bottom of the pores. Thus deposition of Co catalyst also bears an important role along with the other growth parameters like temperature and time of CVD for better graphitization (kushwaha et al, 2008). Pulsed electro deposition of Co in the pores may result in better structures of CVD grown CNTs (Sklar et al, 2005). Therefore, it may be easily concluded that the growth of CNTs is a very complex process which involves the interplay of all the process parameters.

2.2.10 Concluding remarks

All these reviews give brief insight in the selection of a catalyst, which may provide required results, however still, catalyst-growth dynamics-feedstock picture is not yet complete. Therefore, it may be concluded that the outcome of the CNT synthesis is a complex interplay among the metal precursors, the support, and the reaction conditions. However, some results have been found more frequently in the above literature survey, which has provided the much needed guidance for the selection of catalyst and carbon precursor for application in the present case/study. Following are the logics/reasons on

the basis of which various decisions have been made. It is evident that acetylene is the carbon source which can be used at the lowest range of temperatures and CH_4 at the highest range of temperatures in CVD synthesis. In the present case acetylene has been selected because the AAO has been formed on aluminium substrate and is integral with the unoxidized aluminium metal / alloy which has a very low melting temperature(660°C), secondly Co has been selected as the main catalyst for most of the experiments carried out for analyzing effects of other CVD process variables. This decision is based on the knowledge acquired as a result of the abovementioned literature survey, wherein Co has been most frequently used for getting better crystallinity; however other catalysts were also tried occasionally for confirmation as detailed in Chapter 3. NH_3 has been selected as etchent as it decomposes into required quantities of nitrogen (Inert gas) and hydrogen (Etchent) and there is no need to control flow separately for these two constituent gases. The inert gas is required to flush away any air/oxygen present in the reaction chamber.

The formation of CNFs/CNTs is a very complicated process. Any parameters, such as catalyst precursor, catalyst composition, catalyst metal loading, catalyst support, metal particle size, reaction temperature, gas precursors, gas space velocity, hydrogen concentration, or even reaction time can have a significant impact on the structure, yield, and quality of the CNFs/CNTs. .

2.2.11 Characterization of CNTs

A review which gives different techniques available today for the characterization of the atomic structure of carbon nanotubes by Lambin Ph., (2002) is proposed. It c overs electron microscopies, various diffraction techniques, scanning probe microscopies and optical spectroscopies, including Raman scattering. The advantages and limitations of the characterization techniques are discussed in review of literature.

The characterization of CNTs involves the determination of both the diameter and the chirality of CNTs, to which the two wrapping indices identifying the SWCNTs are related. Structural characterization of the nanotubes is also essential to understand the growth mechanism, study the influence of synthesis conditions on CNTs. Several techniques are used routinely to the effects of tube doping, defects etc. High resolution transmission electron microscopy combined with electron diffraction is useful to

understand nature of the self organization of tubes, diameters and atomic configuration of tubes. X-ray and neutron diffraction of CNTs are used to understand the crystallanity and ordering of tubes. The scanning tunneling microscope (STM) investigations of CNTs is an ideal tool for local characterization of electronic and atomic structures of the nanotubes. Raman spectroscopy is also very powerful tool for the characterization of CNTs. Raman spectroscopy provides global information because the laser beam, of micrometer size,. In particular, the low wave number region of spectrum is superposition of breathing modes of many constituent nanotubes whose relative intensities are strongly affected by resonant character of scattering.

2.3   TRIBOLOGY.

2.3.1   Introduction

A lot of information is available in open literature related to general aspects of tribology, but for the specific area of present thesis work, i.e., development of anodized Al-oxide with Carbon nanotubes/Carbon nanofibers in nanopores and its tribological behaviour, very few research reports are available as this is a relatively new area engineering applications. According to Miyoshi et al (2005), the CNTs are still in the early stages of development in the field of tribology, and it will take some more time before practical tribological usage is realized. Only few tribological studies have been conducted for CNTs/CNFs grown in the pores of PAAO at lower loads in the range from few hundreds of mN to few N by Tu and coworkers (Tu et al, 2004, 2005 etc.) and Xia et al (2008). The idea was for possible low load applications, such as in MEMS (Micro electro mechanical systems) and NEMS (Nano- electro mechanical systems). For general technological and engineering applications, where higher loads are encountered, there is a need for exploring the performance of this high potential novel nanocomposite material at appropriate conditions. This nano-composite material having CNTs/CNFs as solid lubricant in the pores promises much extended tribological applications in future for all those cases where normal liquid lubricants on conventional surfaces can not be used. CNTs can also act as liquid lubricant reservoir (Xia et al, 2008) which may provide added wear life to the composite.

An understanding of various friction and wear mechanisms is necessary for one to make the right selection of materials, coatings, surface treatments and operating

conditions for a given application, e.g., developing some novel material combination such as in the present thesis, to get the desired properties as envisaged in this work. Though various wear maps are available (Lim, S.C., 1998), still no single map is enough for predicting performance of all combinations of materials at various operating conditions. Hence a review has been presented in the forthcoming paragraphs covering both the relevant literature for this specific case in detail and the general cases in brief covering all the aspects of tribology.

Tribology is the science and technology of interacting surfaces in relative motion. The word tribology comes from the Greek origin *tribos* meaning rubbing and friction (Jost et al, 1990 and Kawakamea et al, 2006). The terms related to this word are lubricants, lubrification, friction, wear and bearings. Friction and wear processes are inevitable when two surfaces undergo sliding or rolling under load. The tribological behaviour of a couple of materials is, to be described at least by a friction and a wear quantity (Klaffke et al, 2006). Friction is a serious cause of energy dissipation, and wear is the cause of material loss. Considerable savings can be made by reducing the friction and controlling the wear.

2.3.2 Material behaviour under Friction

According to Suh (1973), friction is the resisting force tangential to the common boundary between two bodies when, under the action of an external force, one body moves or tends to move relative to the surface of the other. Friction experienced during a sliding condition is known as *sliding friction*, and that experienced during a rolling condition is known as *rolling friction*. Considerable amount of work has been devoted since the early investigations of Leonardo da Vinci (15th century), Amontons (17th century), Coulomb (18th century), Suh, Archard, Rohatgi, Ray and others (20th century) for understanding friction behaviour of many engineering materials as it is very important in tribology not only because the frictional force between sliding surfaces is of interest, but also because it generally affects the wear behaviour (Rabinowicz, 1977). The three main factors which are responsible for the origin of friction during sliding wear are i) adhesion of flat regions of the sliding surfaces, ii) ploughing by hard particles of wear debris and hard asperities, and iii) deformation of the surface asperities. The relative contributions of these components depend on the conditions of sliding, the materials involved and the environment. In general, it is

observed that the contribution to overall friction coefficient by ploughing and deformation of asperities are greater than that of adhesion (Deuis et al, 1997). The asperity deformation determines the static coefficient of friction and also affects the dynamic coefficient of friction, as the asperities are continuously generated due to delamination of the sliding surface (Suh, 1973). The contribution of the asperity deformation to friction is expected to be the largest when two identical metals slide against each other since the surface always remains rough. In a dynamic situation where the surfaces become smooth, most of the normal load is carried by the entrapped wear particles and the flat contacts. The ploughing component of the frictional force can be due to the penetration of hard asperities or due to the penetration of wear particles. When two surfaces are of equal hardness, the particle can penetrate both surfaces. As the surfaces move with respect to each other, grooves will be formed in one or both of the surfaces. When one of the surfaces is very hard and smooth, the wear particle will simply slide along the hard surface and no ploughing can occur. However, when the hard surface is very rough wear particles can anchor in the hard surface and plough the soft surface. The friction due to ploughing was investigated by Sin and coworkers (1979); they showed that the contribution of ploughing to the friction coefficient is very sensitive to the ratio of the radius of curvature of the particle to the depth of penetration.

Friction is a vital factor leading to energy dissipation in the operation of most mechanisms and is the origin of the resistance of a contacting solid body to sliding. Friction develops in part because rough surfaces tend to lock one another as one surface slides over the other. Surfaces which look like smooth generally have many microscopic ridges and grooves. The ridges of each surface can get stuck in the grooves of the counter surface, creating a type of mechanical bond between the operating surfaces. At the junction of the surfaces atoms of the two surfaces tend to attract one another to form chemical bonds. These bonds can hinder the sliding motion of one surface relative to the other. If an object is in motion, new bonds form and old bonds are broken. Forming and breaking the bonds dissipates energy and takes it away from the motion of the object, which slows down. The force of friction, (F) between an object and a surface can be calculated by the following formula:

$$F = \mu \times N \qquad (2.8)$$

where, F is the force of friction, μ is the coefficient of friction between the object and the surface, and N is the normal load. Frictional force depends on the normal load because increasing the load increases the real area of contact that the object has with

the surface at the microscopic level. When two nominally flat surfaces, no matter how smoothly and finely they are made, are brought into physical contact, they will in fact touch only at a relatively few isolated points and the total area under actual contact is called real areas of contact, A_r as shown in Fig. 2.32.
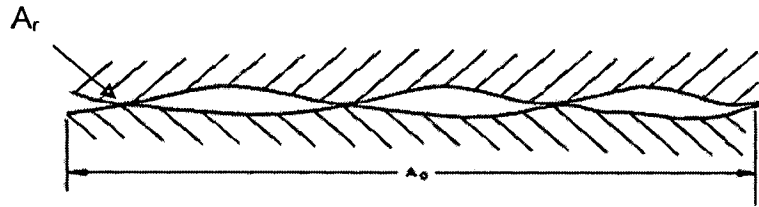
Fig. 2.32: Figure showing real and apparent area of contact

2.3.3 Factors affecting friction

The friction of two rubbing bodies is not independent of velocity as first suggested by Coulomb (Person, 1995).It has been shown by many researchers that friction is a function of velocity and not dependent on load alone (Person, 1995). In general, at low velocities, friction increases with velocity and it decreases with velocity at high velocities. Friction has also been shown to depend on surface roughness. Whitehead and Archard both indicated that the effect of surface roughness is largest at light loads. For hard materials, e.g. steels, friction increases with roughness and for soft materials such as rubber, fibres and nylon friction decreases with roughness. Many research workers have indicated that, friction depends on material properties such as hardness, surface energy, strain, density, shear strength, modulus of elasticity, recrystallization temperature, yield and tensile strength. Bowden and Tabor have indicated that friction is inversely proportional to hardness, and from deformation energy considerations Tsuya has showed that the friction force is proportional to density. Friction has also been reported to depend significantly on temperature and environment. In vacuum, friction can be increased by up to 12 times, probably because of an increase in the area of contact and thereby increasing the adhesion component of friction (Peter, 1983).

The effect of sliding distance on friction depends on the nature of initial deformation of the rubbing surfaces which is governed by surface finish, load, velocity, material properties and environment. During sliding, friction may undergo up to three distinct stages: (1) an intial stage which depends on surface finish, nature and breakdown

72

of oxide films; (2) a second stage consisting of plastic deformation and work hardening the near-surface layers; (3) a third stage which may involve constant microstructure or equilibrium of sliding processes, resulting from temperature stability and equilibrium of oxide formation and breakdown. Rigney and Hirth believe the steady state stage of friction is due to the attainment of a steady state microstructure. Blau suggested that this is probably achieved by crystallographic reorientation of near-surface microstructure, giving rise to preferred crystal texture (Peter, 1983). Generally the plastic deformation takes place either by slip or twinning. In case of aluminium based tribomaterials, the underlying aluminium substrate may get deformed by any of the modes like, e.g. twinning, which is one of the major deformation modes in metals and alloys. Face-centered cubic (fcc) metals and alloys may deform by twinning under one, or a combination of several, material and deformation conditions (Zhu et al, 2009).

2.3.4 Wear of materials

Wear is defined by the American Society for Testing of Materials (ASTM, 1993) as 'damage to a solid surface, generally involving the progressive loss of material, due to relative motion between that surface and a contacting substance or substances.' Wear is a complex system function which depends on contact geometry, surface roughness, microstructural features, grain sizes, fracture toughness, speed, load, temperature, duration, environment, and lubrication (Hsu et al, 2004). Based on the nature of movement or the media involved in an interaction under load, different types of wear have been classified as follows (Sarkar, 1980): (1) abrasive wear, (2) adhesive wear, (3) corrosive wear, (4) erosive wear and (5) fatigue wear.

2.3.4. (a) Abrasive Wear

In the engineering industry abrasive wear is probably the most common cause of mechanical damage. It manifests itself in several forms: in the wear of equipment which engages an abrasive medium, in the wear of seals or machine parts between which abrasive particles can penetrate and wear by abrasives entrained in fluids. The first case in which abrasive particles simply rub against a surface is referred to as two-body abrasive wear. The second and last cases in which the abrasive can become trapped between two sliding surfaces are referred to as three-body abrasive wear. Abrasive wear coefficients are large compared to adhesive ones. Thus, the introduction of abrasive particles into a sliding system can greatly increase the wear rate. The harder

particles causing abrasive wear may belong to one of the two rubbing surfaces or it may be formed between them as a result of chemical process such as oxidation or may be introduced between the two rubbing surfaces as a third body, as in three-body abrasion which is the most common form of abrasive wear. A recent tribological study shows that the largest amount of wear in industrial machinery occurs due to abrasive wear. According to Moore (1974) there are two major mechanisms by which materials are removed during abrasive wear. One is primarily due to plastic deformation and the other is due to fracture with limited plastic deformation.

2.3.4 (b) Adhesive Wear

This is the most fundamental and basic phenomenon of wear that occurs whenever two contacting solid surfaces are in dry rubbing. Adhesive wear is generally defined as the transfer of material from one surface to the other during relative motion as a result of localized bonding between the contacting surfaces. Particles that are removed from one surface are either permanently or temporarily attached to the other surface (Deuis 1997).No matter how smoothly these surfaces are finished, during contact, these surfaces only touch each other at a relatively few isolated points of asperities or protuberances. It is these small areas that carry the entire load between the two surfaces (Ko, 1987). According to Rabinowicz (1965), adhesive wear takes place when surfaces slide against each other and the pressure between the contacting asperities is sufficiently high to cause local plastic deformation. The local pressures are normally very high and exceed the yield stress of the softer of the two materials in contact. According to the adhesive wear theory formulated by Archard, the real area of contact at the asperities is governed by the hardness of the softer material and the wear volume is a function of sliding speed, normal load and material hardness. Hence asperity hardness is more important than bulk hardness. Assuming the wear particles as hemispherical , having the same radius as the contact area, Archard expressed the wear rate, W (volume of material worn) as,

$$\left(W = \frac{KDL}{3H} \right) \qquad (2.9)$$

where K is wear coefficient, D , sliding distance, L , applied normal load and H , bulk hardness of the material. The theory proposed by Archard is based on a mechanism of adhesion at the asperities and has ignored the effect of the

74

microstructure on wear and is limited to idealized sliding conditions. Under these assumptions the wear rate is independent of the apparent area of contact. High local pressures combined with the relative sliding motion, result in minute welds or junctions formed at these local contact areas. However, wear is not an inevitable consequence when junctions are formed. If a junction is weak and shears on its original interface, there will be no material transfer and negligible wear will occur. For dissimilar metals, the junction is generally stronger than the weaker of the two materials in contact and so when the junction is sheared, it fractures through the weak metal and detaches a piece from it. For similar metals, the junction is again stronger than the parent metals because of work hardening, and when shear occurs, the fracture is through either of the sliding. The severity of this damage by sliding wear partly depends on the crystal structure of the material. In general, the greater the number of slip systems the easier it is to initiate plastic deformation because of greater probability of some slip systems favourably oriented for slip and work hardening, thereby, resulting in very little metal transfer. With hexagonal close packed structures in sliding contact, shearing of metal at the interface is more difficult because the structure has only one well developed slip plane (the basal plane). If shear does occur, the wear damage would be severe as a consequence of well-developed separation of slip plane on which shear takes place. It is, therefore, bad practice to slide similar metals over one another. Furthermore, it is good practice to use a softer material for more easily replaceable component. The severity of adhesive wear can be greatly reduced by the presence of surface films such as oxides or by using lubricants in between the sliding surfaces.

2.3.4 (c) Delamination theory of wear

The mechanism of delamination theory of wear has been proposed by Jahanmir et al (1975). During wear, dislocations are generated in the material due to the plastic deformation of the surface by the slider. If an oxide layer is present, it is broken by the passage of the slider thus exposing a fresh clean surface. This then allows those dislocations nearly parallel to the surface to be eliminated due to the action of the image force. Consequently, the material at and very near the surface does not have a high dislocation density. With continued sliding there will be pile-ups of dislocations at

a finite distance from the surface. In due course of time, this will lead to the formation of voids, which gets enhanced if the material contains a hard second phase against which dislocations pile up. Voids can also form by gross plastic flow of the matrix around large hard particles. With time, the voids will coalesce, either by their growth or by shearing of the metal separating the voids. The end result is a crack parallel to the wear surface. When this crack reaches a critical length (dependent upon the material), the material between the crack and the surface will shear, producing a sheet-like particle. It should be emphasized that the delamination theory of wear in its present state is applicable only for the case of low speed sliding where the temperature rise at the contacting surface is so low that diffusion and phase transformation are not involved in the wear process. The delamination theory of wear postulates the existence of a soft, low dislocation-density zone at the sub surface just below the wear track. This layer would be softer than the layer below in the subsurface and could deform continuously without much work hardening. Therefore, if a composite metal surface is created by depositing a thin layer of a relatively softer metal on a harder substrate, heavy plastic deformation and delamination of the substrate may be prevented. This is based on the fact that dislocations are not stable in very thin layers of metals having a low flow stress. In a conventional homogeneous material, the dislocations pile up and tangle beneath the soft layer. When the dislocations are generated in a composite material with an extremely soft outer layer and a much stronger substrate, dislocations pile up at the interface between the deposited metal and the substrate. As the slider moves on, these dislocations escape through the surface of the wear track if the deposited soft metal is very thin. The forces acting on dislocations in metals with low shear modulus are such that these dislocations are repelled from the interface (Hirth and Lothe, 1968). In the case of very high stresses there will be some transfer to and generation of dislocations in the substrate material. However, the dislocation transfer will be considerably less than that, which would be observed on an uncoated material because of the lower tangential force transmitted. Thus the composite surface will markedly delay delamination of the substrate material, (Jahanmir et al, 1974).

(a) Dry Sliding Wear

Dry sliding wear is defined by a wear process in which there is no intentional lubricant or moisture introduced into the contact area.

76

(b) Lubricated Wear.

The wear in the presence of a lubricant is called lubricated wear. The use of lubricants is done to reduce friction and wear. Whenever two bodies in contact are made to slide relative to one another, a resistance to the motion is experienced. This resistance, called friction, is present in all machinery. Approximately 30% of the power of an automobile engine is consumed by friction. Friction and wear can be significantly reduced, and thus relative motion of machine parts made possible, by interposing a lubricant at the interface of the contacting surfaces; the machine elements designed to accomplish this are called bearings. Bearings can be lubricated by solids such as graphite or, more commonly, by liquids and gases. *See also* Antifric tion bearing; Friction; Graphite; Lubricant; Surface and interfacial chemistry; Wear.

Conventionally, lubrication has been divided into (1) fluid-film lubrication (hydrostatic, hydrodynamic, and elastohydrodynamic), where the sliding surfaces are separated by a relatively thick, continuous film of lubricant; and (2) boundary lubrication, where contact surface separation is but a few molecular layers and asperity contact is unavoidable. In the presence of lubricating oil wear is reduced considerably. Use of coatings affects the friction and wear behavior of an oil-lubricated contact in a complex way. Published results on the benefit of coatings in a lubricated contact have been controversial (Ajayi et al, 1992; Bull and chalker, 1992)

2.3.5 Tribological studies of CNTs/CNFs embedded in nanopores of PAAO.

The relatively high specific strength of aluminium and its alloys and their composites have brought extensive applications of these materials in the automotive and aerospace industries to meet the growing demands for increased fuel efficiency, reduced maintenance and environmental protection. Compared with its generally excellent corrosion resistance in many media, the tribological properties of aluminium are often poor, which limits its use for certain engineering purposes. Adhesive and abrasive wear are identified as the predominant operative mechanisms causing severe wear of aluminium (Hutchings, 1992). Adhesive wear is mainly due to the inherent chemical reactivity of aluminium with many common engineering materials, such as steel, which enhances asperity bonding and welding at microscopic contacts, while abrasive wear is mainly related to the general softness of the metal which facilitates cutting by harder mating/ counterface asperities, by both plastic deformation and micro-

fracture processes. Hence, a variety of metallic and ceramic coatings applied by surface modification techniques, such as physical vapour deposition (PVD), plasma spraying, and laser surface alloying, etc., have been evaluated for reduction of both abrasive wear, via increase of the surface hardness, and adhesive wear, via change of surface chemistry. Adhesive wear can be further reduced or avoided by appropriate use of lubricants to reduce friction. Anodization may be a good alternative to these processes, as it is a comparatively simpler technique to improve wear resistance of aluminium alloys and it may meet both the above mentioned requirements. It is also economical as compared to other vacuum based techniques such as ion implantation, sputtering deposition etc.

Hence there are various attempts to increase wear resistance of these materials by various techniques analogous to case hardening of steel so as to retain toughness and ductility in the core region and simultaneously obtain harder and wear resistant contacting outer surface. Anodization is a cheaper and suitable route for this application and its porous structure provides opportunity to infiltrate some lubricating phase also and hence CNTs/CNFs, which are graphitic in nature, just like other solid lubricants, are grown within the pores and tribological tests have been carried out.

Porous anodized alumina has been considered as a good lubricant reservoir and due to its high hardness and wear resistance; it may be used as a solution to the abovementioned problems. Holes can also serve as a micro-trap for wear debris in lubricated or dry sliding (Koszela et al., 2007),

In the past there have been many attempts made to lubricate anodized aluminium alloy surfaces but met with little success, e.g. Wang et al., have applied solid film lubricant to improve poor tribological properties of the aluminium alloys. They have formed self-lubricating, porous anodic films on aluminium by a re-anodizing treatment in ammonium tetrathiomolybdate electrolyte, which was examined by transmission electron microscopy and X-ray photoelectron spectroscopy. Precipitation of mainly amorphous MO &, or a mixture of MoS, and S, was revealed, which lead to a significantly reduced coefficient of friction

Wear of ceramic surfaces with an emphasis to alumina (amorphous / porous) surfaces. As the crystalline alumina is very hard therefore it is not suitable for the application under consideration and therefore amorphous alumina is relevant to discuss. So from literature amorphous alumina part needs to be discussed. In view of the thesis objective, PAAO structure is the prime consideration, therefore the wear behaviour of

the porous alumina structure is to be examined from the literature. CNT embedded PAAO surfaces were investigated by the researchers, but for various purposes and investigations were so far limited to low load only. Because the majority of applications are for sophisticated devices. In the present work the load requirement is relatively high and such investigations have not been reported to any systematic way by the researchers

The CNTs are still in the early stages of development in the field of tribology, and it will be some time before practical tribological usage is realized (Miyoshi et al, 2005). Tribology applications may emerge that can take full advantage of intrinsic structures and properties of carbon-based nanomaterials and films in such areas as solid films for dry lubrication, additives for liquid lubricants and greases, and composites for wear parts. These films and materials may offer attractive new solutions to important lubrication problems as well as exciting challenges to the tribologist or product designer who seeks to exploit the performance and cost-effective potential of these materials.

The relatively high strength to weight ratio of aluminium and its alloys has brought extensive applications of aluminium-based materials in the automotive and aerospace industries to meet the growing demands for increased fuel efficiency, reduced maintenance and environmental protection. Compared with its generally excellent corrosion resistance in many media, the tribological properties of aluminium are often poor, which limits its use for certain engineering purposes.

2.3.6 Wear mechanisms

Various wear mechanisms have been considered: adhesive, abrasive, diffusive, corrosive, fatigue and fretting wear. The existence of abrasive, diffusive and corrosive wear mechanisms has been established reasonably firmly. However, the mechanisms of adhesive, fatigue and fretting wear are not clearly understood (Suh 1973). Increase in the wear and corrosion resistance of nanostructured ceramic coatings as a result of stress-induced phase transformation has also been reported (shukla et al, 2002).In recent years, several new solid lubricant and modern lubrication concepts have been developed to achieve better lubricity and longer wear life in demanding tribological applications (Donnet and Erdemir, 2004).

2.3.7 Tribological testing procedure:

The various types of aluminium based and other composites have been studied using pin on disc configuration by Murali et al (1982) and pan et al (1998). However few other configurations have also been used occasionally (Surappa et al, 1982).

The correlation coefficient (R), sometimes also called the cross-correlation coefficient, is a quantity that gives the quality of a least squares fitting to the original data.

Wear coefficients:

A dimensionless wear coefficient K has been defined (Archard, 1953) as wear volume per unit real area of contact for unit sliding distance, $K = W/A_r D = WH/LD$, where W is the wear volume loss, A_r is the real area of contact, D is the sliding distance, L is applied load.

According to Yang et al (2005), Wear coefficient values obtained from different investigators have been found to vary significantly up to a deviation of 1000%. Jost et al, (1990) have tabulated wear coefficients for different lubrication systems and the same is reproduced here in table 2.2.

Table 2.2:   Wear coefficients for different lubrication systems

Lubrication system	Wear coefficients
Hydrodynamic	10^{-13}
Squeeze film	10^{-13}
Elastohydrodynamic	$10^{-9} - 10^{-13}$
Boundary	$10^{-6} - 10^{-8}$
Composite bearing materials	$10^{-2} - 10^{-7}$
Boundary solid films	$10^{-5} - 10^{-7}$
Unlubricated	$10^{-2} - 10^{-4}$

Wear and friction of PAAO:

In the past there have been many attempts to lubricate anodic aluminium alloy surfaces but met with little success. Wang et al (1996) have applied solid film lubricant to improve poor tribological properties of the aluminium alloys. They have formed self-lubricating, porous anodic films on aluminium by a re-anodizing treatment in ammonium tetrathiomolybdate electrolyte, which was examined by transmission

electron microscopy and X-ray photoelectron spectroscopy. Precipitation of mainly amorphous MO and/or a mixture of MoS and S were revealed, which led to a significantly reduced coefficient of friction. The same research group also extended their work by using duplex anodizing process to form MoS_2 precursor films on aluminium (Skeldon et al, 1997). That encompassed an initial formation of a porous alumina film on aluminium, by anodizing in sulphuric acid, and a subsequent development of the MoS_2 precursors within the pores, by another anodizing treatment in ammonium tetra thiomolybdate electrolyte. The films were then fully examined by optical and electron microscopy, and energy dispersive X-ray analysis. The lubricant was also studied using X-ray diffraction, X-ray photoelectron spectroscopy and selected area electron diffraction. Furthermore, they have also explained the incorporation process of the solid lubricant within the pores. Also they have advanced a model on the basis of the features of the V-t curves of re-anodizing and the determined morphology, microstructure and composition of the film and lubricant. They have also reported the wear properties and micro hardness of the films

Zhao et al (2003) applied carbon nanofibers into the pores of the porous anodized aluminium (PAAO) to improve the wear properties of the alumina film. This involves an initial formation of an ordered PAAO film by re-anodizing in oxalic acid bath and a subsequent development of the carbon precursors within the pores via in-situ polymerization of acrylonitrile within the pores. After polymerization, a series of heat-treating conditions convert the polyacrylonitrile (PAN) polymer structure into a quasi-graphic structure. The sliding wear and friction properties of self-lubrication films were measured by means of a ball-on-plate apparatus using a steel ball as a counterface. The results showed that self-lubricating treatment could improve the wear properties of porous anodic film more efficiently.

Tu et al (2003) synthesized amorphous carbon nanofiber arrays in PAAO templates by pyrolysis of acetylene with cobalt nanoparticles as catalyst at $640°$ C. The carbon nanofibers have amorphous structures observed under high-resolution transmission electron microscopy and Raman spectroscopy examination. The aligned amorphous carbon nanofibers grown within the pores of the aluminum oxide membranes were uniform with lengths of about 2 μm and outer diameters of about 85 nm. The frictional properties of the array film of amorphous carbon nanofibers were investigated using an atomic force and friction force microscopy (AFM–FFM) and a

ball-on-disk machine in air. The adhesion between the amorphous carbon nanofiber arrays and the anodic aluminum oxide membrane remained intact at relatively low loads. The AFM–FFM measurements indicated that the friction forces on the array film of amorphous carbon nanofibers were uniform. The array film had low friction coefficient and high wear resistance under the micro friction tests. The friction coefficient of the array film dry sliding against a corundum counterface was observed to be constant after an initial transient period and decreased with increasing the sliding velocity.

Tu et al (2004) obtained aligned multiwalled carbon nanotubes (MWCNTs) on an PAAO template by chemical catalytic vapor deposition at 650° C. The aligned CNTs grown out of pores of AAO membranes were uniform in diameter and about 3 µm in length. Micro-friction properties of the aligned CNT film were investigated by them using a friction force microscopy (FFM) and ball-on-disk tribotester under dry conditions. The FFM measurements indicated that the aligned CNT film had low friction coefficient due to the self-lubricating effect. Under a relatively low applied load, the friction coefficient of the CNT film dry sliding against a corundum ball decreased with increasing the sliding velocity, and the adhesion between the aligned CNT film and AAO template remained intact.

Tu et al (2005) synthesized the aligned film of amorphous carbon nanorods by chemical vapor deposition at 650° C with the Co catalyst on a PAAO membrane. The morphology and microstructure of the aligned film of amorphous carbon nanorods were examined by field emission SEM, TEM and Raman spectroscopy. The tests sliding against quenched-and-tempered GCr15 steel were conducted using a ball-on-disk tribometer at an applied load of 980mN and a sliding velocity of $0.2ms^{-1}$ in vacuum, humid air (RH 60%) and oxygen-rich environments. The tribological properties of the aligned film of amorphous carbon nanorods on the AAO membrane were influenced by the test environment. As compared to the tests in humid air and oxygen-rich environments, the aligned film of amorphous carbon nanorods showed slightly higher friction coefficient in vacuum, but exhibited higher wear resistance at the same time due to the absence of tribochemical reaction. The mass loss of the aligned film accelerated by the effects of oxygen and atmospheric humidity in humid air due to tribochemical reaction.

Wang and wang (2004) fabricated successfully thick and macroporous alumina layers with a phosphate-base solution. They investigated the anodizing process in this compound solution and the effects on the thickness of the oxide films in detail. The results indicated that the growth of porous layers in this solution undergo three stages during anodizing, same with in the general solution. The electrolyte (phosphate base solution) is sensitive to anodizing temperature which affects current density significantly. The additive (including organic carboxylic acid and Ce salt) in the phosphate-based electrolyte plays an important role on the increase of film thickness. In this compound electrolyte, the pore diameter of the anodic alumina membranes is about 100 nm in average, pore density is 18 pores mm^{-2} and porosity 14%. The thickness can exceed 20 μm with appropriate anodizing time and temperature.

Tu et al (2001) investigated tribological properties of carbon-nanotube-reinforced copper composites using a pin-on-disk test rig under dry conditions. The composites containing 4–16 vol % carbon nanotubes (CNTs) were fabricated by a powder-metallurgy technique. The tests were carried out at normal loads between 10 and 50 N, and the effect of volume fraction of CNTs on tribological behavior of the composites was examined. The composites revealed a low coefficient of friction compared with the copper matrix alloy. Due to the effects of the reinforcement and reduced friction, the wear rate of the composites decreased with increasing volume fraction of CNTs at low and intermediate loads. The composites with a high volume fraction of CNTs exhibited high porosity and their wear resistance decreased under high-load conditions.

Vander Wal et al (2005) observed that surface modification of the tubular or sphere-shaped carbon nanoparticles through chemical treatment, e.g., fluorination, is expected to significantly affect their friction properties. In this study, they carried out a direct fluorination of the graphene-built tubular (single-walled carbon nanotubes) structures to obtain a series of fluorinated nanotubes (fluoronanotubes) with variable C_nF (n = 2–20) stoichiometries. The friction coefficients for fluoronanotubes, as well as pristine and chemically cut nanotubes, were found to reach values as low as 0.002–0.07, according to evaluation tests run in contact with sapphire in air of about 40% relative humidity on a ball-on-disk tribometer which provided an unidirectional sliding friction motion. These preliminary results demonstrated ultra-low friction properties

and showed a promise in applications of surface modified nanocarbons as a solid lubricant.

The tribological behavior of well-aligned carbon nanotube (CNT)/alumina nanocomposites was studied by Xia et al (2008) at multiple length scales. Pin-on-disk, microscratch and atomic force microscopy were used to test three nanomaterials: alumina m atrix, thin-walled and thick-walled CNT/alumina composites. This work demonstrates that the frictional coefficient of the composites tested at all the length scales depends on the buckling behavior of the nanotubes and applied loading. Analysis is presented to assess the role of CNT buckling in determining the friction.

This chapter describes development, partial modification, details of all the experimental set-ups and the experimental procedures used in the present investigation for developing CNTs/CNFs embedded self-lubricated porous anodic aluminium oxide (PAAO) nano composite surfaces. Details pertaining to testing equipments and testing/characterization methods that have been undertaken in this study, right from the PAAO formation to tribological testing in the end are also presented. Bare porous anodic alumina has been characterized for tribological performance for comparison with the CNTs/CNFs embedded PAAO surfaces. In addition these CNTs/CNFs embedded and bare PAAO surfaces both have been soaked in lubricating oil and then their performance has been compared with dry samples in respect of tribological behaviour. Few of the PAAO samples have been sealed and their tribological properties have also been compared with unsealed PAAO samples.

Table 3.1: Chemical compositions of the two types of aluminium samples used. (Based on spectroscopic tests)

Elements	Chemical composition (%)	
	(1) High Purity Aluminium Merck (99.79 %)	(2) Commercial pure Aluminium. Indigeneous (97.3 %)
Aluminium	99.952	97.903
Silicon	0.020	0.621
Iron	0.006	1.185
Manganese	0.002	0.050
Magnesium	-	0.017
Chromium	-	0.038
Nickel	-	0.008
Zinc	0.005	0.312
Titanium	0.005	0.041
Nitrogen	0.005	-
Copper	0.005	-

Two types of aluminium samples have been anodized and later CNTs/CNFs are grown on those samples. The detailed chemical composition of these two types of samples is as given in Table no. 3.1.

The overall experimental work has been divided into following three sections (i) anodization, to form nano-porous aluminium oxide layer (ii) CNTs/CNFs growth within the pores using CVD and (iii) tribological evaluation /studies of the prepared samples.

3.1   ANODIZATION

3.1.1   Pretreatment

The main pretreatment steps that have been conducted are (a) mechanical polishing, (b) annealing, (c) degreasing and (d) electro-polishing. These procedures are described in briefs in the following paragraphs.

(a) Mechanical polishing: In order to get well ordered pore structure, mechanical polishing of the commercially pure aluminium (CPA) samples was done using emery papers having different grades with kerosene as lubricant, so as to flush away the debris (micro particles) generated and thereby preventing possibility of scratches in the polished samples due to debris particles getting entrapped between the emery paper and the shining/polished surface of the sample and then causing abrasion.. However, pure aluminium (PA) samples were not mechanically polished as they had already good surface finish.

(b) Annealing: Both types of aluminium samples (i.e. pure and commercially pure) were annealed at 450-500 °C in the presence of flowing inert gas (nitrogen) for 4-5 hours in a tube furnace.

(c) Degreasing: The samples after annealing were cleaned with acetone and washed with double distilled water; in order to remove dirt that may be present in the samples due to handling. The samples were dried using hot air blower. To remove oxide layer, few commercial aluminium samples were dipped in NaOH solution (30 g/l) for 10 minutes, thereafter rinsed in distilled water, followed by immersing in HNO$_3$ (70%).

(d) Electropolishing: The samples for electropolishing were connected to the positive terminal of the d. c. power source, using crocodile clips by a connected lead. Another aluminium coupon (or any other electrical conducting material) is connected to the negative terminal of the power supply. Both the electrodes were dipped in the agitated

electrolytic polishing bath maintained at 5 °C, using cold water in a tray of ice. The polishing bath contained solution of Ethyl Alcohol (99.9%) and Perchloric acid (70 %) in 5:1 ratio by volume. Electro-polishing was carried out at a current density of 1-2 A /cm² at 20 V until the mirror –like surface finish was obtained. Maximum time required was less than 4 minutes, and after that deterioration of the shine and finish of the anodic sample starts. After electro-polishing the samples were rinsed in double-distilled water, dried in hot dry air and transferred to anodization cell. Fresh solution was prepared each time as used solution doesn't give rise to the surface finish to the level that can be obtained using the fresh solution. Dark and dull coloured oxide, in the form of micro-films, can be easily seen getting liberated from the sample (anode) and rushing away towards cathode and thus resulting in gradual contamination of the solution. The underlying shining, mirror like surface underneath the removed oxide products is obtained. When total surface becomes shining, in about 3 to 4 minutes time, power is switched off. The samples are rinsed in double distilled water and dried in warm air.

3.1.2 Anodization of Aluminium

The electropolished samples were anodized by connecting them to the positive terminal of the d. c. power source as shown in the Fig. 3.1. Both types of aluminium samples were anodized in various electrolytic baths for various time periods at different electrochemical conditions. The details are presented in table 3.1.Anodization were done using power supply, in both modes. of constant voltage' and 'constant current density'. However in most of the cases 'constant voltage' mode was used. Electrolytes of dilute phosphoric acid, oxalic acid, chromic acid and sulphuric acid with different concentrations were used. The chemicals used were of AR grade. The dilute acid solutions were prepared with ultra pure water (millipore). The bath was maintained at various temperatures by varying the quantity of ice in the cold water bath surrounding the glass cell. The cell was kept in a container filled with ice-cooled water. Violent agitation of the electrolyte by a stirrer within the cell ensured an uniform temperature in the electrolytic bath. After having electrical connections made properly, power was switched on to start the anodization process. The process was continued for required time period and the electrical parameters were recorded as a function of time.
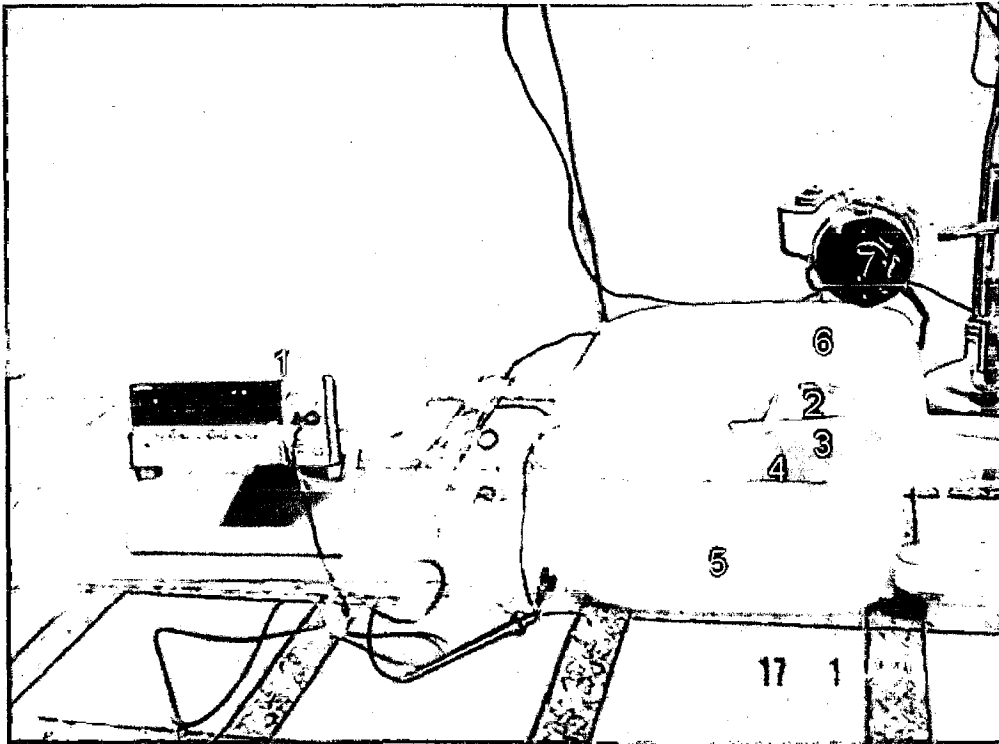
Fig. 3.1:   Experimental set-up used in the anodization process comprises of (1) D. C. Power source meter (Keithley- 2400 series), (2) Anode (the sample),(3) Cathode, (4) Electrolytic   cell, (5) Tray containing cold water/ice, (6) Glass rod of the mechanical stirrer, (7) Electric motor of the mechanical stirrer.

Table 3.2: Anodization process parameters.

Sl. No.	Electrolyte used	Electrical parameters and mode of anodization.		Duration of anodization (hrs.)		Remarks
		Const voltage mode. (V)	*Const current density mode (mA/cm²)*	I STEP	II STEP	
1	Phosphoric acid, (5 wt%)	40	-	1.0	0.5	Both PA and CPA
		50	-	1.0	0.5	PA
		60	-	1.0	0.5	PA
		70	-	1.0 ·	0.5	CPA
		80	-	1.0	0.5	PA
		90	-	1.0	0.5	PA
		100	-	1.0	0.5	CPA
		110	-	1.0	0.5	PA
		120	-	1.0	0.5	PA
		130	-	1.0	0.5	CPA
		140	-	1.0	0.5	PA
		150	-	1.0	0.5	PA
		160	-	1.0	0.5	PA,CPA
		170	-	1.0	0.5	PA
		180	-	1.0	0.5	PA
		190	-	1.0	0.5	PA
		200-	-	1.0	0.5	PA
			5	1.0	0.5	PA
		-	10	1.0	0.5	PA
		-	15	1.0	0.5	PA
		-	20	1.0	0.5	PA
2	Oxalic acid, (3 wt%)	40	-	6-12	0.5, 1.0	Both PA and CPA
3	Chromic acid (3 wt%)	40	-	1	0.5	Both PA and CPA
4	Sulphuric acid. (15 wt%)	15-28	-	1	0.5	Both PA and CPA

Few experiments were also carried out with 'constant current' mode to see the effect of mode selection on the PAAO structure developed. Samples of small sizes (~1cm²) were anodized due to limitation of the capacity of the power supply (source meter) used. However the accuracy and reproducibility in the results that resulted in anodized structure is much higher using the source meter compared to the case with D C

power supply. Anodization was carried out under DC conditions with aluminium samples as the anode and another pure aluminium plate/coupon as the cathode. Current flow in the circuit was automatically recorded by the above mentioned Keithley Source Meter (2400 Series), which is a very precise D.C. power source meter. The nature of the current density variation matches well with the results reported in the literature.

a)   Two-step anodization.

In order to get well-ordered porous anodic alumina, samples were subjected to the standard method of two-step anodization as discussed in chapter-2. The porous alumina film formed after the first anodization step was removed by chemical etching in a mixture of phosphoric (6 wt. %) and chromic acid (1.8 wt. %) at 80 ° C. Subsequently, the Al sheet was anodized for 30 min under identical conditions of the first step anodization process. The anodization time for the second step is controlled so as to obtain pore depth of 5-10 μm, which is suitable for CNTs/CNFs formation inside the pores and stemming out of the pore tips (Pan. et al, 2004).

b)   Barrier layer thinning:

At the end of the second step of anodization, the voltage was reduced from high value that was maintained for whole of the anodization process to a very low value (~10 V) in steps of 5 V, in order to avoid large barrier layer thickness. To observe the effect of time on degree of ordering of the pores, anodization in the first step was conducted for different time periods.
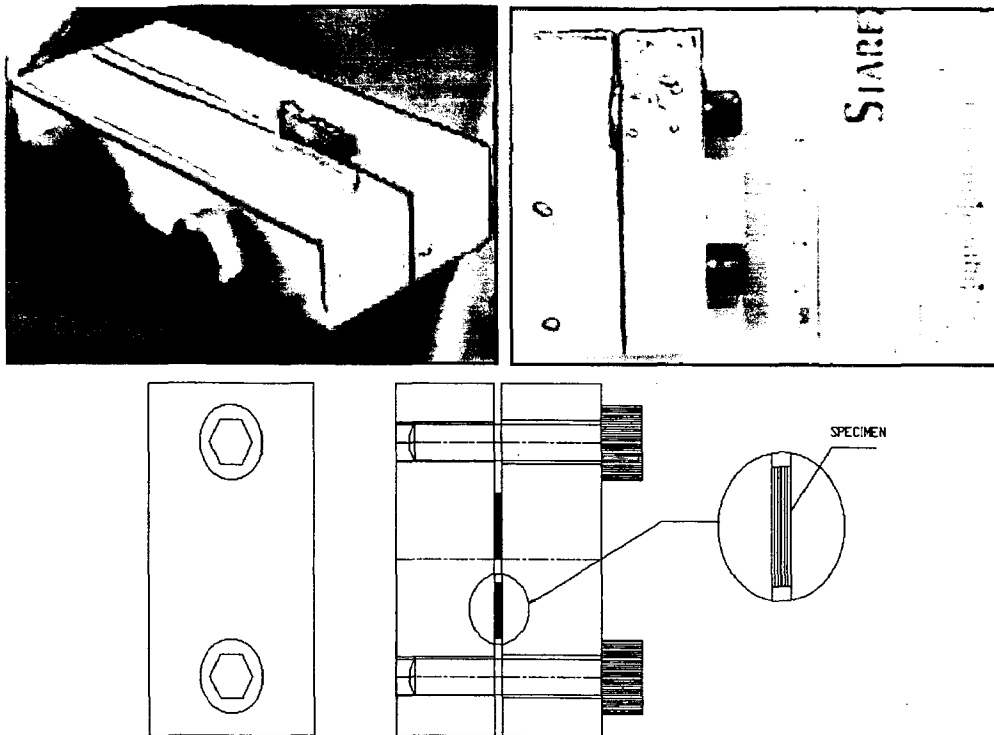
Fig. 3.2: A specially designed aluminium fixture to secure the V-bent (fractured PAAO) specimen between the two halves for observation under SEM and FE-SEM.

3.1.3 Post treatment.

Though following are the optional steps, however are most frequently applied after the anodization step:

(i) Pore widening treatment

(ii) Sealing of pores

After completion of anodization, samples were taken out of the electrolytic bath, rinsed in double distilled/ultra pure water to remove the entrapped electrolyte in the pores and then dried in hot dry air. The samples were then placed in another dilute acid solution (3 wt. % phosphoric acid) electrolytic bath at 60° C, for time period depending on final pore size required. This treatment is called 'pores widening treatment'. Isotropic etching of the formed oxide increases pore diameter and also reduces the thickness of the barrier

91

layer at the pore bottom facilitating electrodeposition of the catalyst at the bottom of the pores for CNTs growth from the bottom. The anodized specimen was bent into a V-shape, producing cracks in the oxide parallel to the specimen sides which had not been bent to measure depth of oxide layer in SEM micrographs. A special fixture was designed and fabricated for this purpose, as shown in Fig. 3.2.

The analysis of anodized microstructures has been done using image analysis software Image.

Catalyst deposition:

Co catalyst has been electrodeposited mostly in the pores of anodic aluminium oxide by using A.C. However few other catalysts, viz., Ni, Li based compound and compounds of Co and Ni were also tried. For Cobalt deposition, the A.C. voltage was 15 V and the electrolyte used was solution of 240 g/l cobaltous sulphate heptahydrate ($CoSO_4 \cdot 7H_2O$), 40 g/l boric acid (HBO_3) and 1 g/l ascorbic acid ($C_6H_8O_6$). The electrolyte temperature was kept at 30 °C. The current was supplied for only 50 seconds and two samples were processed simultaneously in one go as two electrodes. In the alternating polarity, one of them becomes cathodic in the negative half cycle and the other one in the next half cycle, thus deposition takes place during this half cycle and due to rectifying properties of the PAAO, which acts as a diode, in the positive half cycle, current is very less and hence this results in catalyst to be mainly deposited into the bottom of the pores, not on the wall or on the surface and catalyst remains stuck at the bottom of the pores even under alternating /cyclic polarity. Ni was also deposited in this manner; however, for trial of lithium based compound ($LiNi_{0.5}Co_{0.5}O_2$ particles), as a catalyst, for few experiments, separate procedure was used. Catalytic particles were synthesized by sol-gel process using nitrate of nickel, and cobalt (Rankem, 98%) and acetate of lithium (Thomas Baker, 99%). Citric acid was used as a chelating agent. The catalyst was dispersed in iso-propanol solution and the dispersion was spread onto a porous alumina substrate which was kept in an evacuated quartz chamber (pressure/vacuum of the order of 10^{-3} torr), in order to remove the trapped air from within the pores and in this way, some part of the catalyst was expected to enter and settle at the bottom of the pores due to capillary action of the narrow channels of the PAAO. A special quartz attachment was designed and fabricated for this purpose, which was connected to a vacuum pump to meet this objective of catalyst infiltration.

3.1.4 Characterization of the Anodized Samples

3.1.4.1 Optical Microscopy and Scanning Electron Microscopy

Electropolished and anodized sample (prepared in phosphoric acid bath) were subjected to examination under scanning electron microscope (SEM), LEO, Cambridge. The SEM studies were carried out with an electron beam accelerating potential of 15 kV/20 kV. As size of pores is in the order of 100-280 nm in phosphoric acid bath, it can even be seen under optical microscope or SEM, at the magnification of 1000 X .

3.1.4.2 Scanning Electron Microscopy with Energy Dispersive X-Ray Spectroscopy (EDS)

Electropolished and anodized sample (prepared in all acid baths) were subjected to examination under field emission scanning electron microscope (FE-SEM) with EDS attachment, FEI QUANTA 200 FEG, Czech Republic at an accelerating potential of 20 kV. Due to high resolution, small sized pores are clearly seen by this higher resolution and powerful equipment. Both modes, viz., SEE (Secondary electron emission) and BSE (Back-scattered electron emission) imaging modes were used, though SSE has been used frequently. An elemental mapping of the fractured surface of the anodized nano-composites samples was also carried out by EDS. In FESEM, the electrons liberated from a field emission source and are accelerated in a high electrical field gradient. Within the high vacuum column these primary electrons are focused and deflected by electrostatic lenses to produce a narrow scan beam that bombards the object resulting in emission of secondary electrons from the object. These secondary electrons are registered by a detector which produces electronic signals. These signals are amplified and transformed to an image that can be seen on a monitor. There are two classes of electron emission source: thermionic emitter and field emitter. Emitter type is the main difference between the Scanning Electron Microscope (SEM) and the Field Emission Scanning Electron Microscope (FESEM). Thermionic Emitters use electrical current to heat up a filament; the two most common materials used for filaments are Tungsten (W) and Lanthanum Hexaboride (LaB$_6$). When the heat is enough to overcome the work function of the filament material, the electrons can escape from the material itself. Thermionic sources have relatively low (i) brightness, (ii) evaporation of cathode material and (iii) thermal

drift during operation. Field Emission is one way of generating electrons that avoids these problems. A Field Emission Gun (FEG); also called a cold cathode field emitter, does not heat the filament. The emission is reached by placing the filament in a huge electrical potential gradient. The FEG is usually a wire of Tungsten (W) fastened into a sharp point. The significance of the small tip radius (~ 100 nm) is that an electric field can be concentrated to an extreme level, becoming so big that the work function of the material is lowered and electrons can leave the cathode. To see the image of the samples, the samples are first made conductive for current. This is done by coating them with an extremely thin layer (1.5 - 3.0 nm) of gold. Further on, objects must be able to sustain the high vacuum and should not alter the vacuum, for example by losing water molecules or gases. After the object has been covered by a conductive layer it is mounted on a special holder. The object is inserted through an exchange chamber into the high vacuum part of the microscope and anchored on a moveable stage. The "secondary electron emission" detector (scintillator) is located at the rear of the object holder in the chamber. Sketch showing the working of a scanning electron microscope is given in Fig. 3.3

When the primary probe bombards the object, secondary electrons are emitted from the object surface. The secondary electrons, which are attracted by the Corona, strike the scintillator fluorescing mirror that produces photons. The location and intensity of illumination of the mirror vary depending on the properties of the secondary electrons. The signal produced by the scintillator is amplified and transduced to a video signal that is fed to a cathode ray tube in synchrony with the scan movement of the electron beam. The contrast in the 'real time' image that appears on the screen reflects the structure on the surface of the object. Parallel to the analog image, a digital image is generated which can be further processed. In the present study the porous anodized aluminium oxide (PAAO) samples were analyzed under the microscope. For observing pore depths, cross sectional views were taken by bending the anodized specimens at 180° and the fractured samples were clamped in a specially designed and fabricated aluminium fixture as shown in Fig. 3.2.
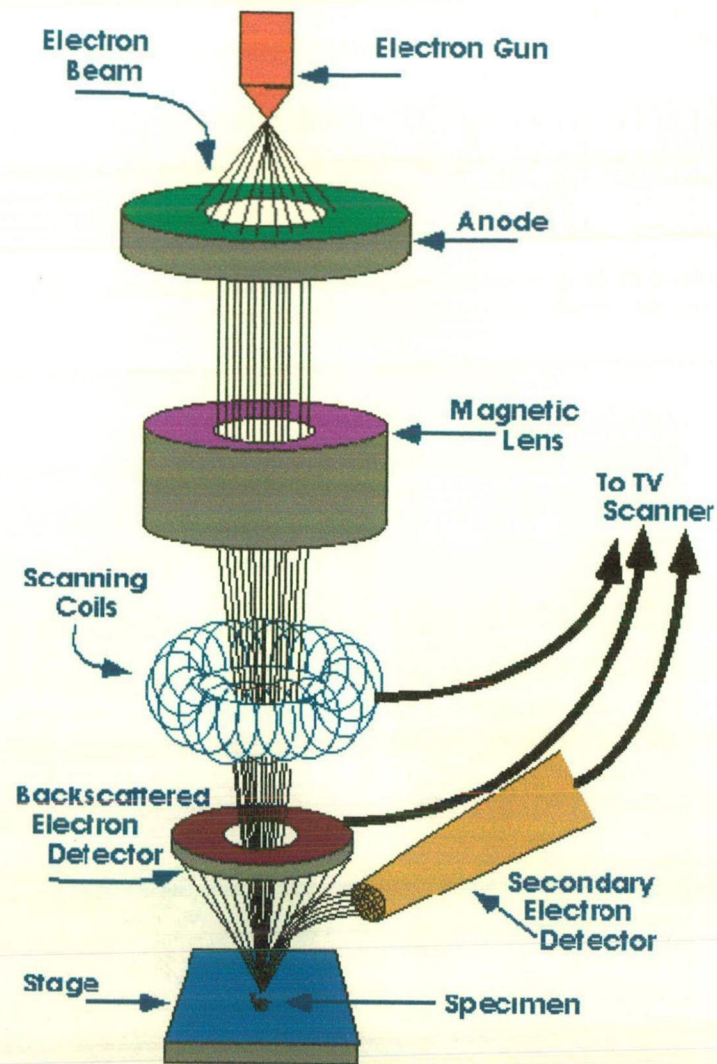
Fig. 3.3: Sketch showing the working of a Scanning Electron Microscope

The sample is initially brought into standard position. The sample is focussed with low magnification and then in high magnification. At low magnification a small object is focused. Then the object is moved to center of the screen and the magnification is increased. Next, the aperture align switch is turned on. If there is any horizontal or vertical swing, the aperture alignment is corrected with the screws provided on the aperture holder until the swing disappears. Now the image can be sharpened by using the X and Y stigmator controls. The focus and stigmator controls are switched until the sharpest image is obtained. Now the image is ready to be captured and could be saved in a computer file. The above mentioned SEM imaging procedure was used to image each

sample. The captured image was used to estimate the formation of films. The porosity of the anodized alumina was also estimated from the SEM images. The SEM images help in comparing the morphology of the films with changes in applied voltage/ current.

Characterization of the structure and morphology of the fabricated membranes was achieved using an FEI Quanta 600 FEG scanning electron microscope (SEM)
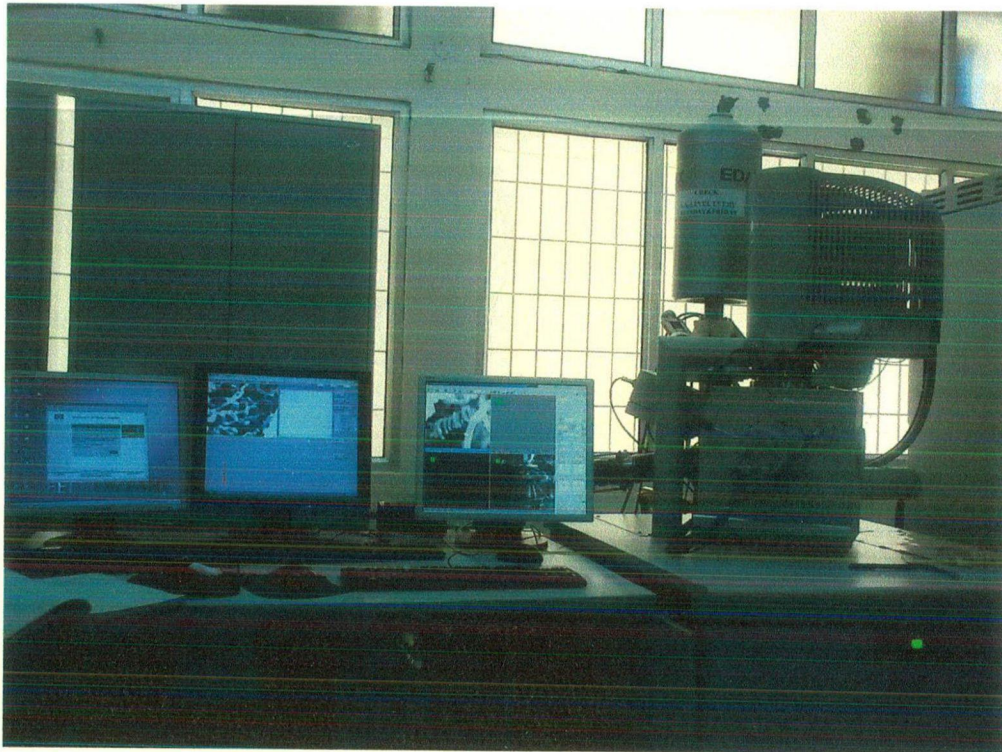
Fig. 3.4: Photographic view of FE-SEM with EDS facility.

The surface roughness is measured either by Surface Roughness Meter or by Optical Profilometer, whose features are given as under. Fig. 3.4 shows the photographic view of FE-SEM with EDS facility.

3.1.4.3   *Optical Profilometer*

Surface Roughness Meter (Mahr Perthometer 4615) was used to measure surface roughness along a line scan and Optical Profilometer (Wyko NT 1100 interfaced with Vision® 32 software) as shown in Fig. 3.5 above was used in VSI mode to measure surface roughness profile of the PAAO at different stages of its preparation.
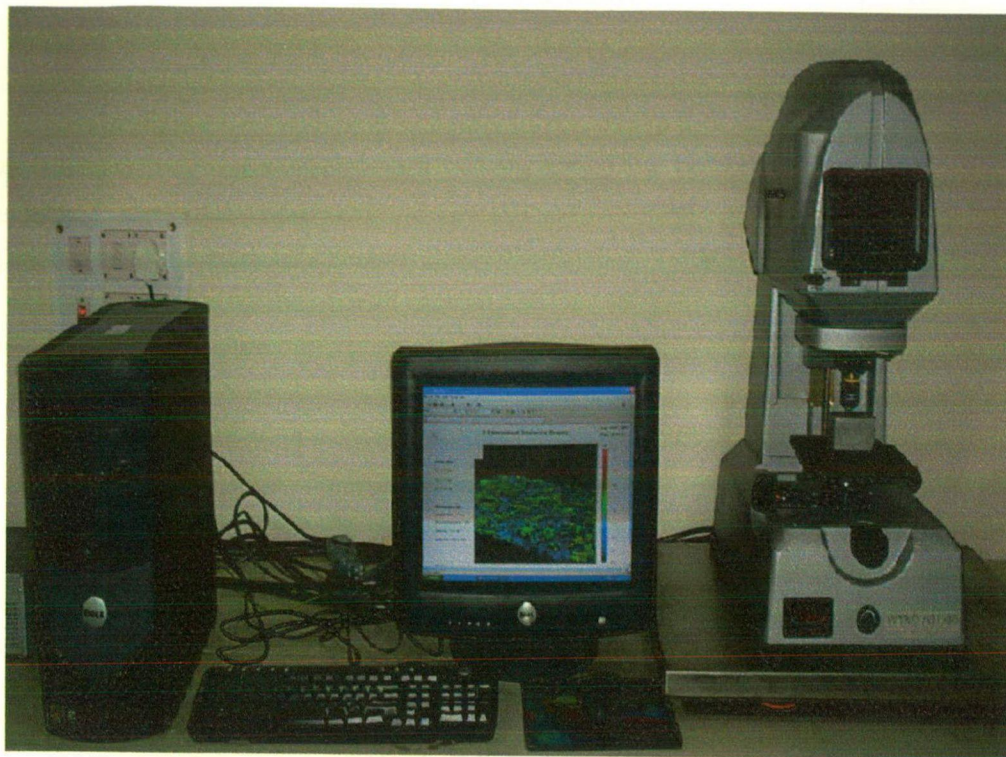
Fig. 3.5: Photographic view of the Optical Profilometer (Wyko NT 1100 interfaced with Vision® 32 software).

3.2 CNTs/CNFs GROWTH IN THE PAAO

CNTs have been grown within the pores of PAAO by chemical vapour deposition (CVD). The catalyst loaded samples were placed in a ceramic boat, which was then loaded in the tube furnace. The furnace was put on and when temperature reached 600° C, ammonia gas was made to flow with a rate of approximately 200 sccm. When the temperature reached 650° C, acetylene gas was also passed with a flow rate of approximately 100 sccm for 5-20 minutes. For styding the effect of temperature, time and gas ratio, experiments were performed at various parameters as scheduled in Table 3.2.

Table 3.3: CVD process parameters.

S. No.	Temp. of the furnace. (° C)	Duration of CVD. (min.)	Ammonia to acetylene ratio (approximately)	Remarks
1	500	10	3	No growth of CNTs/CNFs
2	550	1	3	-
		5	3	-
		10	3	-
		15	3	-
3	600	10	3	-
4	620	10	3	-
5	640	10	3	-
6	650	10	3	Best results

CNTs were produced by the catalytic decomposition of C_2H_2 using a tube furnace which can be operated up to a temperature of 1200 °C at atmospheric pressure. The experimental set-up is shown in Fig. 3.6. The tube used to carry out the deposition has a length of 60 cm with a 45 mm inner diameter. The CNTs growth was carried out on the PAAO template at 650 °C by thermal CVD. Acetylene (C_2H_2) gas was used as a carbon source and ammonia (NH_3) gas was used as a dilution and catalytic gas. The anodized substrate was transferred to the reaction chamber. Subsequently, NH_3 was supplied into the chamber when the furnace temperature reached at 550 °C. Then the temperature was further increased to 650 °C, with the continued supply of ammonia, which is a pre-treatment step of the substrate for surface activation of the deposited catalyst. Later on, C_2H_2 was flown into the chamber for the growth of CNTs for 5-15 min. For the analysis of the morphology, the

microstructure and crystallinity of PAAO and CNTs, field emission scanning electron microscope (FE-SEM), coupled with EDS, high-resolution transmission electron microscope (HR-TEM), atomic force microscopy (AFM) and Raman spectroscopy were employed. Additionally, the cracks and warps which causes due to the differences in the thermal expansion coefficients of the PAAO layer and the aluminum substrate could be avoided by raising slowly the furnace temperature at 5 °C/min up to 650 °C.
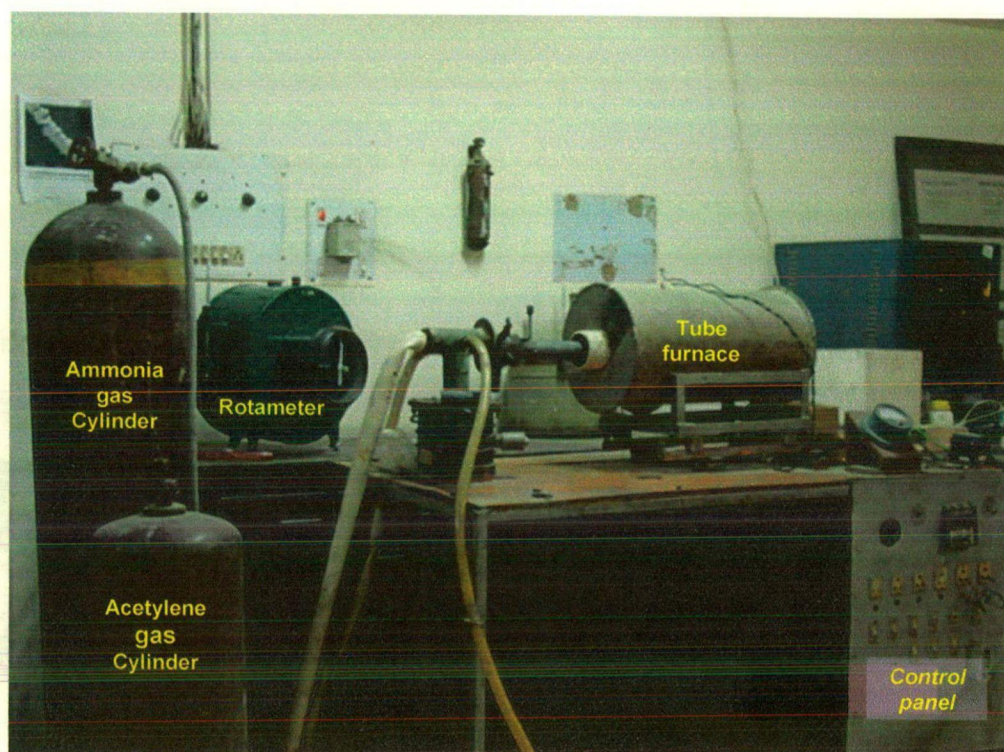
Fig. 3.6: Photographic view of the Chemical vapour deposition apparatus

The samples were furnace cooled to room temperature. The samples were viewed under S.E.M (both conventional and FE-SEM with EDS), TEM, AFM and the formed CNTs were observed. The morphology of the formed CNTs depends on the CVD process parameters. For observing sectional transverse views of the samples, a special type of clamping fixture, as shown in Fig. 3.2 was designed for holding the fractured samples in vertical position, so that the pore depth and growth status of CNTs within the pores may be observed and measured using the scale bar of the SEM/FE-SEM image.

3.2.1 Characterization of CNTs

A excellent review on different techniques for the characterization of the atomic structure of carbon nanotubes by Lambin Ph., (2002) is available in the literature. This review covers the electron microscopies, various diffraction techniques, scanning probe microscopies, and optical spectroscopies, including Raman scattering. The advantages and limitations of the characterization techniques have been discussed in the review.

3.2.1(a)   Transmission Electron Microscope

TEM is a microscopy technique whereby a beam of electrons i s transmitted through an ultra thin specimen, interacting with the specimen as they pass through. An image is formed from the interaction of the electrons transmitted through the specimen, which is magnified and focussed by an objective lens onto an imaging devices such as a fluorescent screen, which is commonly used in most of the TEMs, on a layer of photographic film, or to be detected by a sensor such as a CCD (charge coupled device) camera. A typical block diagram of TEM is shown in Fig. 3.7. It is an important tool for materials characterization. It is generally used to study (i) Morphology (ii) Crystallographic Information and (iii) Compositional Information (if so equipped) of materials.

3.2.1(b)   Principle of transmission electron microscopy

A transmission electron microscope (TEM) works much like a slide projector. A projector shines a beam of light through (transmits) the slide, as the light passes through, it is affected by the structures and objects on the slide. These effects result in only certain parts of the light beam being transmitted. The transmitted beam is then projected onto the viewing screen, forming an enlarged image of the slide. TEMs work the same way except that they shine a beam of electrons (like the light) through the specimen (like the slide).The transmitted part of the beam is projected onto a phosphor screen which can be viewed.

anode

condenser lens 1

condenser lens 2
condenser diaphragm

crystalline
or oriented ‖ ‖‖ ‖‖‖

amorphous
or not oriented

sample

objective lens

objective diaphragm
(back focal plane)

selected area
diaphragm

intermediate lens

projective lens

final image

screen
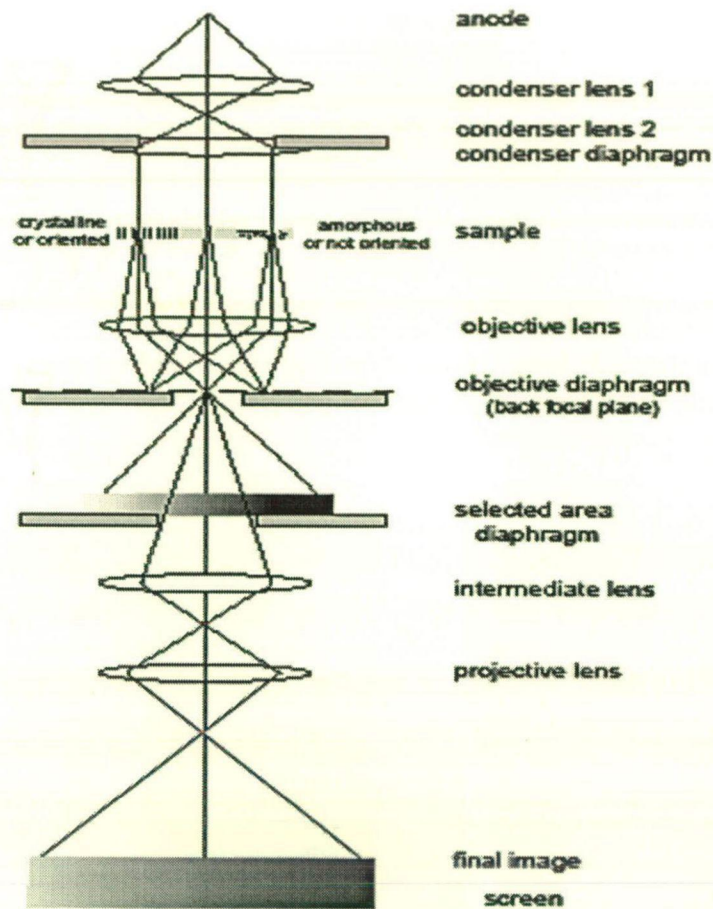
Fig. 3.7:   Schematic diagram of transmission electron microscope in image mode.

3.2.1(c)   Imaging mode methods

(a)   Bright field

The most common mode of operation for a TEM is the bright field imaging mode. In this mode the contrast formation, when considered classically, is formed directly by occlusion and absorption of electrons in the sample. Thicker regions of the sample, and / or regions with a higher atomic number will appear dark, whilst regions with thinner sample in the beam path will appear bright and   hence the term 'bright field' is used.

(b)   Diffraction contrast

Samples can exhibit diffraction contrast, whereby the electron beam undergoes Bragg scattering, which in the case of a crystalline sample disperses electrons into discrete locations in the back focal plane. By the placement of apertures in the back focal plane, i.e. the objective aperture, the desired Bragg reflections can be selected (or

excluded), thus only parts of the sample that are causing the electrons to scatter to the selected reflections will end up projected onto the imaging apparatus. If the reflections that are selected do not include the unscattered beam (which will appear up at the focal point of the lens), then the image will appear dark whereever no sample scattering to the selected peak is present, as such a region without a specimen will appear dark. This is known as a dark-field image.

Applications for this method include the identification of lattice defects in crystals. By carefully selecting the orientation of the sample, it is possible not just to determine the position of defects but also to determine the type of defect present. If the sample is orientated so that one particular plane is only slightly tilted away from the strongest diffracting angle (known as the Bragg Angle), any distortion of the crystal plane that locally tilts the plane to the Bragg angle will produce particularly strong contrast variations. However, defects that produce only displacement of atoms that do not tilt the crystal to the Bragg angle (i.e. displacements parallel to the crystal plane) will not produce strong contrast.

(c)   Diffraction

As previously stated, by adjusting the magnetic lenses such that the back focal plane of the lens is placed on the imaging apparatus a diffraction pattern can be generated. For thin crystalline samples, this produces an image that consists of a series of dots in the case of a single crystal, or a series of rings in the case of a polycrystalline material. For the single crystal case the diffraction pattern is dependent upon the orientation of the specimen. This image provides the investigator with information about the space group symmetries in the crystal and the crystal's orientation to the beam path. This is typically done without utilizing any information but the position at which the diffraction spots appear and the observed image symmetries.

Analysis of diffraction patterns beyond point-position can be complex, as the image is sensitive to a number of factors such as specimen thickness and orientation, objective lens defocus, spherical and chromatic aberration. Although quantitative interpretation of the contrast shown in lattice images is possible, it is inherently complicated and can require extensive computer simulation and analysis. More complex diffraction behavior is also possible, with phenomena such as Kikuchi lines or convergent

beam electron diffraction (CBED) providing additional information, beyond structural data, such as sample thickness.

3.2.1(d) Sample preparation

The TEM is used heavily in material science, metallurgy and the biological sciences. In each case the specimens must be very thin and able to withstand the high vacuum present inside the instrument. Sample preparation in TEM can be a complex procedure. TEM specimens are typically hundreds of nanometers thick, as the electron beam interacts readily with the sample, an effect that increases roughly with atomic number. High quality samples will have a thickness that is comparable to the mean free path of the electrons that travel through the samples, which may be only a few tens of nanometers. Preparation of TEM specimens is specific to the material under analysis and the desired information to obtain from the specimen. As such, many generic techniques have been used for the preparation of the required thin sections. In material science and metallurgy the specimens tend to be naturally resistant to vacuum, but still must be prepared as a thin foil, or etched so some portion of the specimen is thin enough for the beam to penetrate. Constraints on the thickness of the material may be limited by the scattering cross-section of the atoms from which the material is comprised. Materials that have dimensions small enough to be electron transparent, such as powders or nanotubes, can be quickly produced by the deposition of a dilute sample containing the specimen onto support grids or films. For powder samples, first a small amount of sample is poured in acetone or methanol in a beaker. The beaker is the ultrasonicated for 1 hrs so that the particles of the powders are dispersed in the liquid. Then 2-3 drops of the solution so obtained is poured on to the TEM grid and let it dried for 5-10 minutes. The sample is ready for the characterization.

3.2.1(e) Indexing of polycrystalline diffraction rings

In order to understand the geometry of electron diffraction, consider a simple ray diagram of in Fig. 3.8. A beam of electrons impinges on a crystalline specimen. Some of the electron pass through the specimen without interaction, and hit the screen which is at a distance L from the specimen, at O. Other electrons are diffracted through an angle 2θ by the crystal planes of spacing d, and these electrons hit the film at A, which is a distance r from O. From simple geometry, we see that for small angles of diffraction

$$r/L = \tan 2\theta = 2\theta = \sin 2\theta = 2 \sin \theta = \lambda/d$$

$$rd = \lambda L \tag{3.3}$$
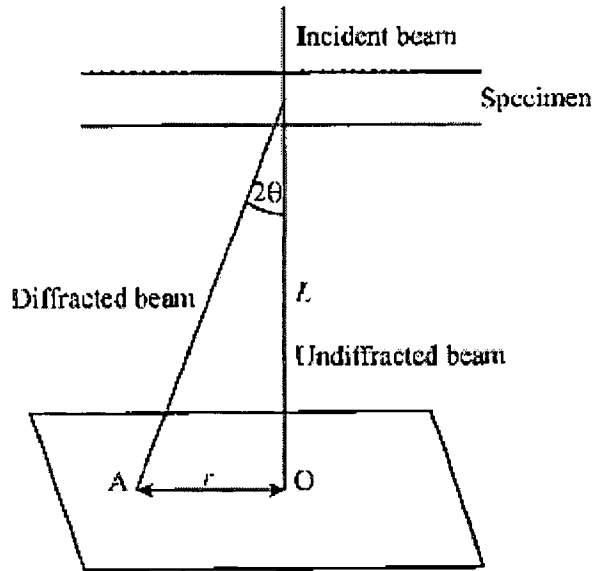
Fig. 3.8: Schematic diagram showing the geometry of diffraction pattern formation

Where L is camera length and λ is wavelength of the electron beam, and both are constant for an instrument. $L\lambda$ is called camera constant. It can be seen that the distance of a diffraction spot from the undiffracted spot, r, is therefore inversely proportional to the d spacing of the diffracting planes. If we know the camera constant for the instrument, than one can determine d simply by measuring r on the pattern. In Fig. 3.9, typical ring diffraction pattern obtained for a polycrystalline sample is shown. The red lines are the diameters (D) of particular rings from which r ($r=D/2$) can be easily calculated. Since each r corresponds to a particular d value, one can index the rings. Indexing of the rings can also be verified by using XRD analysis.
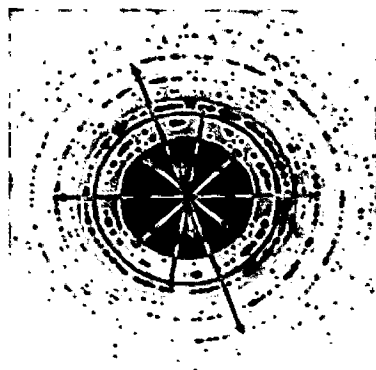
Fig. 3.9: Typical ring diffraction pattern of a well polycrystalline film

3.2.2 Raman Spectroscopy

A LABRAM HR-800 micro-Raman spectrometer with a Argon laser source with 488 nm wavelength focussed on to a spot of ~5 μm size was used for the Raman measurements. The laser power at the sample was less than 5 mw and a CCD detector was used for detection. The spectral resolution was 1cm⁻¹.

CSE Raman spectroscopy is a powerful and sensitive technique for studying the structure of carbonaceous materials. The Raman line at 1580 cm⁻¹ corresponds to E_{2g} modes, which is designated as G line. A very strong Raman line at 1580 cm⁻¹ is observed for single-crystal graphite. Polycrystalline graphite and disordered carbon exhibit an additional line at 1350 cm⁻¹ designated as D line. The intensity at about 1580 cm⁻¹ is much stronger than that at 1350 cm⁻¹ which indicates that the CNTs have a good extent of graphitization.

3.2.2.1   Basic principle

When monochromatic light illuminates a sample, small fraction of it scattered in all directions. The spectrum of the scattered light is found to consist of lines of same frequencies. These addition lines of same frequencies have a small fraction about 0.1% is elastically scattered light of the same frequency as that of the incident light (Rayleigh scattering). An even smaller fraction of incident light about 1 photon in 10^6 or 10^7, will be scattered inelastically (Raman scattering), either towards lower frequencies (Stockes scattering) or higher frequencies (anti-Stockes scattering), than the incident light. The differences in energies between the incident photons and inelastically scattered photon correspond to vibrational frequencies of scattering molecule and intensity is proportional

105

to the fourth power of scattered radiation. For the spontaneous Raman effect, the molecule will be excited from ground state to a virtual energy state and relax into a vibrational excited state, which generates Stokes Raman scattering. If the molecule was already in an elevated vibrational energy state, the Raman scattering is then called anti-Stokes Raman scattering.

The Raman spectra of carbon based materials containing a variable amount of sp^2 structures have been extensively studied by Raman spectra. The application of Raman spectra have been applied on SP^2 bonded carbon based system like graphite, diamond, amorphous carbon and most notably on CNTs, carbon nano fibre. All these materials are characterized by the presence of sp^2 hybridization of the carbons organized into fragments (islands) which can be correlated (in terms of structure and also in terms of their Raman response) to an ideally perfect 2-dimensional crystal of graphite (graphene). The crystallite size, La (Crystaline size in a-direction) calculated using a relation of $L_a = 44/R$ derived experimentally by Tuinstra and Koenig (1970). Usually, particle size has relatively little effect on Raman line shapes unless the particles are extremely small i.e. less than 100 nm. For this reason, high-quality Raman spectra can be obtained from powders and from polycrystalline bulk specimens like ceramics and rocks by simply reflecting the laser beam from the specimen surface. The measurements for Solid samples can be measured in the 90° scattering geometry by mounting a slab of the solid sample or a pressed pellet of a powdered sample so that the beam reflects from the surface but not into the entrance slit.

3.2.2.2   Instrumentation

A typical conventional Raman system consists of the following basic components: i) an excitation source, usually a visible-light laser; ii) optics for sample illumination and collection of sample-scattered light; iii) a monochromator; and iv) a signal processing system consisting of a detector and a data processing unit. A diagram showing the various components of a Raman spectrometer is shown in Fig. 3.10.
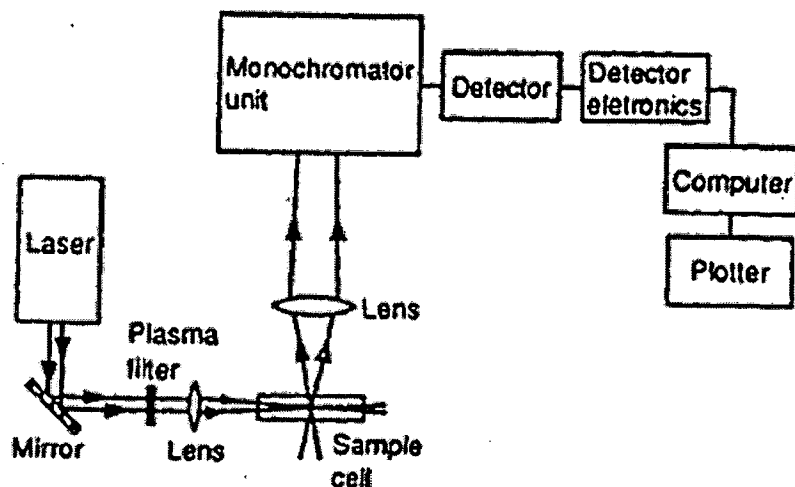
Fig. 3.10: A schematic of the Raman spectroscopy.

A sample is mounted in the sample chamber and laser light is focused on it with the help of a lens. Generally, liquids and solids are sampled in a Pyrex capillary tube. Solids are sampled either as pellets or are examined directly without any sample preparation. The scattered light is collected using another lens and is focused at the entrance slit of the monochromator. Monochromator slit widths are set for the desired spectral resolution. The monochromator effectively rejects Raleigh scattering and stray light and serves as a dispersing element for the incoming radiation, sometimes more than one monochromator is used to obtain high resolution and / or better suppression of the Rayleigh line. The light leaving the exit slit of the monochromator is collected and focused on the surface of a detector. This optical signal is converted to an electrical signal within the detector and further manipulated using detector electronics. In a conventional Raman system using a photomultiplier tube (PMT) detector, the light intensity at various frequencies is measured by scanning the monochromator. In contrast, when a multichannel detector is used, a spectral range is simultaneously recorded.

Generally, there are two geometries in which a sample is studied in Raman spectroscopy (Fig. 3.11). In the 90 degree geometry, the laser beam direction and the axis of the collection lens are at 90 degrees to each other. On the other hand, in the 180 degree scattering geometry (also called back scattering mode) these two axes are coincident. The 90 degree scattering geometry is frequently used in the conventional approach, whereas

both 90 and 180 degree modes are used in the FT (Fourier Transform) Raman spectroscopy.
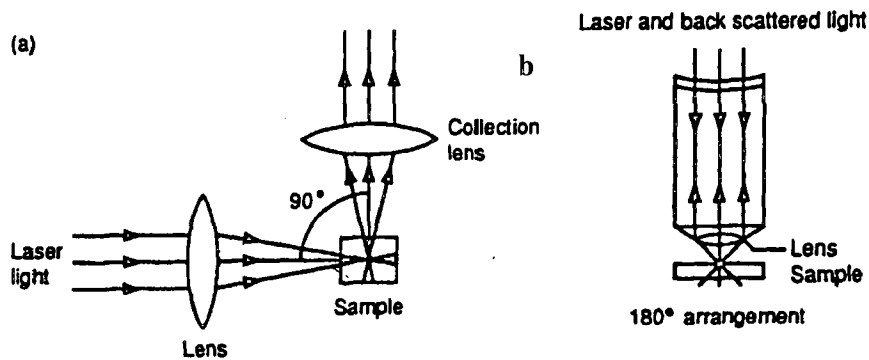
Fig. 3.11:   Two different geometrical modes of Raman spectroscopy.

3.3   TRIBOLOGICAL TESTING

Anodic samples of pure aluminium (PA) and commercial pure aluminium (CPA) were tried for preliminary wear testing in order to establish the methodology of the tribological testing procedure for thin sheets of aluminium. Coupons of diameter 10 mm were cut and glued to the pin of 10 mm diameter made of commercial aluminium, as shown in Fig. 3.12.
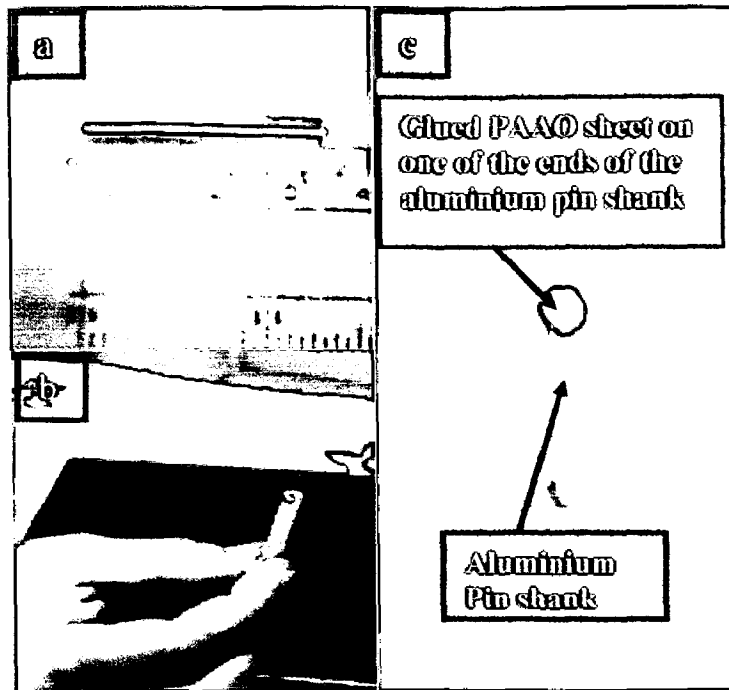
Fig. 3.12: Photographic view of the wear pin shank (a and b) and glued Porous anodized aluminium oxide (PAAO) sheet on one of the ends (c).

Wear testing was performed on pin on disc machine (model MTM 60, (Fig. 3.13 and 3.14)) in the Tribology laboratory of Department of Mechanical and Industrial Engineering, Indian Institute of Technology Roorkee. The tests were conducted at 0.5 m/s speed at normal load of 5, 10, 15 and 20 N with a stationary pin and rotating wear disc (EN-32 steel) cell. The tests were conducted for 1 hour for each sample. Coefficient of friction was found in the range of 0.15 to 0.55, which is same as reported in literature The weight loss of the specimen was recorded every 15 min using a Sartorius digital balance with an accuracy of upto 10^{-4} g. The data was converted to cumulative volume loss as function of time and also in terms of wear rate defined as total volume loss per unit distance.

The material was slid against a hardened steel (EN-32, Fig. 3.15) counterface under unlubricated and lubricated conditions. After tribological testing, worn surfaces of the material were analyzed by scanning electron microscopy (SEM) and field-emission-gun environment SEM (FESEM) equipped with an energy dispersive X-ray spectroscopy (EDS).

109
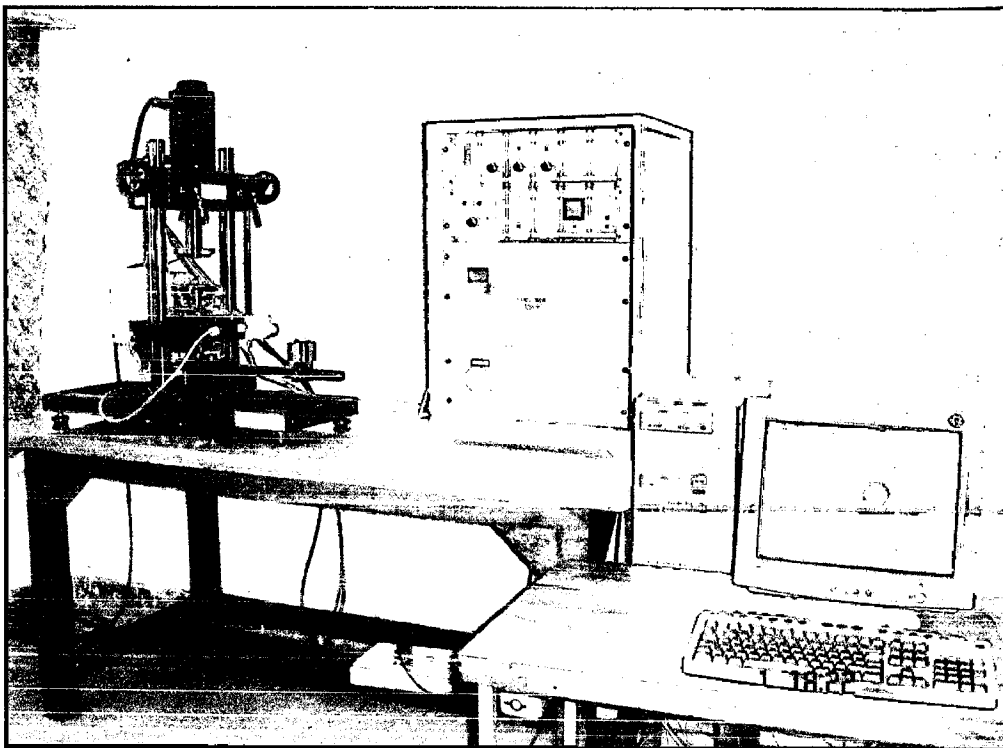
Fig. 3.13: Photographic views of the tribological testing machine (MTM 60)
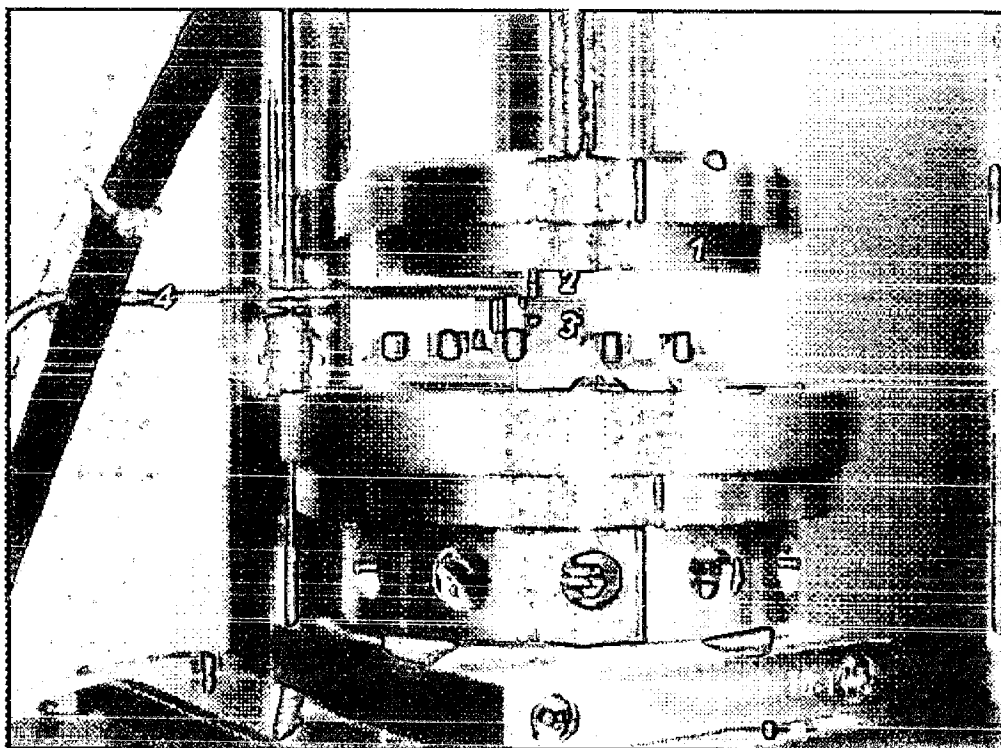
Fig. 3.14: Closer view of the pin and disc of the tribotester (1) Disc, (2) Pin, (3) holder to clamp the pin and (4) temperature sensor touching the sample, which is in contact with the rotating disc.
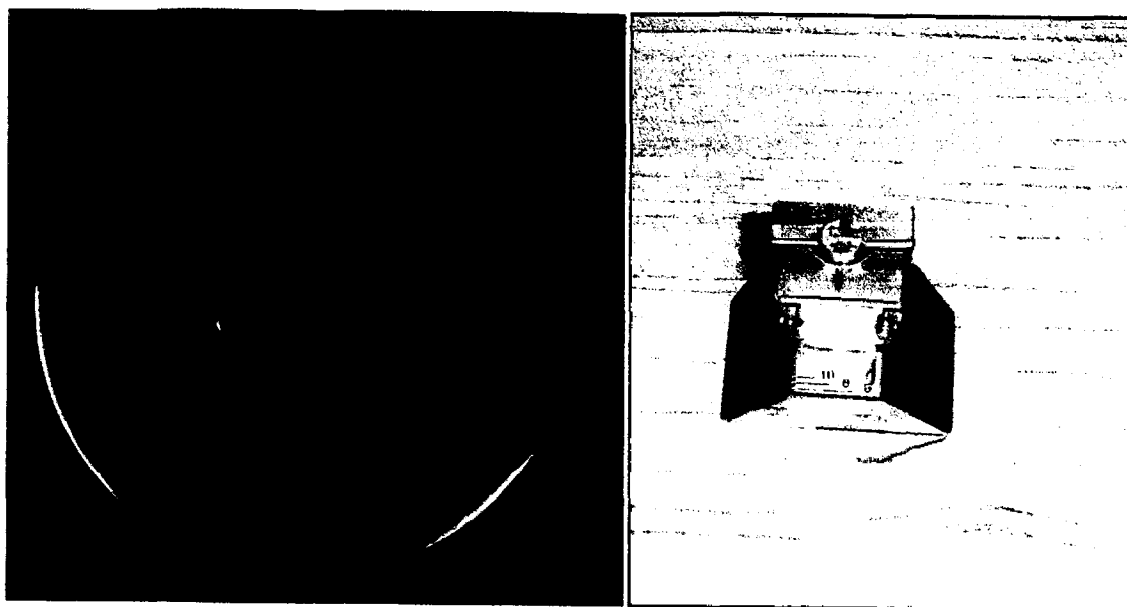
Fig. 3.15: Photographic view of the (a) EN-32 wear disc and (b) wear pin holder

After friction measurements, wear scars were examined using a scanning electron microscope (SEM). The lubricating oil (SAE-15) was infiltrated in the pores of PAAO film due to the capillarity action. In order to take the repeatability into account, the test results for the friction and wear rate under steady state sliding were obtained from the average of three readings.

This chapter contains the results of anodization carried out in phosphoric, oxalic, chromic and sulphuric acid baths on pure aluminium (PA) and commercial pure aluminium (CPA) substrates. The chapter highlights the difference in the results of porous anodized aluminium oxide (PAAO) on the basis of different morphologies observed in terms of characterization parameters including pore diameter, interpore distance, ordering, porosity, oxide layer and barrier layer thicknesses, whichever is applicable. In the beginning of this chapter, the results pertaining to common initial steps of the anodization process, like (i) the effect of pre-treatment of as-received substrate on the morphology of resultant anodized alumina film and (ii) the improvement in the ordering of porous structure in two step anodization instead of one step are reported. The effects of other important process variables like applied voltage/current, temperature, concentration and pH of the electrolyte, on the resulting PAAO structure for each acid electrolyte bath are presented later in this chapter. The results of phosphoric acid, oxalic acid, chromic acid and sulphuric acid baths, which are the four acid electrolytes used for anodization, are reported in four separate sub-sections. Two of these sub-sections have been further divided for reporting the results of anodization of pure aluminium (PA) and commercial pure aluminium (CPA) samples. The chapter ends with a discussion on all of the above mentioned results.

4.1   EFFECT OF PRE-TREATMENT

Figures 4.1(a) and (b) respectively show the top view and the fractured transverse surface of a typical PAAO surface of PA substrate, whose anodization has been carried out in a single step in 5 wt% phosphoric acid bath at 120 V. From the top view, pore diameter 'd' and interpore distance 'L_p' have been measured, while oxide-layer thickness 't_o' and barrier layer thickness 't_b' have been measured from the fractured transverse surface view.
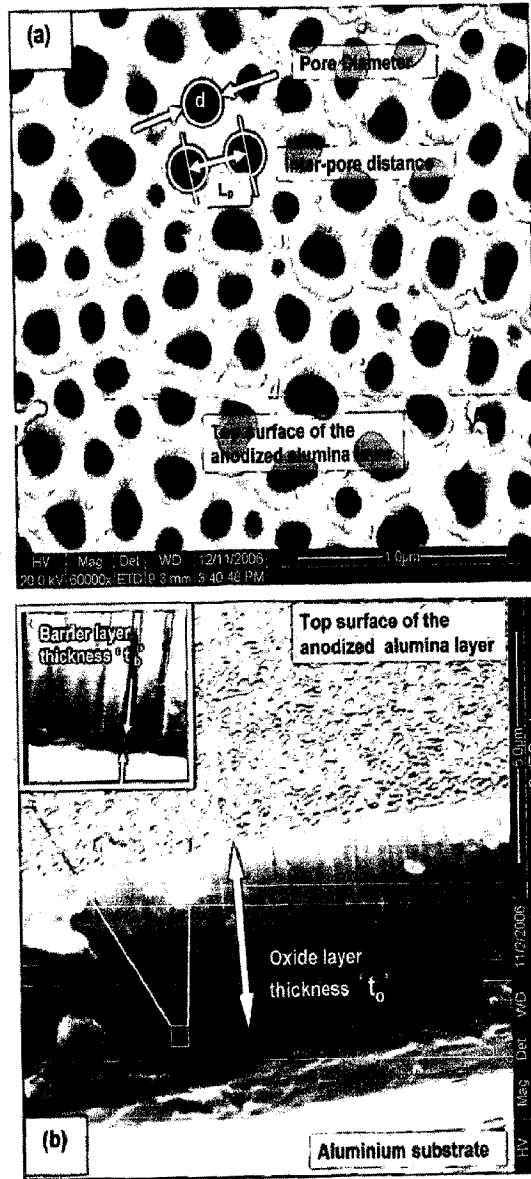
Fig. 4.1: (a) Top view of a typical PAAO on PA substrate and (b) its fractured transverse surface view, showing the thickness of the oxide layer 't_o' and thickness of the barrier layer 't_b' in the inset which is the magnified view of the small square near the bottom of the oxide layer.

114
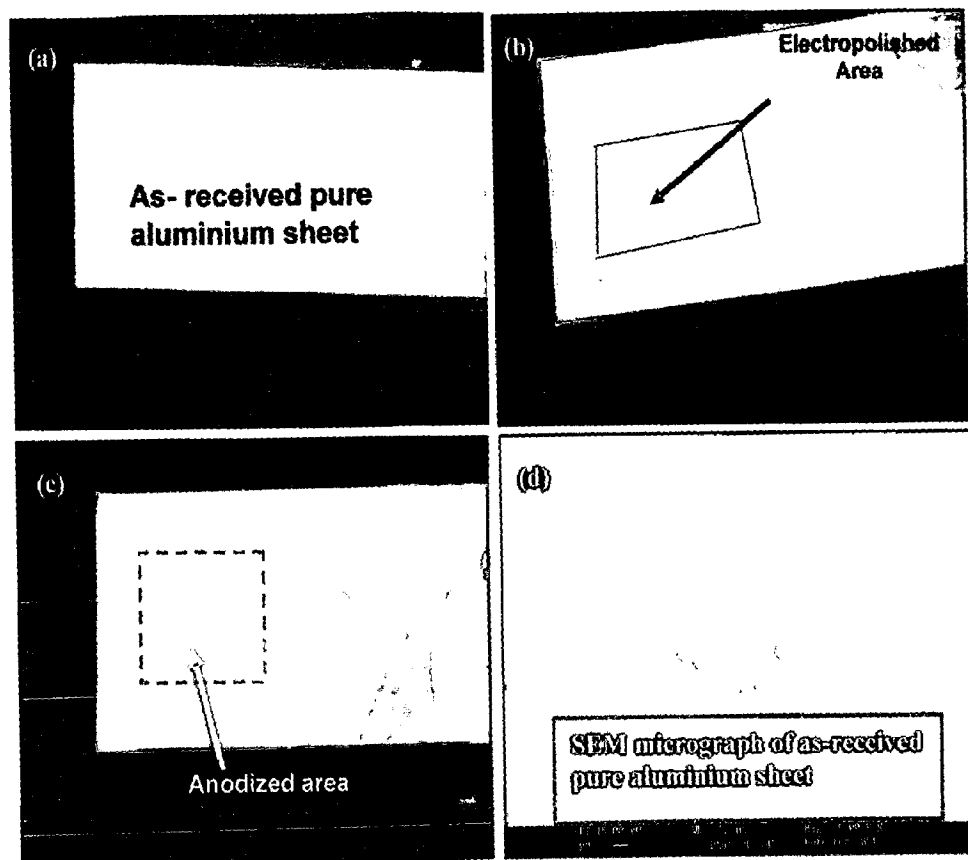
Fig. 4.2: Pure aluminium sample; as-received (a); electropolished (b); anodized at 150 V in 5 wt% phosphoric acid (c). SEM micrograph of the as-received pure aluminium sample with rolling marks/ scratches and minor pits visible (d).

Pre-treatment, as already discussed in earlier chapters, is an essential step for obtaining ordered porous anodized alumina structure and this process consists of the following steps: (a) mechanical polishing, (b) annealing, (c) degreasing and (d) electro-polishing. The pure aluminium samples (99.95 %, Merck, Germany) used have good surface finish and shining characteristics as shown in Fig. 4.2 (a) and so, mechanical polishing has not been performed on these substrates. But the remaining three steps of pre-treatment have been carried out. But mechanical polishing has been carried out on commercial aluminium samples, which have rough surface finish. After electro-polishing, the surface roughness of the substrates as estimated by optical profilometer and Atomic

Force Microscope (AFM) decreases drastically in both pure and commercial aluminium samples, as shown in Table-4.1. In order to show the effect of electropolishing on the visibility of the sample surface a part of the as-received sample area has been electropolished and the combined view is given in Fig. 4.2. The difference in appearance between electropolished and as-received areas in pure aluminium substrate may easily be distinguished by naked eye in Fig. 4.2(b) showing bright electro-polished area and dull as received area masked using cello-tape or lacquer during electro-polishing.

Figure 4.2 (c) shows a typical substrate of pure aluminium anodized at 150 V in 5 wt.% phosphoric acid bath at 20 °C. Colour change in the anodized area may be noted. The results of surface roughness after anodization reveal that there is either no change or marginal increase on anodization as shown in Table 4.1, where average values of surface roughness after different pretreatments and anodization is given. Fig. 4.2 (d) shows SEM micrograph of as-received pure aluminium sample with visible rolling marks/ scratches.

Table 4.1: Average surface roughness after different pre-treatments and anodization

Sl. No.	Type of anode material (substrate)	Average Surface Roughness (Ra)			
		As-received	After mechanical polishing	After electro-polishing	After anodization
1	Pure Aluminium	375.37 nm	Not measured	280.80 nm	353.75 nm
2	Commercial Aluminium	549.44 nm	410.32 nm	265.60 nm	347.45 nm

Figure 4.3 depicts optical profilometry view and detailed statistics of the surface of a typical electropolished pure aluminium substrate. (Ra, Rq, Rz and Rt represents usual surface roughness parameters as per details given in nomenclature.)

Surface Statistics:
Ra: 280.80 nm
Rq: 357.16 nm
Rz: 2.58 um
Rt: 2.85 um

Set-up Parameters:
Size: 368 X 240
Sampling: 1.61 um

Processed Options:
Terms Removed:
Tilt
Filtering:
None
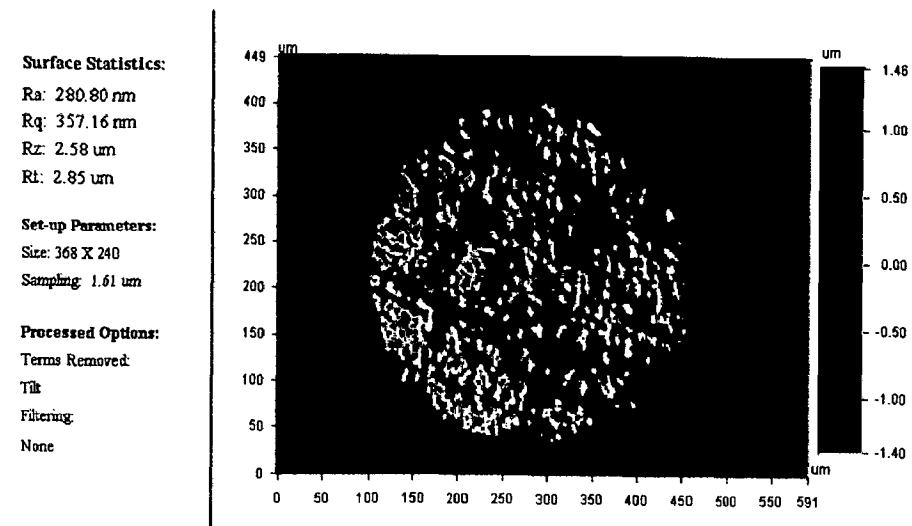
Fig.4.3: Optical profilometry views and detailed statistics of the surface of a typical electropolished pure aluminium substrate

The difference in pore morphology of anodized layer in pure aluminium substrates, as-received and after each step of pretreatment i.e., annealing and electro-polishing, anodized at 120 V for 1 hour, in 5 wt.% phosphoric acid bath at 20 °C, in single step of anodization are clearly visible in SEM micrographs shown in Fig. 4.4. As-received substrate results in aligned pores in the direction of rolling marks, as shown in Fig. 4.4 (a), while the annealed sample shows pore morphology having no such alignment/marks as shown in Fig. 4.4 (b). FFT (inset in the SEM image) response from the pores shows that on annealing the broad halo in as received substrate has transformed to a broad ring due to removal of strain of the as received strip during annealing and also, the line through the origin, indicating the oriented alignment along rolling marks, has disappeared. If one carries out electro-polishing without annealing, it is observed that there is no effect of rolling marks visible as shown in Fig.4.4 (c). But the FFT response shows that the radius of the first broad ring is marginally smaller compared to that from anodized layer on annealed substrate. This is an indication that the inter-pore distances are somewhat larger, which has also been confirmed by direct measurements and secondly, the ring is more diffused and hence broader as compared to FFT ring of only annealed sample. When the substrate is subjected to both annealing and electro-polishing, the pore structure developed is significantly different from those obtained after either annealing or electro-polishing alone as observed in Fig.4.4 (d). Here one observes islands

of hexagonal arrangement of pores having different orientations. When one takes FFT in an island, one gets spot pattern with noises around but FFT from a larger area including a number of islands show rings, whose broadening is less than those obtained either for annealing or electro-polishing treatment alone. The second ring has also become considerably sharper. The radius of the first ring is slightly more than that obtained by electro-polishing alone and similar to that observed for annealed substrate.
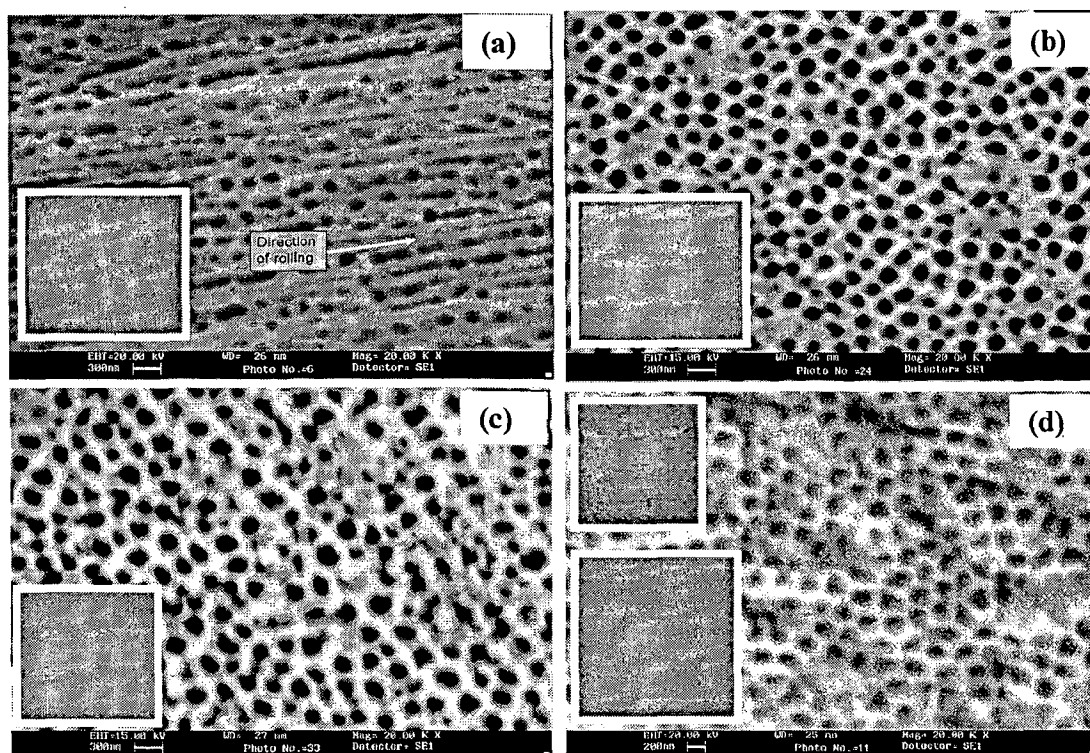
Fig. 4.4: Anodized Sample formed from (a) as-received substrate, arrow shows direction of roll ing, (b) a nnealed substrate, rolling ma rks are no more visible after annealing, (c) electropolished substrate and (d) electropolished as well as annealed substrate. Insets show Fast Fourier Transforms (FFTs) of the images. (Scale bar 300 nm is visible in all of the SEM image strips in all figures); In (d) one additional FFT (left top corner) taken from selected area is clearly showing six distinct hexagonal spots.

The frequency-histogram for pore diameter distribution of anodized layer on pure aluminium substrates subjected to different steps of pre-treatment is shown in Fig. 4.5. The histogram is unsymmetrical for the as received substrate and there is a very high peak

towards the left, at about 125 nm (pore diameter), which is lower than the average of 161.45 nm observed from the measurements as shown in Fig. 4.5(a). A strong, single peak indicates that there is regularity in pore size for most of the pores. However, the range of pore diameter measurements is quite wide and its span is from 50 to 400 nm. This variation may be attributed to the presence of strain in the rolled strip, from where substrate has been sectioned and the associated irregularities in the substrate. The histogram for the annealed substrate is symmetric as strain is removed during annealing as shown in Fig. 4.5(b). But there are two
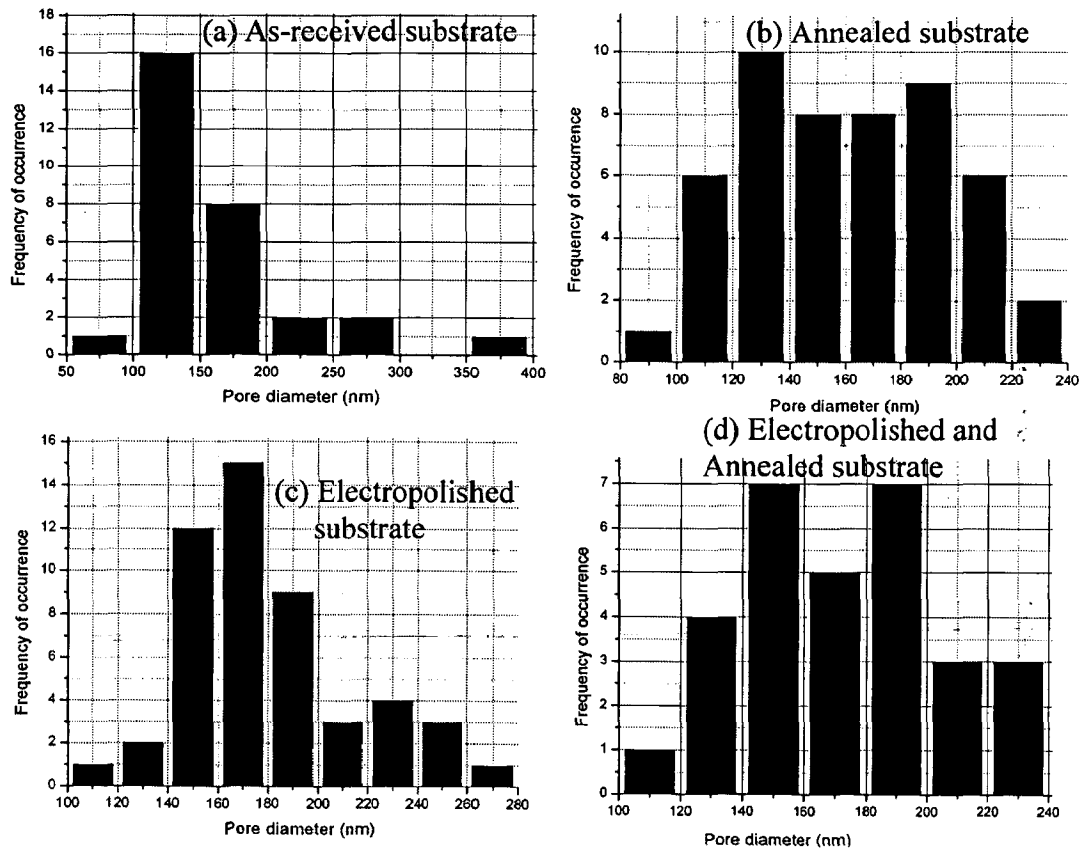
Fig. 4.5:   Frequency histogram for pore diameter distribution for samples anodized from (a) as-received substrate, (b) annealed substrate, (c) electropolished substrate and (d) electropolished as well as annealed substrate. Anodization process parameters: Single step anodization at 120 V for 1 hour in 5 wt.% phosphoric acid bath maintained at temperature of 20 °C.

peaks at about 130 nm and 190 nm, symmetrically placed on both sides of the mean value of 161 nm, but the difference in the heights of the two peaks and that of the central flat

region is not very large, so it could be approximated as normal distribution. The range of pore diameter measurements is quite narrow and its span extends from 80 to 240 nm. The histogram shown in Fig. 4.5 (c) is for anodized layer on the electro-polished substrate without annealing and it is again a little un-symmetric with two peaks - one prominent peak at 170 nm and the other small peak at about 250 nm. However, the histogram in Fig. 4.5 (c) is more symmetrical than that for as received substrate in Fig. 4.5 (a). The range of pore diameter distribution is 100-280 nm for electro-polished substrate, which is slightly wider than that observed for the annealed substrate but narrower than the as received substrate. The histogram shown in Fig. 4.5 (d) is for anodized layer on a substrate subjected to both annealing and electro-polishing and the distribution is the most symmetrical of all cases obtained. However, there are still two peaks just like the annealed one but closer to each other compared to that for annealed substrate. Further, the range of pore diameters is lowest (100 nm-240 nm) if both the treatments of annealing and electro-polishing are carried out on the substrate.

The frequency-histogram for inter-pore distance distribution for anodized substrates of pure aluminium subjected to different steps in pretreatment is shown in Fig. 4.6. The shape of the frequency-histogram in the case of anodized layer made from as received substrate has a single peak as evident from Fig. 4.6 (a) and the distribution is a little asymmetric but fairly close to normal distribution and the inter-pore distance ranges from 150 to 450 nm. For annealed substrates, the distribution of inter-pore distance has many peaks and is slightly unsymmetrical as shown in Fig. 4.6 (b). The major peak is at about 230 nm, while the interpore distance range is narrow which is between 140 and 380 nm, This is due to improved ordering in the anodized layer for the annealed substrates as compared to that from as-received substrates due to removal of strain. The frequency-histogram for the electropolished substrate in Fig. 4.6 (c) is having cluster of two or three peaks, one at the centre and others are on either side of it. The histogram for the substrate subjected to both types of pre treatment shown in Fig. 4.6 (d) is fairly symmetrical and there is a peak at about 290 nm mark and the range is even narrower, i.e. from 200 to 360 nm and hence best ordering is achieved in this case.
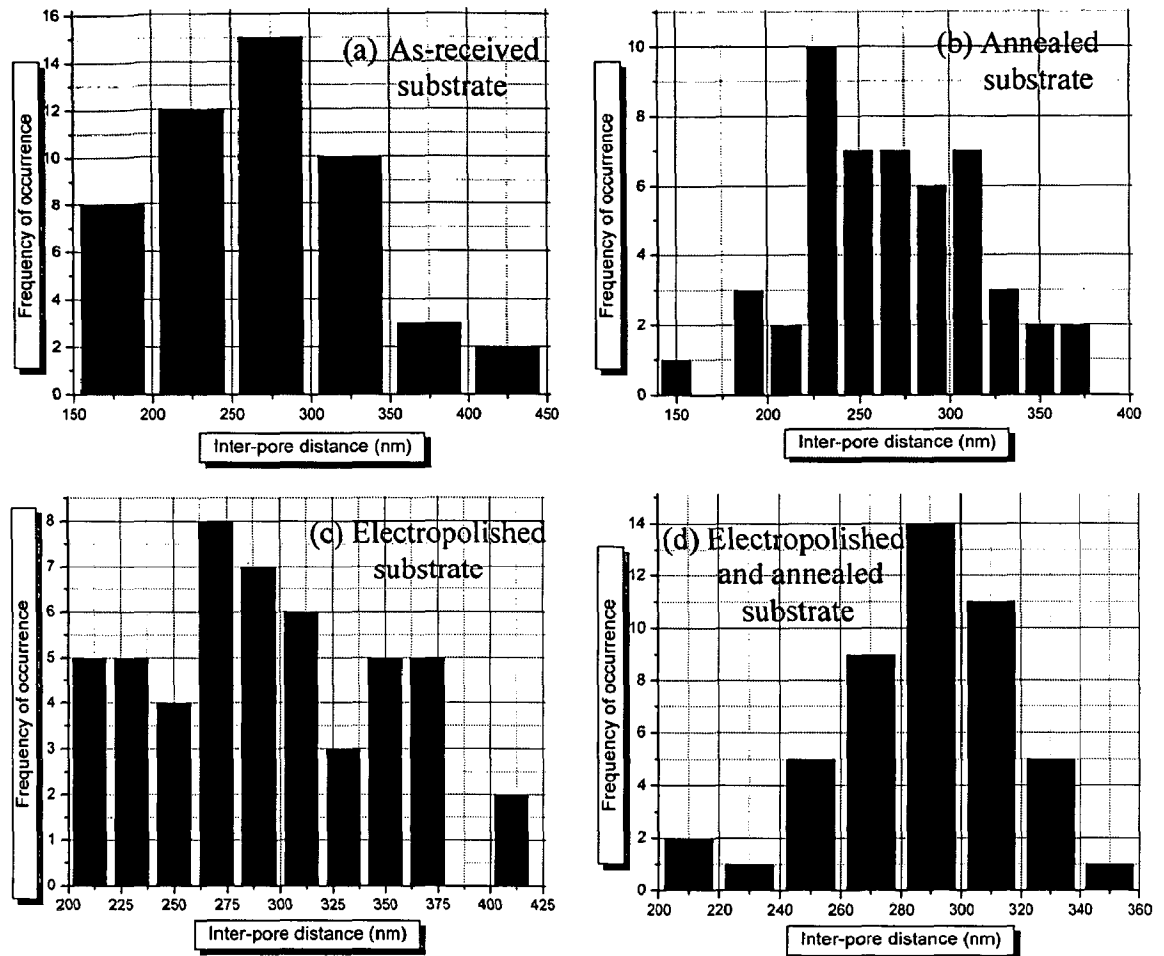
Fig. 4.6: Frequency histogram for inter-pore distance distribution for samples anodized from (a) as-received substrate (b) annealed substrate (c) electropolished substrate and (d) electropolished as well as annealed substrate. Anodization process parameters: Single step anodization at 120 V for 1 hour in 5 wt.% phosphoric acid bath maintained at temperature of 20 °C.

Table 4.2 shows the effect of various pre-treatments on interpore distance and pore diameter of porous anodized alumina structure. From the results, it is clear that the standard deviations for the two parameters decrease more drastically when annealing is carried out on the substrates and substantially when electropolishing is performed as compared to bare as-received samples, which indicates that there is improvement in the ordering of pore arrangement due to annealing and electropolishing and when both the

treatments are carried out on the substrate in sequence, the standard deviation assumes the lowest value and ordering of pores is best achieved.

Table 4.2: Effect of various pre-treatments on parameters of porous anodized alumina structure.

Sl. No.	Condition of sample Before anodization	Average pore dia. (d)/ nm	Std. Dev. of pore dia. (d)/ nm	Average inter-pore distance (L_p)/ nm	Std. Dev. of inter-pore distance (L_p)/ nm
1	As-Received.	161.49	60.547	270.317	65.12
2	Annealed.	161.16	34.512	268.28	49.65
3	Electropolished.	178.65	34.78	292.28	54.17
4	Annealed and electropolished.	173.01	31.9	286.61	30.0

4.2 EFFECT OF TWO-STEP ANODIZATION

Two-step anodization method which has been discussed in detail in earlier chapters has been carried out in almost all of the experiments. To obtain very well-ordered porous anodic alumina structure, it is necessary to carry out first anodization for prolonged time durations, may be several days so as to get improved ordering of porous anodic alumina structure at the bottom of the pores, which also forms well-ordered scalloped shaped barrier layer oxide and s ubsequently on dissolution of this formed oxide, leaves ordered concave shaped dimples on the undissolved aluminium surface. The perfect hexagonal pore ordering is essential in many nanotechnological applications, unlike the present tribological application, where it is not so essential however, here, a few samples were tried for getting well-ordered (hexagonally ordered) porous structure hence were given longer anodization time (6 to 12 hours) in the first step in case of oxalic acid baths. Top view and cross-sectional view of a typical two-step anodized sample are shown in Fig. 4.7 (b) and (d) respectively. Fig. 4.7 (a) and (c) show corresponding microscopic views for single step anodized sample for comparison of degree of ordering between the two cases, all other process parameters have been kept constant.
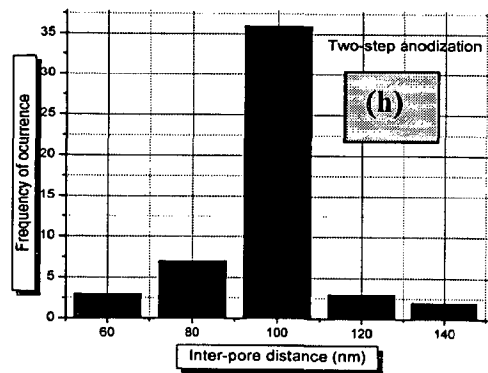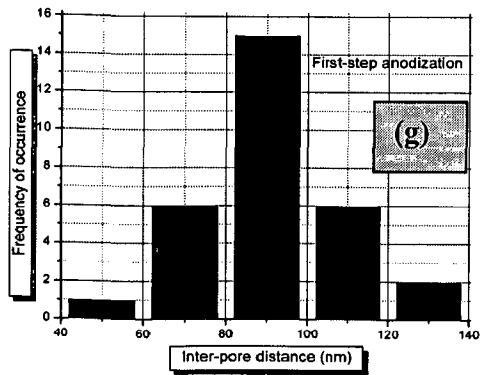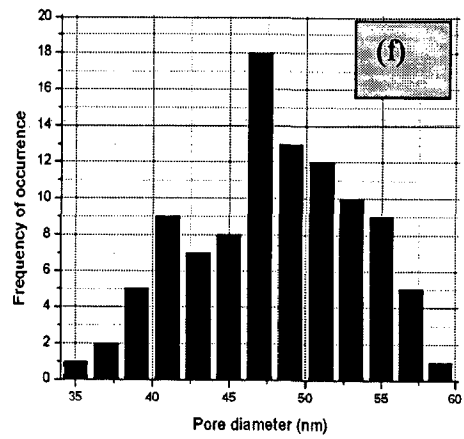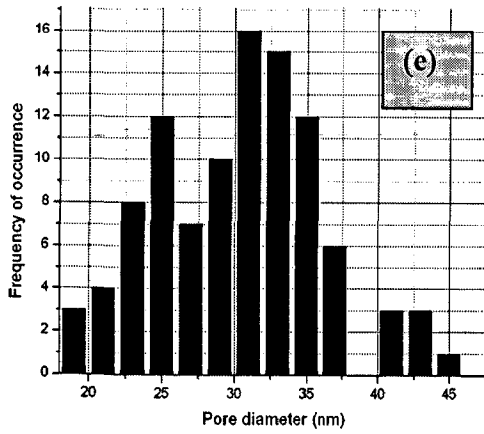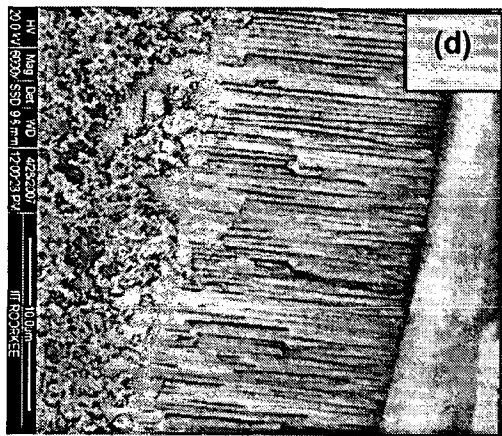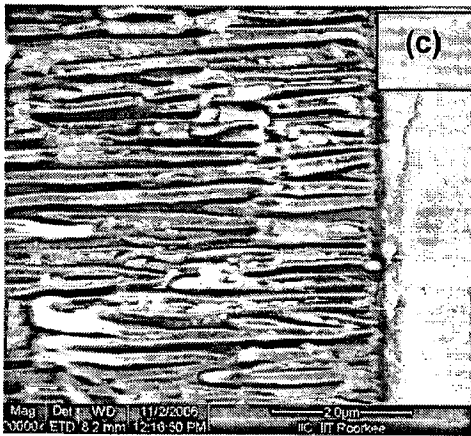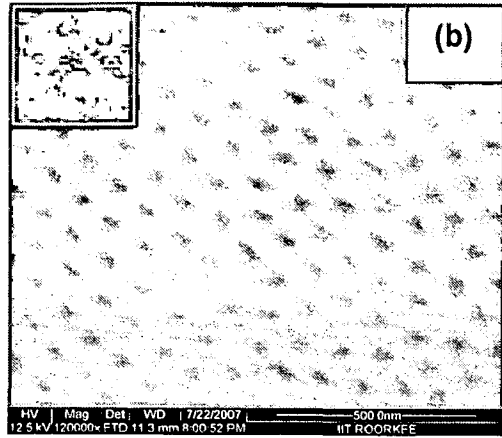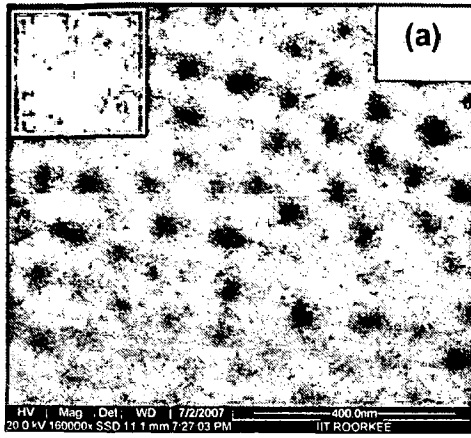
Fig. 4.7: SEM micrographs of the first-step anodized sample; (a) Top view and (c) cross-sectional view, obtained by fracturing the oxide layer. Fig. (b) and (d) show corresponding views in case of the second-step anodized sample; insets in (a) and (b) show Fast Fourier Transform (FFT) of the SEM images of the first and second steps of anodization respectively. (e) and (f) show frequency histograms of pore diameter and (g) and (h) show frequency histograms of interpore distances of anodized layers formed in first and second steps of anodization respectively. The samples have been anodized in 0.3M Oxalic acid bath, maintained at temperature of 10 °C, constant voltage of 40 V for 8 hours in first step and one hour in second step.

It may be easily observed from the Fig. 4.7 that substantial improvement in the ordering of pore morphology takes place, and is evident from both, the top view as well as the cross-sectional view. Fast Fourier Transforms (FFTs) of the top view images (insets in (a) and (b)) clearly confirm the difference in degree of ordering. A diffused ring with a broad halo appears in the case of single step anodized sample (Fig. 4.7a) while six distinct and bright spots are visible in second step anodized sample (Fig. 4.7b).

The frequency histogram for pore diameter in case of first step anodized sample is broadly distributed and appears like a normal distribution and the peak is at about 32 nm value while in case of second step anodization, the histogram is showing a single peak at about 47 nm mark which is significantly higher than the intensity of the second higher peak within the histogram.

The frequency histogram for inter-pore distances in case of first step anodized sample is broadly distributed and appears to be like a normal distribution while in case of second step anodization, the histogram is having almost a single peak at about 100 nm mark, indicating near-perfect ordering.

Table 4.3: Statistical comparison of pore morphology in different steps of anodization.

Step of anodization	Mean pore dia.	Standard deviation.	Size of population	Median
First step	48.11	9.32	75	47.99
Second step	48.09	5.49	100	47.96
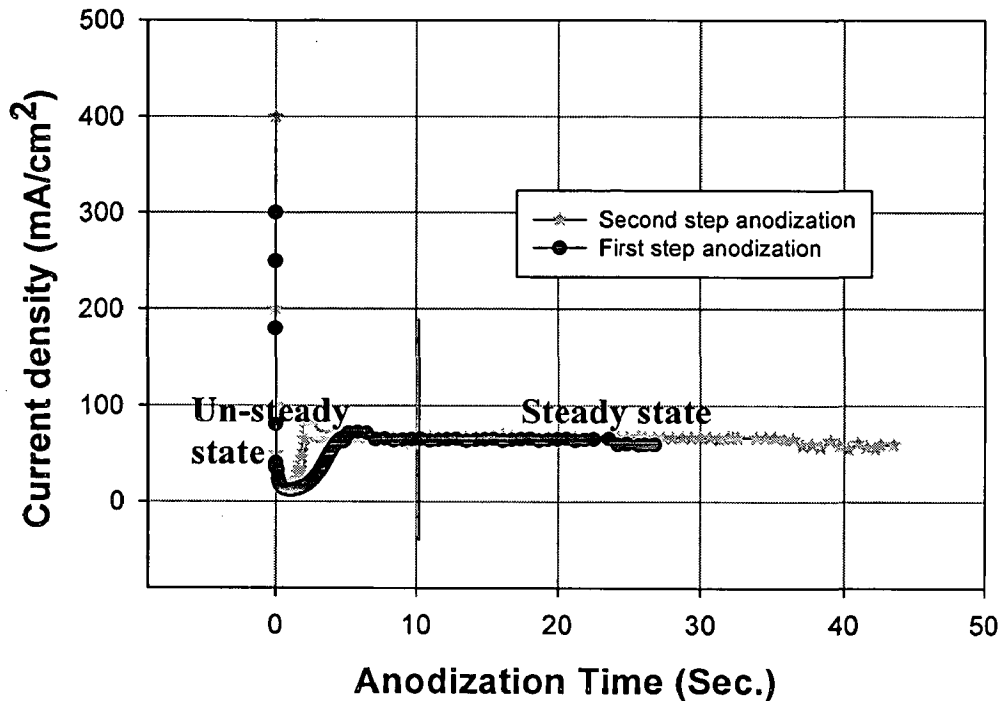
Fig. 4.8: Typical current density-time curves for initial period of both the steps of a two-step anodization process under constant-voltage mode at a voltage of 20 V and in a 15 wt% sulphuric acid bath, maintained at 24 °C.

Figure 4.8 shows typical current-time curves for both the steps of a two-step anodization operation under constant-voltage mode at a voltage of 70 V and in a 5 wt.% phosphoric acid bath, maintained at 24 °C. First and second step of anodization are plotted separately in the Fig. 4.8. However, no significant difference can be observed in the steady state regime of the curves. The current is very high as soon as the power is switched on. This is due to high conductivity of pure aluminium. The anodic oxidation forms oxide film, which increases resistance resulting in fast decrease in the current. This

decrease continues till the onset of pore formation occurs due to electric-field assisted oxide dissolution. At this stage the current begins to increase, due to decrease in resistance as oxide layer thickness reduces in front of the initiating pores. This fluctuation comes to a halt when a dynamic equilibrium is established between oxide formation and dissolution. The current becomes steady and growth of pores continues maintaining constant barrier layer thickness, which is a function of voltage mainly but is also affected by temperature and concentration of the acid.

Figure 4.9 shows typical voltage-time curves for both the steps of a two-step anodization operation under constant-current mode. The anodization was carried out in 5 wt% phosphoric acid at constant current density of 10 mA/cm^2 for about 300 seconds. The voltage first rises to a certain maximum value till oxide barrier layer formation and thickening continues. The voltage decreases as soon as the nucleation of the pores begin and they grow. This growth causes the voltage value to reach to a minimum value due to decrease in the insulating oxide layer thickness. The formation and dissolution of the oxide barrier layer takes place simultaneously and then any variation from the equilibrium condition causes a voltage rise again which becomes almost constant. This indicates an establishment of dynamic equilibrium between oxide formation and dissolution processes. It may be observed from the Fig. 4.9 that the voltage – time profile of second step anodization lies below that of the first step anodization. This is because the pore initiation in second step of anodization takes place earlier than that in the first step
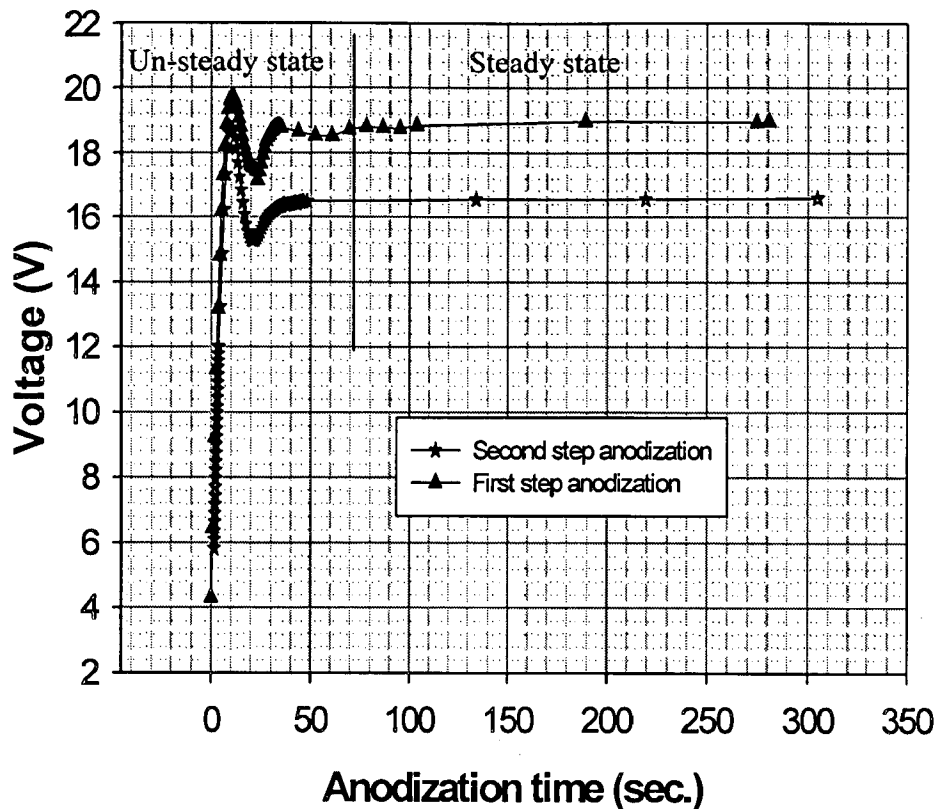
Fig. 4.9: Typical voltage-time curves for both the steps of a two-step anodization process under constant-current mode.

4.3 EFFECT OF ANODIZATION PROCESS VARIABLES

4.3.1 Anodization in Phosphoric acid bath

Anodization of al uminium has been carried out under a given condition of constant voltage / constant current mode of power supply and for a given concentration of phosphoric acid in the first step of anodization and the anodized layer has been dissolved in a mixture of phosphoric and chromic acid. The ordered patterned surface thus formed, has further been anodized under the same condition of power supply in the second step of anodization to obtain well-ordered pore structure in anodized alumina as described in Chapter-3. These two-step anodization experiments have been carried out in phosphoric acid bath with variation of the process parameters like applied voltage/current, temperature, concentration and pH of the electrolyte on both pure and commercial aluminium substrates. The results are given in the following subsections.

127

4.3.1(a)   Anodization of Pure Aluminium (PA)

(i) Effect of voltage

Both the steps of the anodization have been conducted in 5 wt. % phosphoric acid bath for different voltages viz. 40 V, 80 V, 120 V, 160 V and 200 V, using constant voltage mode of power supply. The anodization for the first and second steps has been carried out for one hour and 30 min respectively. In both the steps, the current density at a given constant voltage shows initially an unsteady behaviour before attaining a steady state value as already shown in Fig. 4.8 in the previous section. On increasing voltage, the steady state current density increases with the increase in voltage as shown in Fig. 4.10. The variation can be taken as an exponential.
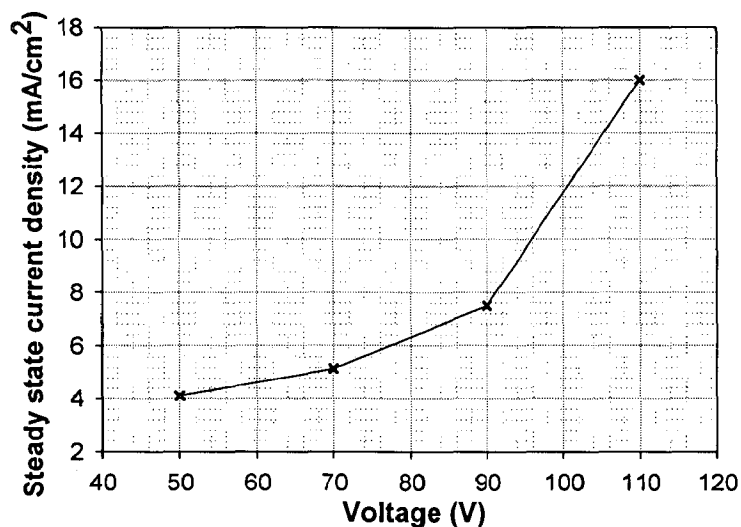
Fig. 4.10:   Variation of steady state current density with Voltage.

The pore diameter and the interpore distance have been estimated by taking an average of about 70 measurements from the SEM micrographs of the anodized layer using image analysis software. It can be seen from Fig. 4.11- 4.12 that the interpore distance and the pore diameter increase almost linearly with increasing voltage. However, with increasing voltage, the increase in interpore distance is relatively higher compared to that observed for pore diameter and the slopes of the lines are accordingly different.

These experimental results have also been compared with the corresponding theoretical values calculated from the empirical relationship given in section (Eq. No. 2.1, chap.-2) It may also be observed that interpore distances are on the higher side than the theoretical values for voltage up to 80 V and on the lower side for voltages on and above 120 V.
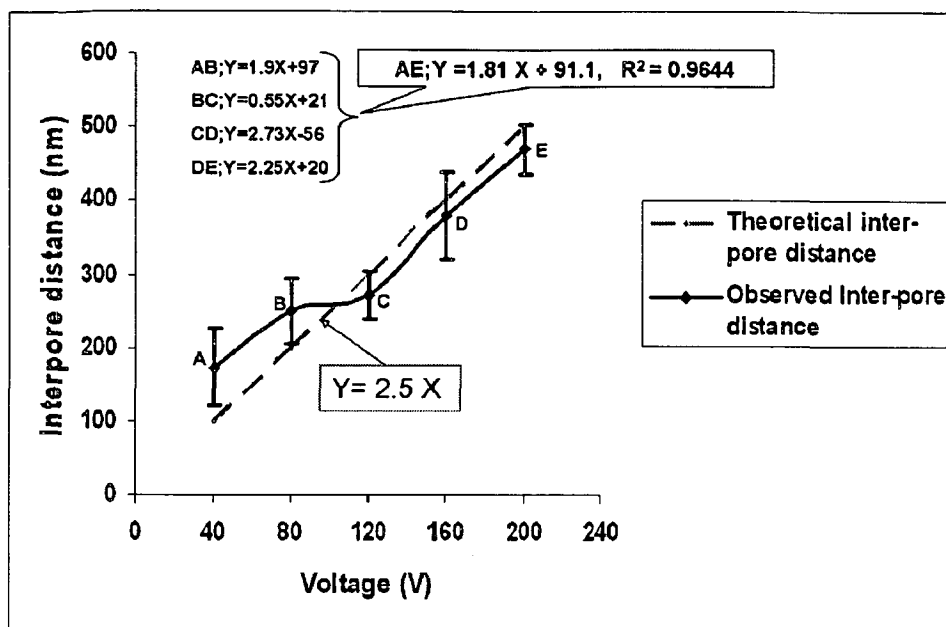
Fig. 4.11: Graph showing variation of interpore distance with voltage and comparison of theoretical and observed (experimental) values in case of pure aluminium substrates.

The observed inter-pore distance line 'AE' is having slope given by its trend line as

$Y = 1.8125 \, X + 91.1 \ (R^2=0.9644)$

The small segments of the line have slopes given by the following respective equations;

AB; $Y = 1.90 \, X + 97$;

BC; $Y = 0.55 \, X + 205$;

CD; $Y = 2.72 \, X - 56$;

DE; $Y = 2.25 \, X + 20$;

While the theoretical inter-pore distance straight line has the slope, given by the equation,

$Y = 2.5 \, X$

Table 4.4: Graph showing standard deviation of interpore distances with voltage.

S. No.	Voltage (V)	STD. DEVIATION OF INTERPORE DISTANCE (nm)
1	40	53.24
2	80	44.31
3	120	31.99
4	160	59.12
5	200	34.29
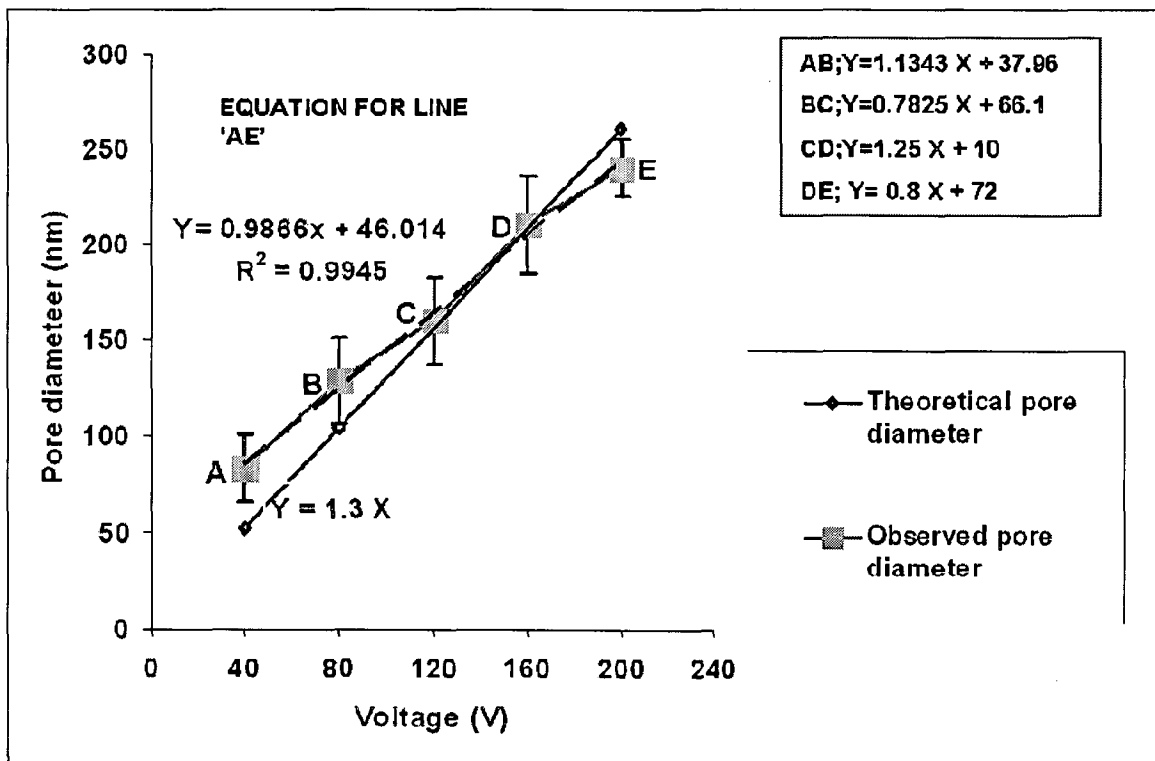
Fig. 4.12: Variation of pore diameter with voltage and comparison of theoretical and observed (experimental) values in case of pure aluminium substrates..

The small segments of the line have slopes given by the following respective equations;

AB = 1.1343 X + 37.96

BC = 0.7825 X + 66.1

CD = 1.25 X + 10

DE = 0.80 X + 72

130

SEM micrographs of the anodized layer obtained at various cell potentials have been taken and the frequency distribution of interpore distance has been plotted as a histogram. Fast Fourier Transform (FFT) of the images using image analysis software has been carried out and presented as insets in Fig. 4.13.
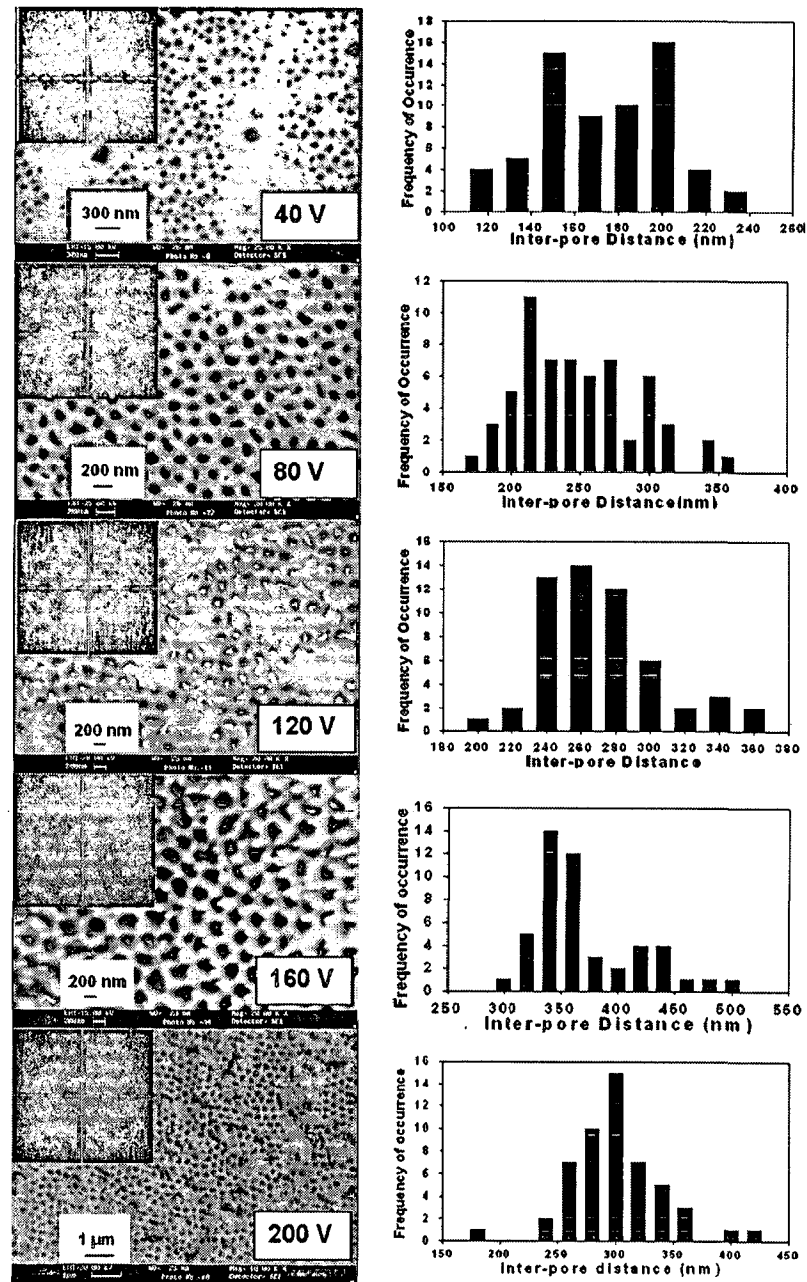
Fig. 4.13: Effect of formation voltage on pore ordering in case of pure aluminium substrates.

It may be observed that non-uniform interpore distance is obtained when formation voltage is 40 V. The frequency distribution has two peaks showing irregularity of pore distances and hence FFT shows diffuse type of ring indicating disordered pore structure. In the anodized layer formed at cell potential of 80 V, pores on the surface are distributed more regularly than that obtained at 40 V and ordered small domains of hexagonal arrangement of nanopores are visible. As a result, the histogram although asymmetric has a single peak and there is a relatively sharper ring with a broad halo around it in FFT image, indicating domains separated by disordered region. When the cell potential is increased to 120 V, the histogram is more symmetric and its range is also becoming relatively smaller with frequency dropping sharply and the FFT image shows a sharper ring with relatively reduced halo, indicating larger domain size and smaller disordered region between the domains. From the sharper FFT image corresponding to 160 V, it may be concluded that the size of the ordered domains has increased but still the histogram is asymmetric with a persistent tail. When the sample is anodized at 200 V, the FFT image consists of the sharpest ring structure. The FFT image shows that the number of domains and boundaries between them is limited. The ordering of pores in the nanoporous structure takes place by increasing domain size with increasing voltage and by reduced region of disordered boundary between the domains. The best ordering is obtained at the highest voltage of 200 V used in this investigation with phosphoric acid bath for pure aluminium samples.

If anodization is carried out at voltages higher than that required for the self-ordering, cell structure becomes defective and consists of broken and burnt cell walls due to excessive current densities and heat generation. A large volume expansion followed by cracking with a bursting noise can occur. Typical defective structures are shown in Fig. 4.14 for PA, which are the results of anodization carried out at 210 V for PA.
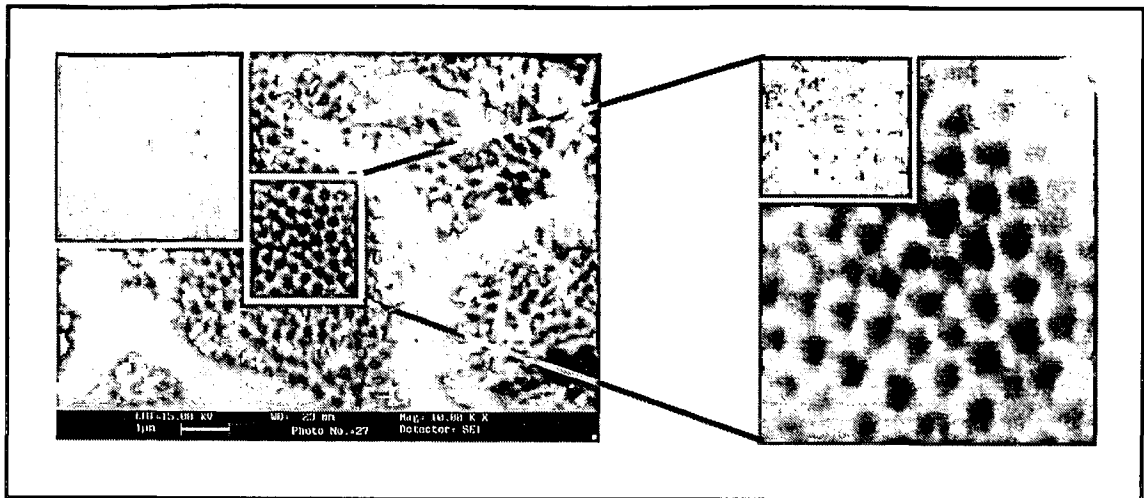
Fig. 4.14: Evidence of (a) discrete broken cells in the sample (PA) anodized at 210 V, (b) an enlarged view showing better ordering and lesser defects in FFT inset.
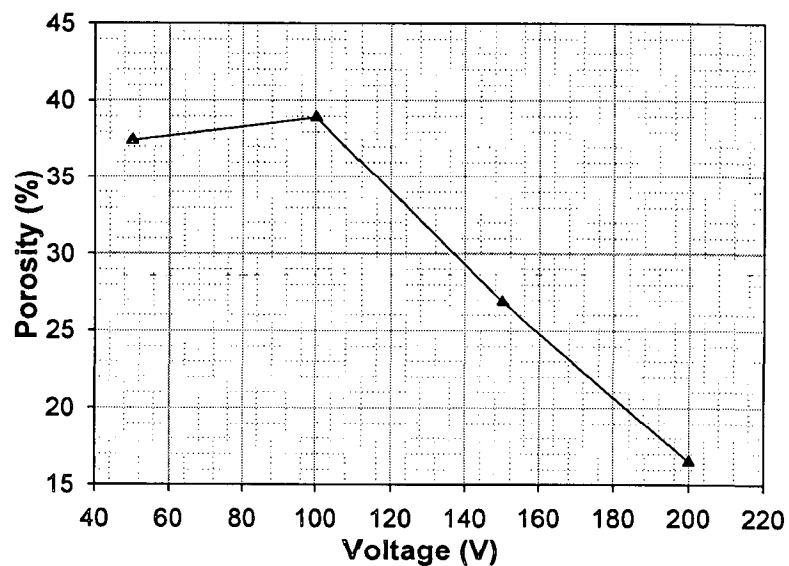
Fig. 4.15: Graph showing variation of porosity with voltage for anodized alumina layers subjected to anodic oxidation at 50V, 100 V, 150 V and 200 V in 5 wt.% phosphoric acid for one hour.

The variation of porosity with voltage is plotted in Fig. 4.15. The porosity of the anodized surface plays a major role in deciding its application in tribological behaviour; therefore, a prior estimation of such factor is an essential to anticipate its engineering performance. It can be seen that from the figure that there is a small change in volume

fraction of porosity till 100 V but beyond this voltage, the extent of porosity decreases almost linearly till 200 V, the highest voltage investigated. The porosity variation observed from about 37.43 % to a lower level of 16.5 % when voltage changes from 100 to 200 V.

(ii)   Effect of Temperature

The variation of steady state current density with increasing temperature of the bath at a given voltage of 150 V is shown in Fig. 4.16. The steady state current density increases exponentially as temperature increases from 10 to 30 °C over which the measurements have been made..   Increasing temperature is equivalently taken as increasing the aggressiveness or decreasing the pH of the electrolyte in most of the cases. Increasing temperature at fixed voltage increases current density exponentially and these results are plotted in the Fig. 4.16. This temperature effect results in soft, more porous and less thick PAAO films with a simultaneous decrease in barrier layer thickness.
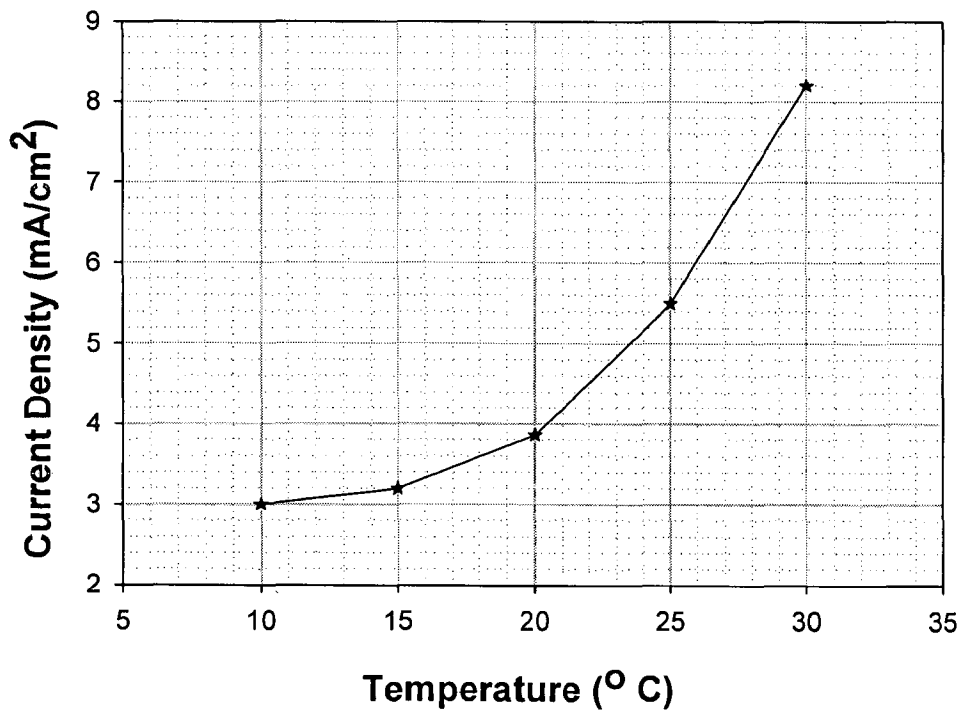
Fig. 4.16:   Effect of temperature on steady state current density in 5 wt. % Phosphoric acid bath, at 150 V, 293 K.

Hence anodization is conducted at low temperatures for obtaining thick, hard and compact films for tribological and other engineering applications requiring hard oxide films (also called hard anodization). Hardness also increases with decrease in porosity

due to small pore diameter and bigger cell diameter as a result of low temperature and high voltage as reported by many researchers. Better pore ordering can be obtained at lower temperatures while keeping other process parameters unchanged.

The variation of barrier layer thickness with temperature has also been observed as can be seen from the Table 4.5.

Table 4.5:   The variation of barrier layer thickness with temperature

Sl. No.	Barrier layer thickness (t_b) (nm)	Temperature (°K)
1	178	280 (7°C)
2	110	288 (15°C)
3	48	298 (25°C)

3 wt.% phosphoric
acid, 150 V, 293 K
Porosity 12.86 %

5 wt.% phosphoric
acid, 150 V, 293 K
Porosity 30.78 %

7 wt.% phosphoric
acid, 150 V, 293 K
Porosity 44.56 %
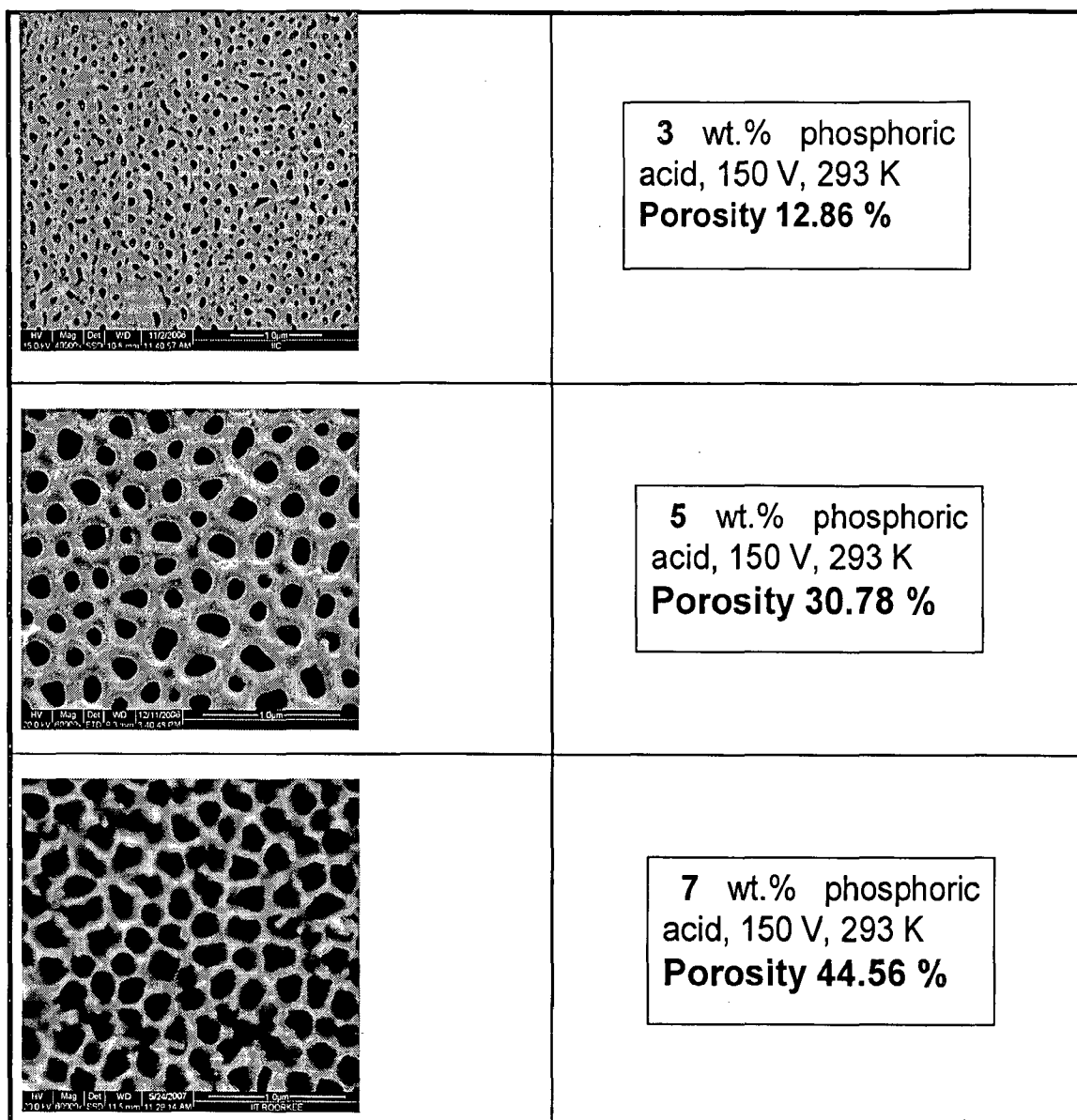
Fig. 4.17:   SEM micrographs showing morphologies of porous anodic alumina samples prepared in baths having various concentrations of phosphoric acid (a) 3 wt. % , (b) 5wt.%, (c) 7 wt. %.
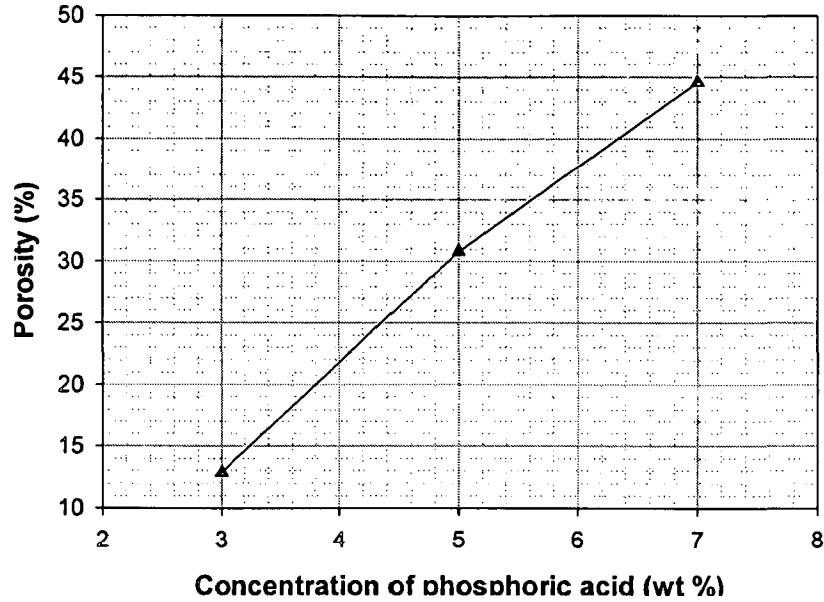
Fig 4.18: Graph showing effect of electrolyte concentration on porosity.

From the Fig. 4.17 and 4.18, it is evident that pore diameter and porosity increases with the increase in concentration of the phosphoric acid electrolyte. Pore shapes also appear to be changing from circular / elliptical at low concentration to hexagonal up to the corners of the hexagonal cell. (i.e., up to the triple point, where three adjacent cells appear to meet) at higher concentration due to increase in dissolving power of the electrolyte. Pores appear to be opening at the top, i.e. pore diameter is slightly bigger at the top surface as compared to that at the slightly lower region and is minimum at the bottom due to different time periods of exposure in the aggressive solution. This fact can be observed either in the longitudinal cross section or by comparing the Secondary electron (SE) and backscattered electron emission (BSE) imaging modes of the FE-SEM as shown in the Fig. 4.19 below.
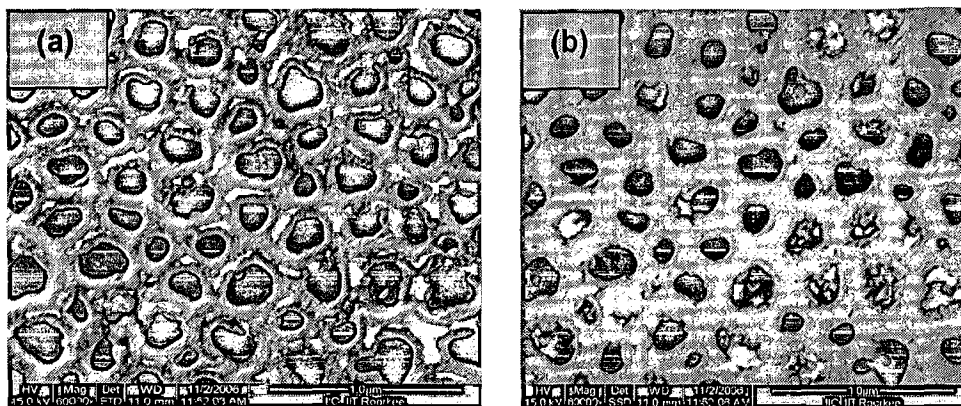
Fig. 4.19:   Comparative views of S.E. (Secondary electron) emission scanning mode image on the left (a) and B.S.E. (Back Scattered Electron) emission mode images of the PA sample on the right side (b), anodized in 5 wt.% Phosphoric acid at 150 V at room temperature.

It is evident that BSE (Back Scattered Electron) emission gives view of the sample from slightly lower region (few microns), thus in the BSE mode, slightly smaller pore diameters are observed compared to that of from SE (Secondary Electron) mode, as the image is from slightly lower region as compared to SE mode, where image is from the top surface. This observation of slightly inverted conical pores at the top surface can be easily observed in highly concentrated electrolytic solutions, while in dilute solutions, this small variation in size is difficult to note and thus may be ignored.

With the increase in concentration of the electrolyte, the CD has been found to increase almost linearly in this investigation, hence, it may be deduced that with the increase in acid concentration of the bath, at fixed voltage, the increased CD results in increased pore diameter and interpore distance.

(iv)   Effect of pH

The pH level of the electrolyte has got a distinctive role towards controlling the rate of dissolution of the oxide films. The higher value of pH, lowers the dissolution and hence associate the effect of voltage. However, the pH variation has an interrelationship with the concentration variation of the electrolyte. The pH of the electrolyte decreases with the increase in the concentration of the acid in the bath electrolyte. The results of concentration of the electrolyte have already been presented and suitably discussed in the

previous subsection 4.3.1 (a) (iii) and therefore no further discussion has been made in this section.

(v) Effect of anodization time

The oxide layer thickness depends on anodization time for a given constant current density. The product of CD. and time gives the quantity of charge passes through the circuit and this is prime cause for oxide formation. Table 4.3 shows the results of effect of time on oxide layer thickness when 5 wt. % phosphoric acid bath is used for anodization at 20 C.

Table 4.6: Effect of time on oxide layer thickness.

Sl. No	Time duration (minutes)	Oxide layer thickness (µm)	Growth rate (µm/minute)
1	10	0.8	0.08
2	60	5	0.0833
3	300	30	0.1

4.3.1(b)   Anodization of Commercial Aluminium

(a) Effect of voltage

In this case also both the steps of the anodization have been conducted in 5 wt. % phosphoric acid bath for different voltages viz. 40 V, 70 V, 100 V, 130 V and 160 V, using constant voltage mode of power supply. The first and the second steps have been carried out for one hour and 30 min respectively. Figure 4.20 shows the variation of the observed interpore distances (nm) with increasing voltage (V) after second step anodization. It can be seen from the Fig. that in this case also, the interpore distance increases almost linearly with increasing voltage, which matches with the earlier results of pure aluminium substrate presented in the previous section (viz. Fig. 4.11 and 4.12). The interpore distance measured from the micrographs as well as calculated theoretically from the empirical relationship, are plotted simultaneously in Fig. 4.20. It can be seen from the Fig. that the experimental plot follow closely the theoretical graph with an over estimation of the experimental value at 40 V and under estimation at 100 V. However, the theoretical and the experimental values match well at 70, 130 and 160 V.

It may also be noted that observed interpore distances are greater than the theoretical values between the voltage range from 40 V to 70 V with a difference between the two values at a given voltage decreases upto 70 V at which the values are identical. The observed values continues to decrease from the theoretical values till 100 V and then starts to rise upwards up to a voltage value of 130 V in the midway they overtake the theoretical values at about 118 V. The slope of the observed interpore distance values once again falls till the two lines coincide at a voltage value of 160 V.
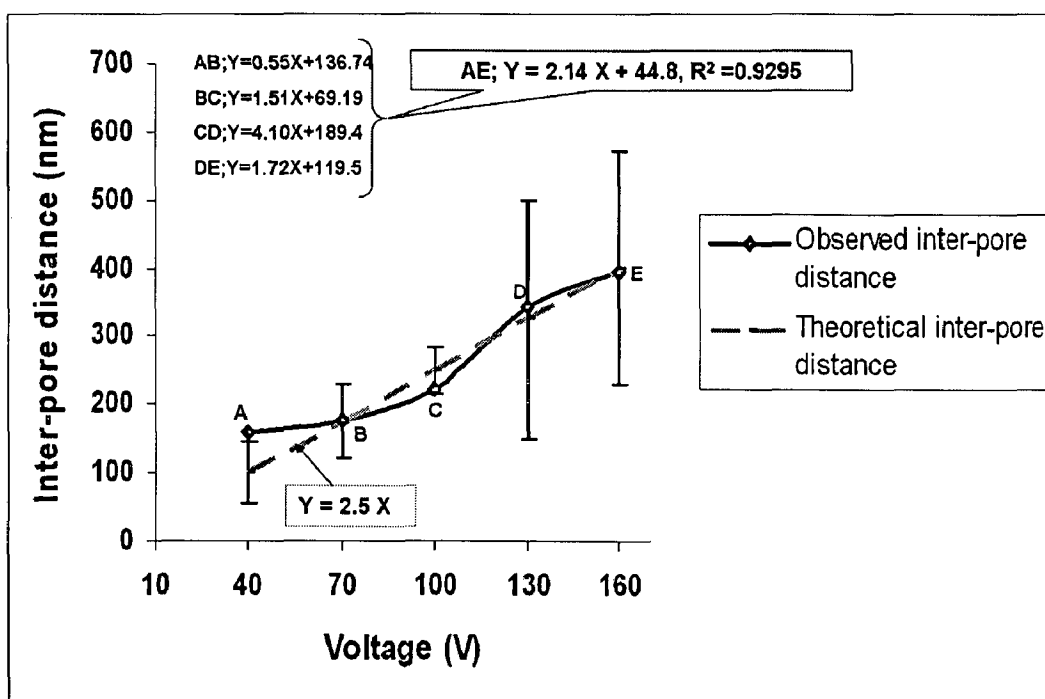
Fig. 4.20: Graph showing variation of interpore distance with voltage and comparison of theoretical and observed (experimental) values in case of commercial aluminium substrates.

Figure 4.21 shows the variation of the observed pore diameters (nm) with increasing voltage (V) after second step anodization. It can be seen from the Fig. that in this case also, the diameters increase almost linearly with increase in voltage, which matches with the earlier results of pure aluminium substrate, presented in the previous section (viz. fig. 4.12). The observed pore diameters are lower than that of theoretical values at all the

voltages except 130 V at which the pore diameter is slightly above than the theoretical value.
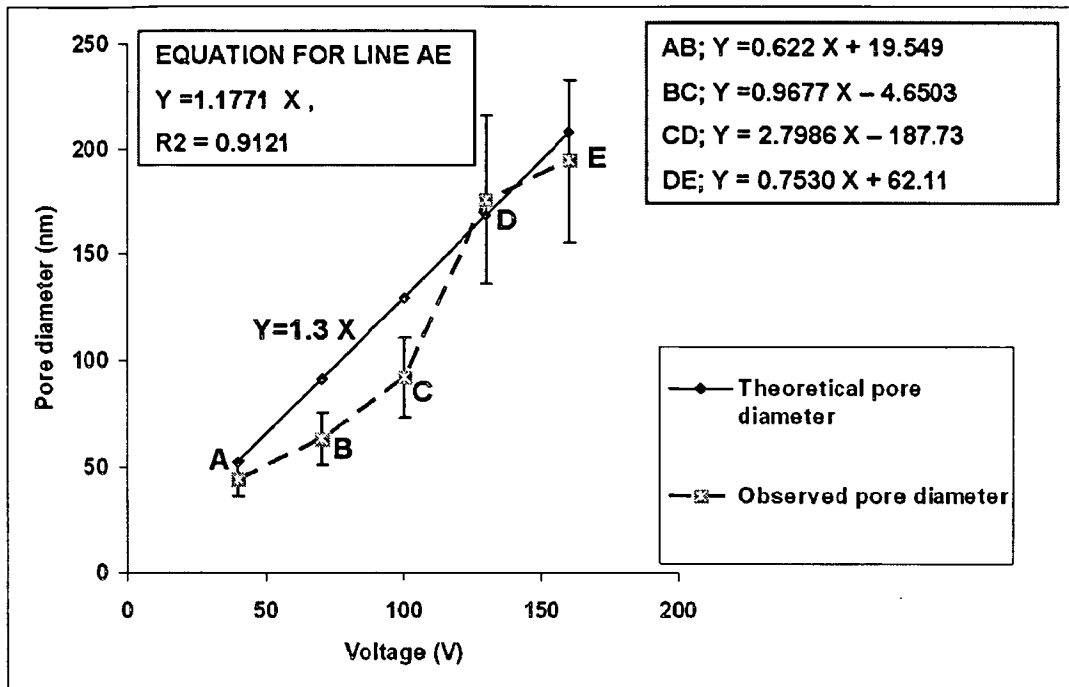
Fig. 4.21: Graph showing variation of pore diameter with voltage and comparison of theoretical and observed (experimental) values in commercial aluminium substrates.

SEM micrographs along with FFT images and the frequency distribution histograms for the interpore distance in the porous anodized layers formed at different cell potentials using commercial aluminium substrates are shown in Fig. 4.22. It may be observed that the histogram for the 40 V is asymmetric correspondingly showing diffused FFT image pattern. The intense frequency bars lie in the lower side of the range of interpore distances measured, showing the pore arrangement is far from well-ordered. The histogram for 70 V shows the peaks are clustered in the lower interpore distance in the range. FFT image of the pore arrangement is also diffused showing the disorder in the pore pattern. The shift of high frequency bar for 100 V towards the center of the interpore distance range is an indication of the pore ordering initiation. A substantial improvement in pore ordering can be found with the increase in voltage for anodization i.e. from 100 V to 160 V. The effective range of interpore   distance has decreased considerably for 160

V and the intense peak lies almost at the middle of the range showing the pore ordering is best corresponding to this voltage value.
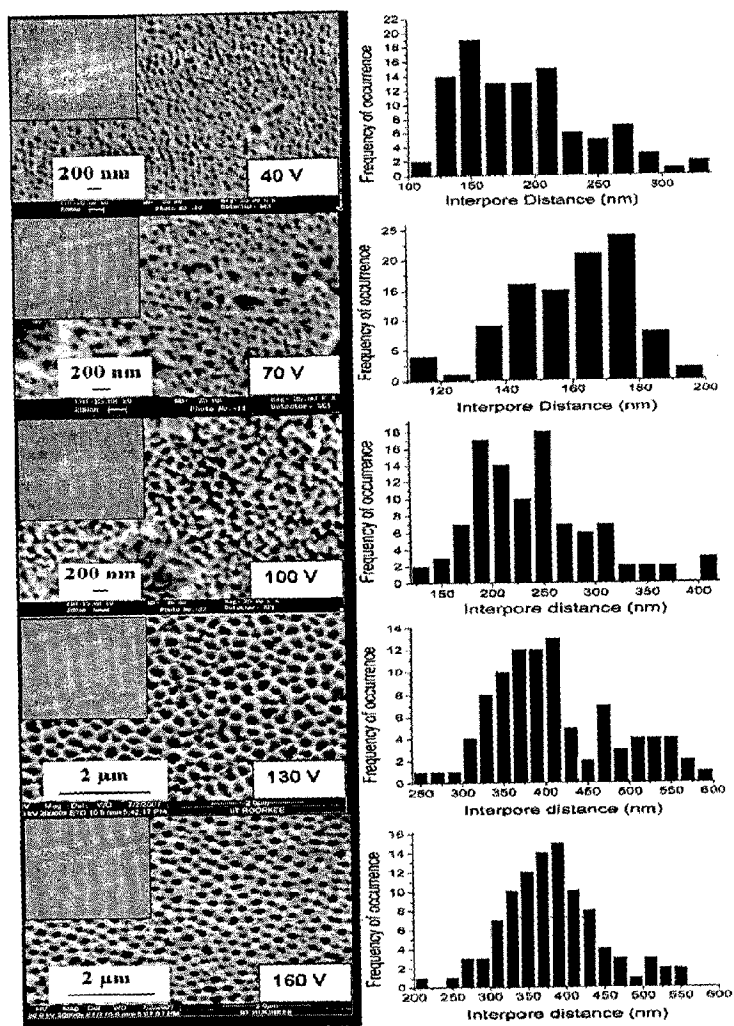
Fig 4.22: Effect of formation voltages on self-ordering of porous anodic alumina structures based on commercial aluminium.
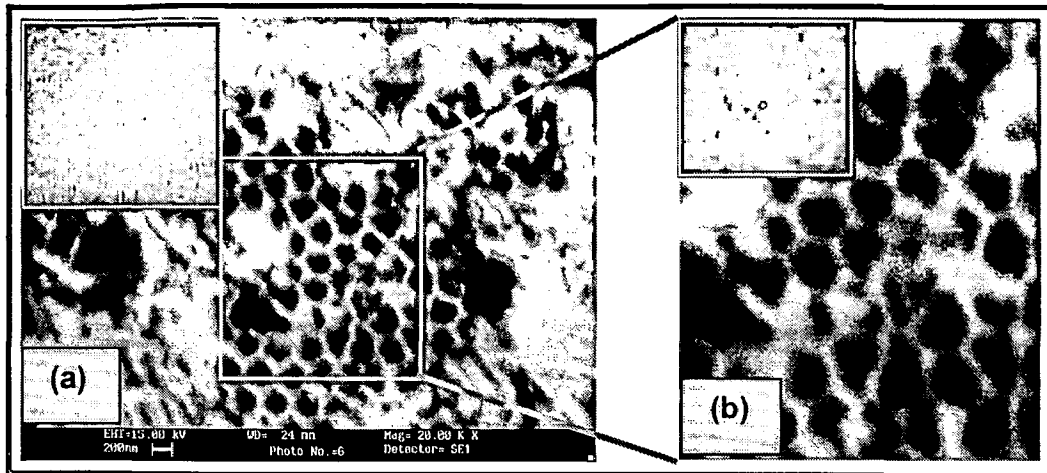
Fig.4.23: Evidence of discrete broken cells in the sample (Commercial Aluminium) anodized at 200 V (a) is shown enlarged in (b) as an enlarged view showing better ordering and lesser defects in FFT inset.

If anodization is carried out at voltages higher than that required for the self-ordering, cell structure becomes defective and consists of broken and burnt cell walls due to excessive current densities and heat generation. A large volume expansion followed by cracking with a bursting noise can occur. A typical defective structure as shown in fig. 4.23 is the result of anodization carried out at 200 V. On the other hand at very low voltages, low expansion takes place and disordered structures are obtained. Moderate volume expansion of 1.3 times for anodization at 200 V is reported to be the best for obtaining hexagonal self-ordered pore structure on pure aluminium substrate in phosphoric acid electrolyte.(reference). This matches exactly with the observation in the present investigation on pure aluminium. The corresponding voltage for obtaining self ordered pore structure in commercial aluminium substrate is 160 V.

Fig. 4.24 shows variation of percentage of porosity in PAAO on commercial aluminium substrate with anodization voltage. It has been observed that porosity decreases with increase in the anodization voltage and the porosity decrease is maximum between 100 and 130 V.
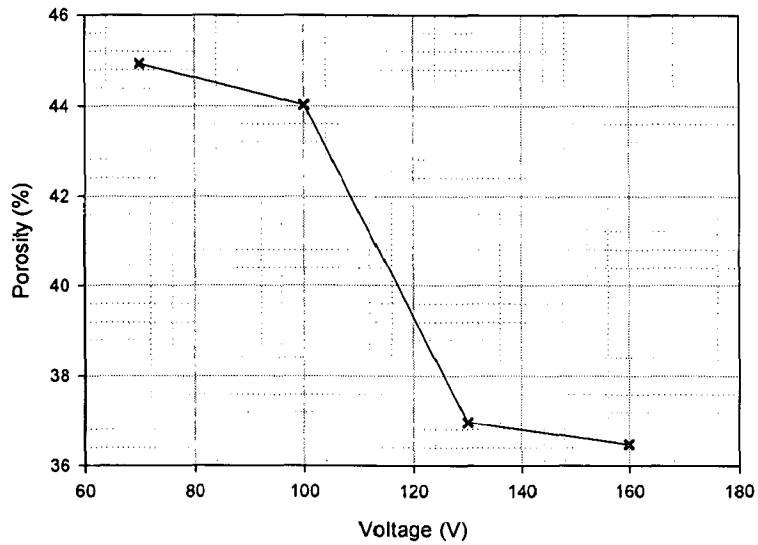
Fig. 4.24: Variation of porosity with voltage in commercial aluminium substrates.

Fig. 4.25 shows variation of steady-state current density with voltage in commercial aluminium substrates. It may be observed that the increase in current density is exponential with increase in voltage.
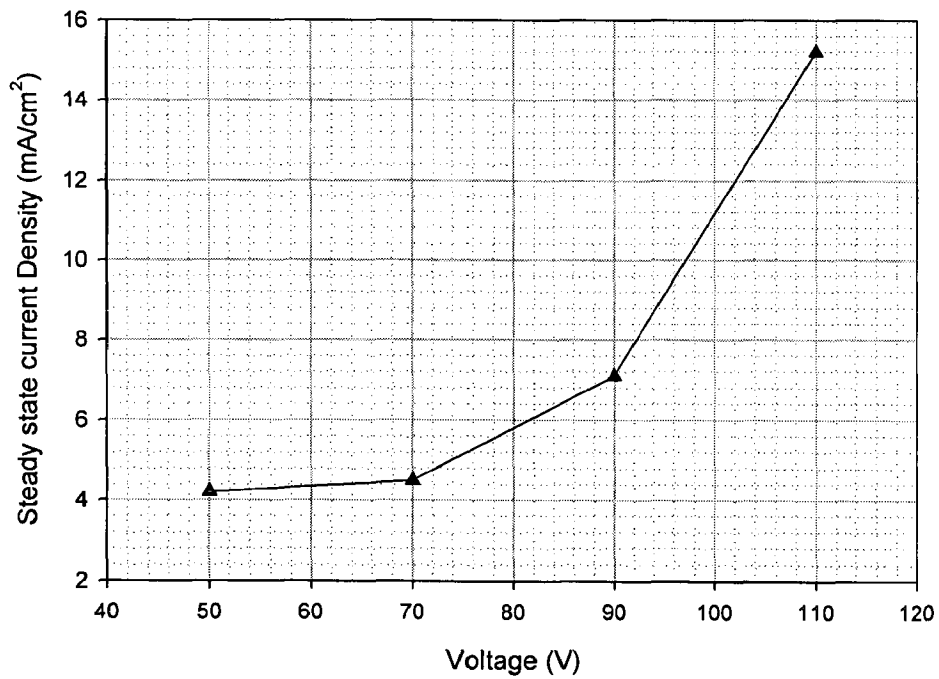
Fig. 4.25: Variation of steady-state current density with voltage.

144

(b) Effect of Temperature.

Table 4.7:   The variation of barrier layer thickness with temperature

SI. No.	Barrier layer thickness (t b) (nm)	Temperature (°K)
1	167	280 (5 °C)
2	124	288 (15 °C)
3	44	298 (25 °C)

However this undesirable voltage dependent increase (thicker barrier layers at higher voltages) can be countered by controlling the barrier layer thickness by placing the samples after anodization in 3-5 wt. % phosphoric acid at 60 °C for predetermined time period depending on final PAAO barrier layer thickness required. (However this chemical dissolution rate is not linear as the PAAO structure is having composition gradient, the inner portion is less prone to dissolution than outer portion)

4.3.2   Anodization in Oxalic acid bath

The anodization time during the first step anodization has a direct bearing on the final ordering that results in two step anodization. Therefore first step anodization for different time periods in oxalic acid electrolyte has been carried out. The anodizations of both the pure aluminium and commercial aluminium substrates have been done in 0.3 M oxalic acid electrolyte at 15 ° C at 40 V (constant voltage mode) of power supply. Investigations have been carried out mainly for the effect of time period of first step anodization on the degree of ordering in the anodized layer obtained by two- step anodization method using besides some regular investigations. The results are presented in two separate sub-sections in the following paragraphs.

4.3.2 (a)   Anodization of pure aluminium.

Figure 4.26 shows SEM micrographs of pore structures of anodized layers subjected to different time periods in the first step of anodization and same duration of one hour in the second step of anodization. so as to study influence of time in the first step on degree of ordering. Fig. (a) shows the resulting porous structure of a sample subjected to 1 hour in the first step and also 1 hour in the second step. It may be observed

that the FFT pattern is a sharp ring or multi-hexagon superimposed on each other, indicating that there are many
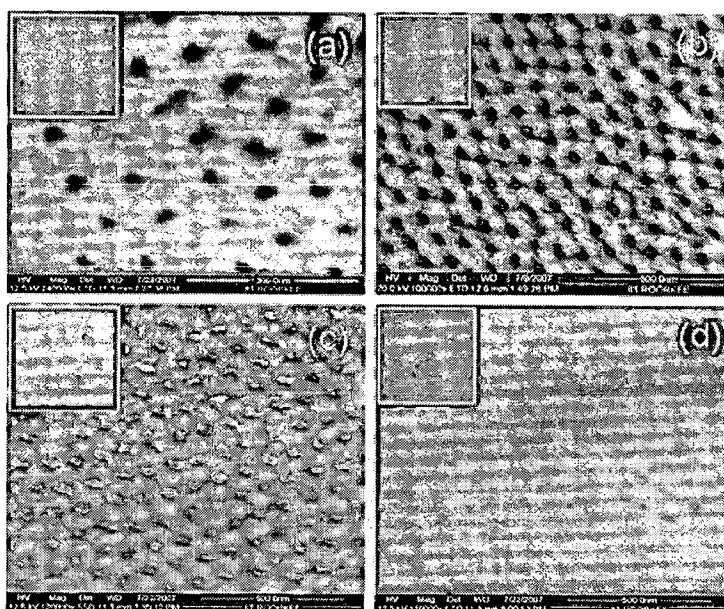
Fig. 4.26: SEM micrographs of PA obtained by two stage anodization in 0.3 wt.% oxalic acid at 15 ° C for (a) 1hour (b) 4 hours (c) 8 hours and (d) 12 hours in first step and for a same period of 1 hour in second step for all the cases. Inset in the micrographs show the FFTs of the respective pore structures.

ordered domains, having different orientation, while overall ordering is poor. The FFT pattern of the sample anodized for 4 hours in first step and 1 hr. in second step shows relatively sharper spots constituting hexagonal arrangement. The FFT pattern of the sample anodized for 8 hours in first step and 1 hr. in second step is also a sharp hexagon and the SEM image also resulted in well - ordered porous structure and the pores seem even more well ordered and regular shaped. Pore are found to have aligned in a series of parallel straight lines and their FFT image shows the appearance of hexagonal arrangement of bright spots at the corners of the hexagon and at the center.

The FFT pattern of the sample anodized for 12 hours in first step and 1 hr. in second step is again a sharp hexagon and the SEM image also resulted in the most well - ordered porous structure and the pores seem even better ordered and regular shaped and interpore distance is more regular. Fig. (d). It becomes evident that degree of ordering improves with increasing the anodization time but the improvement rate varies like a hyperbolic curve, i.e. initially the rate is very high which goes on decreasing with time and thus 8 hours time may be considered as the optimum time for getting well-ordered

146

pore structure in oxalic acid. The anodized surfaces have also been examined by AFM to reveal features. Figure 4.27 shows an AFM view of the of anodized sample subjected to 8 hours of anodization in the first step and 1 hour in the second step.
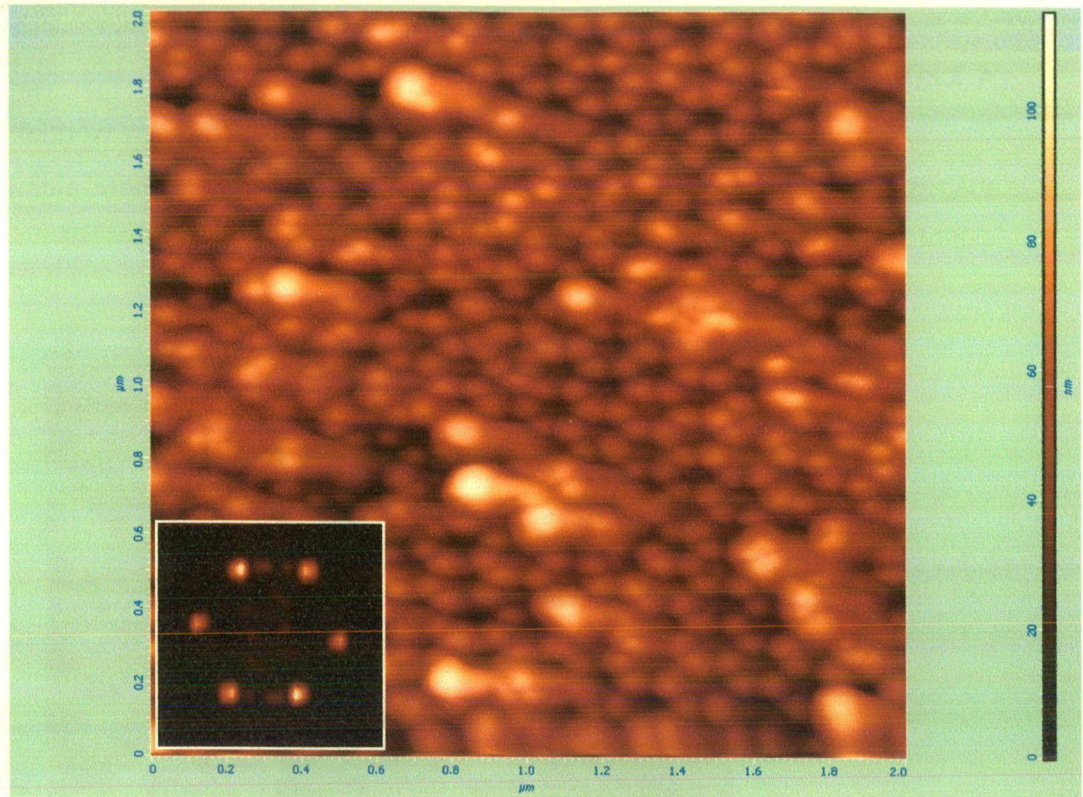
Fig. 4.27: A.F.M. view of the anodized sample subjected to 8 hours of anodization in the first step and 1 hour in the second step and inset shows its FFT.
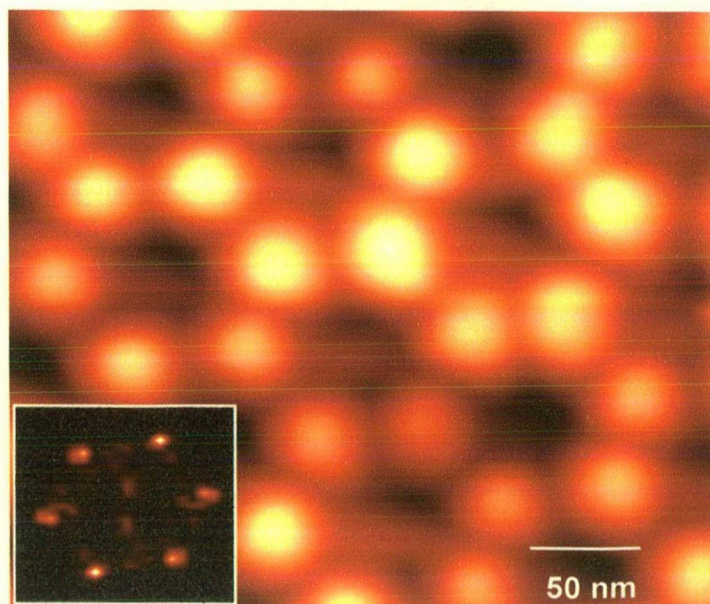
Fig. 4.28:   A.F.M. view at higher magnification of the PAAO subjected to 8 hours of anodization in the first step and 1 hour in the second step and inset shows its FFT.

4.3.2(b)   Anodization of commercial aluminium

The pore ordering in commercial aluminium has also been worked out and the microstructural results are found to be nearly same as that of pure aluminium based samples.
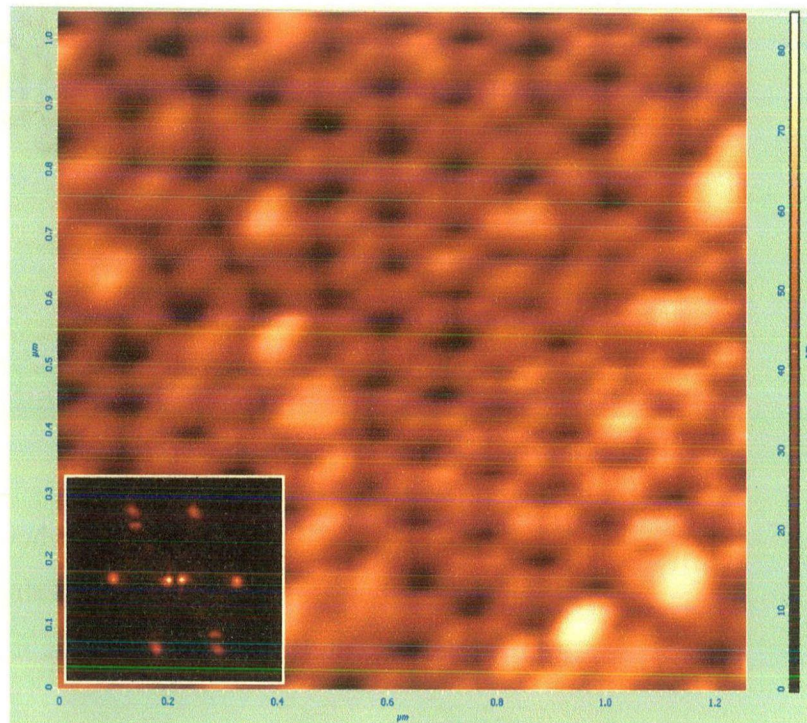
Fig. 4.29:   A.F.M. view of the anodized sample subjected to 8 hours of anodization in the first step and 0.5 hour in the second step and inset shows its FFT.

However, the degree of ordering achieved is more in the case of pure aluminium substrates, as can be observed by the FFTs of the AFM images obtained after anodization of both pure and commercial aluminium substrates at same voltage and duration of anodization (Fig. 4.29).

4.3.3 Anodization in chromic acid bath

Figure 4.30 shows the results of the first step anodization experiments conducted on pure aluminium substrates in 3 wt.% chromic acid bath without stirring, at 10 °C. Although pores are seen but they are aligned in some short channel like porous alumina structures.
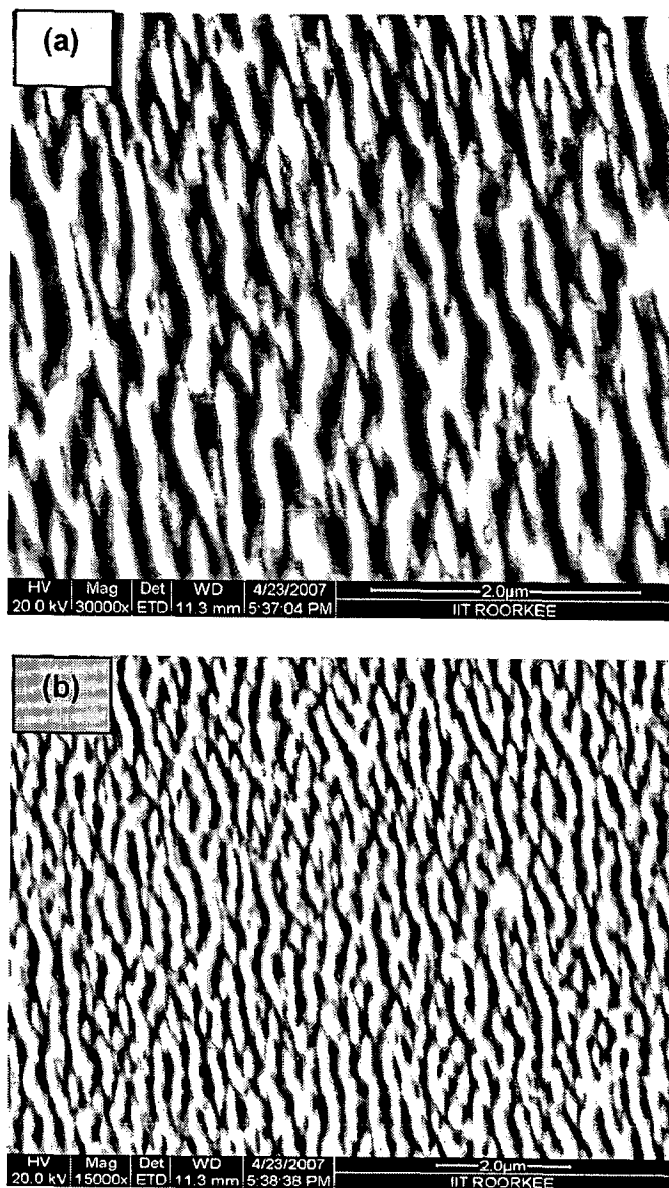
Fig. 4.30: A.F.M. view of the anodized sample subjected to 8 hours of anodization in the first step and 0.5 hour in the second step and inset shows its FFT.

149

4.3.4 Anodization in Sulphuric acid bath

Though a large number of experiments were conducted on sulphuric acid bath, but in most of the cases barrier layers structures or defective pore structures like channel shaped pores, micron size pores etc. were obtained. However, nanosized pores were obtained in 15 wt% acid bath maintained at 10 °C, at 25 V, in first step anodization conducted for twenty minutes. The average pore diameter and depth were found approximately as 33 nm and 50 μm respectively. The resulting structure has been shown in Fig. 4.31.
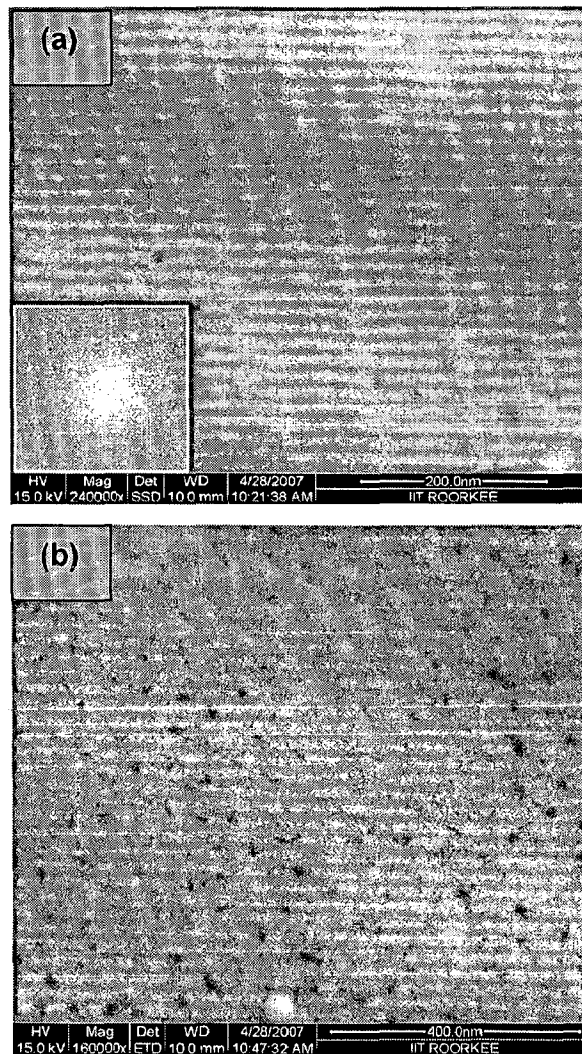
Fig. 4.31: SEM views of pore structures of alumina layers anodized for 20 minutes in first step in 15 wt% sulphuric acid bath maintained at 10°C, at 25 V.
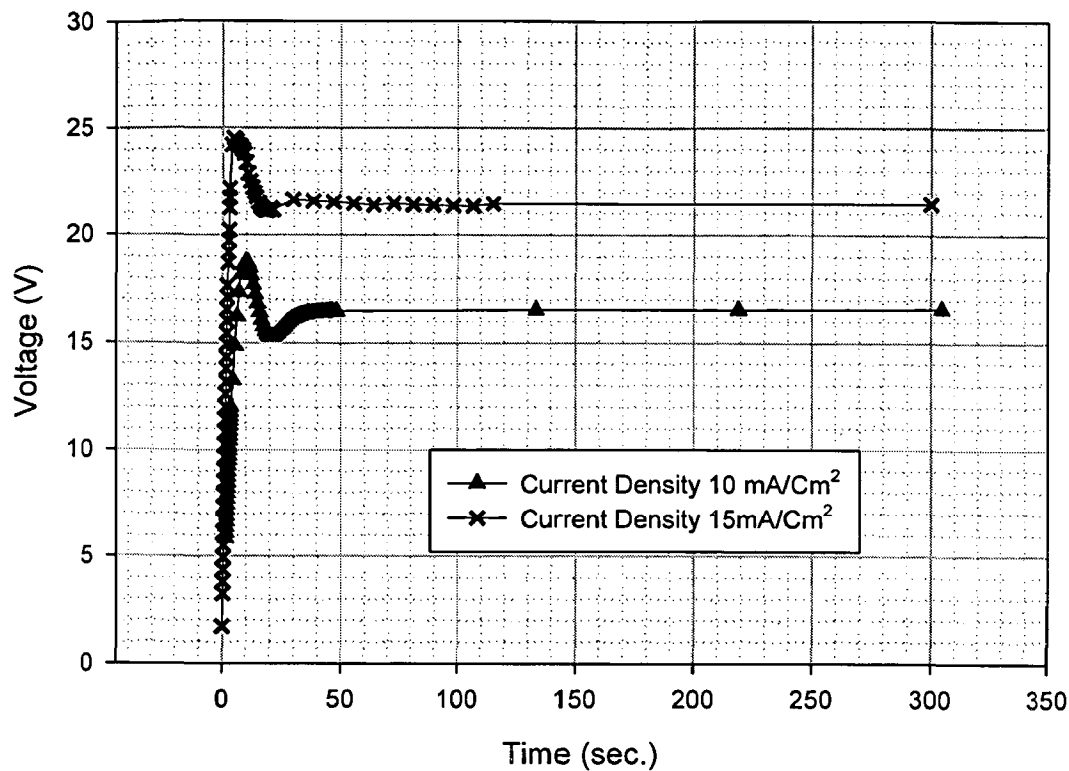
Fig. 4.32: Comparison of steady state voltage values for various constant current densities modes in first step of anodization conducted for 1 hr in an 5 % sulphuric acid bath maintained at 10 °C.

The shapes of the electrical transients i.e. voltage vs time and current density vs time curves for sulphuric acid bath were found almost similar as mentioned in chapter 2. However the repeatability of results in pore-structure were not found and it is observed that sulphuric acid bath is more sensitive to anodization process parameters as compared to other three acid baths. Fig. 4.32 shows a voltage-time curve for constant current density mode in first step of anodization conducted for one hour in a 5 % sulphuric acid bath maintained at 10°C. In order to show the dependence of steady state voltage to be attained on the current density, the anodization has been carried out for two CDs of the voltage-time curves shows that steady-state voltage values increases with the increase in current density, from about 16.2 V to 18.5 V for the CD of 10 and 15 mA/cm^2 respectively. This shows that anodization with higher CD leads to increased barrier layer thickness.

RESULTS AND DISCUSSION

(CNTs/CNFs growth within Porous Anodic Aluminium Oxide)

The CNTs / CNFs have been grown in Porous anodized aluminium oxide (PAAO) templates using acetylene as carbon precursor gas and ammonia as etchent / dilution gas by thermal chemical vapor deposition (thermal CVD) process. The PAAO templates were prepared by anodization in phosphoric, oxalic, chromic and sulphuric acid baths. In the synthesis, cobalt has been used as catalyst in most of the experiments as it has been found most suitable for the targeted results. Other catalysts viz. nickel, cobalt-nickel combination and transition metal oxide compound containing lithium (LiNi$_{0.5}$Co$_{0.5}$O$_2$ particles) have also been attempted. The influence of morphology and structure of PAAO templates and CVD process parameters on the growth and morphology of resulting CNTs/CNFs embedded PAAO nanocomposite thus produced have been presented in the following paragraphs, though, the first section (5.1) presents detailed results of a representative CNTs/CNFs sample, having average properties and elemental distribution, obtained as a result of the CVD. The findings shown in this example are common to most of the samples with slightly higher and lower values and hence all those results have not been repeatedly presented.

5.1 GROWTH OF CNT/CNF

Single Line scan (EDS) from point 1 at the top to point 2 along the slanted fractured surface of PAAO template with CNT/CNF grown in the pores using cobalt catalyst, as shown in Fig. 5.1(a), clearly indicates the presence of cobalt catalyst deep inside the pores by the pink colored line (bottom most).
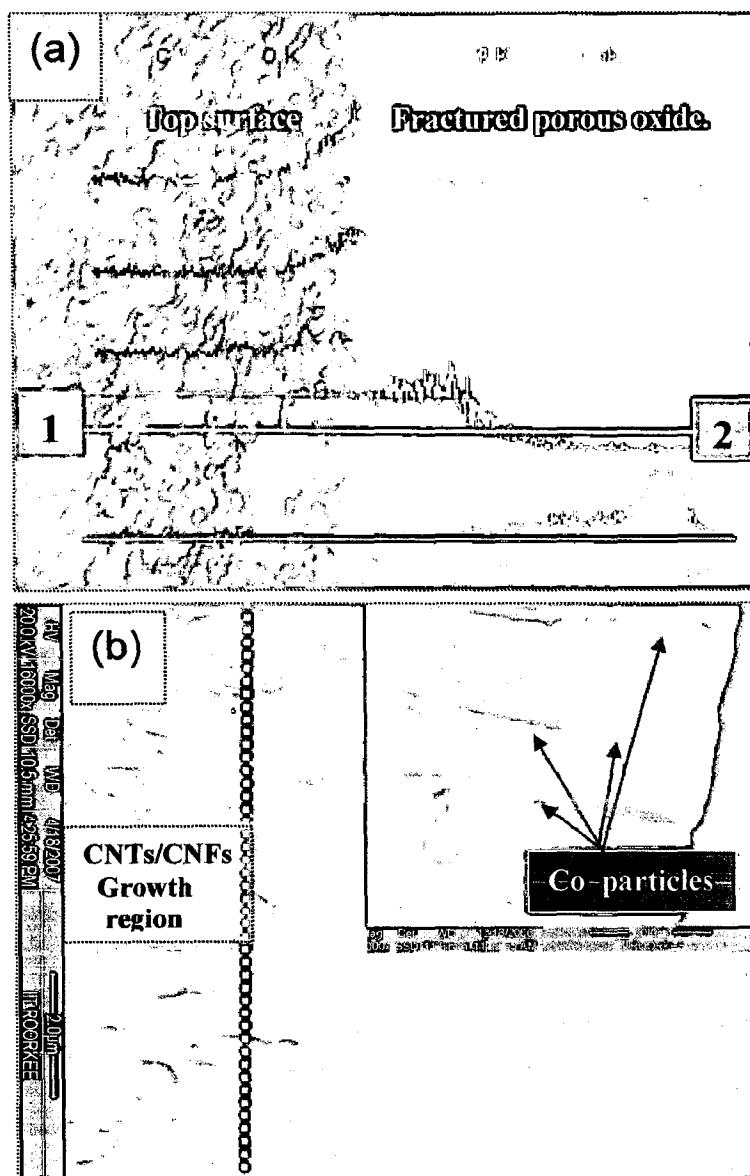
Fig. 5.1: FE-SEM micrograph of (a) Top surface of PAAO template along with transverse fractured surface (slanted) with CNT/CNF grown in the pores using cobalt catalyst and EDS line scan along 1 at the top to point 2 on the fractured surface. (Color Code: Pink-cobalt, cobalt blue–phosphorus, blue- aluminium, green – oxygen and red-carbon) (b) the fractured surface at higher magnification showing CNT/CNF growth, often starting from a catalyst stuck midway in the pores.

154

The other elements indicated in the line scan are carbon, oxygen, aluminium and phosphorous. The carbon nano-tubes/fibres are seen growing at a distance of about 25 % of pore depth from the top surface. EDS also indicates this growth by the presence of peaks in the red line (red colour line indicating presence of carbon) at corresponding locations, as shown in Fig. 5.1 (a). This growth of CNTs/ CNFs from a point above the bottom of the pore is due to the presence of small cobalt catalyst particles, stuck at the pore walls, instead of getting deposited right at the pore bottom as shown in the inset in Fig. 5.1 (b). It may be observed from the closer view of the pink line (which is an indicator of the cobalt) in the fractured porous oxide region, that cobalt particle's presence is indicated by shallow peaks in the line, all along the pore walls, showing scattered or sparse distribution/sticking of catalyst particles. Presence of oxygen (green coloured line) and aluminium (blue coloured line) is also evident in the figure due to presence of alumina. Indication of phosphorous is due to incorporation of phosphate anions in alumina from the phosphoric acid electrolyte during anodization.

However if some specific sets of CVD process parameters/conditions called as recipes, explained in chapter 2, and PAAO template having suitably wide pore sizes and straight pores are used, CNTs/CNFs growth may start right from the bottom of the pores and project beyond the top surface also as shown in Fig. 5.2. Part (a) of Fig. 5.2 shows FE-SEM image of the fractured surface of the sample, while part (b) contains details of elemental composition, obtained by EDS taken from a small area marked by white square in (a) From the EDS analysis presence of CNTs is evident even in the lower portions in the cross-sectional of the fractured pores. Co and Ni are the catalysts, while Si present is due to some dust particles in the sample. Presence of Au is due to Au coating, which is carried out to make the sample electrically conductive.
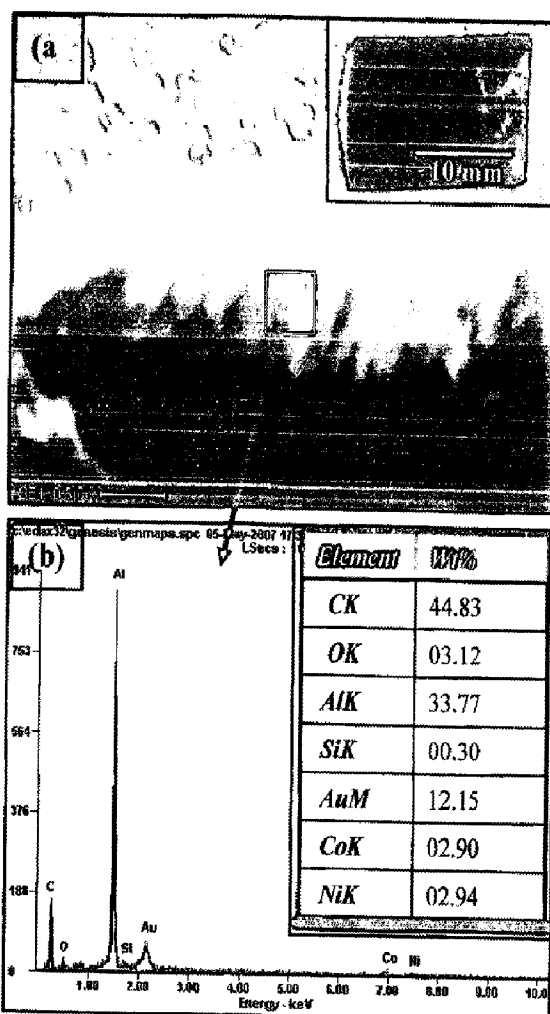
Fig. 5.2: FE- SEM micrographic view (Fig. a) and EDS (Fig. b) of a sample, in which growth of most of the CNTs/CNFs has started from bottom of the pores depth. Part (a) of Fig. 5.2 shows FE-SEM image of the fractured surface of the sample and its inset shows photographic view of the sample, while part (b) contains details of elemental composition, obtained by EDS taken from a point marked by a square in Fig. (a).
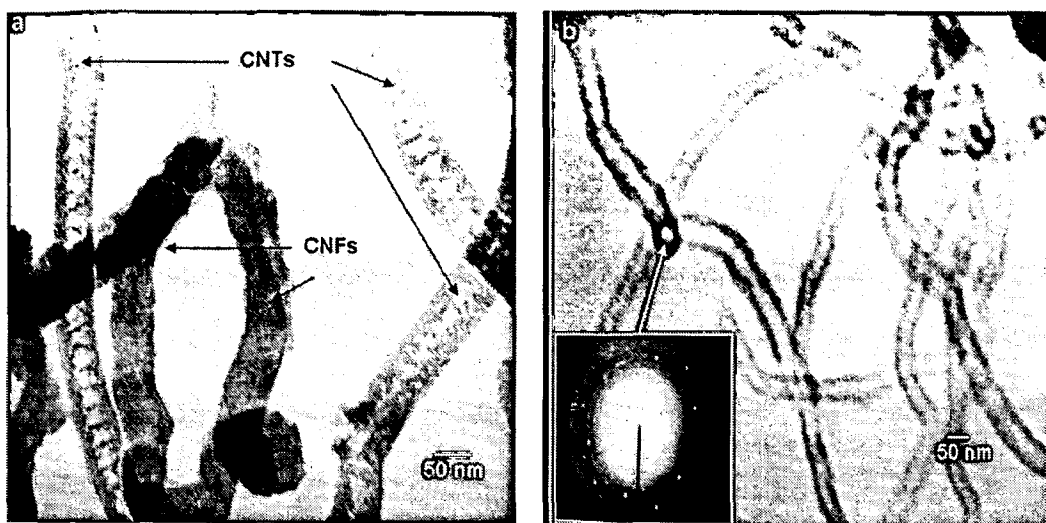
Fig. 5.3: TEM micrographs of the same sample as in the previous figure. (a) CNTs and CNFs, (b) only CNTs; inset showing SAED pattern of the catalyst marked by an arrow.

The CNTs/CNFs were separated from a typical anodized template surface by scrapping the top surface of the sample received from CVD reactor. The separated CNTs/CNFs were observed under TEM. Microstructural views at 70,000 X and 40,000 X are shown in Figs. 5.3 (a) and (b) respectively. The presence of CNTs along with CNFs is indicated by arrows separately in Fig. 5.3 (a). The CNTs are bamboo- like or having small compartments. While CNFs are not hollow from inside and graphitic layers possess some angles other than zero degree with the fibre axis. Further HRTEM studies are required to confirm these two types of nanostructures. The SAED pattern in Fig. 5.3 (b) in the inset shows a fairly hexagonal arrangement of the diffraction spots, which confirms the presence of cobalt catalyst in the TEM sample, whose SAED pattern shows six spots (Ma et al, 2003).

5.2 EFFECT OF MORPHOLOGY OF THE PAAO TEMPLATE

The diameter of the CNTs/CNFs synthesized in pores of PAAO is found to vary from as low as 20 nm to as high as 250 nm depending upon the diameter of the pores of the AAO template as the anodization has been carried out in four different electrolytes in the range of voltages 15-195 V, The diameters and lengths of isolated CNTs/CNFs may either be measured using SEM or TEM. Fig. 5.4 shows TEM images of CNTs

prepared in various PAAO templates, obtained by using different electrolytic baths during anodization, and thus having different diameters and lengths.
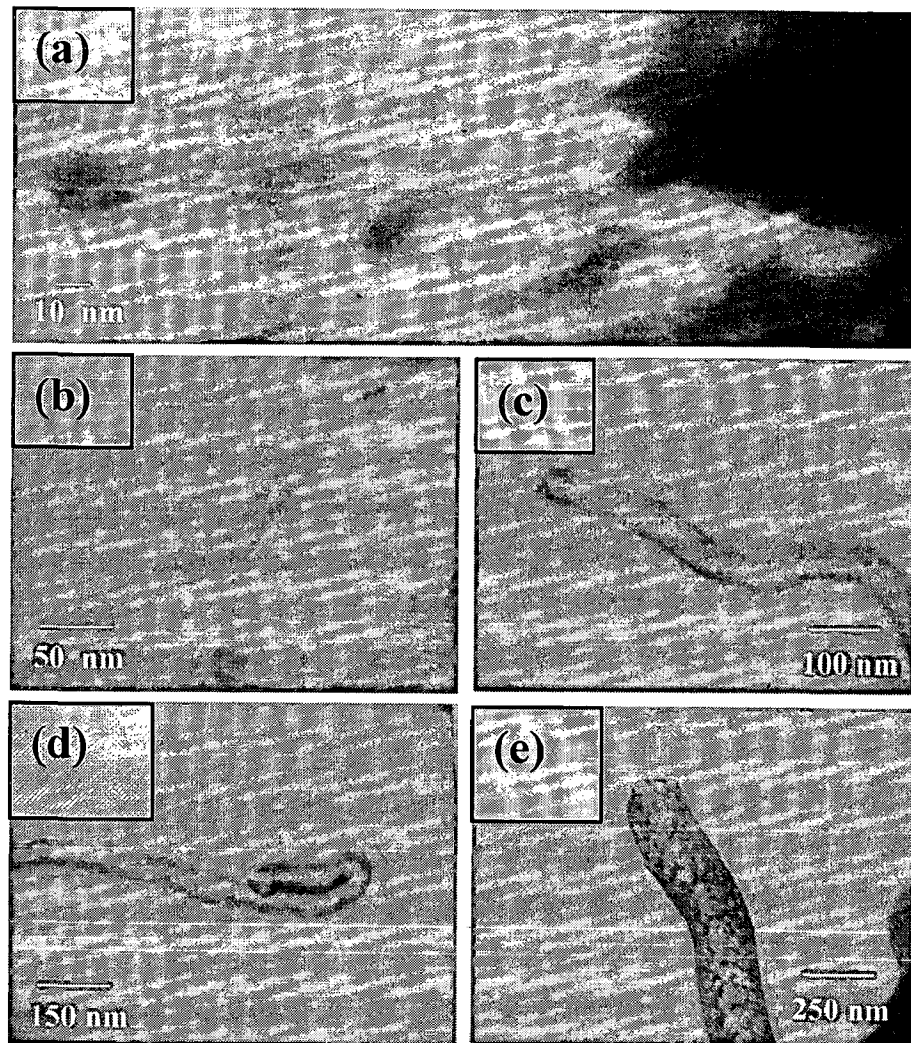
Fig. 5.4: TEM micrographs of various samples of CNTs/CNFs having various diameters.

158

CNTs/CNFs generally completely fill the space available in the pores of PAAO and hence their size may be controlled by diameter and depth of the pores(. Some experimental results in this regard are presented in Table 5.1

Table 5.1: Dependence of CNTs diameter on pore diameter.

S. No.	Average Pore diameter (nm)	Average CNTs/CNFs Diameter (nm)	Remarks
1	35	32	Growth from top surface
2	52	43	Growth from top surface
3	90	83	Growth from top surface
4	156	140	Growth from bottom of the pores
5	220	210	Growth from bottom of the pores

It has been found that for PAAO templates having bigger size of pores, CNTs/CNFs growth can start from deeper locations in the pores and even right from the bottom of the pores. For smaller size of the pores, due to physical constraints, growth of CNTs/CNFs is found to start midway of the pores in some cases and from mouth of the pores (at the top surface) in many cases. This may be attributed to the presence of metal catalyst, which gets stuck anywhere in the pore waals at these locations, which decides the initiation of CNTs/CNFs growth. However in case of pores of bigger size in the PAAO, due to easy transport of catalyst as well as acetylene, growth process. Starts from bottom.
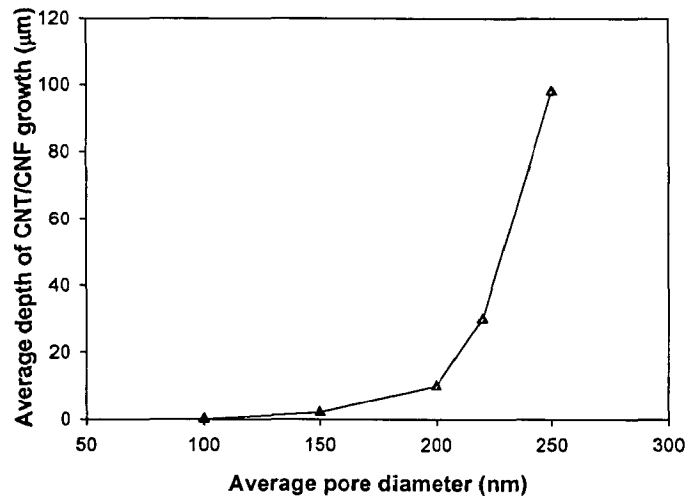
Fig. 5.5:   Graph showing dependence of CNTs growth on average pore diameter.

As pore size decreases, the average depth of catalyst deposition from the top of PAAO surface and hence average depth of CNTs/CNFs growth from the top of PAAO surface also starts decreasing due to diffusion related problems in the narrow pores, which is clear from Fig. 5.5.

If pore widening and barrier layer thinning is not carried out at all or properly after second step of anodization for sufficient time duration, or pores are not formed straight and mutually parallel and normal to the surface, then in this case also, catalyst particles may get stuck/deposited at the top surface only instead of entering pores and traveling all along the depth of the high aspect ratio pores to reach at the bottom of the pores where it should get deposited. Sometimes clusters of catalyst in the form of cauliflower are observed (Sklar et al, 2005). The resulting template after CVD will have CNTs growing either from the surface or from an intermediate place where the diffusing carbon precursor gas (acetylene) first finds metal catalyst particles stuck in the pore channels. However when all the conditions are favourable for electrodeposition of the catalyst and later access of the precursor gas up to the bottom of the pores, growth starts right from the bottom as depicted in figure 5.6 and 5.7 below.
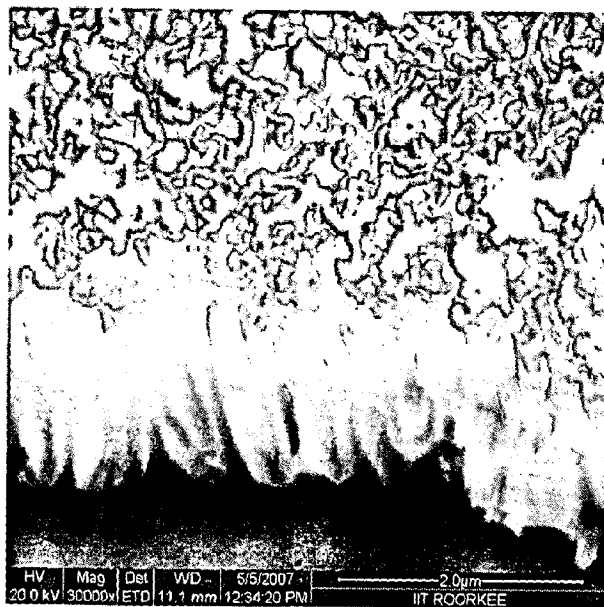
Fig. 5.6: FE-SEM micrograph clearly showing growth of CNTs/CNFs right from the bottom of the pores.
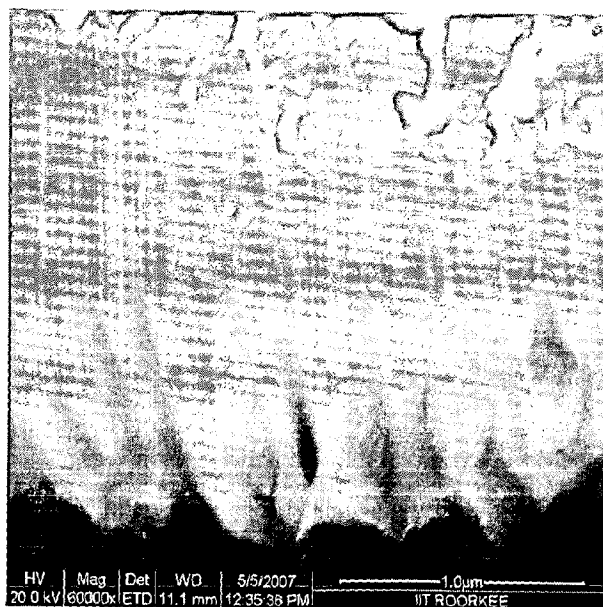
Fig. 5.7: Higher magnification view of the same sample shown in previous figure.

161

When pore sizes are smaller than 100 nm and some smaller catalyst particles are deposited due to sticking on the top surface, CNTs/CNFs growth is restricted and starts at the top surface only. In this case no growth has been seen within the pores. However in the literature, there are few reports, where, due to more stringent control, accurate process parameters and use of sophisticated equipments, CNTs growth has been possible starting from the bottom of the pores which are having smaller size (as small as 20-25nm). Figure 5.8 shows various types of samples due to different process conditions.
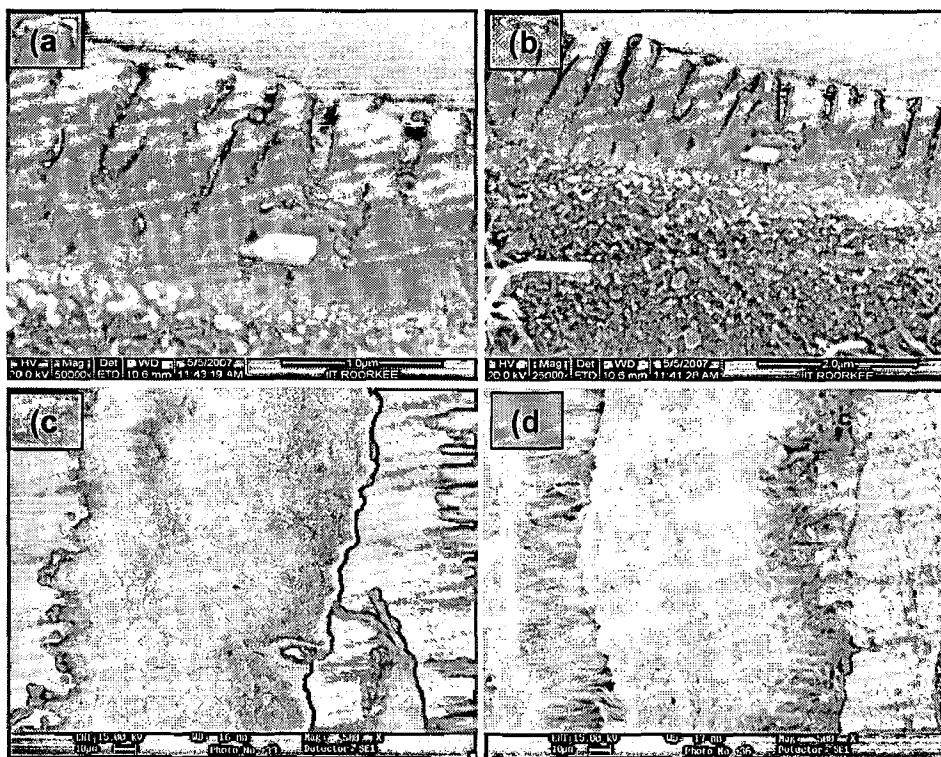
Fig. 5.8:   FE- SEM micrographic view of various defective samples in which growth of most of the CNTs/CNFs has started at top surface of the anodized layer, because of the curved pores obtained due to single step anodization and catalyst particles deposited at various depths as visible in (a) and (b) at different magnifications. Fig (c) and (d) shows CNTs/CNFs growth on the top surface.

5.3   EFFECT OF CATALYST AND CATALYST DEPOSITIONS IN PAAO

5.3.1   Influence of Catalyst Deposition process

Porous anodized aluminium oxide (PAAO) has a rectifying property, acting like a schottky diode, and hence, an AC voltage can be applied to deposit cobalt or other catalysts electrochemically into the bottom of the pores through wet route. Although the applied voltage is sinusoidal, the current is greater during the cathodic half-cycles, making deposition possible without subsequent removal during the anodic half-cycles. This results in catalyst deposition into the bottom of the pores, not on the wall or on the surface because catalysts tries to follow the least resistance path and this is facilitated by thinning of alumina barrier layer for higher electric field, which is insulator. Hence voltage and time duration are needed for required quantity of catalyst deposition at the pore bottom.

Element	Wt%
CK	16.24
OK	28.61
AlK	04.59
CoK	28.82
NiK	21.74
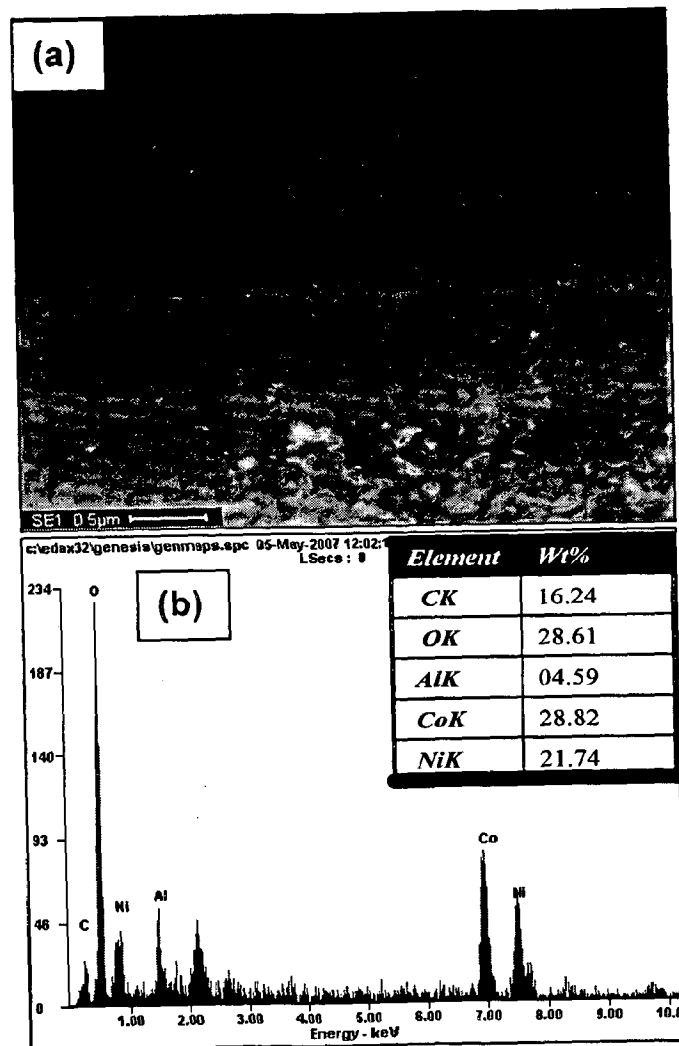
Fig. 5.9: Improper catalyst deposition (for Co-Ni compound) leads to growth of CNTs/CNFs at the top surface only during CVD (Sklar et al, 2005).

Figure 5.9 (a) shows cross sectional view of a typical sample obtained after catalyst electrodeposition, while part (b) of the Fig. shows its EDS spectrum taken from the whole region. It can be seen that growth of CNTs/CNFs has taken place entirely on the top surface. Catalyst particles are visibly stuck at the pore walls. EDS analysis shows presence of Co and Ni catalyst as well as and carbon along with alumina.

'The top view of similar type of sample is shown in Fig. 5.10, where even some clusters of catalysts are visible stuck at the top surface, from where CNTs are growing.
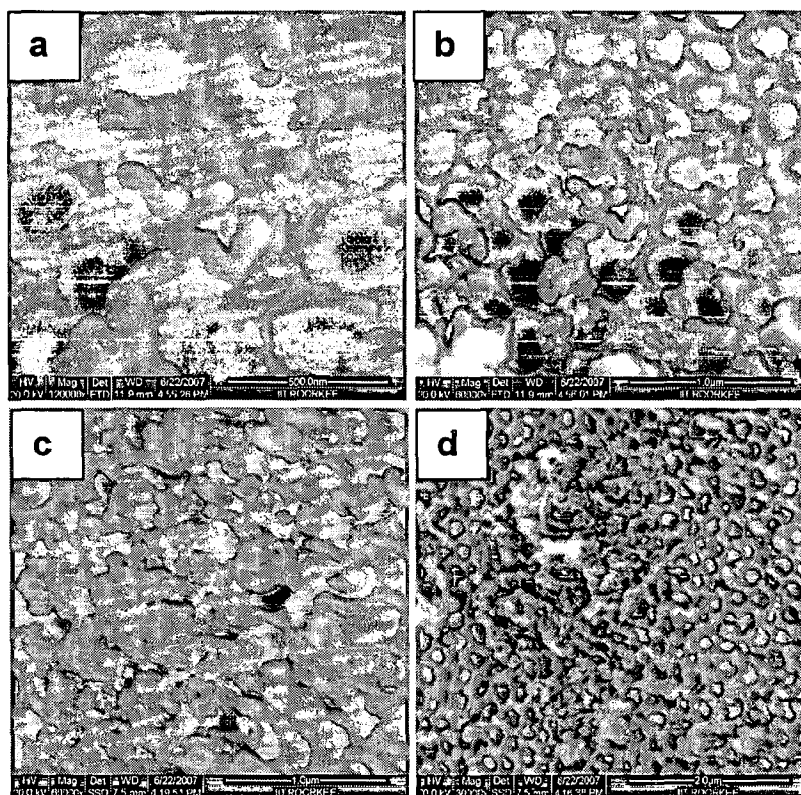
Fig. 5.10:   FE-SEM images of a top surface of PAAO, where improper catalyst deposition has led to start of growth of CNTs/CNFs at the top surface only during CVD

Fig. 5.11 shows the top views of a porous anodized aluminium oxide surface (PAAO), on which over-filling of the pores has lead to large 'cauliflower' cobalt-Nickel clusters on the surface and its EDS spectrum taken from whole region has also been presented.

164
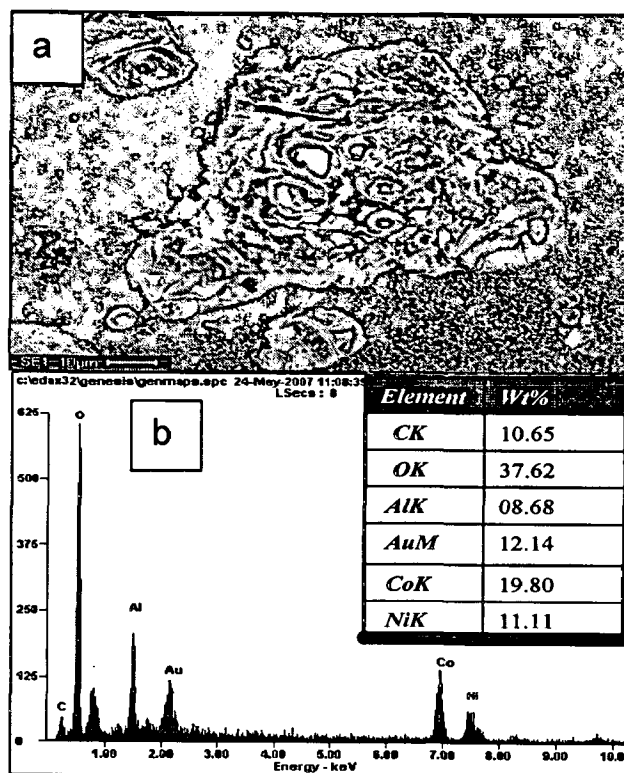
Fig. 5.11: (a) Top views of a porous anodized aluminium oxide surface (PAAO), on which over-filling of the pores has lead to large 'cauliflower' cobalt-Nickel clusters on the surface and (b) its EDS spectrum taken from whole region.

In Fig. 5.12, FE-SEM images show cross sectional views of various PAAO samples having irregular and varying depths of electro-deposition of the catalyst particles. In order to solve this problem Xu et al (2005) has used catalyst reduction and pulse electrodeposition technique to uniformly fill all the pores of AAO, while Sklar et al (2005) have further advanced the improvement in this direction as discussed in detail in chapter 2.
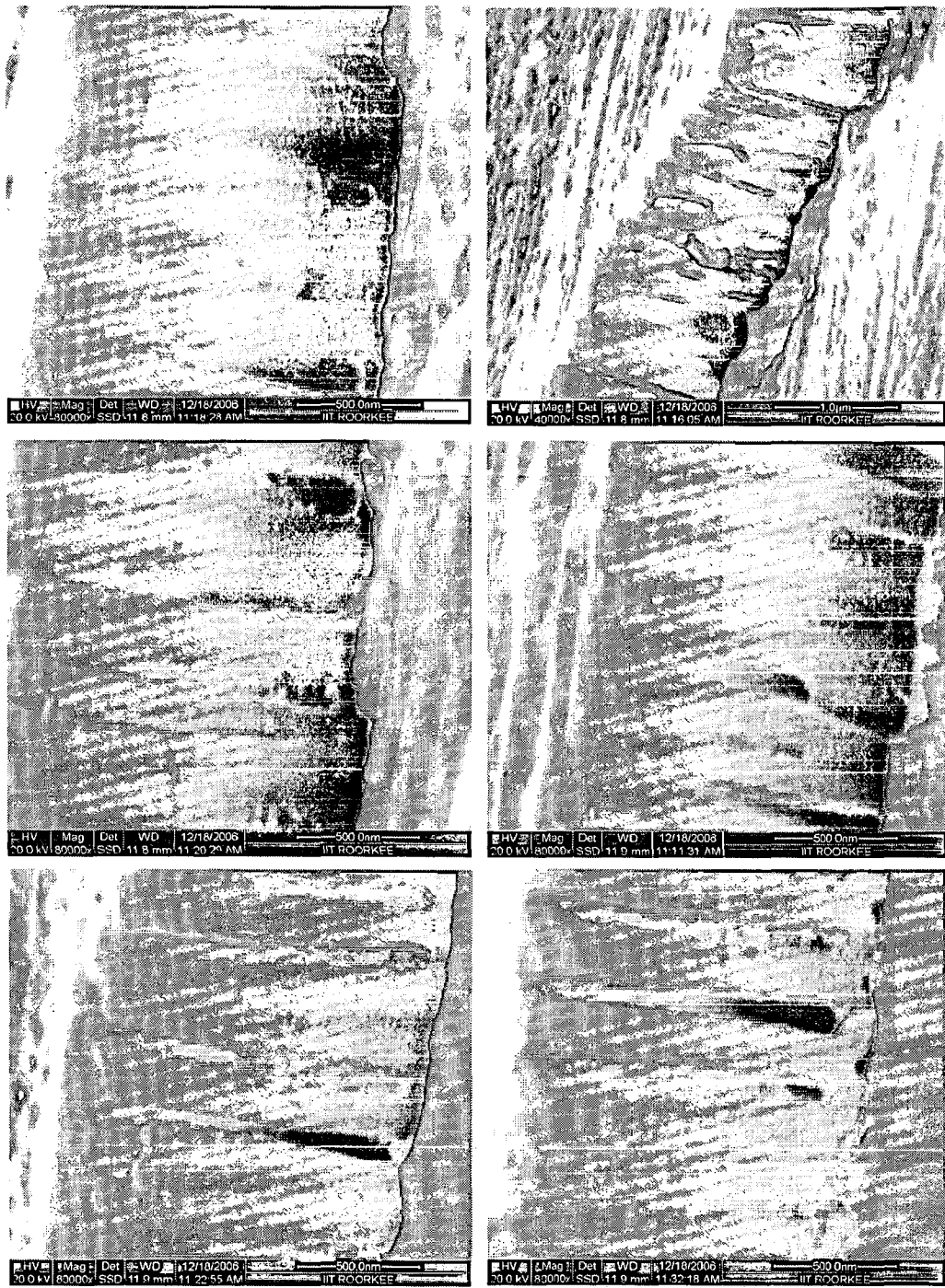
Fig.5.12: FE-SEM images showing cross sectional views of various PAAO samples having irregular and varying depths of electrodeposition of the catalyst particles.

5.3.2 Type and nature of Catalyst.

To compare the influence/effect of catalysts on resulting morphology and structure of grown CNTs/CNFs on similar type of PAAO substrates, when subjected to same type of CVD treatment, following catalysts, viz.:

(i)   Cobalt

(ii)   Nickel

(iii)   Cobalt-Nickel compound and

(iv)   Lithium containing compound

have been used.

(i)   ***Cobalt catalyst:***   Fractured view micrographs by FE-SEM of as prepared CNTs/CNFs using Cobalt catalyst are presented along with their Raman spectrum in Fig 5.14 (a) and (b) respectively. From the micrograph, it can be observed that a good yield of CNFs/CNFs is obtained. CNTs/CNFs are growing from the bottom of the pores and completely filling the pores. However few of the pores are devoid of CNTs/CNFs as the embedded CNTs/CNFs mass has been shared almost equally by another half of the fractured surface (not visible in this view) and hence almost alternate pore section contains CNTs/CNFs in both of the halves. At the top surface of the sample, many CNTs/CNFs having smaller diameter and entangled with each other due to Van-der Waal's attractive forces are seen. The variation in structure, morphology and diameters between these two types of CNTs/CNFs may be attributed to different size of the catalysts and reaction conditions at these places (Kushwaha et al, 2008). At the top surface smaller diameter CNTs are produced due to presence of smaller size catalyst particles there. It seems that few /some catalyst particles might have left stuck or remained at the mouth of the pore during the cleaning process which is carried out after electrochemical catalyst deposition process before CVD. The cleaning is necessary so that CNTs growth may take place from the bottom of the pores and not from the top surface or sub-surface. However even after serious efforts in cleaning, few particles remained uncleaned, which has resulted in the growth at the top surface. Hence some better method of cleaning needs to be explored. The tubular shaped structures seen within the pores are appearing bigger in diameter and amorphous as compared to smaller and more crystalline tubes at the top surface. This may be attributed to the superior /proper growth conditions at the top and inferior growth conditions within the pores due to clogging of the pores mouth during growth of CNTs/CNFs at the top surface of PAAO as well as mild catalytic activity by PAAO itself as reported widely in the literature.

The bending of the tubes present at the top may be due to gravity effects especially in case of tubes, with small diameters and larger lengths (Zhu et al, 2002).
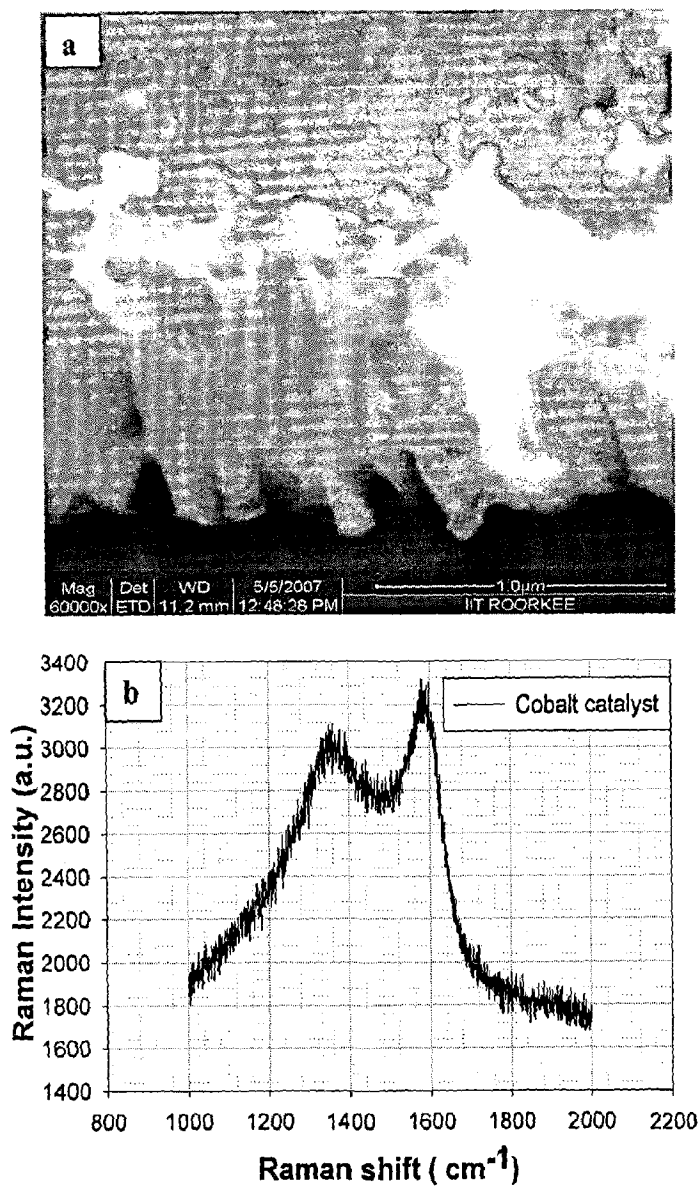
Fig. 5.13: (a) FE-SEM micrograph and (b) Raman spectrum of CNTs prepared using Cobalt catalyst

There are two peaks at around 1350 cm^{-1} and 1585 cm^{-1} in the Raman spectrum shown in Fig. 5.14 (b). The peak at 1585 cm^{-1} corresponds to the E_{2g} longitudinal optic

168

(LO) component of the G mode for HOPG (Highly oriented pyrolytic graphite) ideally located at 1582 cm^{-1}, while the peak at 1350 cm^{-1} (D line) signifies the disorder in graphitization. It appears that the pyrolysis of acetylene produced substantial amount of amorphous or defective crystalline carbon nanostructures as well. If catalyst deposition process parameters are not controlled properly, besides proper cleaning, growth of CNTs may start at the top of the pores which may block the passage of carbon precursor gas to the bottom of the pores. Thus deposition of cobalt catalyst also bears an important role along with the other growth parameters like temperature, precursor gas supply conditions and time of CVD for better morphology and structure. Graphitization developed in CNTs can be estimated by the intensity ratio (R) of the D-band vs G-band (R=I_D/I_G). The smaller is the value of R, higher is the graphitization in CNTs. The value of R obtained is 0.9405 in this case indicating that the degree of graphitization, as reported earlier by Tu et al, (2004), is suitable for tribological application. In addition, the majority of CNTs have very few kinks and bends, which is an added advantage when cobalt is used as catalyst.

(ii)   *Nickel catalyst:*   Figure 5.15 (a) shows the morphology from the top view and (b) Raman spectroscopy of CNTs/CNFs grown using Nickel catalyst. From the Fig. 5.15 (a), it is clear that yield is not as good as in the previous case and variation in structure and diameters in the tubular nano-structures can be easily noted. As most of the pores, no growth of CNTs has taken place. Some fullerene type structures are also seen in series, which appear like tubes and gives a false impression.
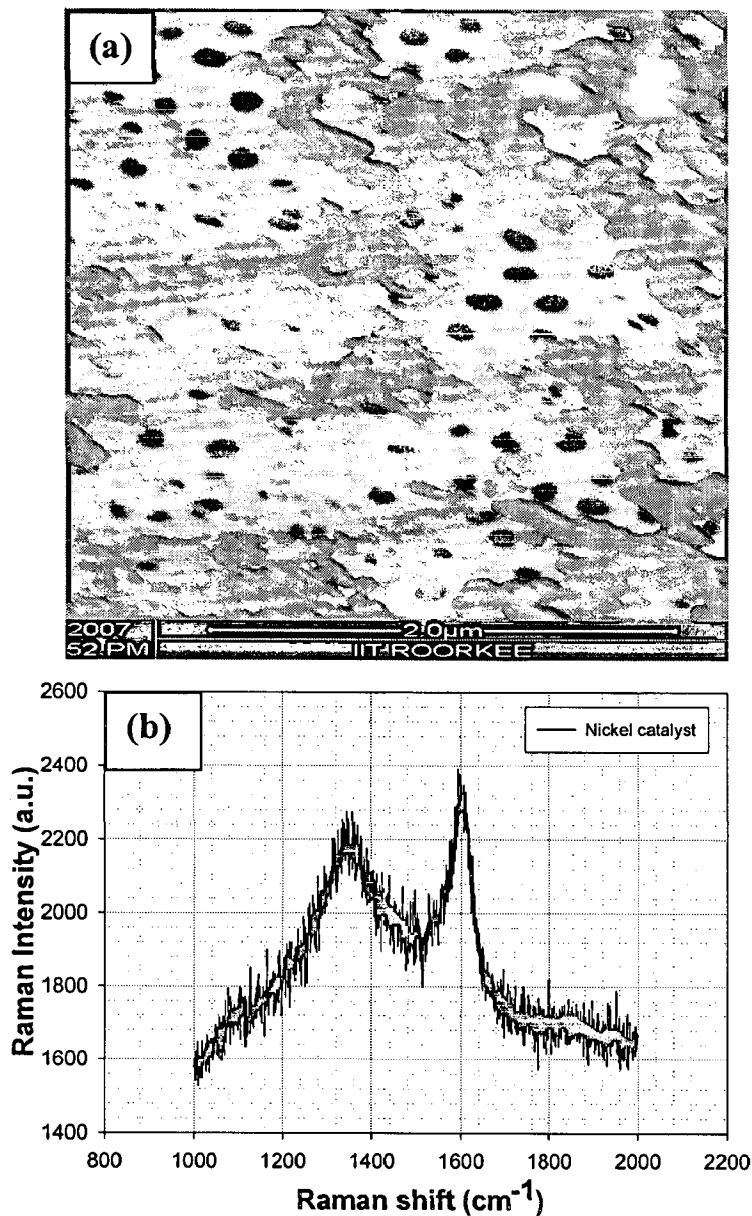
Fig. 5.14: (a) FE-SEM micrograph and (b) Raman spectrum of CNTs prepared using Nickel catalyst.

Raman spectrum of CNTs is given in Fig. 5.15(b) showing two peaks at around 1350 cm^{-1} and 1596 cm^{-1}. The ratio (R) obtained is 0.9491, which is slightly inferior to previous case of cobalt catalyst but still, the degree of graphitization is suitable for tribological applications.

Nickel-Cobalt catalyst: Figure 5. 16 (a) show the morphology and (b) Raman spectroscopy of CNTs/CNFs grown using Nickel-Cobalt catalyst. From the Fig. 5.16 (a) it is clear that yield is better than the previous cases though variation in structure and diameters in the tubular structures can be easily noted. Comparatively fewer pores

170

are seen open at the bottom/lower part of the image, where no growth of CNTs has taken place.
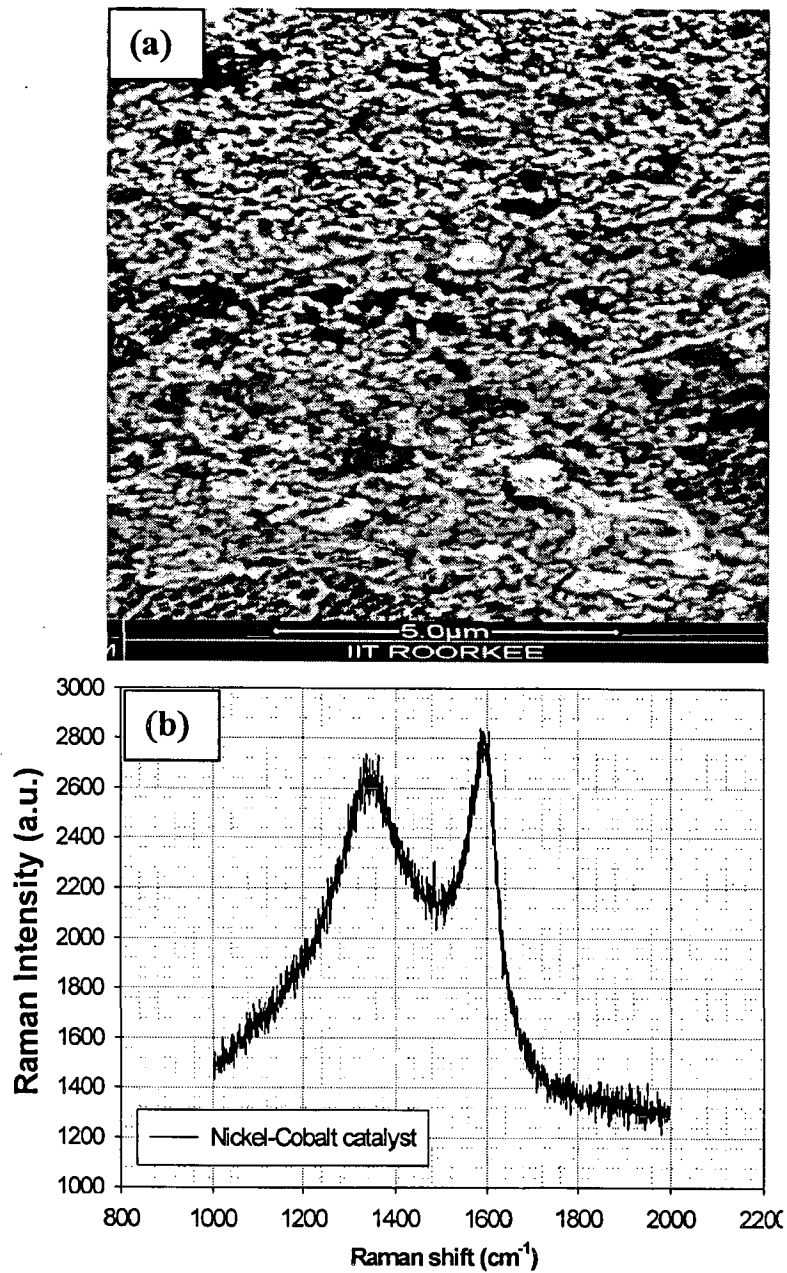
Fig. 5.15: (a) FE-SEM micrograph and (b) Raman spectrum of CNTs prepared using Nickel-cobalt catalyst.

Raman spectrum of CNTs is given in Fig. (b), showing two peaks at around 1348 cm^{-1} and 1593 cm^{-1}. The ratio (R) obtained is 0.9644 which is the maximum of all

the cases, but still suitable for tribological application as yield is better than previous case of nickel.

(iii) **Lithium compound catalyst (LiNi$_{0.5}$Co$_{0.5}$O$_2$ particles):** Figure 5.17 (a) shows the morphology and (b) Raman spectroscopy of CNTs/CNFs grown using Lithium compound catalyst. From the figure it is clear that yield is best in these cases and lengths of CNTs are about 50 μm, though variation in structure and diameters in the tubular structures can be easily noted. Very few pores are seen open, otherwise whole top surface is covered with CNTs/CNFs.
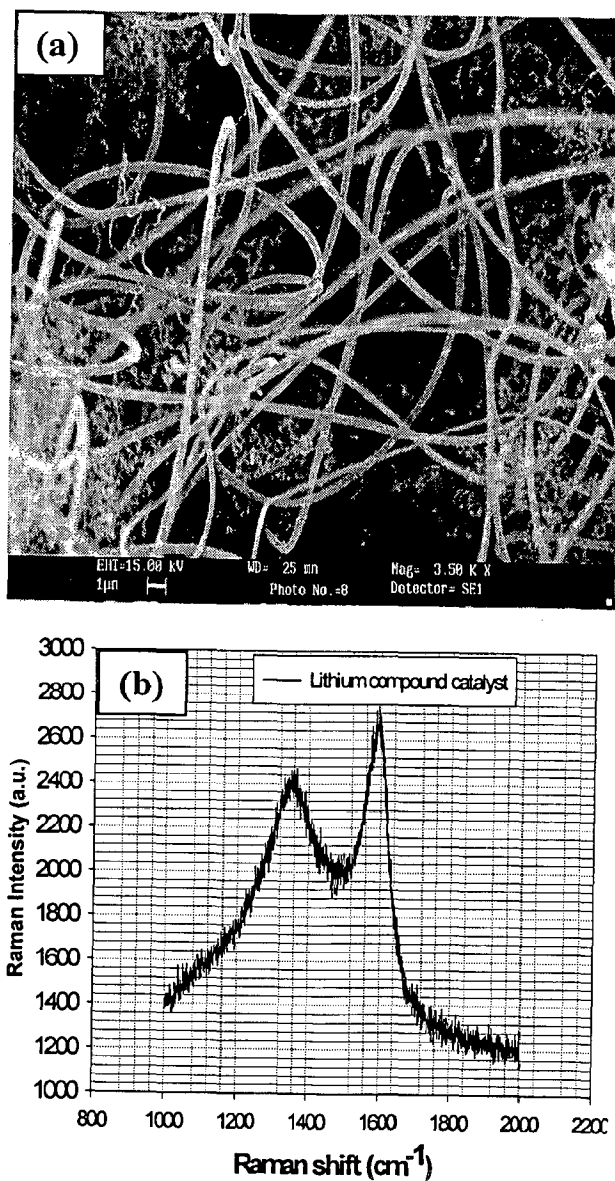
Fig. 5.16: (a) FE-SEM micrograph and (b) Raman spectrum of CNTs prepared using Lithium compound catalyst (LiNi$_{0.5}$Co$_{0.5}$O$_2$ particles).

172

Raman spectrum of CNTs is given in Fig. 5.17 (b) showing two peaks at around 1350 cm^{-1} and 1595 cm^{-1}. The ratio (R) obtained is 0.8951 indicating that the degree of graphitization is best achieved so far and is suitable for tribological applications. Fig. 5.18 show comparison of Raman spectra for all the samples.
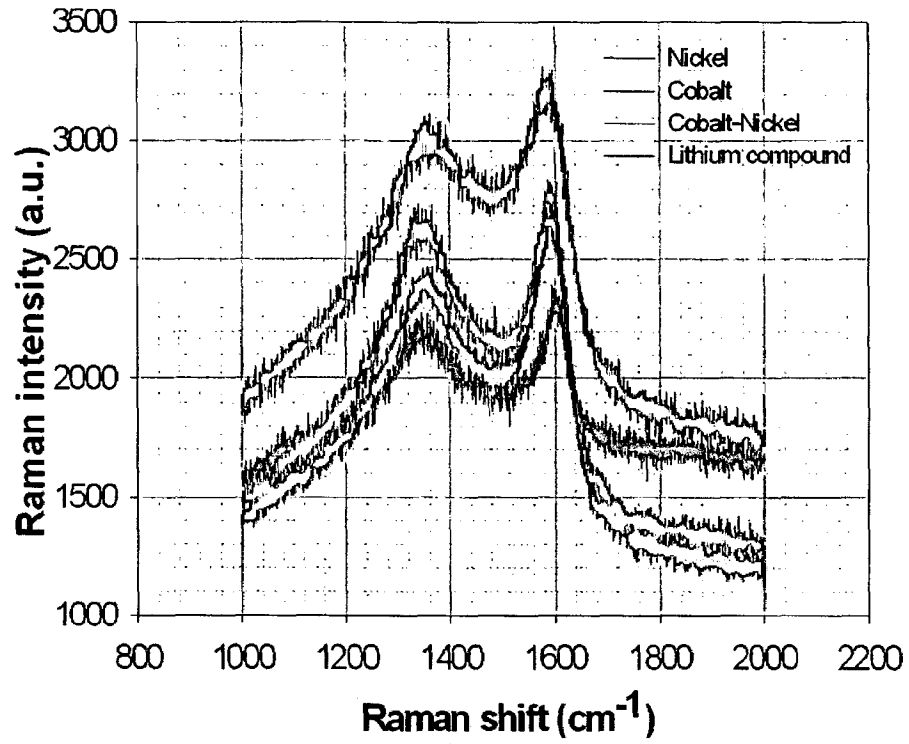
Fig. 5.17: Comparative plot for Raman spectra for various catalysts.

The important values have been further presented in a tabular form (table 5.2)

Table 5.2: Comparative values of Raman spectra for various catalysts.

Sl. No.	Catalyst	Intensity		Raman shift		Ratio (R) D/G band	Remarks about growth
		D band	G band	D band	G band		
1	Cobalt	3102	3298	1350	1585	0.9405	Moderate
2	Nickel	2278	2400	1350	1596	0.9491	Moderate
3	Cobalt-Nickel	2738	2839	1348	1593	0.9644	Poor
4	Lithium compound	2460	2744	1350	1595	0.8951	Best but at surface

The values in the table may be analyzed easily and It may be concluded that the best results are obtained in case of Lithium compound catalyst, which is having minimum value of R, due to better graphitization or less disorder or defects. However in this case the catalyst slurry/solution was simply poured manually on the PAAO substrate, as per details given in chapter 3

5.3.3 Effect of PAAO as catalyst

Fig. 5.18 is a fractured view of a sample which shows the resulting morphology of CNTs growth when AAO itself has been tried to act as a catalyst. It is quite clear from the Fig. 5.18 that CNTs/CNFs have grown sparsely on the top surface of the anodized layer in the absence of metal catalyst deposited at the bottom of the pores and two parts of the fractured oxide are clearly seen, in one of them pores are seen at both places i.e. top and bottom.
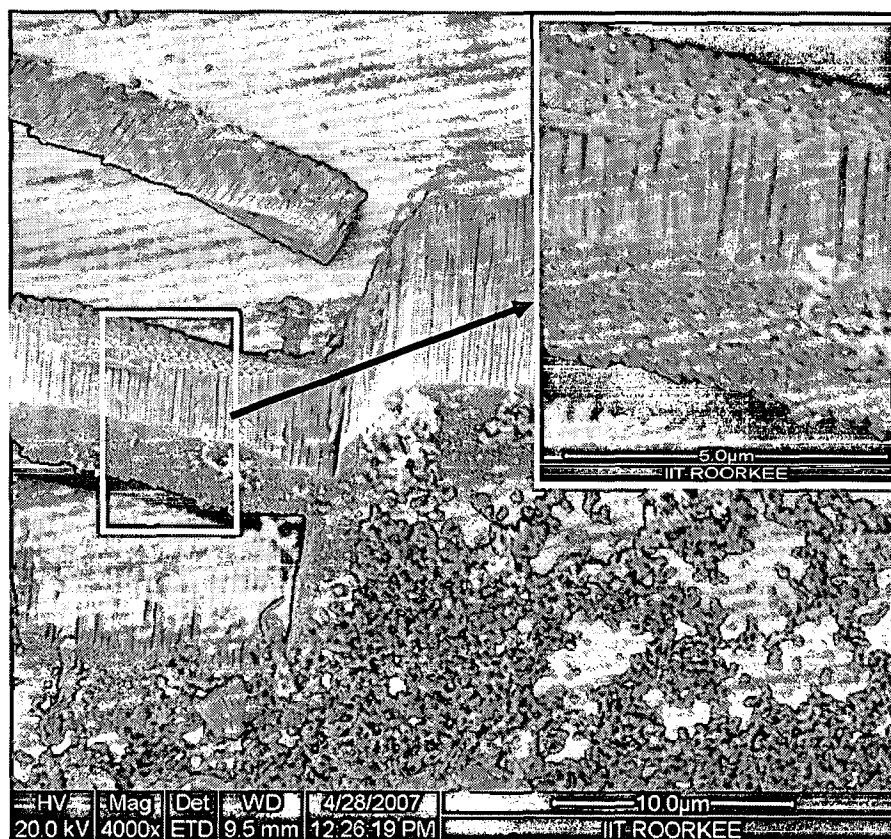
Fig. 5.18: FE-SEM micrograph of fractured view of a sample using PAAO itself as catalyst.

5.4 EFFECT OF TIME DURING CVD

In order to determine optimum time required for CNTs/CNFs growth, for a given PAAO substrate, the chemical vapour deposition (CVD) process was conducted for four different time periods of 1,5,10 and 15 minutes on an anodized sample, formed in 5 wt. % Phosphoric acid bath at 150 V, maintained at 20 °C and the results are shown in Figs. 5.19 (a), (b), (c) and (d) respectively, which indicate that a period of 10 minutes is sufficient for the optimum growth of CNTs/CNFs at 650 °C.
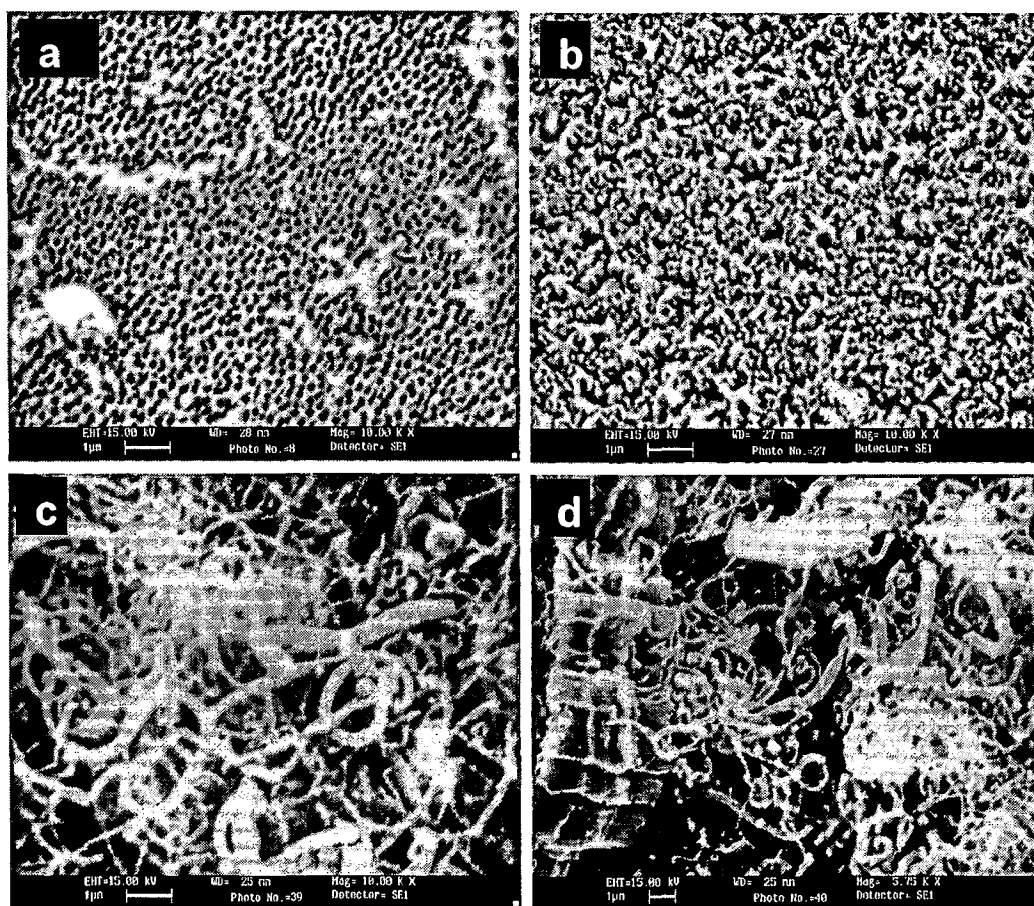
Fig. 5.19: Growth of CVD synthesized CNTs/CNFs for different time periods: (a) 1 minute, (b) 5 minutes, (c) 10 minutes and (d) 15 minutes.

5.5 EFFECT OF TEMPERATURE OF CVD REACTOR

Temperature is the most important parameter in the synthesis of CNTs/CNFs. and to study its influence on the morphology of CNTs/CNFs, CVD has been carried out at various temperatures, which is possible within the constraints of the present

equipment/investigation.. The upper limit of temperature has been fixed at 650°C, which is 10°C lower than the melting point (660° C) of the underlying aluminium substrate material. Hence CVD has been carried out at various temperatures lower than 660° C, viz., 500° C, 550° C, 600° C and 650° C using the same type of anodized aluminium substrate. and the resulting morphology and structures of CNTs/CNFs are presented in the following paragraph.

When CVD temperature is kept at 500 °C, no growth of CNTs is observed except few points. This may be due to non occurrence of decomposition of acetylene due to insufficient energy available for cracking at low temperatures. When reactor temperature is increased to 550 °C, growth of CNTs has been observed and the yield and quality seems to be moderate. The microstructures are shown in the following figures. When the temperature is increased further, the diameter of the obtained CNTs has been found to increase with slight improvement in the yield, evident from Figs. 5.20 (c) and (d).
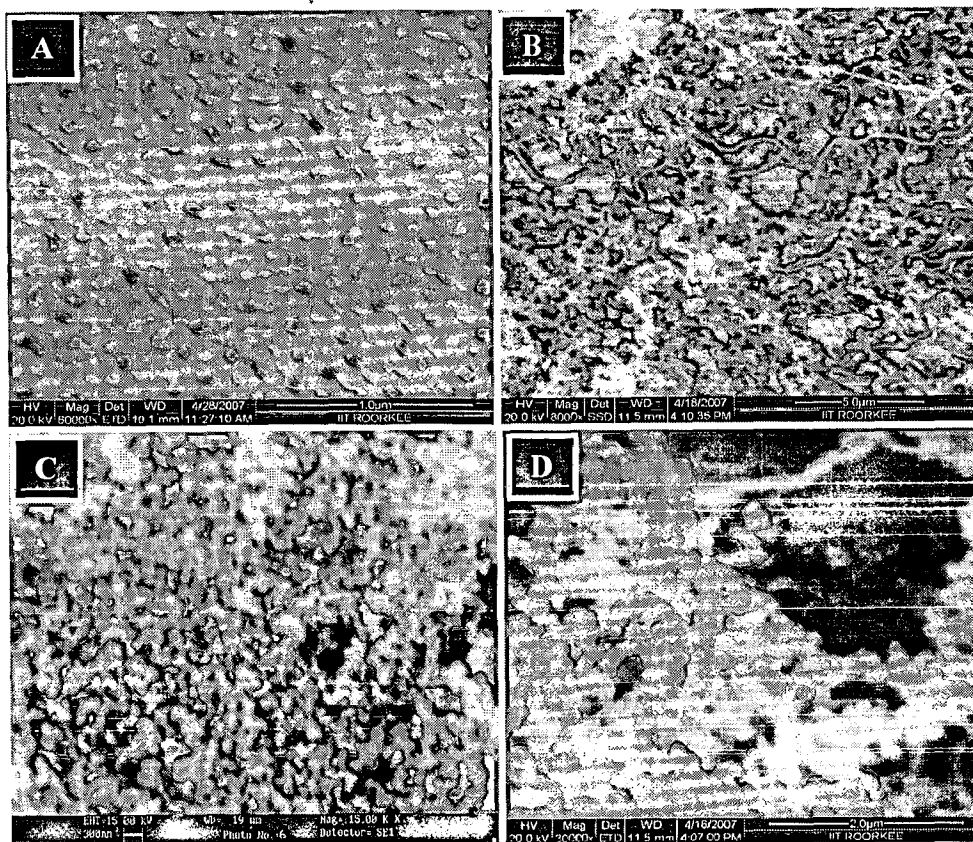
Fig. 5.20:   Morphological views showing results of CVD carried out at temperatures of (a) 500 °C, (b) 550 °C, (c) 600 °C and (d) 650 °C.
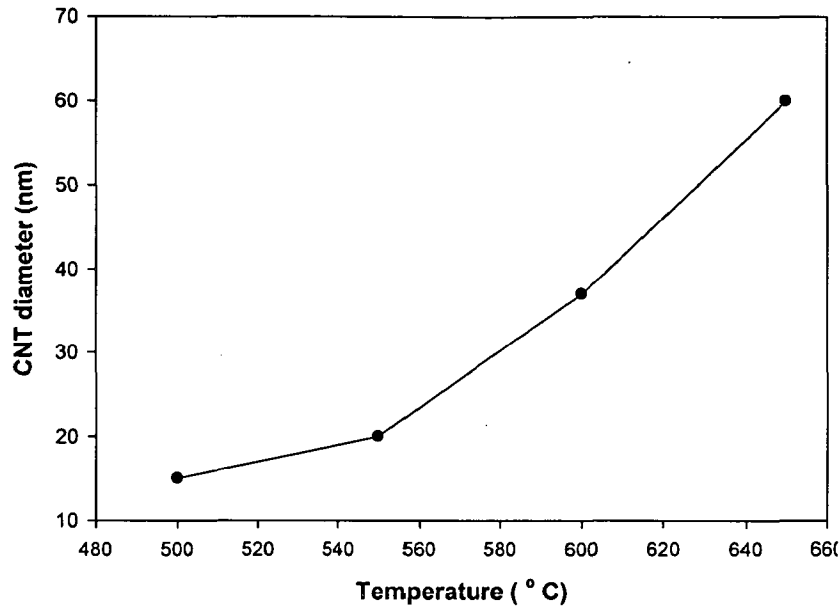
Fig5.21: Effect of temperature on CNTs diameter

A growth configuration of CNTs/CNFs confined by PAAO template with Co catalysts at bottom could be deduced from above experimental results. The Co particles being more active catalyst than PAAO, initiate the nucleation of carbon structures and act as the seed for subsequent CNTs/CNFs growth. The space limited reaction within the PAAO pore waals and the mild catalytic action of the PAAO wall itself forces the continuous CNTs/CNFs growth adhering to the inner wall of PAAO template pores. When the tip of the CNTs reaches at the top ends of the pores, their growth continues for some time due to the existence of dangling bonds. Due to van der Waals interaction, this growth gets terminated soon after the top ends of the CNTs get aggregated. The strain induced by the pore walls due to the lattice mismatch between alumina and carbon structures makes the wall of CNTs disordered and hence the quality in terms of graphitization is poor as reported widely in literature ((Kyotani et al, 1996; Sui et al, 2001).

The optimal parameters have been observed as following: 10 min of growth time, 600 °C of temperature, using Co as catalyst in a PAAO structure obtained by anodizing pure aluminium substrate in a 5 wt.% phosphoric acid bath at 150 V. These

parameters gave rise to good results in respect to satisfactory metal catalyst reduction, negligible surface catalyst deactivation and high CNTs/CNFs yield. .

RESULTS AND DISCUSSION:
Dry and lubricated sliding friction and Wear

CNTs/ CNFs embedded in porous anodized aluminium oxide (PAAO) surfaces formed on pure aluminium substrates in phosphoric and oxalic acid electrolytes by anodization have been evaluated for their dry sliding friction and wear behaviour in a pin on disc set-up under different normal loads and compared with that of the surface of PAAO alone. In addition, the tests have also been conducted under lubrication for comparing the results with those obtained under dry sliding conditions. The results of these investigations have been reported in this chapter followed by discussion in the context of existing knowledge in open literature.

6.1   CNTs/CNFs IN PAAO ANODIZED IN PHOSPHORIC ACID
6.1.1   *Dry Sliding Wear*

Dry sliding wear tests have been carried out by sliding a cylindrical pin (glued with different types of samples on the mating surface of the pin shank) against a counterface of EN-32 hardened steel disc under ambient conditions using a pin-on-disc machine following the procedures as described in section 3.11 o f Chapter-3. The sliding wear tests have been conducted at four different normal loads of 5, 10, 15 and 20 N and a constant sliding speed of 0.5 m/s. The relative humidity has been kept in the range between 40-70% during the conduct of wear tests. The cumulative weight loss with increasing sliding distance has been measured and converted into cumulative volume loss by dividing with the density of the test specimen. Identical tests have been carried out three times and the average cumulative volume loss (V in mm^3) as a function of sliding distance (D in m) has been reported as the basic result under a given condition of dry sliding. The wear rate (V/D) expressed in mm^3/m, for a given specimen under a given condition of sliding, has been determined from the slope of the linear variation of cumulative volume loss with sliding distance as estimated by the linear least square fit. The wear coefficient defined as ($\frac{VH}{DL}$) has been calculated by multiplying the slope estimated by linear least square fit, of the linear variation of wear rate with normal load (L), by the hardness (H) of the specimen. The wear tests have been conducted with CNTs/CNFs embedded PAAO samples and the results have been presented.

(a) Wear of CNTs/CNFs embedded PAAO

Figure 6.1 shows the variation of cumulative volume loss with sliding distance conducted at different normal loads of 5, 10, 15 and 20 N for a fixed sliding speed of 0.5 m/s for CNTs/CNFs embedded in PAAO. For a given normal load, the cumulative volume loss increases linearly with increasing sliding distance. The linear least square fit equations relating cumulative volume loss, V in mm^3, with sliding distance, D in m, for the loads of 5, 10, 15 and 20 N are respectively,

$$V = 0.07646\,D - 0.82 \qquad \qquad \qquad (6.1)$$

$$V = 0.05922\,D - 1.2 \qquad \qquad \qquad (6.2)$$

$$V = 0.04790\,D - 0.4 \qquad \qquad \qquad (6.3)$$

$$V = 0.04620\,D - 1.4 \qquad \qquad \qquad (6.4)$$

and the coefficients of correlation respectively are 0.99837, 0.99888, 0.99969 and 0.99198. The lines do not pass through the origin because of run-in conditions in the beginning.
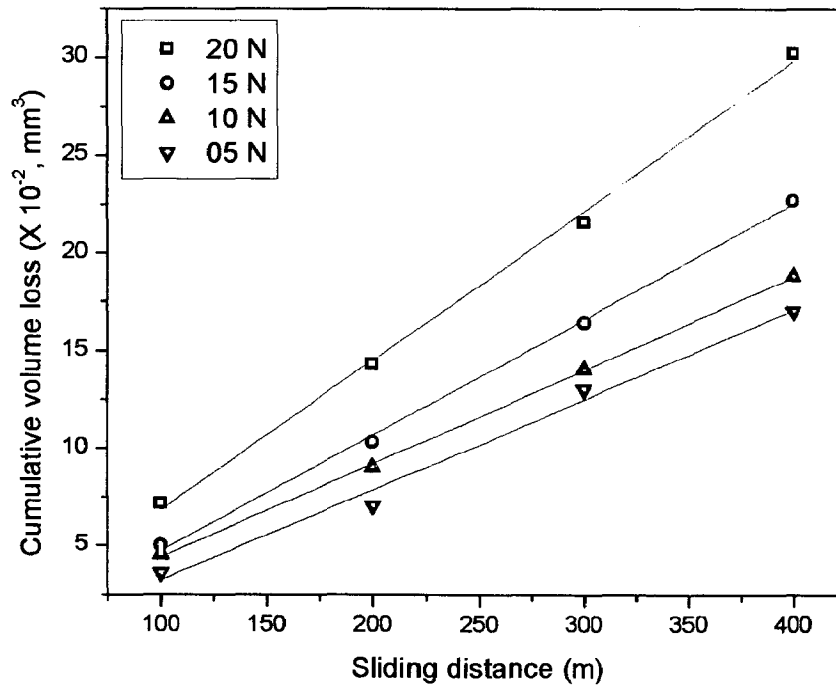
Fig. 6.1: The variation of cumulative volume loss with sliding distance at different normal load of 5, 10, 15 and 20 N and a sliding speed of 0.5 m/s for CNTs/CNFs embedded PAAO.

Figure 6.2 shows the variation of wear rate (V/D) with increasing load (L), the variation has been expressed by two linear segments, viz, first less steep segment is in the load range of 5 to 10 N and second steeper segment, which is obtained by least square fit of this variation, is in the load range of 10 to 20 N (R value, 0.98577). The equations for the two linear segments, respectively for the lower load (<10 N) and upper load (>10 N) segments are as follows,

$$(V/D) = 0.00034 \ L + 0.0445 \qquad\qquad (6.5)\ (a)$$
$$(V/D) = 0.00286 \ L + 0.01835 \qquad\qquad (6.5)\ (b)$$
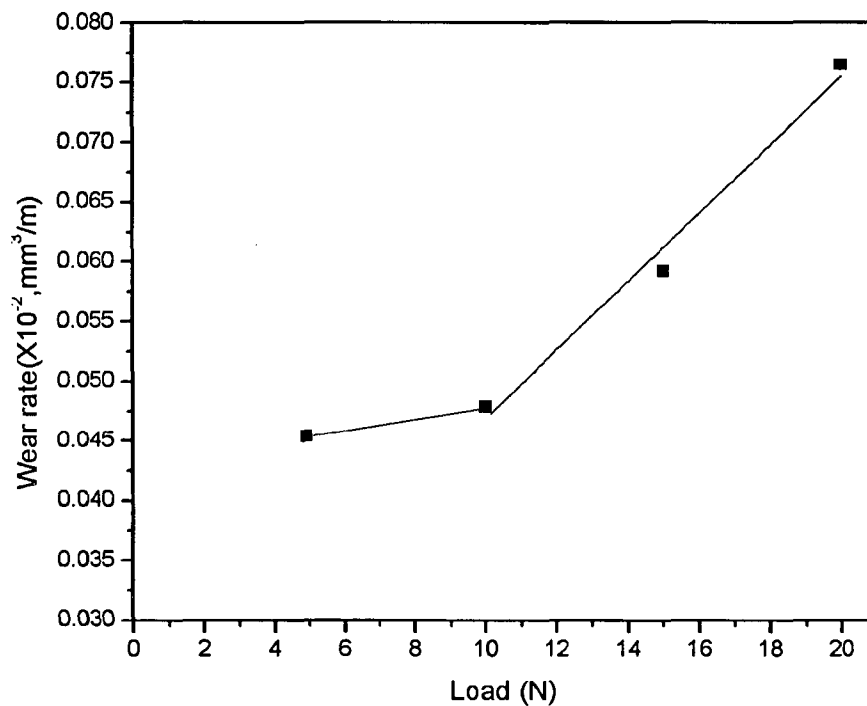
Fig. 6.2: The variation of wear rate at different normal load of 5, 10, 15 and 20 N for a sliding speed of 0.5 m/s for CNTs/CNFs embedded PAAO.

The wear coefficient may thus be calculated using the hardness (H) of 19 GPa (Mo et al, 2005) for CNT/CNF embedded PAAO as 3.8×10^{-4}.

(b)   Wear of PAAO

Figure 6.3 shows the variation of cumulative volume loss with sliding distance conducted at different normal loads of 5, 10, 15 and 20 N and a fixed sliding speed of 0.5

m/s for porous alumina anodized (PAAOO in phosphoric acid bath. For a given normal load, the cumulative volume loss increases linearly with increasing sliding distance as shown in fig. 6.2. The linear least square fit equations relating the cumulative volume loss, V in mm^3, with sliding distance, D in m, for the loads of 5, 10, 15 and 20 N are respectively given by,

$$V = 0.23\ 37\ D - 2.415 \tag{6.6}$$

$$V = 0.17768\ D + 2.43 \tag{6.7}$$

$$V = 0.12667\ D - 2.595 \tag{6.8}$$

$$V = 0.06891\ D - 2.045 \tag{6.9}$$

and the correlation coefficients are respectively 0.99317, 0.99204, 0.99665 and 0.98609.
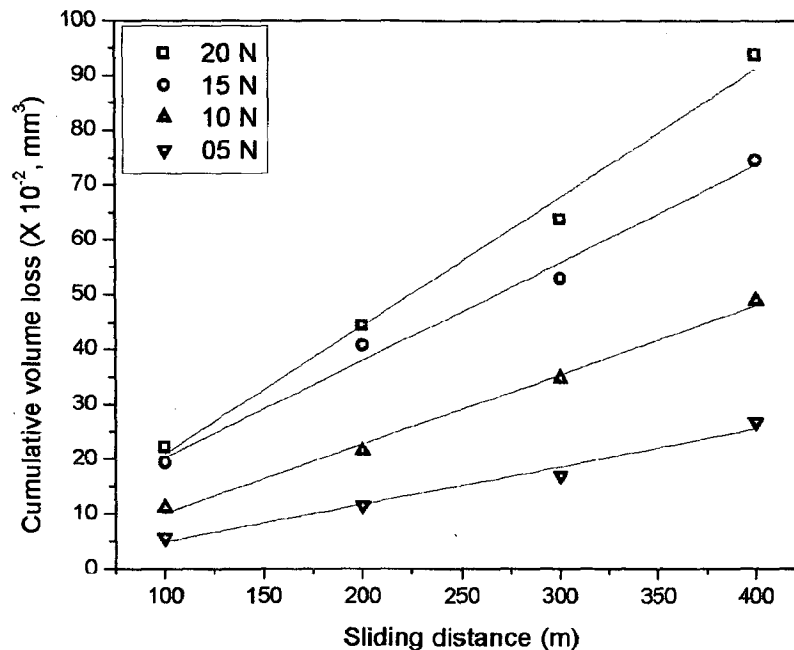
Fig. 6.3:   The variation of cumulative volume loss with sliding distance during dry sliding at different normal load of 5, 10, 15 and 20 N and a sliding speed of 0.5 m/s for PAAO.

Figure 6.4 shows the variation of wear rate (V/D) with increasing load (L), which is linear. The linear least square fit of this variation yields the following equation with coefficient of correlation as 0.999.

$$(V/D) = 0.01091 \, L + 0.0154 \qquad\qquad (6.10)$$

The wear coefficient may thus be calculated using the hardness of 13 GPa for PAAO (Ko et al, 2006) as 14.1×10^{-4}.
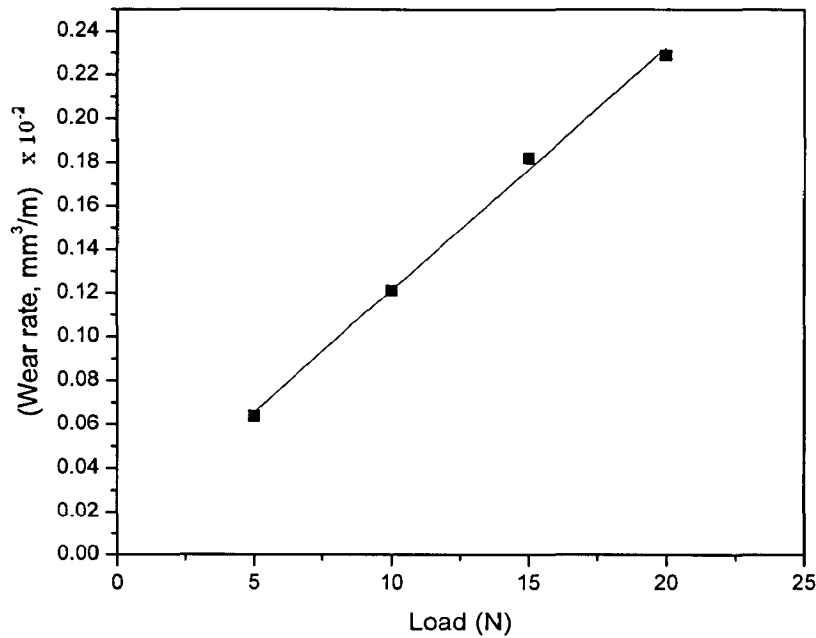
Fig. 6.4: The variation of wear rate at different normal load of 5, 10, 15 and 20 N for a sliding speed of 0.5 m/s for PAAO.

6.1.2 Oil-Lubricated Sliding Wear

(a)   **Wear during Lubricated Sliding of CNTs/CNFs embedded PAAO.**

Figure 6.5 shows the variation of cumulative volume loss in CNTs/CNFs embedded PAAO with sliding distance for oil-lubricated sliding against the counterface of hardened steel. conducted at different fixed normal loads of 5, 10, 15 and 20 N and for a fixed sliding speed of 0.5 m/s. SAE − 15 engine oil has been used for lubrication throughout the study. The variation in the Fig. 6.5 has been subjected to linear least square fit and the equations obtained for cumulative volume loss, V in mm^3, with sliding distance, D in m, for the loads of 5, 10, 15 and 20 N are respectively,

$$V = 0.0099 \, D + 0.0 \qquad\qquad (6.11)$$

$$V = 0.0072 \, D + 0.05 \qquad\qquad (6.12)$$

$$V = 0.0055 \, D - 0.0 \qquad\qquad (6.13)$$

$$V = 0.0033 \, D - 0.05 \qquad\qquad (6.14)$$

and the coefficient of correlations are 0.99588, 0.98345, 0.99259 and 0.99772 respectively.
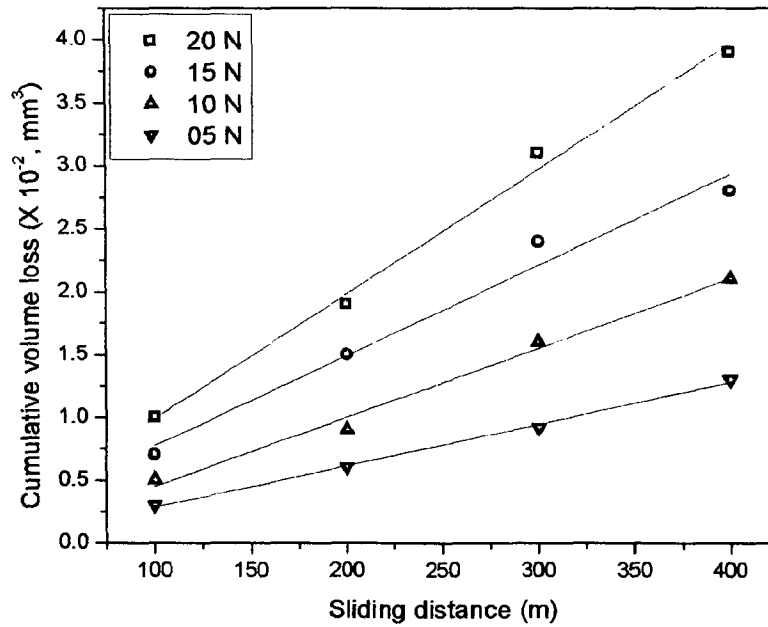
Fig. 6.5: The variation of cumulative volume loss with sliding distance at different normal load of 5, 10, 15 and 20 N for a sliding speed of 0.5 m/s during lubricated sliding of CNTs/CNFs embedded in PAAO.

Figure 6.6 shows the variation of wear rate (V/D) with increasing load (L), which is almost linear. The linear least square fit of this variation yields the following equation with coefficient of correlations of 0.9899.

$$(V/D) = 0.0037 \, L + 0.00157 \tag{6.15}$$
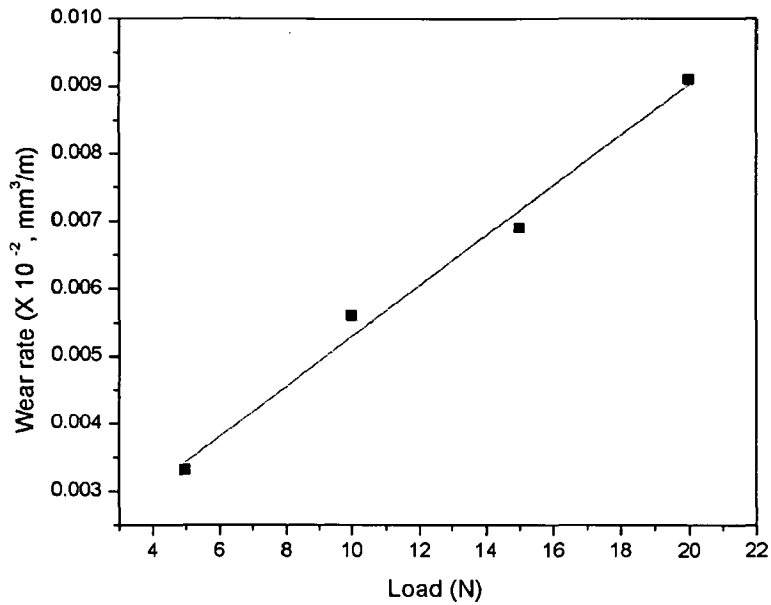
Fig. 6.6: The variation of wear rate with increasing normal load at a fixed sliding speed of 0.5 m/s, during lubricated sliding of CNTs/CNFs embedded in PAAO.

The wear coefficient may thus be calculated using the hardness (H) of 19 GPa (Mo et al, 2005) for CNT/CNF embedded PAAO as 5.7×10^{-5}.

(b)   Wear during Lubricated Sliding of PAAO.

Figure 6.7 shows the variation of cumulative volume loss in PAAO with sliding distance for lubricated sliding against the counterface of hardened steel, conducted at different fixed normal loads of 5, 10, 15 and 20 N and for a fixed sliding speed of 0.5 m/s. The variation in Fig. 6.7 has been subjected to linear least square fit and the equations obtained for cumulative volume loss, V in mm^3, with sliding distance, D in m, for the loads of 5, 10, 15 and 20 N are respectively,

$$V = 0.03442\ D - 0.375 \tag{6.16}$$

$$V = 0.02457\ D + 0.37 \tag{6.17}$$

$$V = 0.01675\ D - 0.055 \tag{6.18}$$

$$V = 0.00625\ D - 0.003 \tag{6.19}$$

and the coefficients of correlation are 0.99578, 0.97850, 0.95186 and 0.95405 respectively.
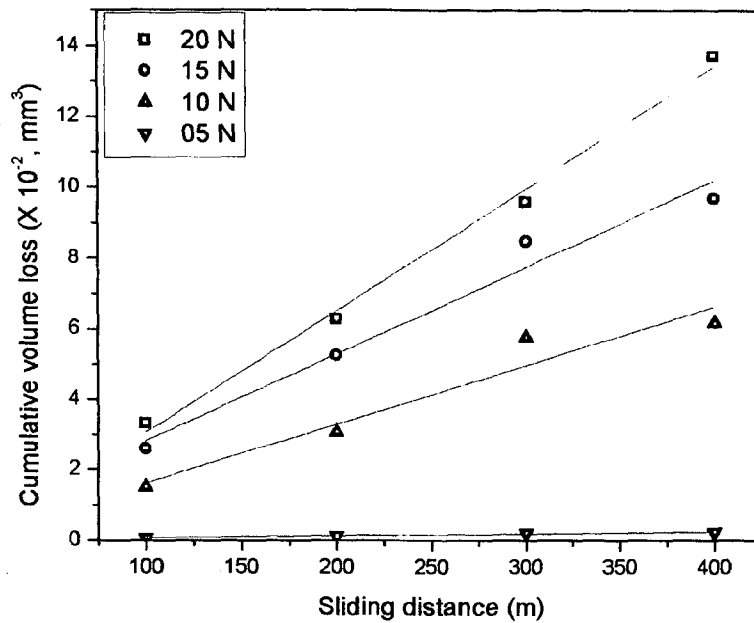
Fig. 6.7: The variation of cumulative volume loss with sliding distance at different normal load of 5, 10, 15 and 20 N for a fixed sliding speed of 0.5 m/s during lubricated sliding of PAAO.

Figure 6.8 shows the variation of wear rate (V/D) with increasing load (L), which is linear. The linear least square fit of this variation yields the following equation with coefficient of correlation of 0.9899.

$$(V/D) = 0.00185 \ L - 0.00259 \qquad (6.20)$$
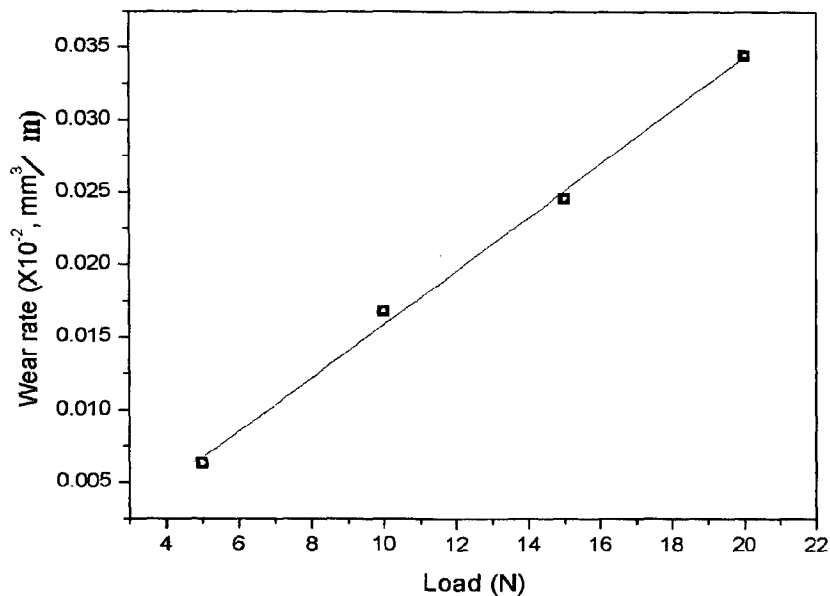
Fig. 6.8: The variation of wear rate at different normal load of 5, 10, 15 and 20 N for a sliding speed of 0.5 m/s for lubricated PAAO.

186

The wear coefficient may thus be calculated using the hardness of 13 GPa for

PAAO (Ko et al, 2006) as 2.39×10^{-5}.

6.1.3 Comparison of Wear Behaviour of PAAO and PAAO with Embedded CNT/CNF

Figure 6.9 shows the comparison of cumulative volume loss of (a) porous anodized aluminium oxide (PAAO), (b) CNTs/CNFs embedded PAAO (c) Lubricated PAAO and (d) Lubricated CNTs/CNFs embedded PAAO at 20 N load and sliding speed of 0.5 mps, after sliding a distance of 400 m. It is found that volume loss is the maximum (93.7×10^{-2} mm^3) in case of PAAO and it decreases by almost 85% in case of lubricated sliding. When CNT/CNF is embedded in PAAO, the volume loss under dry sliding wear decreases by about 54 %. In case of lubricated sliding of CNTs/CNFs embedded in PAAO the volume loss decreases by about 91 % from that observed under dry sliding wear of this surface.
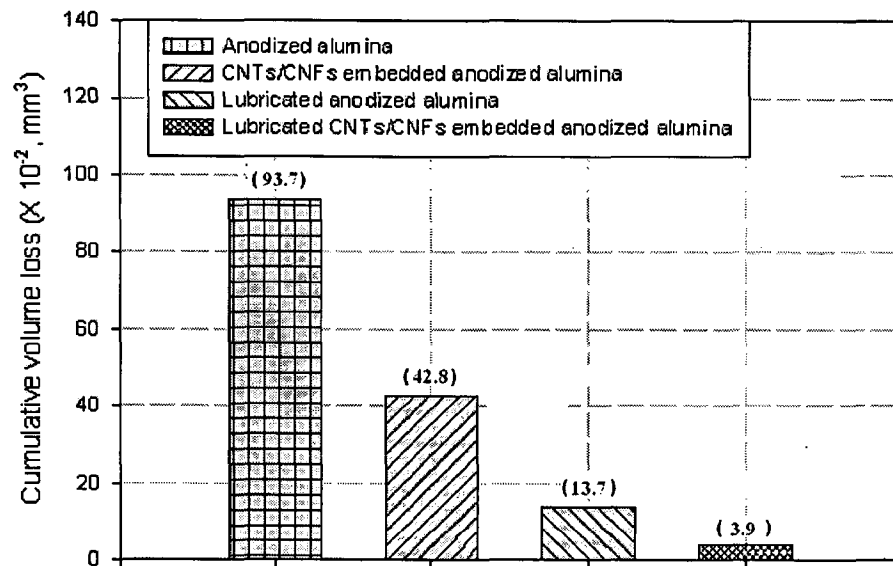
Fig. 6.9: Comparison of cumulative volume loss of (a) Anodized alumina (PAAO), (b) CNTs/CNFs embedded anodized alumina (c) Lubricated anodized alumina and (d) Lubricated CNTs/CNFs embedded anodized alumina at 20 N load and sliding speed of 0.5 m/s, after sliding a distance of 400 m in phosphoric acid bath.

187

Figure 6.10 shows the comparison of wear rate at different normal loads observed during dry and lubricated sliding of porous anodized aluminium oxide (PAAO) and CNTs/CNFs embedded PAAO at sliding speed of 0.5 m/s. The wear rate increases with load during dry sliding but in lubricated sliding the wear rate and the rate of its increase with increasing load significantly reduces because of lubrication. When CNT/CNF is embedded in PAAO, the wear rate under dry sliding is lower than that observed for lubricated sliding of PAAO for the loads investigated but the slope is a little higher for the dry sliding. For lubricated sliding of CNTs/CNFs embedded PAAO, the wear rate is lower, more for the higher load, but the slope has decreased compared to that for dry sliding of this surface. It is, thus, observed that wear rate is the maximum in case of porous anodized aluminium oxide (PAAO) and minimum in case of Lubricated CNTs/CNFs embedded PAAO.
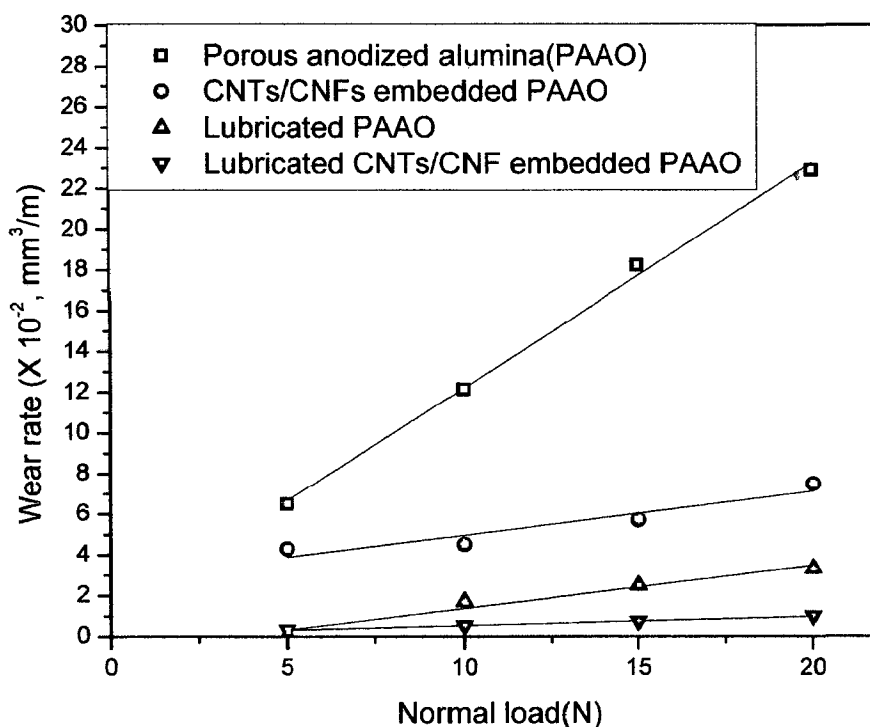
Fig. 6.10: Variation of wear rate with normal load for (a) Porous anodized alumina (PAAO), (b) CNTs/CNFs embedded PAAO; (c) Lubricated PAAO and (d)

Lubricated CNTs/CNFs embedded PAAO in 5 wt.% phosphoric acid electrolytic bath.

Figure 6.11 shows the comparison of wear coefficients for dry and lubricated sliding of porous anodized alumina (PAAO) and CNTs/CNFs embedded PAAO, obtained by anodization of aluminium in 5 wt. % phosphoric acid electrolytic bath. For dry sliding, PAAO has shown the highest wear coefficient but after embedding CNT/CNF, the wear coefficient has come down but it is higher than that observed for lubricated sliding of PAAO, which, although, shows a higher wear rate. Lubricated sliding of PAAO embedded with CNT/CNF has shown the smallest wear rate amongst all the materials investigated here.
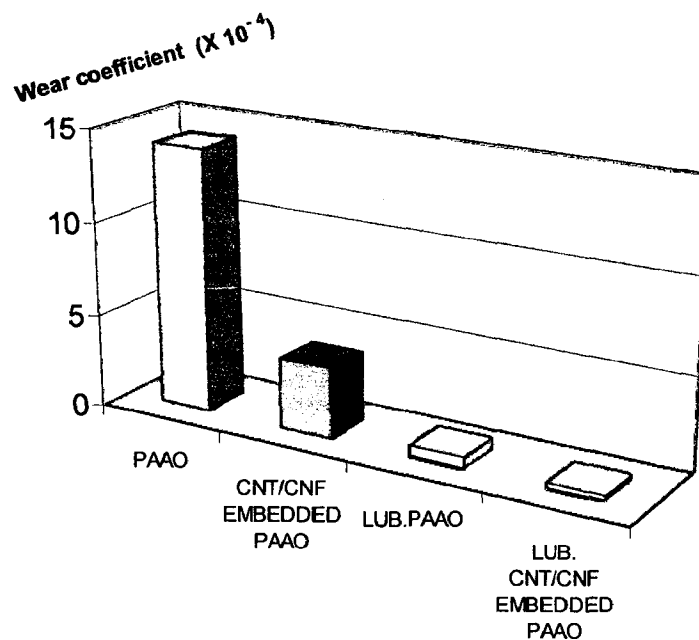
Fig. 6.11: Comparison of wear coefficients for dry and lubricated sliding of Porous anodized alumina (PAAO) and CNT/CNF embedded PAAO Obtained by anodization in 5 wt.% phosphoric acid electrolytic bath.

6.1.4 Dry and Lubricated Sliding Friction behaviour

The changes in coefficient of friction (μ) in both PAAO and CNT/CNF embedded PAAO surfaces anodized in 5 wt.% phosphoric acid has been obtained under dry sliding and lubricated sliding against the counterface of hardened steel. The same is presented in the following paragraphs.

(a)   Dry Sliding friction in PAAO and CNT/CNF embedded PAAO

Figure 6.12 shows a typical variation of friction coefficient (μ) with sliding distance at applied load of 20 N and at a sliding speed of 0.5 m/s in case of both, a PAAO sample and CNTs/CNFs embedded PAAO sample, anodized in phosphoric acid bath. It has been observed that during run-in period the sliding starts with a high value of coefficient of friction but it decreases with sliding to arrive at a fairly steady value during steady state contact. This trend of variation of coefficient of friction is common for all the behaviour
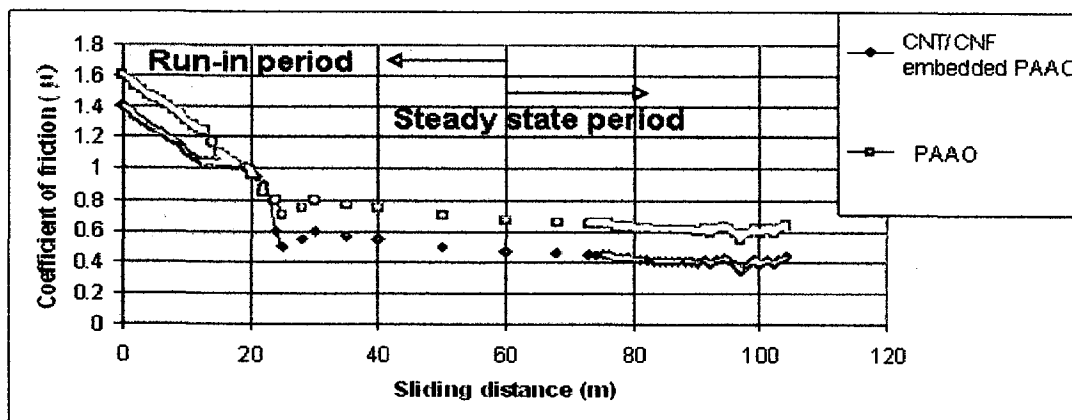
Fig. 6.12: Variation of coefficient of friction (μ) with sliding distance at a constant sliding speed of 0.5 m/s, in case of (a) PAAO and (b) CNTs/CNFs embedded PAAO samples.

Figure 6.13 shows variation of average value of coefficient of friction (μ) with normal load in dry sliding at a constant speed of 0.5 m/s, for PAAO and

190

CNTs/CNFs embedded PAAO samples, obtained by anodization of aluminium in 5 wt. % phosphoric acid. It is observed that coefficient of friction decreases with increasing load and the friction is less in PAAO after embedding of CNTs/CNFs. At a load of 20 N, the coefficient of friction for dry sliding is as low as 0.2 in CNTs/CNFs embedded PAAO.
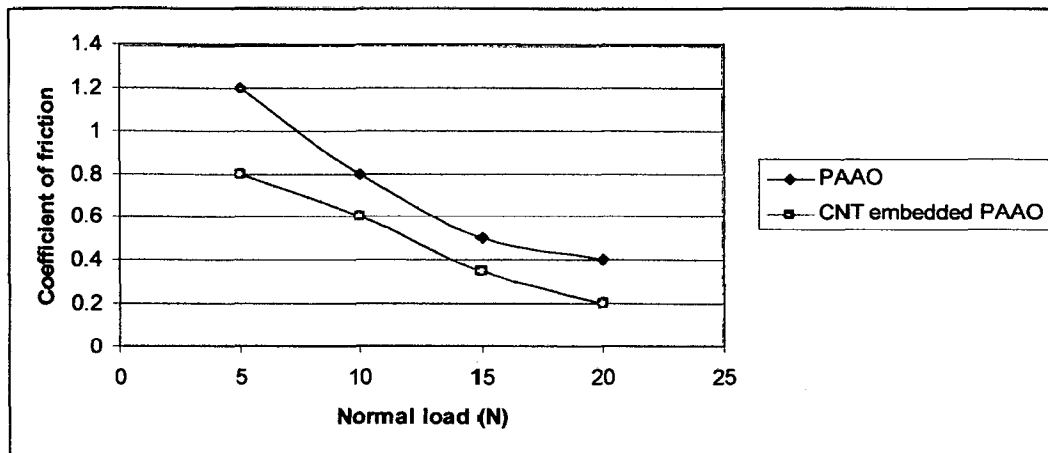
Fig. 6.13: Variation of Average value of coefficient of friction (μ) with normal load at a constant sliding speed of 0.5 m/s, in case of (i) PAAO and (ii) CNTs/CNFs embedded PAAO samples.

(b)   Lubricated Sliding friction in PAAO and CNT/CNF embedded PAAO

Figure 6.14 shows a typical variation of friction coefficient (μ) with sliding distance at applied load of 20 N and at a sliding speed of 0.5 m/s in case of both, a lubricated PAAO sample and lubricated CNTs/CNFs embedded PAAO sample, anodized in phosphoric acid bath. It has been observed in this case also, just like the previous case, during run-in period the sliding starts with a high value of coefficient of friction but it decreases with sliding to arrive at a fairly steady value during steady state contact. However, it may be observed that the run-in stage is short in presence of lubrication and the steady state is more stable.
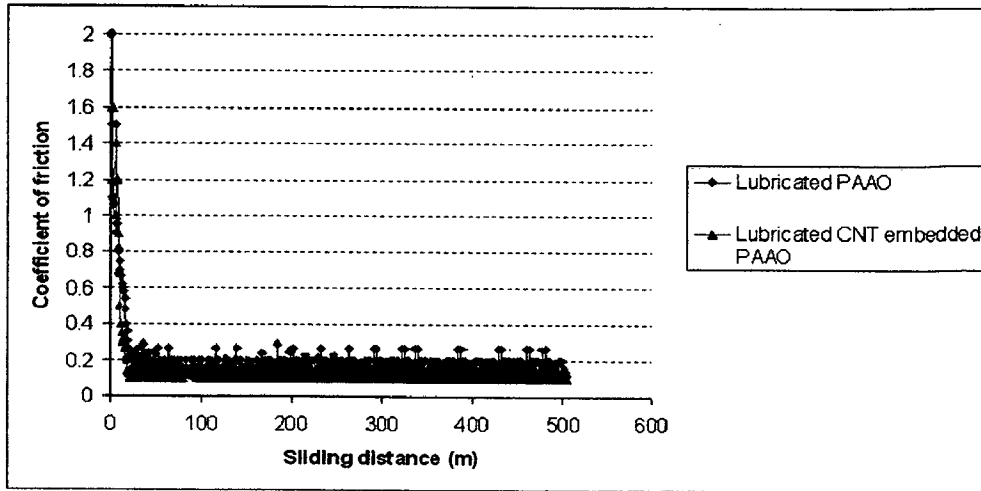
Fig. 6.14: Variation of coefficient of friction (μ) with sliding distance at a constant sliding speed of 0.5 m/s, for lubricated sliding of PAAO and CNTs/CNFs embedded PAAO samples.

Figure 6.15 shows variation of average value of coefficient of friction (μ) with normal load at a constant sliding speed of 0.5 m/s, for the lubricated sliding of PAAO and CNTs/CNFs embedded PAAO samples. The coefficient of friction decreases with increasing normal load as it has been observed for dry sliding wear as well. But the coefficient of friction is considerably reduced due to lubrication for both PAAO and CNTs/CNFs embedded PAAO. At a load of 10 N, the coefficient for lubricated sliding is as low as 0.2 in CNTs/CNFs embedded PAAO.
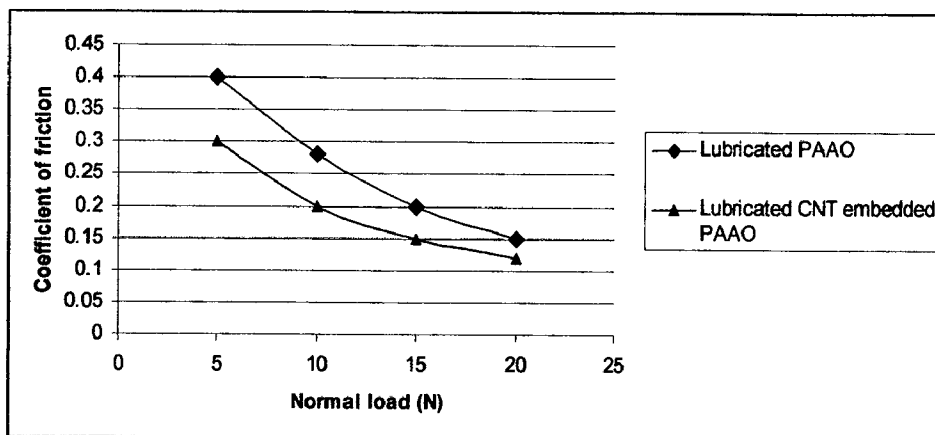
Fig. 6.15: Variation of Average value of coefficient of friction (μ) with normal load at a constant sliding speed of 0.5 m/s, in case of lubricated PAAO and lubricated CNTs/CNFs embedded PAAO samples.

192

Figure 6.16 shows comparison of variation of average value of coefficient of friction (μ) with normal load at a constant sliding speed of 0.5 m/s, for the lubricated and dry sliding of PAAO and CNTs/CNFs embedded PAAO samples. The coefficient of friction decreases with increasing normal load for all the cases. But the coefficient of friction (μ) is considerably reduced due to lubrication for both PAAO and CNTs/CNFs embedded PAAO. The advantage of embedding of CNTs/CNFs in PAAO in dry sliding is evident at higher loads. At 20 N load, μ has reduced to 0.2 from a higher value of 1.2 at 5 N load and the value is very close to the values of lubricated PAAO and CNT/CNFs embedded PAAO samples.
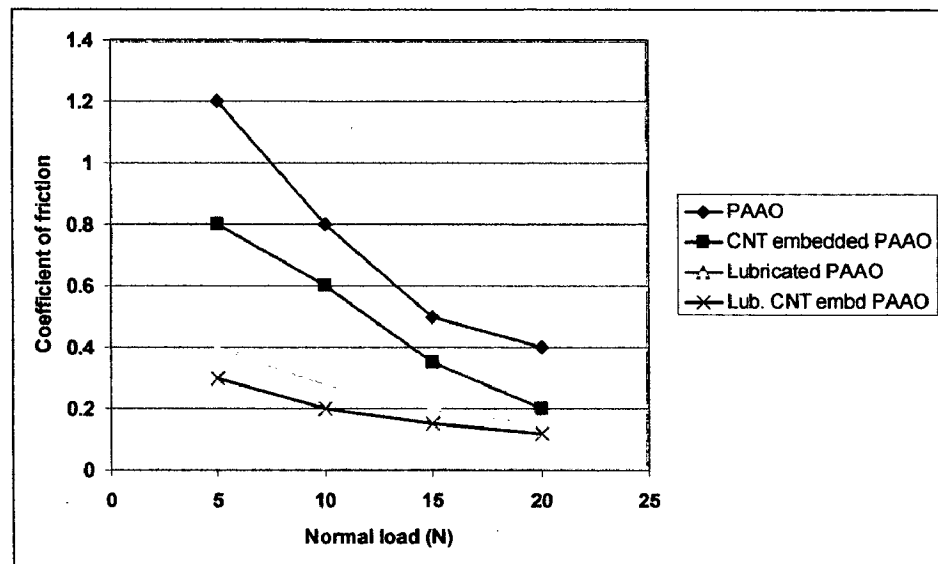
Fig. 6.16: Comparison of variation of average value of coefficient of friction (μ) with normal load at a constant sliding speed of 0.5 m/s, in case of dry and lubricated sliding wear of PAAO anodized in phosphoric acid.

(c)   Nature of Sliding Surface and Wear Debris Generated

FE-SEM micrographs of CNT embedded PAAO sample before and after dry sliding wear test, is shown in Figure 6.17 (a) and (b) respectively. Fig 6.17 (c) and (d) show the Energy dispersive spectroscopy (EDS) spectra of samples in Fig. 6.17 (a) and (b) respectively. It is clearly observed that the CNT/CNF observed on the PAAO substrate in Fig. 6.17 (a) has got fragmented and mixed with debris particles generated as shown in Fig. 6.17(b). The EDS analysis of the virgin surface show

carbon on alumina but after dry sliding, the debris particles generated has significant iron content coming from the counterface of hardened steel, since PAAO substrate is considerably harder than the counterface of EN-32 steel disc.
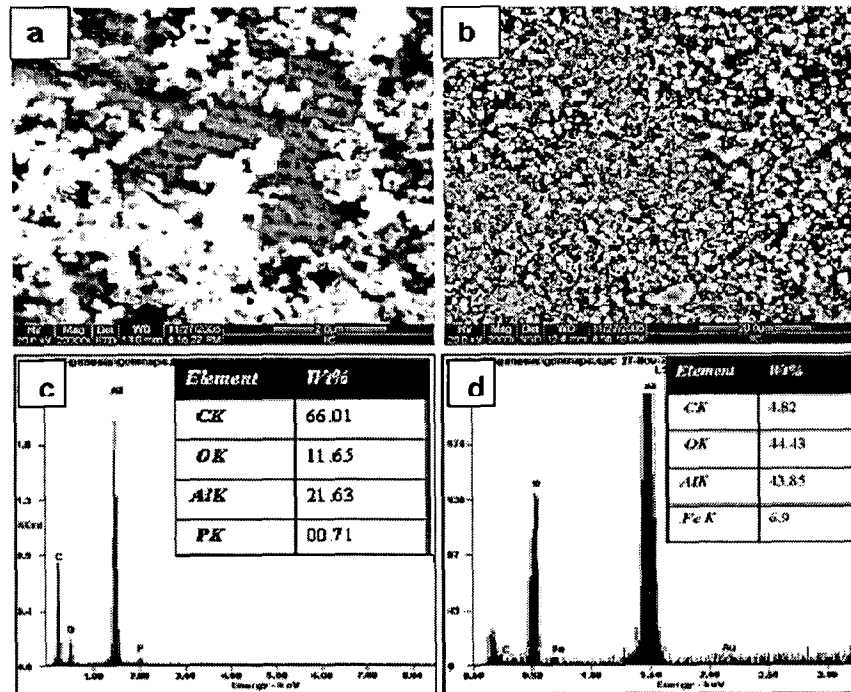
Fig. 6.17: FE-SEM of CNT embedded PAAO (a) before and (b) after dry sliding wear test. (c) EDS of the surface before dry sliding and (d) EDS of the surface after dry sliding

Figures 6.18 (a) and (b) show the transfer layer forming after consolidation of debris particles during dry sliding of PAAO substrate embedded with CNT/CNF. One may observe flaking out of part of transfer layer as in Fig. 6.18(a). In case of lubricated sliding, similar transfer layer forms as shown in Fig. 6.18 (c) and (d). The transfer layer in case of lubricated sliding has shown cracks as noticed in Fig. 6.18 (d).
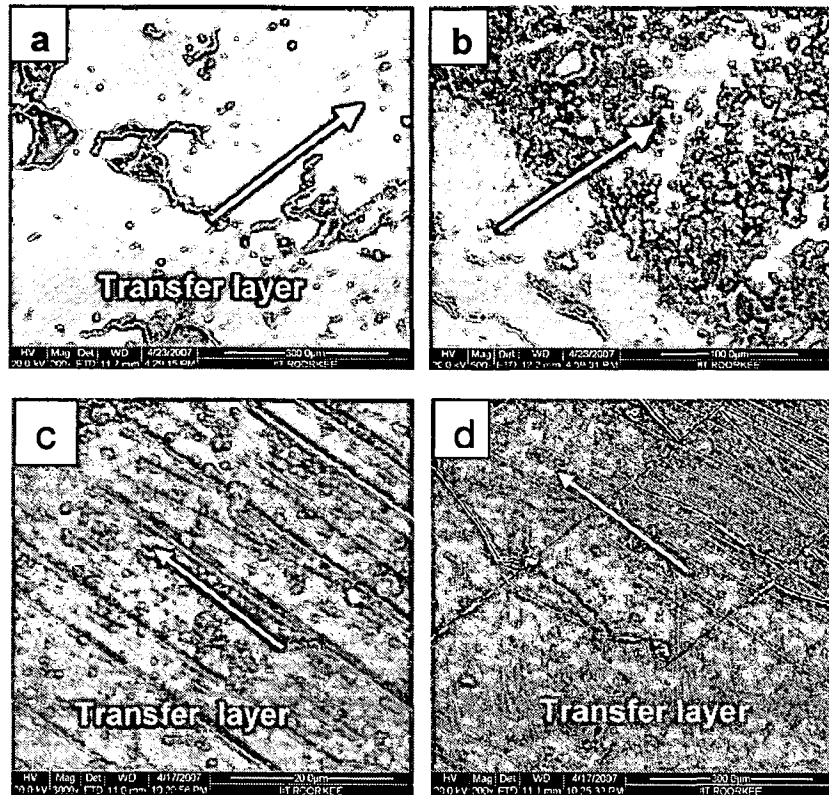
Fig. 6.18: FESEM images of the worn surface of CNT/CNF embedded PAAO (a) & (b) after dry sliding wear and (c) & (d) after lubricated sliding wear tests conducted at a normal load of 20 N and constant sliding speed of 0.5 m/s.

Figure 6.19 depicts FESEM–EDS images of worn out bare PAAO samples anodized in 5 wt.% phosphoric acid bath after tribology test conducted at a constant sliding speed of 0.5 mps and 20 N normal load. The debris particle generated shows oxides of aluminium and iron as given by EDS analysis.
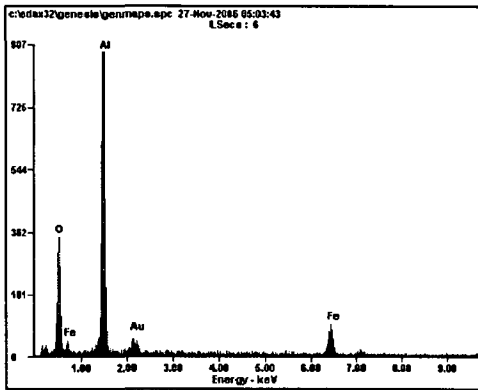
Element	Wt%	At%
OK	26.83	43.58
AlK	50.67	48.80
AuM	08.56	01.13
FeK	13.94	06.49
Matrix	Correction	ZAF
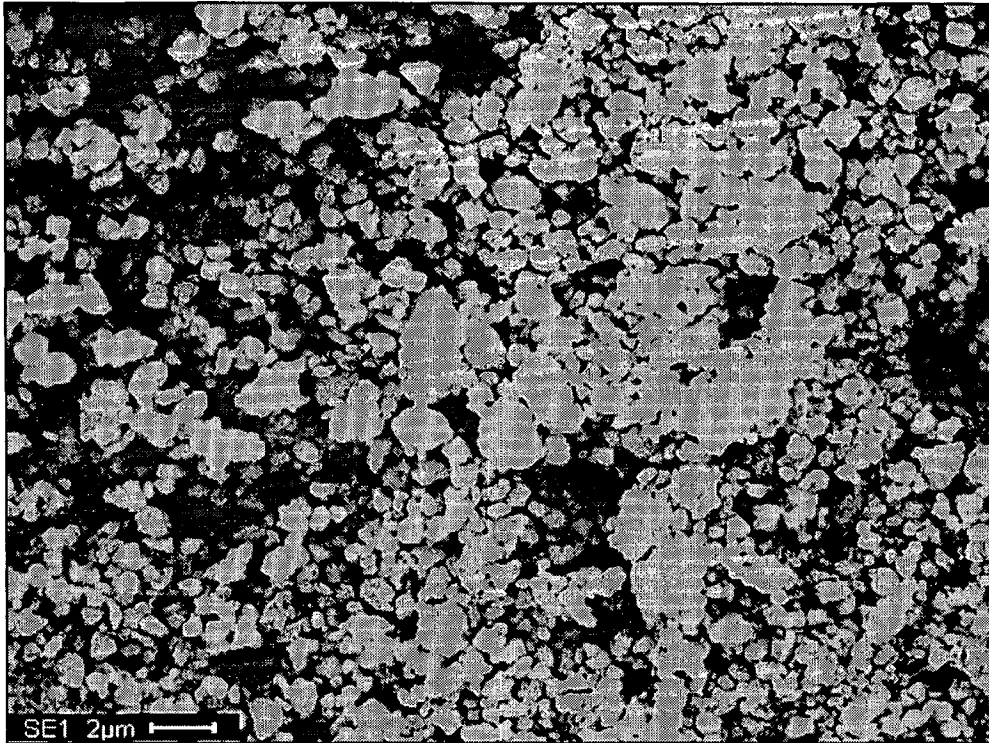
Fig. 6.19: FESEM –EDS images of worn out bare PAAO samples anodized in 5 wt.% phosphoric acid bath at 120 V after tribology test conducted at a constant sliding speed of 0.5 mps and 20 N normal load.

Figure 6.20 shows FE-SEM of the worn surface of PAAO after dry sliding in (a) and (b) at different magnifications. The surface clearly shows transfer layer formation and its cracking.
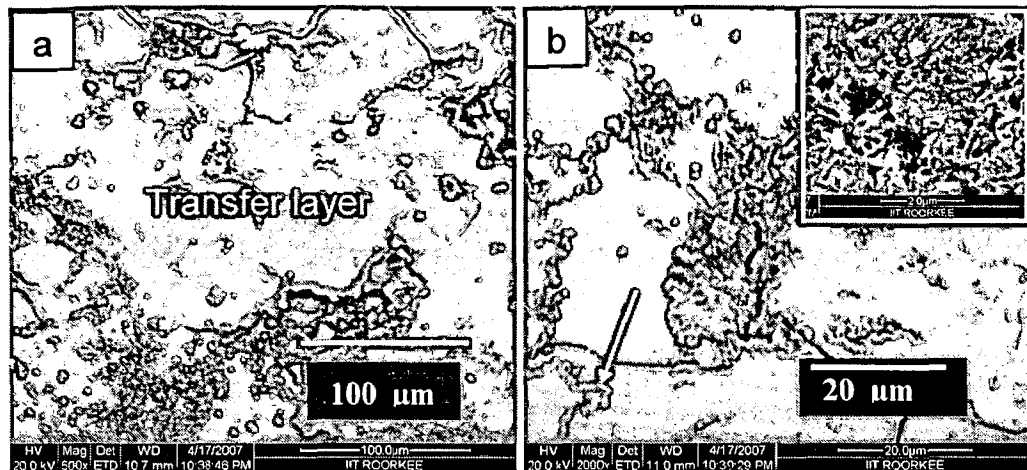
Fig. 6.20: FE-SEM of wear scars CNT embedded PAAO sample after dry sliding over a distance of 400 m at a normal load of 20 N and constant sliding speed of 0.5 m/s, at different magnifications. Arrow marks indicate direction of sliding.

6.2 CNTs/CNFs IN PAAO ANODIZED IN OXALIC ACID.

Tribological behaviour of selected PAAO samples anodized in 3 wt. % oxalic acid bath and the PAAO embedded with CNTs / CNFs under dry sliding and sliding in presence of lubricant oil have been studied. The results have been presented in the following paragraphs:

6.2.1 Dry Sliding Wear

Dry sliding wear tests have been carried out by sliding a cylindrical pin with glued test sample sliding against a counterface of EN-32 hardened steel disc at four different normal loads of 5, 10, 15 and 20 N and a constant sliding speed of 0.5 m/s. The relative humidity has been kept in the range between 40-70% during the conduct of wear tests. The cumulative volume loss, wear rate and wear coefficients have been determined following the same procedure described earlier.

(a) Wear of CNTs/CNFs embedded PAAO

Figures 6.21 shows the variation of cumulative volume loss with sliding distance conducted at different fixed normal loads of 5, 10, 15 and 20 N and a fixed sliding speed

197

of 0.5 m/s for CNTs/CNFs embedded porous anodized alumina. For a given normal load, the cumulative volume loss increases linearly with increase in sliding distance. The variation has been subjected to linear least square fit and the equations for cumulative volume loss, V in mm^3, with sliding distance, D in m, for the loads of 5, 10, 15 and 20 N are respectively,

$$V = 0.06356\ D + 0.5 \tag{6.21}$$

$$V = 0.04962\ D + 0.4 \tag{6.22}$$

$$V = 0.0388\ D + 0.35 \tag{6.23}$$

$$V = 0.0342\ D + 0.1 \tag{6.24}$$

and the correlation coefficients are 0.97701, 0.98881, 0.99744 and 0.9975 respectively
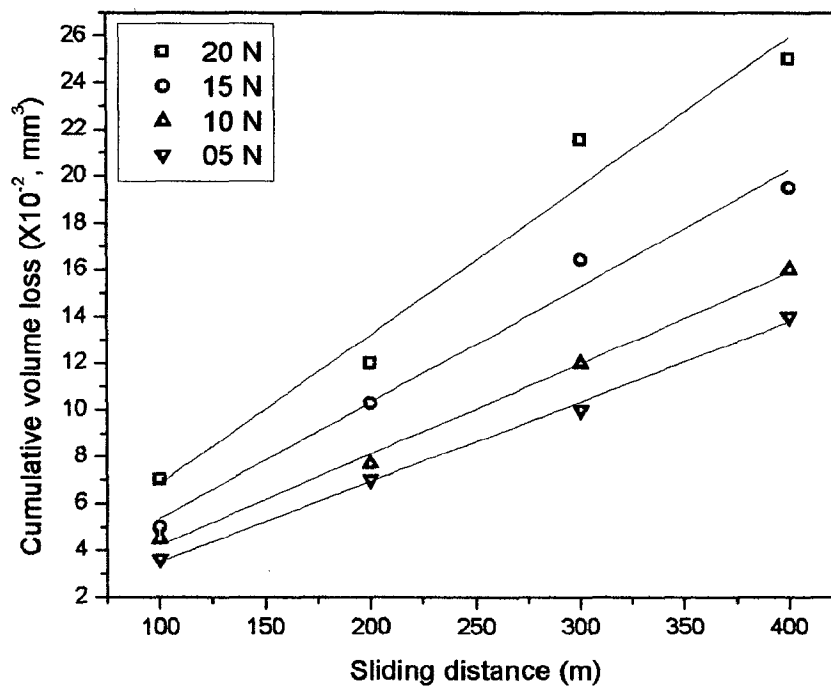
Fig. 6.21:   The variation of cumulative volume loss with sliding distance at different normal load of 5, 10, 15 and 20 N at a sliding speed of 0.5 m/s for CNTs/CNFs embedded porous anodized alumina prepared in 3 wt. % Oxalic acid electrolytic bath.

Figure 6.22 shows the variation of wear rate (V/D) with increasing load (L), the variation has been expressed by two linear segments, viz, first less steep segment is in

the load range of 5 to 10 N and second steeper segment. The linear least square fit equations for lower load (<10 N) and at higher load (>10 N) are as follows:

$$(V/D) = 0.00248 \ L + 0.01352 \qquad\qquad (6.25)\ (a)$$
$$(V/D) = 0.00292 \ L + 0.0296 \qquad\qquad (6.25)\ (b)$$
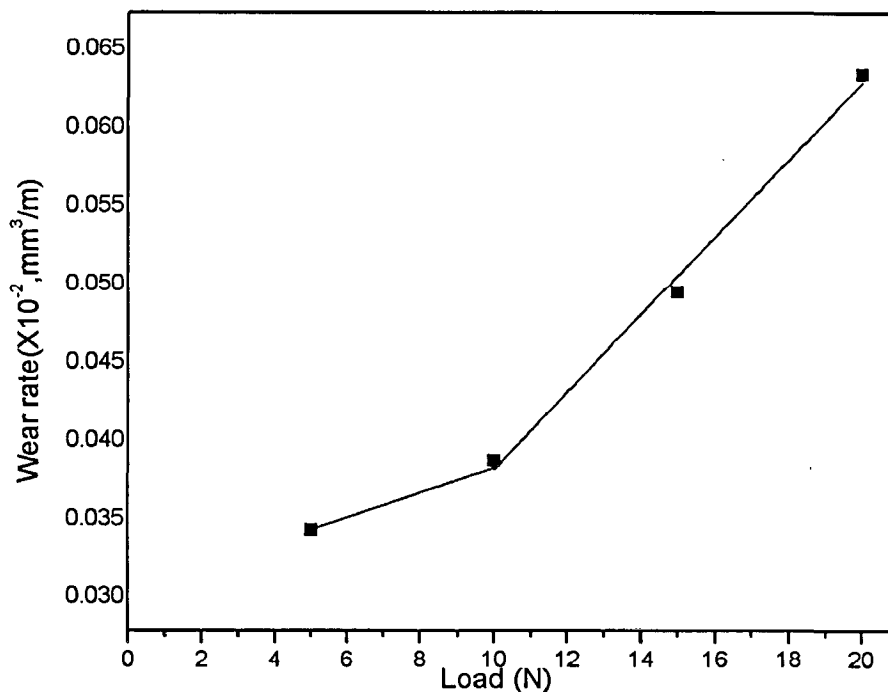
Fig. 6.22: The variation of wear rate at different normal load of 5, 10, 15 and 20 N for a sliding speed of 0.5 m/s for CNTs/CNFs embedded PAAO, prepared in 3 wt. % oxalic acid bath.

The wear coefficient may thus be calculated using the hardness (H) of 19 GPa (Mo et al, 2005) for CNT/CNF embedded PAAO as 5.548×10^{-4}.

(b) Dry Sliding Wear of PAAO

Figure 6.23 shows the variation of cumulative volume loss with sliding distance conducted at different normal loads of 5, 10, 15 and 20 N and a fixed sliding speed of 0.5 m/s for PAAO anodized in oxalic acid bath. For a given normal load, the cumulative volume loss increases linearly with increasing sliding distance as shown in fig. 6.2. The

199

linear least square fit equations relating the cumulative volume loss, V in mm³, with sliding distance, D in m, for the loads of 5, 10, 15 and 20 N are respectively given by,

$$V = 0.2113 \, D - 1.65 \qquad (6.26)$$

$$V = 0.1480 \, D - 2.0 \qquad (6.27)$$

$$V = 0.0939 \, D - 1.0 \qquad (6.28)$$

$$V = 0.0513 \, D + 0.1 \qquad (6.29)$$

and the correlation coefficients are respectively 0.99332, 0.99945, 0.99788 and 0.99160.
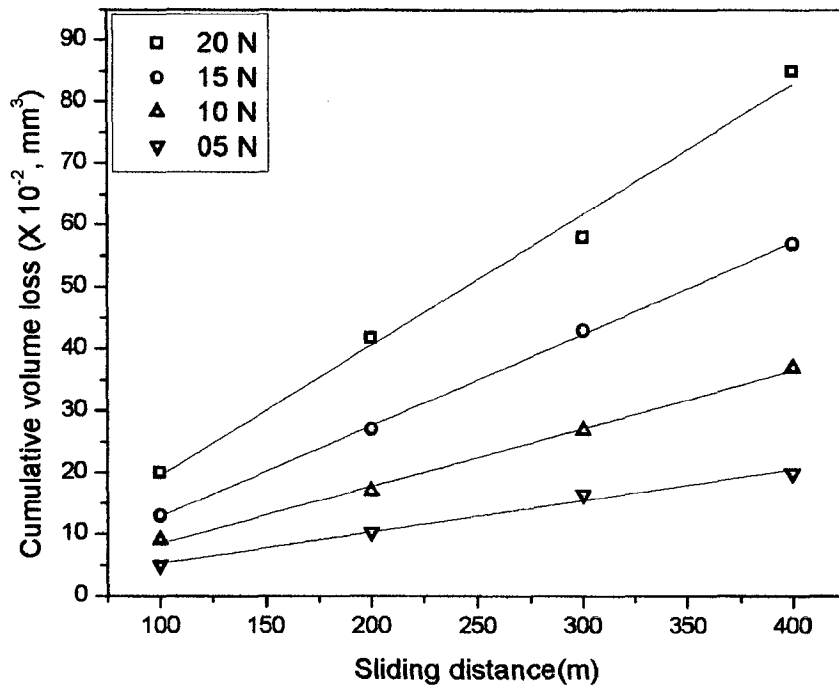
Fig.6.23: The variation of cumulative volume loss with sliding distance at different normal load of 5, 10, 15 and 20 N and a sliding speed of 0.5 m/s for PAAO prepared in 3 wt. % oxalic acid bath.

200

Figure 6.24 shows the variation of wear rate (V/D) with increasing load (L), which is linear. The linear least square fit of this variation yields the following equation with coefficient of correlation of 0.99.

$$(V/D) = 0.01068 \ L - 0.0074 \qquad\qquad (6.30)$$
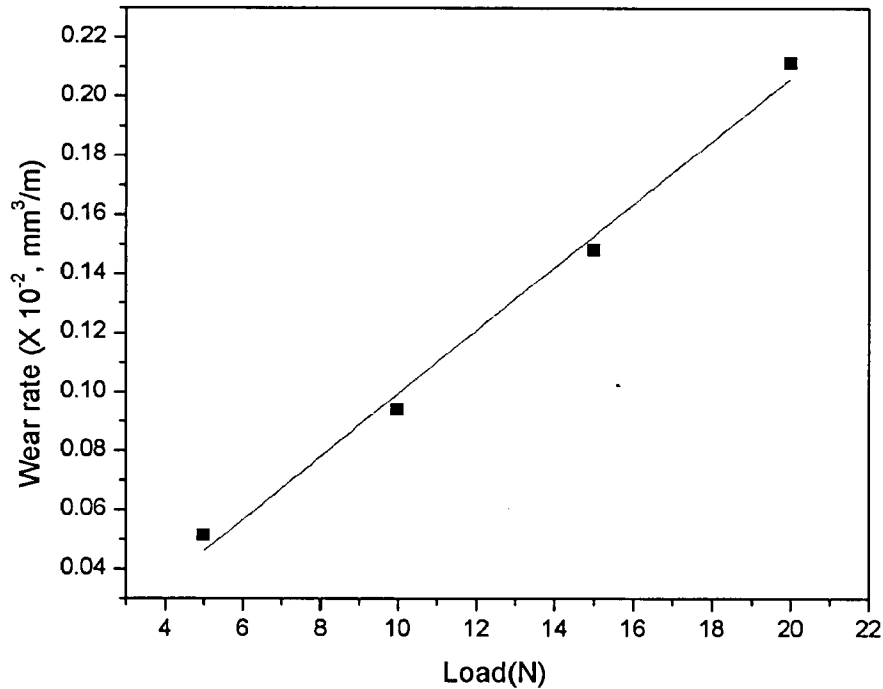
Fig. 6.24: The variation of wear rate at different normal load of 5, 10, 15 and 20 N for a sliding speed of 0.5 m/s for PAAO prepared in 3 wt. % oxalic acid bath.

The wear coefficient may thus be calculated using the hardness of 13 GPa for PAAO (Ko et al, 2006) as 13.815×10^{-4}.

6.2.2 Lubricated wear (PAAO and CNTs/CNFs embedded porous anodized alumina)

(a) Wear of lubricated CNTs/CNFs embedded PAAO

Figures 6.25 shows the variation of cumulative volume loss with sliding distance conducted at different fixed normal loads of 5, 10, 15 and 20 N and a fixed sliding speed

of 0.5 m/s for CNTs/CNFs embedded PAAO. For a given normal load, the cumulative volume loss increases linearly with increasing sliding distance. The linear least square fit equations cumulative volume loss, V in mm^3, with sliding distance, D   in m, for the loads of 5, 10, 15 and 20 N are respectively,

$$V = 0.0091\ D + 0.25 \qquad (6.31)$$

$$V = 0.0069\ D + 0.3 \qquad (6.32)$$

$$V = 0.0056\ \ D + 0.0 \qquad (6.33)$$

$$V = 0.00332\ D - 0.05 \qquad (6.34)$$

and the correlation coefficients   are 0.99154, 0.97320, 0.95753 and 0.9977174 respectively
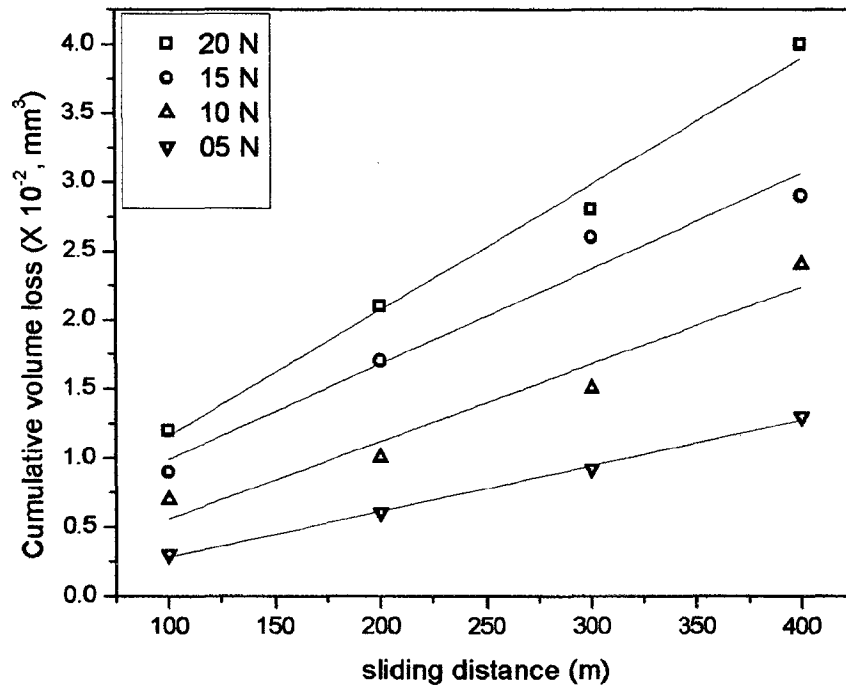
Fig.6.25:   The variation of cumulative volume loss with sliding distance at different normal load of 5, 10, 20 and 30 N and a sliding speed of 0.5 m/s for lubricated CNTs/CNFs embedded PAAO prepared in Oxalic acid electrolyte.

Figure 6.26 shows the variation of wear rate (V/D) with increasing load (L), which is linear. The linear least square fit of this variation yields the following equation with coefficient of correlation of 0.99.

$$(V/D) = 0.00037 \, L + 0.00157$$

(6.35)
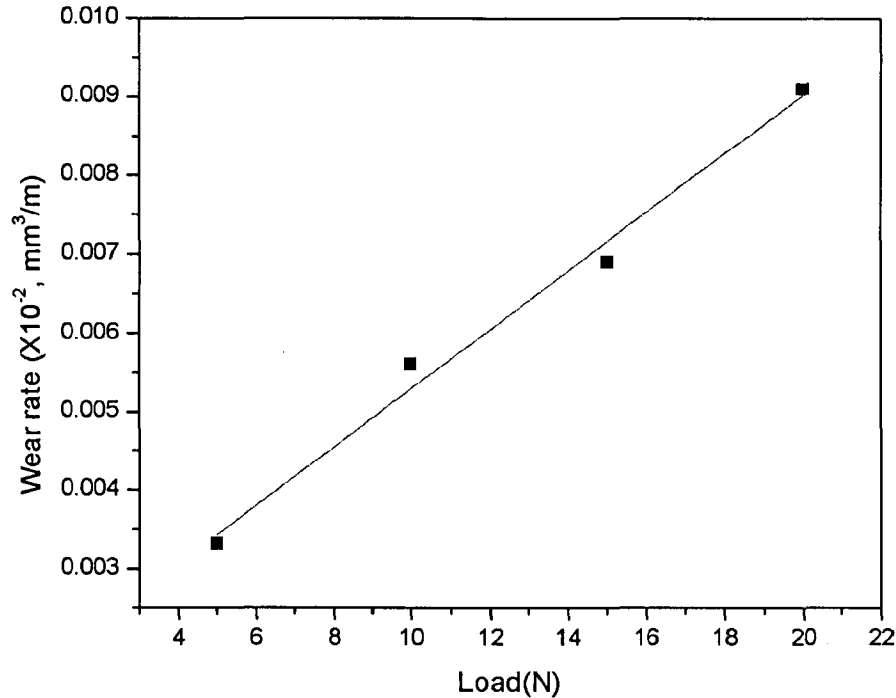
Fig.6.26: The variation of wear rate at different normal load of 5, 10, 15 and 20 N for a sliding speed of 0.5 m/s for lubricated CNTs/CNFs embedded PAAO prepared in 3 wt. % oxalic acid bath.

The wear coefficient may thus be calculated using the hardness (H) of 19 GPa (Mo et al, 2005) for lubricated CNT/CNF embedded PAAO as 7.068×10^{-5}.

(b)   Wear of lubricated porous anodized alumina.

Figure 6.27 shows the variation of cumulative volume loss with sliding distance conducted at different fixed normal loads of 5, 10, 15 and 20 N and a fixed sliding speed of 0.5 m/s for oil lubricated PAAO. For a given normal load, the cumulative volume loss increases linearly with increase in sliding distance. The variation (in the fig. 6.3) has been subjected to linear least square fit and the equations relating cumulative volume loss, V in mm^3, with sliding distance, D in m, for the loads of 5, 10, 15 and 20 N are respectively,

$$V = 0.0329 \, D - 0.45 \tag{6.36}$$

$$V = 0.0206 \, D + 1.7 \tag{6.37}$$

$$V = 0.0192 \ \ D - 0.4 \tag{6.38}$$

$$V = 0.00642 \, D + 0.004 \tag{6.39}$$

and the correlation coefficients are 0.99824, 0.950099, 0.97264 and 0.968978 respectively.
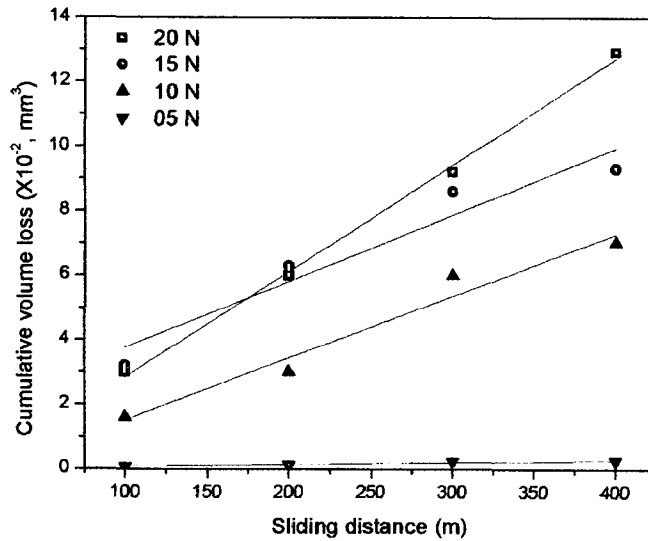
Fig. 6.27: The variation of cumulative volume loss with sliding distance at different normal load of 5, 10, 15 and 20 N and a sliding speed of 0.5 m/s for lubricated PAAO prepared in oxalic acid electrolyte.

Figure 6.28 shows the variation of wear rate (V/D) with increasing load (L), which is linear. The linear least square fit of this variation yields the following equation with coefficient of correlation of 0.94.

$$(V/D) = 0.00162 \, L + 0.00043 \tag{6.40}$$

Wear rate (X 10^{-2}, mm^3/m)

0.22
0.20
0.18
0.16
0.14
0.12
0.10
0.08
0.06
0.04

4   6   8   10   12   14   16   18   20   22

Load(N)
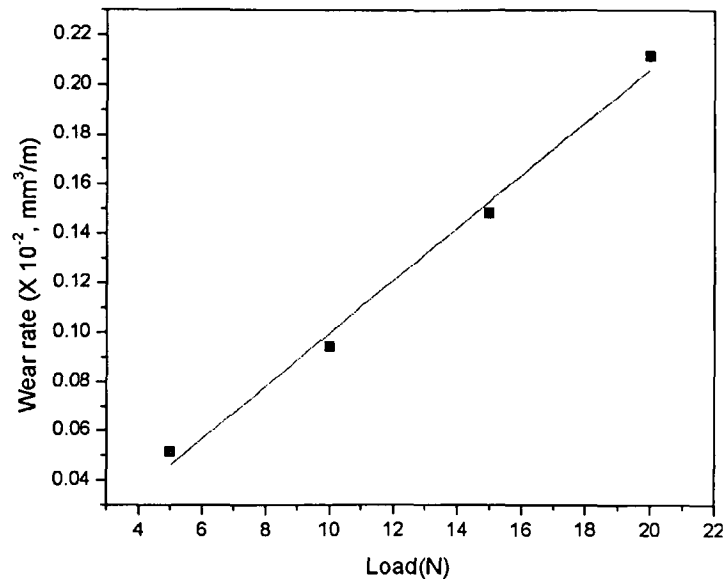
Fig. 6.28: The variation of wear rate at different normal load of 5, 10, 15 and 20 N for a sliding speed of 0.5 m/s for lubricated PAAO prepared in 3 wt.% oxalic acid bath.

The wear coefficient may thus be calculated using the hardness of 13 GPa for PAAO (Ko et al, 2006) as 2.01 x 10^{-4}.

6.2.3 Comparison of Wear Behaviour of PAAO and PAAO with Embedded CNT/CNF

Figure 6.29 shows the comparison of cumulative volume loss of (a) porous anodized aluminium oxide (PAAO), (b) CNTs/CNFs embedded PAAO (c) Lubricated PAAO and (d) Lubricated CNTs/CNFs embedded PAAO at 20 N load and sliding speed of 0.5 mps, after sliding a distance of 400 m. It is found that volume loss is the maximum (85 x 10^{-2} mm^3) in case of porous anodized aluminium oxide (PAAO) and it decreases by almost 85% in case of lubricated sliding. When CNT/CNF is embedded in PAAO, the volume loss under dry sliding wear decreases by about 50 %. In case of lubricated sliding of CNTs/CNFs embedded in PAAO the volume loss decreases by about 91 % from that observed under dry sliding wear of this surface.
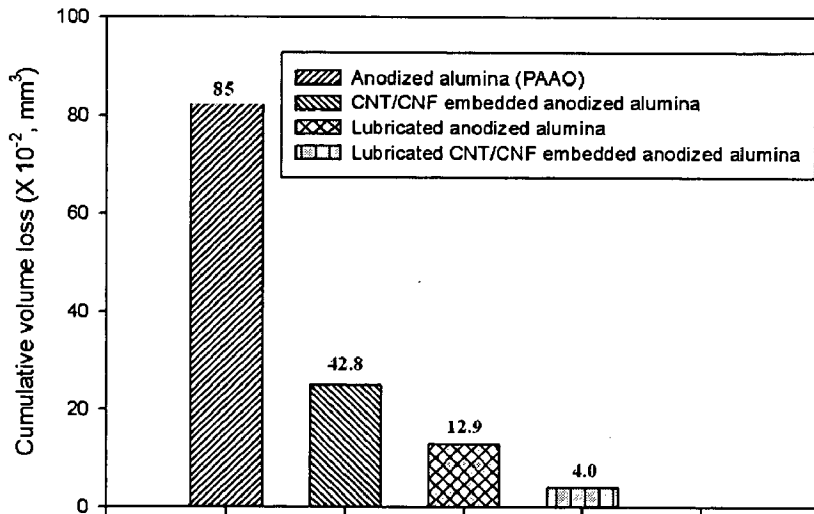
Fig. 6.29: Comparison of cumulative volume loss of (a) PAAO, (b) CNTs/CNFs embedded PAAO (c) Lubricated PAAO and (d) Lubricated CNTs/CNFs embedded PAAO at 20 N load and sliding speed of 0.5 m/s, in oxalic acid bath after sliding a distance of 400 m.

6.3 SLIDING WEAR OF PAAO ANODIZED IN PHOSPHORIC AND OXALIC ACID BATH BEFORE AND AFTER EMBEDDING CNT/CNF

Figure 6.30 shows the wear rates of PAAO obtained after anodization in phosphoric acid and oxalic acid bath and it is interesting to observe that the PAAO layer anodized in oxalic acid has a relatively lower wear rate compared to that for PAAO anodized in phosphoric acid at all the loads investigated. Similarly, PAAO embedded with CNT/CNF also shows lower wear when PAAO is obtained in oxalic acid bath compared to that in phosphoric acid bath. It is interesting to observe that PAAO obtained in phosphoric acid bath and embedded with CNT/CNF shows under dry sliding similar wear rates observed for PAAO anodized in oxalic acid under lubricated condition. However, for PAAO anodized in either phosphoric acid or oxalic acid bath and embedded with CNT/CNF show similar wear rates under lubricated sliding.
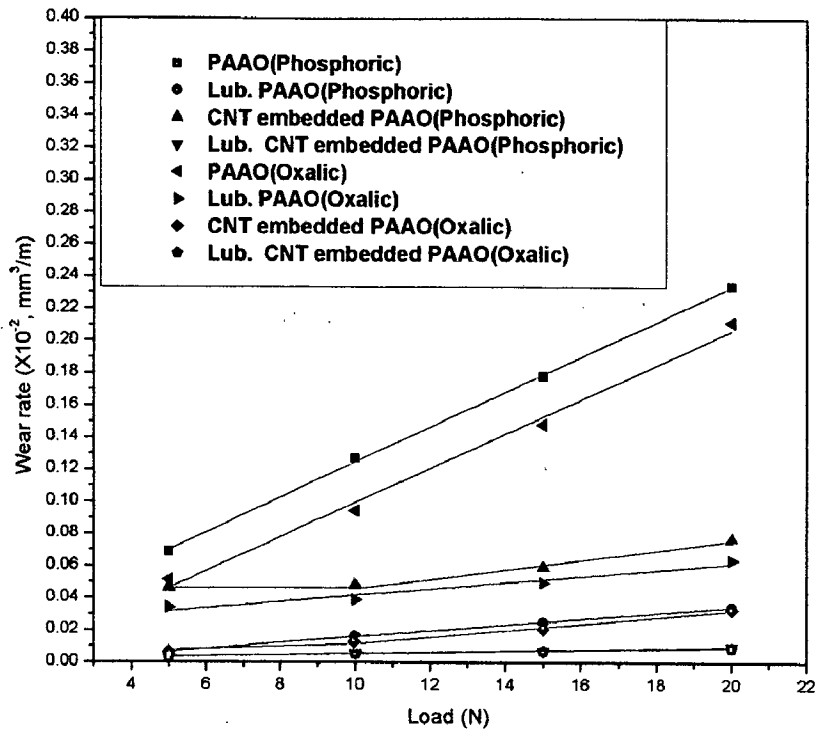
Fig. 6.30: Comparison of wear rate with normal load for Porous anodized alumina
(PAAO), CNTs/CNFs embedded anodized alumina; Lubricated porous
anodized alumina and Lubricated CNTs/CNFs embedded porous
anodized alumina samples prepared in phosphoric and oxalic acid
electrolytic bath.

Figure 6.31 shows the comparison of wear coefficients for Porous anodized

alumina (PAAO) and CNTs/CNFs embedded PAAO for PAAO anodized in either

phosphoric acid or oxalic acid bath while under dry or lubricated sliding against

counterface of hardened EN-32 steel. (observations)
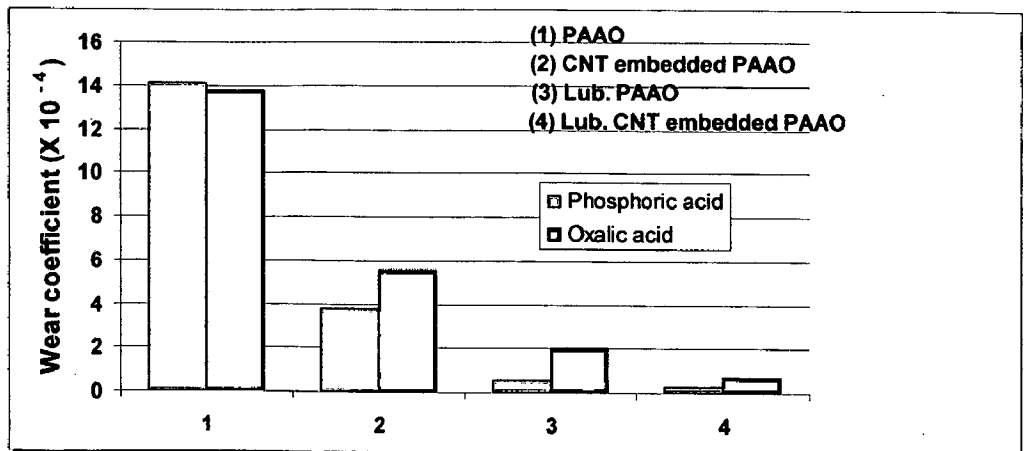
Fig. 6.31:   Comparison of wear coefficients of Porous anodized alumina (PAAO), CNTs/CNFs embedded PAAO; Lubricated PAAO and Lubricated CNTs/CNFs embedded PAAO samples prepared in phosphoric and oxalic acid electrolytic bath.

6.4   SLIDING FRICTION OF PAAO ANODIZED IN PHOSPHORIC AND OXALIC ACID BATH BEFORE AND AFTER EMBEDDING CNT/CNF

Figure 6.32 shows the comparison of variation of Average value of coefficients of friction with load under dry sliding for PAAO obtained after anodization in phosphoric acid and oxalic acid baths. One can easily observe that the PAAO layer anodized in oxalic acid has higher friction coefficient compared to that for PAAO anodized in phosphoric acid at all the loads investigated. Similarly, PAAO embedded with CNT/CNF under dry sliding also shows higher friction coefficient when PAAO is obtained in oxalic acid bath compared to that in phosphoric acid bath. It is interesting to observe that PAAO obtained in phosphoric acid bath and embedded with CNT/CNF shows lower friction coefficient under dry sliding than those observed under lubricated sliding of PAAO anodized in oxalic acid bath.
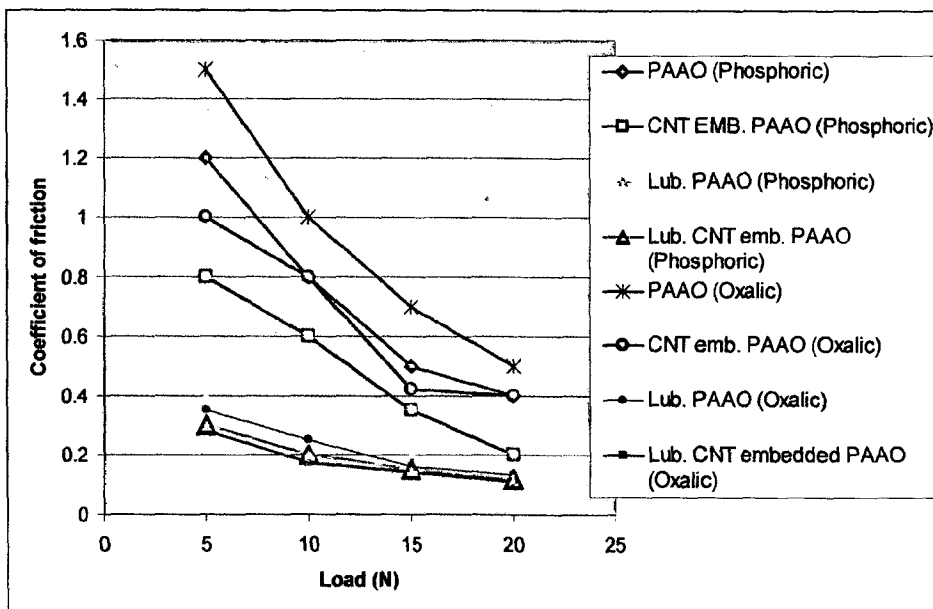
Fig. 6.32: Variation of Average value of coefficient of friction (μ) with normal load at a constant sliding speed of 0.5 m/s, in case of PAAO and CNTs/CNFs embedded PAAO samples.

6.3. DISCUSSION

Dry sliding friction and wear behaviour of the PAAO alone and that with CNT/CNF embedded has been studied in a pin on disc set-up against the counterface of hardened steel under different normal loads and fixed sliding speed. PAAO has been obtained by anodization of aluminium in phosphoric acid and oxalic acid baths. In addition, wear tests on the same surfaces have been carried out in presence of lubricating oil and the results have been compared with the corresponding results for dry sliding.

For a given normal load, the cumulative volume loss increases linearly with increasing sliding distance during dry sliding of PAAO embedded with CNTs/CNFs for PAAO anodized either in phosphoric acid bath or oxalic acid bath as shown in Figs. 6.1 and 6.1 respectively. But the wear rate in both the materials shows a similar trend of relatively smaller slope with increasing load when the load is 10 N or lower but beyond the load of 10 N, the slope increases significantly as shown in Fig. 6.2 and 6.22. It is thus evident that above 10 N, there could be cracking and faster removal of flakes of transfer layer as indicated in Fig. 6.18(a). It is interesting to observe that the PAAO anodized in oxalic acid bath and embedded with CNT/CNF has significantly lower wear rates compared to those observed in PAAO anodized in phosphoric acid bath and embedded with CNT/CNF as shown in Fig. 6.30. The strength of PAAO is dependent on the details of pore structure and it is responsible for this difference in wear rates (Ko et al, 2006 and Xia et al, 2004).

When the cumulative volume loss during dry sliding wear of PAAO prepared in phosphoric acid bath is compared with that of PAAO embedded with CNT/CNF as shown in Figs. 6.3 and 6.1 respectively, it is observed that embedding by CNT/CNF has reduced cumulative volume loss from 93.7 to 42.8 x 10^{-2} mm^3 (i.e. about 54%) as shown in Fig. 6.9 and the coefficient of friction reduces by about 50% to 0.2 at normal load of 20N, as shown in Fig. 6.13. It is thus, evident that CNT/CNF which has a graphene structure of low shear strength over it, is very effective in reducing both wear and friction. The variation of wear rates with normal load is linear for PAAO as shown

in Fig. 6.4 and it does not show two linear segments as observed after embedding of CNT/CNF as shown in Fig.6.2.

Figures 6.23 and 6.21 represent the cumulative volume losses during dry sliding wear of PAAO prepared in oxalic acid bath and that of PAAO embedded with CNT/CNF. It can be observed that embedding by CNT/CNF has reduced cumulative volume loss from 85.0 to 42.8 x 10^{-2} mm^3 (i.e. about 50%) as shown in Fig. 6.29 and the coefficient of friction reduces by about 20% to 0.4 at normal load of 20N, as shown in Fig. 6.32. Therefore, the reduction in coefficient of friction in this case is less compared to the case of phosphoric acid treated PAAO. However, no significant change in cumulative volume loss has been observed between the samples prepared in phosphoric acid and oxalic acid baths. It can further be noticed that the nature of the variation of wear rates with normal load is for PAAO and PAAO embedded with CNT/CNF are similar to the phosphoric acid case.

In case of lubricated sliding for PAAO prepared in phosphoric acid bath, the cumulative volume loss increases more or less linearly with increasing sliding distance for PAAO embedded with CNT/CNF as shown in Fig. 6.5. The same trend is observed for lubricated sliding of PAAO as shown in Fig. 6.7 and it is interesting to observe that there is very little volume loss at the lowest load of 5 N under lubricated sliding. But at higher load the situation changes considerably to result in increased volume loss from 3.9 to 13.7 mm^3 after sliding for 400 m distance at 20 N load, as shown in Fig.6.9. Under lubricated sliding the run-in period is considerably less than that in dry sliding as indicated by friction and the steady state is more steady in terms of friction as could be inferred by comparing Figs.6.12 and 6.14. Under lubricated sliding, the coefficient friction is lower than those observed under dry sliding for both PAAO and PAAO embedded with CNT/CNF but the former has a higher friction than the latter as indicated in Fig. 6.15. It may also be observed that the difference in friction between PAAO and PAAO embedded with CNT/CNF decreases with increasing load. The wear and friction on the surface of PAAO alone and that with CNTs/CNFs embedded in pores decrease markedly in presence of lubricating oil over those observed under the dry sliding condition due to formation of a lubricating oil film which has even lower shear resistance than CNT/CNF.

In the case of PAAO samples prepared in oxalic acid bath, the coefficients of friction were measured for the lubricated PAAO and lubricated PAAO with CNT/CNF embedded samples for all the loads used in the case of PAAO prepared in phosphoric

acid bath. Fig 6.30 shows a combined view of the variation of coefficients of friction with different loads for all types of the samples studied.

The wear coefficient of the PAAO and PAAO embedded with CNT/CNF prepared in phosphoric acid under dry and lubricated sliding condition shows that PAAO has the highest wear coefficient followed by PAAO embedded with CNT/CNF under dry sliding and the lubricated sliding shows considerably lower wear coefficient but in the same order as shown in Fig. 6.11. Fig. 6.31 shows comparison of wear coefficients for samples prepared in both types of electrolytic baths, viz. phosphoric and oxalic acid. It can be noted that the trend in case of oxalic and phosphoric acid anodized samples is the same, while the wear coefficient of oxalic acid anodized samples have been found more than those observed for PAAO anodized in phosphoric acid bath, except for the case of the surface of PAAO alone.

Wear resistance of PAAO surface anodized in oxalic acid is generally more than that of the surface anodized in phosphoric acid bath. However, the friction coefficient is significantly lower on the surface anodized in phosphoric acid bath as compared to that on the surface anodized in the oxalic acid bath but there is a trend reversal for friction in presence of lubricating oil i.e. friction is less on surface anodized in oxalic acid bath compared to that anodized in phosphoric acid bath. The increased wear resistance under dry sliding in case of oxalic acid is attributed to the lower porosity as the PAAO has been obtained by anodization at lower temperatures leading to approximately 20 % porosity as against 30- 40 % porosity obtained in PAAO anodized in phosphoric acid bath. The wear resistance of a more porous film should be less as its hardness is less as determined by nano-indentation (Ko et al, 2006).

The friction in PAAO embedded with CNTs/CNFs is less when PAAO is obtained by anodization in phosphoric acid bath as compared to that obtained in oxalic acid bath. CNT/CNF growth has taken place generally at the top surface in case of PAAO anodized in oxalic acid and so, it is removed quickly during wear. While PAAO obtained in phosphoric acid bath has larger size pores and CNT/CNF grows right from the bottom of the pores and so, during dry sliding there is continuous supply of CNT fragments in the transfer layer. However, the trend is reversed in case of oil lubrication, there is enhanced stability of the transfer layer as the wear rate is considerably reduced and the initial transfer layer with more carbon gives an advantage in terms of friction to the PAAO grown in oxalic acid bath. For very long sliding time this advantage may go away.

The study of friction and wear under dry and lubricated sliding of PAAO surface anodized in phosphoric acid and oxalic acid bath before and after embedding CNT/CNF has indicated that the wear debris generated during sliding, forms a transfer layer, which protects the underlying material. This transfer layer is continuously flaking off and re-forming. At lower load, sometimes the process of flaking off does not take place as in PAAO embedded in CNT/CNF leading to two regimes of wear as indicated by the wear rate. Presence of lubricant lowers the friction and the tangential force which reduces the tendency of the transfer layer to flake off leading to truly low friction and low wear surface of PAAO embedded with CNT/CNF. It is interesting to observe that even PAAO without CNT/CNF also provides reasonably low friction and wear.

The major conclusions of the present investigation are given here in three segments. The first segment includes conclusions related to the formation of porous anodized aluminium oxide (PAAO). The second segment describes the in-situ synthesis of CNTs/CNFs in pores of PAAO to prepare composite surface. The conclusions pertaining to the tribological behaviour of CNTs/CNFs embedded PAAO composite surface developed are outlined in the third segment.

A.   PAAO ON PURE AND COMMERCIAL ALUMINIUM SUBSTRATES

1. Anodizations of pure and commercial aluminium in 5 wt.% phosphoric acid at 10 ° C show that the pore ordering can be obtained for anodization voltage of 200 V in the case of pure aluminium and of 160 V for commercial pure aluminium.

2. Defective structures with broken cell walls in PAAO develop when anodizations are carried out at above self-ordering voltages. Such defective structures have been observed in the anodized layers developed from pure aluminium and commercial pure aluminium at 210 V and 200 V respectively.

3. The pre-treatment of the samples in both pure aluminium and commercial pure aluminium lead to better pore-ordering and out of three types i.e. annealing, electropolishing and combined operations of electropolishing and annealing, the last type has been proved to be resulting in best pore ordering.

4. Anodizations have been carried out by two-step process. An well-ordered pore structure has been found for both pure aluminium and commercial pure aluminium substrates.

5. The anodization was carried out at different bath temperatures (10° to 30 °C). The anodization in higher temperature results in soft, higher porous and relatively thin PAAO films with simultaneous decrease in barrier layer thickness. Therefore lower temperature is favourable for better pore ordering in PAAO.

6. The porosity variation has not been found significant over the voltage range 40 to 100 V, the porosity level decreases from 37.43% at 100 V to about 16.5% at 200 V for pure aluminium substrate.

7. The effect of time period for anodization was studied using oxalic acid bath. Anodizations of pure aluminium samples in 3 wt % oxalic acid electrolyte have been carried out by two step process by taking anodization time for first step as a parameter. PAAO samples have been prepared for four different time periods 1, 4, 8 and 12 hours for first step, while keeping second step time fixed at 1 hour. Visual inspection on the pore structure micrographs and their FFT analysis shows that the pore ordering improves with the increase in first step anodization time period. While significant improvement is noticeable in 8 hour treated sample compared to the samples treated for 1 and 4 hours, the improvement is insignificant when observed on 12 hour treated sample. Therefore first step anodization for 8 hour under the present experimental situation can be considered as optimum time period.

8. Anodizations have been carried out in three different electrolytes of concentrations 3, 5, 7 wt% phosphoric acid solutions at 20°C at a fixed voltage. Current density increases almost linearly with the increase in concentration which in turn results in increased pore diameter and interpore distance.

9. Average pore diameters and interpore spacing in well-ordered PAAO structures are respectively 250 nm and 490 nm for phosphoric acid, 52 nm and 100 nm for oxalic acid and 26 nm and 50 nm for sulphuric acid.

10. The effect of experimental conditions (viz. stirring, replenishment of the electrolyte, etc) and parameters (e.g. nature and concentration of electrolyte, temperature, processing time, pre-treatment schedule etc. for anodizations) on the PAAO structures developed on both pure aluminium and commercial pure aluminium has been studied. The experimental conditions and the parameters have thus been optimized with an objective to obtain a well-ordered structure in the anodized film.

B   CNTs/CNFs EMBEDDED PAAO COMPOSITE SURFACE

11. The optimized PAAO structures has been used as template for in-situ synthesis of CNTs/CNFs by catalytic CVD method using acetylene gas as carbon precursor and ammonia gas etchant medium. The CVD process was conducted in a specially designed (laboratory) experimental setup.

12. The temperature of the decomposition has been optimized to 650 °C from the conduct of several experiments at different temperatures between 500° and 650 °C, with a highest yield of CNTs/CNFs.

13. The experiments with different types of catalysts such as Co, Ni, Co-Ni and oxid e compound ($LiNi_{0.5}Co_{0.5}O_2$), have shown several contrasting features. While, CNTs with Co catalyst are mostly grown from the bottom of the pores, but the CNTs grown with $LiNi_{0.5}Co_{0.5}O_2$ catalyst are relatively more graphitized, however growth takes place primarily on the template surface.

14. It has also been observed that the CNTs growth takes place from middle of the pores. This is due to catalyst particles get stuck at the walls of the pores instead of getting deposited at the bottom of the pores.

C   TRIBOLOGICAL BEHAVIOUR OF THE COMPOSITE SURFACE

15. Sliding friction and wear behaviour of PAAO and PAAO embedded CNT/CNF under dry and lubricated conditions has been studied. The samples were prepared in phosphoric acid and oxalic acid baths. Experiments were conducted for different normal loads and fixed sliding speed in dry as well as lubricated conditions.

16. The cumulative volume loss under a given normal load increases linearly with increase in sliding distance during dry sliding of PAAO embedded with CNT/CNF.

17. The wear rate in both the materials shows a similar trend of relatively smaller slope with increase in load up to 10 N and the slope increases significantly beyond 10 N.

18. The PAAO anodized in oxalic acid bath and embedded with CNT/CNF has significantly lower wear rates compared to those in PAAO anodized in phosphoric acid bath and embedded with CNT/CNF.

19. Embedding PAAO with CNT/CNF reduces cumulative volume loss from 93.7 to 42.8 x 10^{-2} mm^3 (about 54 %). The coefficient of friction reduces from 0.4 to 0.2 (about 50 %) at 20 N.

20. Embedding PAAO with CNT/CNF reduces cumulative volume loss from 85.0 to 42.8 x 10^{-2} mm^3 (about 50 %). The coefficient of friction reduces from 0.5 to 0.4 (about 20 %) at 20 N.

21. In lubricated sliding for PAAO prepared in phosphoric acid bath the cumulative volume loss increases almost linearly with increase in sliding distance when embedded with CNT/CNF. At higher load an increased volume loss from 3.9 to 13.7 mm^3 after sliding of 400m distance at 20 N load occurs.

22. Under lubricated sliding the coefficient of friction is lower than under dry sliding conditions for both PAAO and PAAO embedded with CNT/CNF.

23. PAAO has the highest wear coefficient followed by PAAO embedded with CNT/CNF under dry sliding. The lubricated sliding shows considerably lower wear coefficient.

24. Wear resistance of PAAO surface anodized in oxalic acid is generally more than that anodized in phosphoric acid bath. Friction coefficient is less for PAAO sample prepared in phosphoric acid bath compared to the one prepared in oxalic acid bath, but there is trend reversal for friction in presence of lubricating oil, i.e., friction is less on surface anodized in oxalic acid bath as compared to that in case of phosphoric acid bath.

REFERENCES

1. Ajayan, P.M., (1999), "Nano tubes from carbon", *Chem. Rev.*, 99, 1787.

2. Ajayan, P.M., (2000), in Handbook of Nano-structured materials and nanotechnology, ed. H.S. Nalwa, Organic polymers and biological materials, Academic Press.

3. Ajayi, O. O., Erdemir, A., Fenske G. R. and F. A. Nichols, (1992), "Tribological behavior of oil-lubricated TiN-coated steel", *Surface and Coatings Technology*,54/55.

4. AlMawlawi D, Cooms N, Moskovits M., (1991), "Magnetic properties of Fe deposited into anodic aluminum oxide pores as a function of particle size". *J Appl Phys*, 70, 4421

5. Alsyouri, H. M., Langheinrich, C., Lin, Y. S., Ye, Z., & Zhu, S., (2003), "Cyclic CVD modification of straight pore alumina membranes", *Langmuir*, 19(18), 7307.

6. Amelinckx, S., Zhang, X. B., Bernaerts, D., Zhang, X. F., Ivanov, V., & Nagy, J. B. (1994), "A formation mechanism for catalytically grown helix-shaped graphite nanotubes", *Science*, 265(5172), 635

7. Andriotti, A.N., M. Menou, G. Frandakis, (2000), *Phys. Rev. Lett.*, 85(1), 3193.

8. Anne-Claire Dupuis, (2005), "The catalyst in the CCVD of carbon nanotubes-a review", *Progress in Materials Science*, 50(1), 929.

9. Annual book of ASTM Standards, (1979), Part 9 B 374, ASTM. Philadelphia, PA, 173.

10. Archard, J. F., (1953), "Contact and rubbing of flat surfaces", *Journal of Applied Physics*, 24, 981.

11. Asoh, H. Nishio, K., Nakao, M., Tamamura, T. and Masuda, H., (2001), "Conditions for Fabrication of Ideally Ordered Anodic Porous Alumina Using Pretextured Al", *J. of electrochemical society*, 148, B152

12. Ba, L. and Li, W.S., (2000), "Influence of anodizing conditions on the ordered pore formation in anodic alumina", *J. Phys. D: Appl. Phys.*, 33, 2527

13. Baker R. T. K. and P. A. Harris.,(1978), "Chemistry and Physics of Carbon", edited by P. L. Walker and P. A. Thrower, Marcel Dekker, New York ,14, 83,165.

14. Baker, R.T.K., (1989), "Catalytic growth of carbon filaments", *Carbon*, 27, 315.

15. **Baker, R.T.K., Kim, M.S., Chambers, A., Park, C., Rodriquez, N. M., (1997),** "The relationship between metal particle morphology and the structural characteristics of carbon deposits", *Stud. Surf. Sci. Catal.*, 111, 99.

16. **Bandyopadhyay, S., Millerz, A E , Changz, H C Banerjeez, G., Yuzhakovz, V** Yuex, D-F Rickerk, R E Jonesk, S., **(1996),** " Electrochemically assembled quasi-periodic quantum dot arrays", *Nanotechnology* ,7(1),360

17. **Bera, M.K. Sanyal, M.K.** Banerjee, R., Kalyanikutty, K.P., Rao, C.N.R., **(2008),** "Effect of vibrations on the formation of gold nanoparticle aggregates at the toluene–water interface", *Chemical Physics Letters*, 461, 97.

18. **Bethune, D.S., Kiang, C.H., De Vries, M.S., Gorman, G., Savoy, R., Vazquez, J., Beyers, R., (1993),** "Cobalt-catalysed growth of carbon nanotubes with single-atomic-layer walls", *Nature*, 363(1), 605.

19. **Bhushan, IB and Gupta, B.K., (1991),** Handbook of Tribology: Materials, Coatings and Surface Treatment, McGraw hill, New York,

20. **Binnig, G., Quate CF, Berber C.,(1986),** "Atomic force microscope", *Phys. Rev. Lett.*,56,930.

21. **Biro, L.P., Bernardoca, C.A., Tibbetts, G.G., (2001),** Ph. Lambin (Ed.), Carbon Filaments and Nanotubes: Common Origin, Differing Applications? Kluwer Academic Publishers, Dordrecht.

22. **Biswas, S. K., Pramanik, P., (2008),** "Studies on the gas sensing behaviour of nanosized $CuNb_2O_6$ towards ammonia, hydrogen and liquefied petroleum gas", *Sensors and Actuators B*: Chemical, 133(2), 449

23. **Bocchetta, P., Sunseri,C., Chiavarotti, G., and Quarto, F.D., (2003),** "Microporous alumina membranes electrochemically grown" , *Electrochimica Acta*.48,3175.

24. **Boskovic, B.O., Stolojan, V., Khan, R.U.A., Haq, S. Silva, S.R.P.,(2002),** "Large-area synthesis of carbon nanofibres at room temperature", *Nature Mater.*, 1, 165.

25. **Bower C, Zhou O, Zhu W, Werder, D.J, Jin S., (2000a),** " Nucleation and growth of carbon nanotubes by microwave plasma chemical vapor deposition", *Appl Phys Lett.*, 77(17),2767

26. **Bower, C., Zhu, W., Jin, S. and Zhou, O., (2000b),** "Plasma-induced alignment of carbon nanotubes", *Appl. Phys. Lett.*, 77, 830

27. **Bradhurst, D. H. and Leach, J. S. L., (1966),** "The Mechanical Properties of Thin Anodic Films on Aluminum", *J. Electrochem. Soc.*, 113, 1245.

28. **Brown**, G.M.,K. Shimizu, Kobayashi, K., Skeldon, P. , Thompson, G.E., Wood, G.C.,**(1998)**, "The growth of a porous oxide film of a unique morphology by anodic oxidation of an Al-0.5 wt% Ni alloy", *Corros. Sci.*, 40, 1575.

29. **Brukh**, R., & Mitra, S.,**(2006)**, "Mechanism of carbon nanotube growth by CVD", *Chemical Physics Letters*, 424(1-3),126

30. **Bull** S. J. and Chalker P. R., **(1992)**, "Lubricated sliding wear of physically vapour deposited titanium nitride", *Surface and Coatings Technology*, 50,117.

31. **Burgos**, N. Marı́a Paulis and Mario Montes, **(2003)**, "Preparation of Al2O3/Al monoliths by anodisation of aluminium as structured catalytic supports", *Journal of material chemistry*,13,1458.

32. **Cai** H, Yuan FY, Xue, QJ.,**(2004)**, "Investigation of tribological properties of polyimide/carbon nanotube nanocomposites", *Mater Sci Eng A-StructMater Prop Microstruct Process*,364(1-2),94

33. **Cai**, A. Zhang, H., Hua, H. and Zhang, Z., **(2002)**, "Direct formation of self-assembled nanoporous aluminium oxide on SiO_2 and Si substrates", *Nanotechnology*, 13, 627

34. **Cantrell**, J.H., Qian, M. , Ravichandran, M.V. and **Knowles, K.M.**, **(1990)** 'Scanning electron acoustic microscopy of indentation-induced cracks and residual stresses in ceramic materials', *Applied Physics Letters*, 57, 1870.

35. **Carpick** RW, Flater EE, Sridharan K., **(2004)**, "The effect of surface chemistry and structure on nano-scale adhesion and friction", *Polym. Mater.*, 90, 197.

36. **Casell**, A.M., Raymakers, J.A., Kong, J. and Dai, H.J., **(1999)**, "Large scale CVD synthesis of single-walled carbon nanotubes", *Journal of Physical Chemistry B,* 103, 6484.

37. **Chambers**, A., Nemes, T., Rodriquez, N.M., Baker, R.T.K., **(1998)**, J. *Phys. Chem. B,* 102(1),2251.

38. **Charlier**,J.C. and S. Iijima, **(2001)**, "Carbon Nanotubes, Topics in Applied Physics", edited by M. S. Dresselhaus, G. Dresselhaus, and Ph. Avouris, Springer-Verlag, Berlin 80(1),55.

39. **Che**, G., Che, G.; Lakshmi, B. B.; Fisher, E. R.; Martin, C. R., **(1998)**, "Carbon nanotubule membranes for electrochemical energy storage and production" ,*Nature,* 393(1),346.

40. Che, G., Lakshmi, B.B., Martin, C.R., Fisher, E.R., Ruoff, R.S. and Leticia Banos, **(1998)**, "Chemical vapor deposition based synthesis of carbon nanotubes and nanofibres using a template method", *Chem. Mater.*, 10 (1), 260.

41. Che, G.; Lakshmi, B. B.; Martin, C. R.; Fisher, E. R.; Ruoff, R. S., **(1998)**, "Chemical Vapor Deposition Based Synthesis of Carbon Nanotubes and Nanofibers Using a Template Method", *Chem. Mater.*, 10, 260.

42. Che, G.; Lakshmi, Fisher, E.R., Martin, C. R., **(1998)**, "Carbon nanotubule membranes for electrochemical energy storage and production", *Nature*,393, 346.

43. **Chen, P**, Zhang, H.B, Lin, G.D, Hong, Q, Tsai K.R.,**(1997)**, "Growth of carbon nanotubes by catalytic decomposition of CH4 or CO on a Ni–MgO catalyst", *Carbon*,35,1495.

44. **Chen, P. L.**, Chang, J. K., Pan, F. M., & Kuo, C. T.,**(2005)**, "Tube number density control of carbon nanotubes on anodic aluminum oxide template"' *Diamond & Related Materials*, 14(3-7), 804.

45. **Chen, W.X**, Li F, Han, G, Xia, J.B, Wang, L.Y, Tu, J.P., **(2003)**, "Tribological behavior of carbon-nanotube filled PTFE composites", *Tribol. Lett.*,15(3), 275.

46. **Chen, W.X**, Tu JP, Wang, L.Y, Gan, H.Y, Xu, Z.D, Zhang, X.B.,**(2003)**, "Tribological application of carbon nanotubes in a metal-based composite coating and composites" *Carbon*,41(2),215.

47. **Chen W.X.** , Tu J.P. , Wang L.Y. , Gan H.Y., Xu Z.D., Zhang X.B., **(2003)**, "Tribological application of carbon nanotubes in a metal-based composite coating and composites", *Carbon*, 41, 215.

48. **Chik**, H. and Xu,J.M.,**(2004)**, "Nanometric superlattices: non-lithographic fabrication, materials, and prospects", *Materials Science and Engineering R*,.43, 103.

49. **Choi** J, Sauer G, Nielsch K, Wehrspohn RB, Gosele U.,**(2003)**, "Hexagonally arranged monodisperse silver nanowires with adjustable diameter and high aspect ratio", *Chem. Mater.*, 15, 776.

50. **Choi**, J, Luo, Y., Wehrspohn,R.B., Hillebrand, R., Schilling, J. and Go¨sele, U., **(2003(a))**, "Perfect two-dimensional porous alumina photonic crystals with duplex oxide layers", *J. of applied physics*, 94(1),4757.

51. **Choi**, J. Sauer,G. Nielsch, K. Wehrspohn, R. B. and Go¨sele, U.,**(2003(b))**, "Hexagonally Arranged Monodisperse Silver Nanowires with Adjustable Diameter and High Aspect Ratio", Chem. Mater, 15, 776.

52. **Ciambelli, P.,** Sannino, D., Sarno, M., Leone, C., & Lafont, U., **(2007)**. "Effects of alumina phases and process parameters on the multiwalled carbon nanotubes growth", *Diamond & Related Materials*, 16(4-7), 1144.

53. **Couteau E,** Hernadi K, Seo JW, Thie^n-Nga L, Miko' C, Gaa'l R, **(2003)** "CVD synthesis of high-purity multiwalled carbon nanotubes using CaCO$_3$ catalyst support for large-scale production", *Chem. Phys. Lett.* 378, 9.

54. **Christian P.** Deck, Vecchio Kenneth, **(2006),** "Prediction of carbon nanotube growth success by the analysis of carbon–catalyst binary phase diagrams", Carbon 44, 267.

55. **Diggle, J.W.** Downie, T.C. and Goulding, C.W., **(1969),** "Anodic oxide films on aluminium" , *Chem. Rev.69,365.*

56. **Dai, H. J., (2001),** Carbon Nanotubes, Topics in Applied Physics, edited by M. S. Dresselhaus, G. Dresselhaus, and Ph. Avouris, Springer-Verlag, Berlin.,80(1),29.

57. **Dai, H.J. (2002)** "Carbon Nanotubes: Synthesis, Integration, and Properties", Acc. Chem. Res. 35,1035.

58. **Dai, H.J., (2002),** "Carbon nanotubes: opportunities and challenges", *Surf. Sci.,* 500 218.

59. **Davis, J.R., (1993),** Aluminum and Aluminum Alloys, ASM International, OHIO, 88.

60. **Debuyck, F.** Moors M. and Peteghem, A.P. Van, **(1994),** "Correlation between the thickness and the specific mass of an anodization layer on aluminium and the measured current transient", *Materials Chemistry and Physics,* 38,169.

61. **Deck, C. P.,** Vecchio,K. **(2006),** "Prediction of carbon nanotube growth success by the analysis of carbon–catalyst binary phase diagrams", Carbon 44 , 267.

62. **Deuis, R. L.,** Subramanian,C. & Yellupb, J. M., **(1997),** "Dry Sliding Wear Of Aluminium Composites-A Review", *Composites Science and Technology,* 57(4),415.

63. **Diggle, D.** Routkevitch, T. Bigioni, M. Moiskovits, and J. M. Xu, J. **(1969)** *Phys. Chem.,* 100, 14037.

64. **Diggle, J. W.,** Downie, T. C., & Goulding, C. W.,**(1969),** "Anodic oxide films on aluminum", *Chemical Reviews,* 69(3), 365.

65. **Donnet, C.,** Erdemir, A., **(2004),** "Historical developments and new trends in tribological and solid lubricant coatings", *Surface and Coatings Technology,* 180/181,76

66. **Dupuis, A. C. (2005),** "The catalyst in the CCVD of carbon nanotubes—a review", *Progress in Materials Science*, 50(8), 929.

67. **Ebbesen T.W., (1996),** "Carbon nanotubes Preparation and properties.", *Boca Raton*: CRC press.

68. **Edwards J. D. and Keller F., (1944),** "The structure of Anodic oxide coatings," *Trans. Am. Inst.Mining Met. Engrs.*, 156(1), 288,

69. **Edwards, J. D. and Keller, F.,(1941),**"Formation of Anodic Coatings on Aluminium,"*Trans. Electrochem. Soc.*,79(1),135.

70. **Endo, M. Kim, Matusita, Y.A., Hayashi, T., Biro, T., Bernardoca, L.P., Tibbetts, C.A., Lambin Ph. G.G., (Ed.), (2001),** Carbon Filaments and Nanotubes: Common Origins, Differing Applications? Kluwer Academic Publishers, Dordrecht, 51.

71. **Falvo, MR, Taylor, RM, Helser, A., Chi, V., Brooks, F.P, Washburn, S., (1999),** "anometre-scale rolling and sliding of carbon nanotubes",*Nature*,397(6716),236.

72. **Fan, R. Buczko, A. Puretzky, A., Geohegan, D. B., Howe, J.Y., Pantelides, S.T. and Pennycook, S. J., (2003),** "Nucleation of Single-Walled Carbon Nanotubes", *Physics Review Letters*, 90(14),145501.

73. **Kibria, F. A. K. M., Mo, Y. H., Nahm, K. S., & Kim, M. J., (2002),** 'Synthesis of narrow-diameter carbon nanotubes from acetylene decomposition over an iron–nickel catalyst supported on alumina', *Carbon*, 40(8), 1241.

74. **Flahaut, E., Govindaraj, A., Peigney, A., Laurent, Ch., Rousset, A., and Rao, C.N.R. (1999),** " Synthesis of single-walled carbon nanotubes using binary (Fe, Co, Ni) alloy nanoparticles prepared in situ by the reduction of oxide solid solutions", *Chem. Phys. Lett.*, 300, 236.

75. **Fratila, L.E -Apachitei , Graeve,I.D.,. Apachitei,I. ,. Terryn ,H., Duszczyk ,J.,(2006),** "Electrode temperature evolution during anodic oxidation of AlSi(Cu)alloys studied in the wall-jet reactor" , *Surface and Coatings Technology*, 200,5343.

76. **Gao, H., Mu, C., Wang, F., Xu, D., Wu, K., Xie, Y., et al., (2003),** "Field emission of large-area and graphitized carbon nanotube array on anodic aluminum oxide template", *Journal of Applied Physics*, 93(1), 5602.

77. **Gaponenko, N. V.,. Molchan, I. S., Thompson, G. E., Skeldon, P., Pakes,A., Kudrawiec, R. , Bryja, L. , Misiewicz, J. , (2002),** "Photoluminescence of Eu-doped titania xerogel spin-on deposited on porous anodic alumina," *Sensors and Actua tors A-Physical*, 99(1),71.

78. **Habazaki, H.,** Shimizu, K., Skeldon, P., Thompson, G.E., Wood G.C, Zhou, X., **(1997),** "Nanoscale Enrichments Of Substrate Elements In The Growth Of Thin Oxide Films" *Corros. Sci.* .39(4),731.

79. **Han, Y. -H.,** Taylor, A. and **Knowles, K.M., (2008).** 'Characterisation of organic-inorganic hybrid coatings deposited on aluminium substrates', *Surface & Coatings Technology,* 202(1), 1859.

80. **Harris, P.J.F.** Carbon Nanotubes and Related Structures: New Materials for the Twenty-first Century, Cambridge University Press, Cambridge, 1999.

81. **Harris P. J. F., (2004),** "Carbon nanotube composites", *International Materials Reviews* ,41(3),77.

82. **Harris, P. J. F.,** (2004) ,"Carbon nanotube composites", *International Materials Reviews,*49,31.

83. **Harris, P.J.F.** ,(**1999),** "Carbon Nanotubes and Related Structures: New Materials for the Twenty-first Century", Cambridge University Press, Cambridge,

84. **Helveg, S,** Lo'pez-Cartes C, Sehested, J, Hansen ,P.L, Clausen, BS, Rostrup-Nielsen, JR, **(2004),** "Atomic-scale imaging of carbon nanofibre growth". *Nature,;*427:426.

85. **Hernadi, K. (2002),** "Cat alytic synthesis of multiwall carbon nanotubes from methylacetylene", *Chemical Physics Letters,* 363(1-2), 169.

86. **Hernadi, K.,** Konya, Z., Siska A., Kiss J., Oszko A., Nagy J. B., Kiricsi I., **(2002),**

87. **Hirata, A,** Yoshioka N., **(2004),** "Sliding friction properties of carbon nanotube coatings deposited by microwave plasma chemical vapor deposition", *Tribol. Int.,*37(11–12),893.

88. **Hirth,** J. P. and Lothe, J. **(1968),** "Theory of Dislocations", McGraw-Hill, New York.

89. **Hoar,** T. P., & Mott, N. F. **(1959),** "A mechanism for the formation of porous anodic oxide films on aluminium", *J. Phys. Chem. Solids,* 9, 97.

90. **Hornyak, GL,** Dillon AC, Parilla PA, Schneider JJ, Czap N, Jones KM., **(1999),** "Template synthesis of carbon nanotubes", *Nanostruct Mater;*12:83–8.

91. **Hsu, S.M.,** Ming Shen, **(2004),** "Wear prediction of ceramics", *Wear,* 256, 867.

92. **Hu. W.,** Gong, D. and Chen, Z., Yuan, L. and Saito, K., Grimes, C.A. and Kichambare, P., **(2001),** "Growth of well-aligned carbon nanotube arrays on silicon substrates using porous alumina film as a nanotemplate", *Applied Physics Letters,* 79(19),3083

93. **Huang,** Z.P., Wang, D.Z., Wen, J.G., Sennett, M., Gibson, H., Ren, Z.F., **(2002),** "Effect of nickel, iron and cobalt on growth of aligned carbon nanotubes", *Appl. Phys. A* 74,387.

94. **Huh,** Yoon Jeong Yong Lee, Jinwoo Cheon,b Young Kyu Hong,c Ja Yong Koo,c Tae Jae Leed and Cheol Jin Lee **(2003),** "Controlled growth of carbon nanotubes over cobalt nanoparticles by thermal chemical vapor deposition", *J. Mater. Chem.,* 13, 2297.

95. **Hulteen,** J. C., Chen, H. X., Chambliss, C. K. and Martin, C. R. , **(1997),** "Template synthesis of carbon nanotubule and nanofiber arrays", *Nano-Structured Materials,* 9, 133.

96. **Hunter,** M. S. and Fowle, P.E., **(1954a),** "Determination of Barrier Layer Thickness of Anodic Oxide Coatings", *J. Electrochem. Soc.,* 101, 481.

97. **Hunter,** M. S. and Fowle, P.E., **(1954b),** "Fact ors affecting the formation of anodic oxide coatings", *J. Electrochem. Soc.,*101,514.

98. **Hutchings,** I. M., **(1992),** "Tribology: Friction and wear of Engineering Materials," Edward Arnold, London.

99. **Harris, P.J.F.** Carbon Nanotubes and Related Structures: New Materials for the Twenty-first Century, Cambridge University Press, Cambridge, 1999.

100. **Iijima,** S., ".(1991),** "Helical microtubules of graphitic carbon", *Nature,*354,56.

101. **Ismagilov,**Z.R., Kerzhentsev, M.A. Shikina, N.V. Lisitsyn, A.S. Okhlopkova, L.B. Barnakov, Ch.N. Sakashita, M. T.and Tadokoro, K. Catal. **(2005),** *Today,* 102(103) 58.

102. **Iwasaki,** T, Motoi T, Den T., **(1999),** "Multiwalled carbon nanotubes growth in anodic alumina nanoholes", *Appl Phys Lett.,* 75, 2044.

103. **Jahanmir,** S., Suh, N. P. , Abrahamson, E. P., **(1974),** "Microscopic observations of the wear sheet formation by delamination", *Wear,* 28, 235.

104. **Jahanmir,** S.,Suh, N. P., Abrahamson, E. P., **(1975),**"The Delamination theory of wear and the wear of a composite surface", *Wear,*32,33.

105. **Jeong,** S., Lee, K.H., **(2003),** "Fabrication of the aligned and patterned carbon nanotube field emitters using the anodic aluminum oxide nano-template on a Si Wafer", *Synth. Met.,* 139(1),385.

106. **Jeong,** S.H., Hwang, HY, Lee, K.H, Jeong, Y., **(2001),** "Template-based carbon nanotubes and their applications to a field emitter", *Appl Phys Lett,*78(1),2052.

107. **Jeong,** SH, Hwang, HY, Hwang SK, Lee, KH., **(2004),** "Carbon nanotubes based on anodic aluminum oxide nano-template", *Carbon,*42(1), 2073.

108. Jessensky, O. Muller, F. Gosele, U., **(1998(a))**, "Self-Organized Formation of Hexagonal Pore Structures in Anodic Alumina", *J. Electrochem. Soc.*,145(11), 3735.

109. Jessensky, O., Müller, F., & Gösele, U.,**(1998)**, "Se lf-organized formation of hexagonal pore arrays in anodic alumina", *Applied Physics Letters*, 72, 1173.

110. Jia, Y., Zhou, H., Luo, P., Luo, S., Chen, J., Kuang, Y.,**(2006)**, "Preparation and characteristics of well-aligned macroporous films on aluminum by high voltage anodization in mixed acid.", *Surface & Coatings Technology*, 201(1),513

111. José - Yacamán, M. , Miki-Yoshida, M., and Rendón, L., **(1993)**, "Ca talytic growth of carbon microtubules with fullerene structure", *Appl. Phys. Lett.* 62 (6),657.

112. Juang, Z.Y., Chien, I.P., Lai, J.F., Lai, T.S., Tsai, C.H., **(2004)**, "The effects of ammonia on the growth of large-scale patterned aligned carbon nanotubes using thermal chemical vapor deposition method," *Diamond and Related Materials* , 131, 1203.

113. Jung, K.H., Boo, J.H., Hong, B., **(2004)**, "Synthesis of carbon nanotubes grown by hot filament plasma-enhanced chemical vapor deposition method", *Diamond Relat. Mater.* 13(1), 299.

114. Kaatz, F. H., Siegal, M. P., Overmyer, D. L., Provencio, P. P., & Jackson, J. L.,**(2003)**, "Diameter control and emission properties of carbon nanotubes grown using chemical vapor deposition", *Materials Science & Engineering C*, 23(1-2), 141.

115. Kaatz, F.H., Siegal, M.P., Overmyer, D.L., Provencio, P.P., Jackson,J.L., **(2003)**, "Diameter control and emission properties of carbon nanotubes grown using chemical vapor deposition." *Materials Science and Engineering C*, 23, 143

116. Kaur, Narinder, **Dharamvir, K.**, Jindal, V.K., **(2008)**, "Dimerization and fusion of two C60 molecules", *Chemical Physics* 344 (1), 176.

117. Kawakamea M., Bressan, J. D., **(2006)**, "Study of wear in self-lubricating composites for application in seals of electric motors", *J. of matls. Proc. Tech.*, 179 74

118. Keller, F., Hunter M. and Robinson D. L., **(1953)**, "Structural Features of Oxide Coatings on Aluminium", *Journal of the Electrochemical Society*,100(9), 411.

119. Kim, M.J., T.Y. Lee, J.H. Choi, J.B. Park, J.S. Lee, S.K. Kim, J.B. Yoo and C.-Y. Park, **(2003)**, "Growth of carbon nanotubes with anodic aluminum oxide formed on the catalytic metal-coated Si substrate", *Diamond Relat. Mater.* 12,870.

120. **Kirchner, A.**, MacKenzie, K.J.D, Brown, I.W.M., Kemmitt, T., Bowden, M.E, **(2007),**"Structural characterisation of heat-treated anodic alumina membranes prepared using a simplified fabrication process", *Journal of membrane science* . 287, 264.

121. **Klaffke, Dieter., W¨asche, Rolf, Janakiraman, Narayanan, Aldinger, Fritz, (2006),** "Tribological characterisation of siliconcarbonitride ceramics derived from preceramic polymers", *Wear,* 260(1),711.

122. **Ko, P.L., (1987),** "Metallic wear- A review with special references to vibration-induced wear in power plant components", *Tribology International,* 20, 67.

123. **Ko, S., Lee, D., Jee, S., Park, H., Lee, K., Hwang, W. (2006),** "Mechanical properties and residual stress in porous anodic alumina structures" *Thin Solid Films,* 515, 1932.

124. **Kroto, H.W.,** Heath, J.R., O'Brien, S.C., Curl, R.F., Smalley, R.E., **(1985),** "C_{60}: Buckminsterfullerene", *Nature,* 318, 162.

125. **Kukovitsky, E. F.,** L'Vov, S. G., & Sainov, N. A., **(2000),** "VLS-growth of carbon nanotubes from the vapor", *Chemical Physics Letters,* 317(1-2), 65.

126. **Kushwaha M.K., Sil Anjan and Ray S. (2008).** ,"Carbon nanotube/nanofiber embedded nanoporous Anodized aluminium oxide surface and its tribological properties", *Journal of Nanoscience and nanotechnology,* American Scientific Publishers 8(8),4152 .

127. **Kvande, I.,** Yu, Z., Zhao, T., Rønning, M., Holmen, A., & Chen, D. "Towards Large Scale Production of CNF for Catalytic Applications", catalyst, 1, 1.

128. **Kyotani, T.,**L-F. Tsai and A. Tomita, **(1996),** "Preparation of Ultrafine Carbon Tubes in Nanochannels of an Anodic Aluminum Oxide Film. Chemistry of Materials", *Chem. Mater.* 8(1),2109 .

129. **Kashi, M. A.,** Ramazani, A , Rahmandoust M and Noormohammadi **(2007),** "The effect of pH and composition of sulfuric–oxalic acid mixture on the self-ordering configuration of high porosity alumina nanohole arrays", *J. Phys. D: Appl. Phys.,* **40** 4625

130. Kornelius Nielsch, Frank Mller, An-Ping Li, and Ulrich Gsele, (2000) "Uniform Nickel Deposition into Ordered Alumina Pores by Pulsed Electrodeposition"*Adv. Mater.*, 12, No. 8

131. Lambin, P., Loiseau, A., Culot, C., & Biro, L. P. (2002), "Structure of carbon nanotubes probed by local and global probes", *Carbon*, 40(10), 1635.

132. Landolt, D., (1987), "Review article:-Fundamental aspects of electropolishing" *Electrochemica Acta*, 32(1),1.

133. Lee, C. J., Lyu, S.C., Kim, H.-W., Park, J.W., Jung, H.M., and Park, J. (2002a), Carbon nanotubes produced by tungsten-based catalyst using vapor phase deposition method", *Chemical Physics Letters*, 361(1),469.

134. Lee, C. L, Lyu SC, Cho YR, Lee JH, Cho KI. (2001), "Diameter-controlle growth of carbon nanotubes using thermal chemical vapor deposition", *Chem Phys Lett*; 341:245

135. Lee, C.J., Park, J., and Yu, J.A.,(2002b), "Catalyst effect on carbon nanotubes synthesized by thermal chemical vapor deposition", *Chemical Physics Letters,*360(2),250.

136. Lee, J.H. Park, Kang, S.Y., (2000), "Growth of well-aligned carbon nanotubes on a large area of Co–Ni co-deposited silicon oxide substrate by thermal chemical vapor deposition", *Chem. Phys. Lett.*, 323 (3), 554.

137. Li A P, Muller F, Birner, A, Nielsch K and Gosele, U., (1999), "Polycrystalline nanopore arrays with hexagonal ordering on aluminium", *J. Vac. Sci. Technol. A.*17(1),1428.

138. Li J, Moskovits M, Haslett TL.,(1998), "Nanoscale electrodeless metal deposition in aligned carbon nanotubes", *Chem Mater,*10(1),1963.

139. Li J, Papadopoulos C, Xu JM, Moskovits M., (1999(a)), "Highly ordered carbon nanotube arrays for electronics applications", *Appl Phys Lett,*75:367.

140. Li Q, Rydberg A, Kim KS., (2006), "Lateral force calibration of an atomic force microscope with a diamagnetic levitation spring system"' *Rev. Sci. Instr.,*77(3),065105.

141. Li W.Z, Wen, JG, Ren, Z.F., (2001), "Straight carbon nanotube Y junctions", *Applied Physics Letters,*79(2),1879.

142. Li, A. P., Muller, F. and Gosele, U,(2000), "Polycrystalline and Monocrystalline Pore Arrays with Large Interpore Distance in Anodic Alumina", *Electrochem. and Solid- State Letters*, 3,131.

143. Li, A.P. Muller F. Birner A.. Nielsch K. and Gosele U., (1998(a)), "Hexagonal pore arrays with a 50–420 nm interpore distance formed by self-organization in anodic alumina" *J. Of Applied Physics*,84(11), 6023.

144. Li, J., Papadopoulos C, Xu J. (1999(b)), "Nanoelectronics: growing Y-junction carbon nanotubes", *Nature*, 402,253.

145. *Li*, Yanbo, Zheng, Maojun, Li. Ma, and Wenzhong Shen, (2006) "Fabrication of highly ordered nanoporous alumina films by stable high-field anodization" *Nanotechnology* 17, 5101

146. *Li*, Z. J. and Huang, K. L. *(2007)*, "Electrochemical Fabrication of Sandwich Nanostructures Based on Anodic Alumina". *J. Braz. Chem. Soc.*, Vol. 18, No. 2, 406-409,

147. Lo, D. and Budimanz R.A., (2007), "Fabrication and Characterization of Porous Anodic Alumina Films from Impure Aluminum Foils" *Journal of The Electrochemical Society*, 154 (1), C60.

148. Lakhtin, Y 1998, "Engineering physical metallurgy", MIR publisher. Moscow.

149. *Liu*, N.W. Datta A., Liu, C.Y, Wang, Y.L. (2003) "High-speed focused-ion-beam patterning for guiding the growth of anodic alumina nanochannel arrays", *Appl. Phys. Lett.* 82 1281,

150. Li J, Moskovits M, Haslett TL. (1998) "Nanoscale electrodeless metal deposition in aligned carbon nanotubes". *Chem Mater;* 10 1963

151. Lu, B., Bharathulwar, S., Laughlin, D.E. and Lambeth, D.N., (2000), "Time and orientation dependence of ordering in anodized aluminium for self- organized magnetic arrays" *Journal of App. Physics*, 87(9), 4721.

152. Lucas, A.A. Bruyninck V., Lambin1, Ph., Bernaerts, D., Amelinckx, S. Landuyt, J. Van, and Tendeloo, G. Van , (1998), "Electron diffraction by carbon nanotubes" *Scanning Microscopy*, 12(3),415.

153. Marangoni, R. Serp, P. Feurer, R. Kihn, Y. Kalck, P. Vahlas, C., (2001), *Carbon*, 39,443.

154. Marcelo, Kawakamea, Jos'e Divo Bressan, (2006), "Study of wear in self-lubricating composites for application in seals of electric motors", *Journal of Materials Processing Technology*, 179, 74.

155. Martin, C.R., (1994), "Nanomaterials – a membrane-based synthetic approach", *Science, 266.*

228

156. *Montero-Moreno*, J.M., Sarret, M., Müller, C. (2007 a), "Influence of the aluminum surface on the final results of a two-step anodizing" *Surface & Coatings Technology* vol. 201, pp. 6352–6357.

157. Maruyama, S., Kojima, R., Miyauchi, Y., Chiashi, S., and Kohno, M., (2002), "Low-temperature synthesis of high-purity single-walled carbon nanotubes from alcohol" *Chem. Phys. Lett.*, 360: 229.

158. Maschmann, M. R., Franklin, A. D., Amama, P. B., Zakharov, D. N., Stach, E. A., Sands, T. D, (2006), "Vertical single-and double-walled carbon nanotubes grown from modified porous anodic alumina templates", *Nanotechnology*, 17(15), 3925.

159. Masuda, H. and Hasegwa, F., (1997(b)), "Self-Ordering of Cell Arrangement of Anodic Porous Alumina Formed in Sulfuric Acid Solution". *J. Electrochem. Soc.*, 144(5), 128.

160. Masuda, H. and Satoh, M., (1996), "Fabrication of gold nanodot array using anodic porous alumina as an evaporation mask", *Japanese Journal of Applied Physics*, 35, L126.

161. Masuda, H. Kanezawa, K., Nishio, K., (2002), "Fabrication of Ideally Ordered Nanohole Arrays in Anodic Porous Alumina Based on Nanoindentation Using Scanning Probe Microscope" *Chem. Lett.* 12(3), 1218.

162. Masuda, H., Yada, K. and Osaka, A., (1998), "Self-ordering of cell configuration of anodic porus alumina with large-size pores in phosphoric acid solution", Jpn. *J. Appl. Phys.*, 37, L1340- L1342.

163. Masuda H, Fukuda K., (1995), "Ordered metal nanohole arrays made by a two-step replication of honeycomb structure of anodic alumina", *Science*, 268 1466.

164. McCaldin, S., Bououdina, M., Grant, D. M., & Walker, G. S., (2006), The effect of processing conditions on carbon nanostructures formed on an iron-based catalyst. *Carbon*, 44(11), 2273.

165. Metzger, R. M., Konovalov, V. V., Sun, M., Xu, T., Zangari, G., Xu, B., (2000), "Magnetic nanowires in hexagonally ordered pores of alumina", *IEEE Transactions on Magnetics*, 36(1) Part 1), 30.

166. Miao J. Y., Cai Y., Y. Chan F. and Wang N., (2005), "Structural Characterization of Carbon Nanotube Arrays Formed in Ultra-Long Nanochannels of Porous Alumina Templates", *Microsc Microanal* 11(Suppl 2), 1414.

167. Mikulskas, I., Juodkazis S., Tomasiunas R., Dumas J.G., (2001), "Aluminum Oxide Photonic Crystals Grown by a New Hybrid Method", Adv. Mater. 13 1574.

168. Miyoshia K., StreeK.W. t Jr., R.L. Vander Wal, Rodney Andrewsc and Ali Sayir, (2005), "Solid lubrication by multiwalled carbon nanotubes in air and in vacuum", *Tribology Letters*,19(3)

169. Montero-Moreno, J.M., Sarret, M., Müller, C. (2007 a), "Influence of the aluminum surface on the final results of a two-step anodizing" *Surface & Coatings Technology*. 201, 6352.

170. Moore, M.A., (1974), "A Review of two body abrasive wear", *Wear*, 27, 1-17

171. Mukhopadhyay, K., Koshio, K., Tanaka, N., and Shinohara, H., (1998), "A simple and novel way to synthesize aligned nanotube bundles at low temperature" *Jpn. J. Appl. Phys.*, 37: L1257.

172. Murali, T. P., Prasad, S. V., Surappa, M.K., Rohatgi, P.K. and Gopinath, K., (1982), "Friction and wear behaviour of aluminium alloy coconut shell char particulate composites", *Wear*, 80,149

173. Nagaraju N., Fonseca A., Konya, Z. Nagy J. B., (2002), "Alumina and silica supported metal catalysts for the production of carbonnanotubes", *J. Mol. Catal. A* 181, 57

174. Nagaura T., Takeuchi, F., Inoue, S., (2008), "Fabrication and structural control of anodic alumina films with inverted cone porous structure using multi-step anodizing", *Electrochimica Acta* 53, 2109.

175. Nagy, J. B G. Bister, A. Fonseca, D. Mehn, Z. Konya, I. Kiricsi, Z.E. Horvath,L.P. Biro, "On the Growth Mechanism of Single-Walled Carbon Nanotubes by Catalytic Carbon Vapor Deposition on Supported Metal Catalysts", *J. Nanosci. Nanotechnol.*, 4 (2004) 326.

176. Nielsch K, Choi J, Schwirn K, Wehrspohn R B and G"osele U., (2002), "Self-ordering regimes of porous alumina: the 10% porosity rule", *Nano Lett.* . 2, 677.

177. Nielsen J.R., Trimm D.L., (1977), "Mechanisms of carbon formation on nickel-containing catalysts", *J. Catal.* 48(1), 155.

178. Olevsky, E.A, Wang, X, Bruce, E., Stern, M.B., Wildhack, S. and Aldinger, F., (2007), "Synthesis of gold micro- and nano-wires by infiltration and thermolysis", *Scripta Materialia,* 56, 867

179. Öncel, Ç, & Yürüm, Y., (2006), "Carbon Nanotube Synthesis via the Catalytic CVD Method: A Review on the Effect of Reaction Parameters. Fullerenes", *Nanotubes and Carbon Nanostructures*, 14(1), 17.

180. Ono, S. and Masuko, N., (2003), "Evaluation of pore diameter of anodic porous films formed on aluminum", *Surface and Coatings Technology*. 169 –170,139.

181. Ono, S. Kato, N M. Saito, H. Asoh, The Electrochemical Society Proceedings Series, *Pennington*, NJ, in press.

182. Ono, S. M. Saito, H. Asoh, (2004 (b)) "Controlling Factor of Self-Ordering of Anodic Porous Alumina", *Electrochem. Solid State Lett.*, 7(1), B21.

183. Ono, S., (2005), "Self-ordering of anodic porous alumina formed in organic acid electrolytes", *Electrochimica Acta,* 51, 827.

184. *Ono,* S., Saito, M., Ishiguro, M., Asoh,H., (2004(a)) "Controlling Factor of Self-Ordering of Anodic Porous Alumina" *J. Electrochem. Soc.* 151 (8) B473.

185. *Ono,* S. M. Saito, H. Asoh, (2004 (b)) "Controlling Factor of Self-Ordering of Anodic Porous Alumina", *Electrochem. Solid State Lett.* 7, B21.

186. Paez, M.A. O. Bustos, G.E. Thompson, P. Skeldon, K. Shimizu, G.C. Wood, (2000), "Porous Anodic Film Formation on an Al-3.5 wt % Cu Alloy", *J. Electrochem. Soc.*, 147, 1015.

187. Pal, B.N., Chakravorty, D., (2006), "Humidity sensing by composites of glass ceramics containing silver nanoparticles and their conduction mechanism", *Sensors and Actuators B* 114 ,1043–1051

188. Pan ZW, Xie S. S, Chang BH, Wang CY, Lu L, Liu W, (1998), "Very long carbon nanotubes", *Nature*, 394, 631.

189. Pan, H., Gao, H., Lim, S. H., Feng, Y. P., & Lin, J., (2005), "Highly ordered carbon nanotubes based on porous aluminum oxide: fabrication and mechanism", *Journal of nanoscience and nanotechnology*, 5(2), 277.

190. Pan, H., Gao, H., Lim, S.H., Feng, Y.P., Lin, J., (2004), "Highly ordered carbon nanotubes based on porous aluminum oxide", *Journal Of Nano Science And Nano Technology*, 4(8), 1014.

191. Pan, J., Surappa, M.K., Saravanan, R.A. Liu, B.W., Yang, D.M., (1998), "Fabrication and characterization of SiC:MoSi$_2$ composites", *Materials Science and Engineering, A*244 ,191.

192. **Pan**, S.L., Zeng D.D., Zhang, H.L. Li, H.L., **(2000)**, Preparation ordered array nanoscopic gold rods by template method and its optical properties applied physics A: Material Science & Processing, 70, 637

193. **Pannala** and Wood R.F., **(2004)**, "Multiscale Simulations", *J. Nanosci. Nanotech*, 4(1), 463.

194. **Paolo** Ciambelli , Diana Sannino , Maria Sarno , Caterina Leone , Ugo Lafont, **(2007)**, "Effects of alumina phases and process parameters on the multiwalled carbon nanotubes growth", *Diamond & Related Materials*, 16, 1144.

195. **Papadopoulos** C, Rakitin A, Li J, Vedeneev AS, Xu JM., **(2000)**, "Electronic transport in Y-junction carbon nanotubes", *Phys Rev Lett*, 85:3476–9.1999; 75:2044.

196. *Patermarakis*, G. and Papandreadis, N., **(1993)**, "Study on the kinetics of growth of porous anodic al2O3 films on al metal", *Electrochim. Acta.*, 38, 1413

197. **Park**, Jong-Hee and sudershan,T.S., **(2001)**, "Chemical vapor deposition", (surface engineering series, v-2, ASM international, metals park, ohio, 44073

198. **Parkhutik** V. P. and Shershulsky V. I., **(1992)**, "Theoretical modelling of porous oxide growth on aluminium", *J. Phys. D*, 25, 1258 .

199. **Parthasarathy**, R.V., Phani K.L.N. and Martin C.R., **(1995)**, "Template synthesis of graphitic nanotubes", *Adv. Mater.* 7(2), 896

200. **Persson**, B.N.J., **(1995)** "Theoty of friction: stress domains, relaxation, and creep" *Physical review B*, 51, 568

201. **Piao**, Y., Lim, H., Chang, J.Y., Lee, W. Y. and Kim, H., **(2005)**, "Nanostructured materials prepared by use of ordered porous alumina membranes", *Electrochimica Acta*, 50(3), 2997

202. **Popov**, V.N. (2004), "Carbon nanotubes: properties and application", *Mater. Sci. Eng.* R 43 61.

203. **Rabinowicz**, E., **(1965)**, "Friction and wear of materials". Wiley, New York

204. **Rabinowicz**, E., **(1977)**, "Proceedings of International Conference on Wear of materials", Louis, *ASME*, New York, pp. 36-40.

205. **Ranjan**, K., Dharamvir, K., Jindal, V.K., **(2005)** "Cohesive energy of potassium doped C60 solids", *Physica B*, 365 121.

206. **Rehim** S.S.A., 'Hassan, H. H., Amin, M.A., **(2002)** "Galvanostatic anodization of pure Al in some aqueous acid solutions Part I: Growth kinetics, composition and

morphological structure of porous and barrier-type anodic alumina films", *Journal of Applied Electrochemistry*, 32(4), 1257.

207. **Ren**, Z.F., Huang ZP, Xu JW, Wang JH, Bush P, Siegal MP, (**1998**), "Synthesis of large arrays of well aligned carbon nanotubes on glass", *Phys Lett*, 378,9.

208. **Rodriguez**, N.M., (**1993**), "A review of catalytically grown carbon nanofibers", *J Mater Res*, 8(12), 3233.

209. **Routkevitch** D, Tager AA, Haruyama J, Almawlawi D, Moskovits M, Xu JM., (**1996**), "Nonlithographic nano-wire arrays: fabrication, physics, and device applications", *IEEE T Electron Dev*, 43(5), 1646.

210. **Saito**, M., M. Kirihara, T. Taniguchi, and M. Miyagi, (**1994**), "Micropolarizer made of the anodized alumina film", *Appl. Phys. Lett.*, 55, 607.

211. **Salvetat**-Delmotte, J. P., & Rubio, A., (**2002**), "Mechanical properties of carbon nanotubes: a fiber digest for beginners", *Carbon*, 40(10), 1729.

212. **Samudrala**, Saritha & Bandyopadhyay S., "Nanocomposites for electronic applications" –Chapter 6 SPRINGER: Hybrid Nanocomposites for Nanotechnology Electronic, Optical, Magnetic and Bio/Medical Applications Merhari, Lhadi ISBN: 978-0-387-72398-3

213. **Sarkar**, J., Khan, G.G. and Basumallick, A., (**2007**), "Nanowires: properties, applications and synthesis via porous anodic aluminium oxide template", *Bull. Mater. Sci.*, 30, (3) 271.

214. **Sarkar**, A. D., (**1980**), "Friction and wear", *Academic Press Inc.*, London, Great Britain.

215. **Sarkar**, A. D. and Clarke, J., (**1980**), "Friction and Wear of Aluminum Silicon Alloys", *Wear*, 61, 157.

216. **Seal** S., Sudipta S., Rashmi V., Bandyopadhyay, S. and Rahman Zia, (**2002**), "Effect of Nanocrystallite Morphology on the Metastable Tetragonal Phase Stabilization in Zirconia", *Nanoletters*, 2 (9), 989.

217. **Schwartz** G.C. & Platter,V.,(**1975**). "An anodic process for forming planar interconnection metallization for multilevel LSI", *J. Electrochem. Soc.*, 122, 1508.

218. *Shawaqfeh*, A.T. Baltus R. E., (**1998**)"Growth Kinetics and Morphology of Porous Anodic Alumina Films Formed Using Phosphoric Acid," *J. Electrochem. Soc.,* 145, 2699

219. **Shimizu**, K., Kobayashi, K., Thompson, G.E., Wood, G.C., (**1992**), "Development of porous anodic films on aluminium", *Phil. Mag. A,* 66,643.

220. **Shingubara** S. A., **(2003)**, "Fabrication of nanomaterials using porous alumina templates", *Journal of Nanoparticle Research*, 5, 17–30,

221. **Shingubara**, S., K. Morimoto, H. Sakaue, T. Takahagi, **(2004)**, "Self-Organization of a Porous Alumina Nanohole Array Using a Sulfuric/Oxalic Acid Mixture as Electrolyte", *Electrochem. Solid State Lett.* 7 E15.

222. **Shingubara**, S., Okino, O., Sayama, Y., Sakaue, H., and Takahagi, T., **(1997)**, "Ordered two-dimensional nanowire array formation using self-organized nanoholes of anodically oxidized aluminum", *Jpn. J. Appl. Phys.*, 36,part 1, no. 12 B,7791

223. **Shukla**, S., Seal, S., Rahman, Z., Viz. R. and **Bandopadhyay, S., (2002)**, "Effect of Nanocrystallite morphology on the metastable Tetragonal Phase Stability in Zirconia", *Nano Letters*, 2, 989.

224. **Sigurdson**, S., Sundaramurthy, V., Dalai, A. K., & Adjaye, J., **(2009)**, "Effect of anodic alumina pore diameter variation on template-initiated synthesis of carbon nanotube catalyst supports" *Journal of Molecular Catalysis. A, Chemical*, 306 (1-2), 23.

225. **Singh**, G. K, Golovin A. A., Aranson I. S., and Vinokur V. M., **(2005)** "Formation of nanoscale pore arrays during anodization of aluminum", *Europhys. Lett.*, 70, 836.

226. **Skeldon** P., Wang H.W., Thompson G.E., **(1997a)**, "Formation and characterization of self lubricating MoS_2 precursor films on anodized aluminium", *Wear*, 206, 187.

227. **Skeldon**, P. Wang, H.W and Thompson, G.E., **(1997b)**, "Fabrication and characterization of self-lubricating MoS_2 precursor films on anodic aluminum", *wear*, 206,187.

228. **Sklar** GP, Paramguru K, Misra M, LaCombe JC., **(2005)**, "Pulsed electrodeposition into AAO templates for CVD growth of carbon nanotube arrays", *Nanotechnology*, 16 1265.

229. **Sklar**,G P, Paramguru, K, Misra, M. and LaCombe, J C., **(2005)**, "Pulsed electrodeposition into AAO templates for CVD growth of carbon nanotube arrays", *Nanotechnology* ,16(1),1265.

230. **Skoneczny** W., **(2004)**, "Investigations of the surface morphology of $Al2O3$ layers by atomic force microscopy", *Material science-Poland*, 22(3), 345

231. Song I. K, Cho Y S, Choi G S, Park J B, Kim D J., **(2004)**, "The growth mode change in carbon nanotube synthesis in plasma-enhanced chemical vapor deposition", *Diamond Relat Mater,* 13 (4-8): 1210.

232. Song, I.K., Yu, W.J., Cho, Y.S., Choi, G.S., and Kim, D., **(2004)** "The determining factors for the growth mode of carbon nanotubes in the chemical vapor deposition process." *Nanotechnology,* 15, S590

233. Stasi V, Cattaneo G., Franz S., Bestetti M., Ubaldi M.C., Piccinin D., Pietralunga S.M., **(2007)**, "Aluminium pre-patterning for highly ordered nanoporus anodized alumina", Photonics and Nanostructures – Fundamentals and Applications, 5(3) 136.

234. Stein, N., Rommelfangen, M., Hody, V., Johann, L., & Lecuire, J. M., **(2002)**, "In situ spectroscopic ellipsometric study of porous alumina film dissolution", *Electrochimica Acta,* 47(11), 1811.

235. Strong, D. R., & Somorjai, C. A., **(1991)**, "Catalytic ammonia synthesis: fundamentals and practice", In J. R. Jennings (Ed.): Plenum Pub Corp.

236. Suh, J. S., **(1999)**, "Highly ordered two-dimensional carbon nanotube arrays", *App. Ph. Letters,* 75(14), 2047

237. Suh. NP., **(1973)**, "The Delamination Theory Of Wear", *Wear,* 25,111

238. Sui, Y.C., Acosta, D.R., Gonza´lez-Leo´n, J.A., Bermu´dez, A., Feuchtwanger, J., Cui, B.Z., Flores, J.O., Saniger, J.M., **(2001)**, "Structure, thermal stability, and deformation of multi-branched carbon nanotubes synthesized by CVD in the AAO template", *J. Phys. Chem., B,* 105, 1523.

239. Sui, Y.C., Cui, B.Z., Guardian, R., Acosta, D.R., Martýnez, L., Perez, R., **(2002)**, "Growth of carbon nanotubes and nanofibres in porous anodic alumina film" *Carbon,* 40, 1011.

240. Sulka, G. D., Stroobants, S., Moshchalkov, V., Borghs, G. and Celis, J.-P., **(2002)**, "Synthesis of Well-Ordered Nanopores by Anodizing Aluminum Foils in Sulfuric Acid", *Journal of The Electrochemical Society,* 149 (7), D97.

241. Sullivan J. P. O. and Wood, G. C., **(1970)**, "The morphology and mechanism of formation of porus anodic films on aluminium", *Proc. R. Soc London, Ser. A,* 317, 511.

242. Sun L. F., Mao J. M., Pan Z. W., Chang B. H., Zhou W. Y., Wang G., Qian L. X., and S. S. Xie, **(1999)**, "Growth of straight nanotubes with a cobalt–nickel catalyst by chemical vapor deposition", *Appl. Phys. Lett.,*74(5), 644.

235

243. **Sung, S.L.,** Tsai SH, Tseng CH, Chiang FK, Liu XW, Shih HC., **(1999),** "Well-aligned carbon nitride nanotubes synthesized in anodic alumina by electron cyclotron resonance chemical vapor deposition", *Appl. Phys. Lett.,* 74,197.

244. **Surappa, M. K.,** Prasad, S. V. and Rohatgi, P. K., Wear and abrasion of cast al-alumina particle composites, *Wear,* 77 (1982) 295 – 302

245. **Tajima, S.** in Advances in Corrosion Science and Techology. 1 (eds Fontana, M. G. & Staehle, R. W.) 229–362 (Plenum, New York, **1970**).

246. **Takahashi, H.** and Nagayama, M., **(1978),** "The determination of the porosity of anodic oxide films on aluminium by the pore-filling method", *Corrosion Science,* 18, 911.

247. **Terrado, E.,** Redrado, M., Muñoz, E., Maser, W.K., Benito, A.M. Martínez, M.T., **(2006),** "Carbon nanotube growth on cobalt-sprayed substrates by thermal CVD", *Materials Science and Engineering C,* 26(8), 1185.

248. **Terrones, M.,** Grobert N, Olivares J, Zhang JP, Terrones H, Kordatos K, **1997;** "Controlled production of aligned-nanotube bundles". *Nature* 388,52

249. **Thamida S. K.** and H.-C. Chang, **(2002),** "Nanoscale pore formation dynamics during aluminum anodization", *Chaos,* 12, 240.

250. **Thompson, G. E.** and Wood, G. C., **(1983),** in "Treatise on material science and Technology", 23, corrosion; Aqueous processes and passive films" pp 205-329, J. C. Scully (editor), academic press, New York

251. **Thompson, G.E.** H. Habazaki, K. Shimizu, **(1999),** "Anodizing of aluminium alloys" Aircraft Eng. Aerospace Technol. 71, 228.

252. **Thompson, G.E.,** **(1997),** "Porous anodic alumina: fabrication, characterization and applications", *Thin Solid Films,* 297, 192.

253. **Tibbetts G. G.,** **(1984),** "Why are carbon .laments tubular?", *J Cryst Growth,* 66,632

254. **Toebes, M. L.,** Bitter, J. H., van Dillen, A. J., & de Jong, K. P., **(2002),** "Impact of the structure and reactivity of nickel particles on the catalytic growth of carbon nanofibers", *Catalysis Today,* 76(1), 33

255. **Toebes, M.L.,** Bitter, J.H., Dillen, A. J.V., Jong, K.P.de, **(2002),** "Impact of the structure and reactivity of nickel particles on the catalytic growth of carbon nanofibers", *Catal. Today.* 76, 33.

256. Tsai, H., F.K. Chiang, T.G. Tsai, F.S. Shieu and H.C. Shih, (2000), "Synthesis and characterization of the aligned hydrogenated amorphous carbon nanotubes by electron cyclotron resonance excitation", Thin Solid Films 366, 11

257. Tu J.P., Jiang CX, Guo SY, Fu MF., (2004), "Synthesis and frictional properties of array film of amorphous carbon nanofibers on anodic aluminum oxide", Carbon; 41:1257.

258. Tu JP, Yang YZ, Wang LY, Ma XC, Zhang XB., (2001), "Tribological properties of carbon-nanotube-reinforced copper composites" Tribol. Lett.,10(4), 225.

259. Tu, J.P, Xiang, C. X. Guo, S.Y Zhao, X.B. and. Fu, M.F, (2005), "Tribological properties of aligned film of amorphous carbon nanorods on AAO membrane in different environments", Wear, 259, 759.

260. Tu, J.P. Xiang, C.X., Guo S.Y and. Fu M.F, (2004), "Micro-friction characteristics of aligned carbon nanotube film on an anodic aluminum oxide template", Material Letters, 581 646.

261. Tuinstra and Koenig (1970), "Characterization of Graphite Fiber Surfaces with Raman spectroscopy". Journal of Composite Materials.; 4, 492

262. Terrones, M., Grobert N, Olivares J, Zhang JP, Terrones H, Kordatos K, (1997) "Controlled production of aligned-nanotube bundles", Nature, 388, 52.

263. Uchi, H., Kanno, T. and Alwitt, R. S., (2001), "Structural Features of Crystalline Anodic Alumina Films", J. Electrochem. Soc., 148 (1), B17.

264. Veziri, C. M., Karanikolos, G. N., Pilatos, G., Vermisoglou, E. C., Giannakopoulos, K., Stogios, C., (2009), Growth and morphology manipulation of carbon nanostructures on porous supports. Carbon, 1(3), 21.

265. Veziri, Ch.M Karanikolos, G.N., Pilatos, G.,Vermisoglou, E.C., Giannakopoulos, K., Stogios, Ch., Kanellopoulos, N.K., (2009), "Growth and morphology manipulation of carbon nanostructures on porous supports", Carbon, 47, 2161

266. Vrublevsky I., Parkoun V, Schreckenbach J., Marx, G., (2003), "Effect of the current density on the volume expansion of the deposited thin films of aluminum during porous oxide formation", Applied Surface Science, 220, 51.

267. Vrublevsky I., Parkoun V, Sokol V., Schreckenbach J., Marx, G., (2004), "The study of the volume expansion of aluminum during porous oxide formation at galvanostatic regime", Applied Surface Science, 222(7), 215

268. *Vander Wal*, R.L., Miyoshi, K., Street, K.W., Tomasek, A.J., Peng, H., Liu, Y., Margravem, J.L., Khabashesku,V.N, **(2005)**, "Friction properties of surface-fluorinated carbon nanotubes" *Wear,* 259, 738.

269. **Waldemar** Koszela, Pawel Pawlus, Lidia Galda, **(2007)**, "The effect of oil pockets size and distribution on wear in lubricated sliding", *Wear,* 263(3),1585.

270. **Wang** H.W., Skeldon P., G.E. Thompson, **(1996)**, "Development and tribological assessment of self-lubricating anodic films on aluminium", *Surface and Coatings Technology,* 88 (1), 269.

271. **Wang** Y, Wei F, Luo G, Yu H, Gu G., **(2002)**, "The large-scale production of carbon nanotubes in a nano-agglomerate fluidized-bed reactor", *Chem. Phys. Lett.,* 364(2), 568.

272. **Wang,** C., Li, M., Pan, S. & Li, H., **(2000)**, "Well-aligned carbon nanotube array membrane synthesized in porous alumina template by chemical vapor deposition", *Chinese Science Bulletin,* 45 (15), 27.

273. **Wang,** H. and Wang, H., **(2004)**, "Thick and macroporous anodic alumina membranes for self-lubricating surface composites" *Applied Surface Science* doi:10.1016/j.apsusc.2004.11.058.

274. **Wei** S., Kang W. P. , Hofmeister W. H. , Davidson J. L. , Wong Y. M. , Huang, J.H. **(2005)**, "Effects of deposition and synthesis parameters on size, density, structure, and field emission properties of Pd-catalyzed carbon nanotubes synthesized by thermal chemical vapor deposition" *J. Vac. Sci. Technol.,* B 23 ,793.

275. **Wei** YY, Eres G, Merkulov VI, Lowndes DH., **(2001)**, "Effect of catalyst .lm thickness on carbon nanotube growth by selective area chemical vapor deposition", *Appl Phys Lett,*78 1394.

276. **Wernick** , S., Pinner R., Sheasby P., **(1990)**, "The surface treatment and finishing of Aluminium and its alloys" ASM International Finishing Publications Ltd.

277. **Wood,** G.C., **(1973)**, "Porous anodic films on aluminium." chapter 3 in 'oxides and oxide films', v 2, edited by John W. Diggle, p 169.mercell dekker inc. NEW YORK.

278. **Wu,** M. T, Leu, I.C. and Hon, M.H., **(2004)**, "Growth characteristics of oxide during prolonged anodization of aluminum in preparing ordered nanopore arrays", *J. Vac. Sci. Technol. B* 22(5) 2326.

279. Wu, M. T. (2002) "Effect of polishing pretreatment on the fabrication of ordered nanopore arrays on aluminum foils by anodization", *J. Vac. Sci. Technol. B* 20. 3 (3) 776.

280. Xia, Z., Riester, L., Sheldon, B. W., Curtin, W. A., Liang, J., Yin, A., (2004), "Mechanical properties of highly ordered nanoporous anodic alumina membranes", *Rev. Adv. Mater. Sci*, 6, 131.

281. Xu, J., Zhang, X., Chen, F., Li, T., Li, Y., Tao, X., (2005), "Preparation and modification of well-aligned CNTs grown on AAO template", *Applied Surface Science*, 239(3-4), 320.

282. Yadav, B.C., Srivastava, Richa, Dwivedi, C.D. and Pramanik, P., (2008), "Moisture sensor based on ZnO nanomaterial synthesized through oxalate route", *Sensors and Actuators B*, 131, 216.

283. Yanagishita T., Sasaki M, Nishio K and Masuda H, (2004), "Carbon Nanotubes with a Triangular Cross-section, Fabricated Using Anodic Porous Alumina as the Template", Adv Mater. 16, 429.

284. Yang Z, Xu H, Li MK, Shi YL, Huang Y, Li HL., (2004), "Preparation and properties of Ni/P/single-walled carbon nanotubes composite coatings by means of electroless plating", *Thin Solid Films*, 466(1-2) 86.

285. Yang, Y., Hu, Z., Wu, Q., Lü, Y. N., Wang, X. Z., & Chen, Y., (2003), "Template-confined growth and structural characterization of amorphous carbon nanotubes", *Chemical Physics Letters*, 373(5-6), 580.

286. Yen, H.-M., Jou, S., (2005), "Si–O–C nanotubes from pyrolyzing polycarbosilane in a mesoporous template", *Materials science and engineering B*, 122(3), 240.

287. Yin, A., Tzolov, M., Cardimona, D. A. and Xu, J., (2006), "Template-Growth of Highly Ordered Carbon Nanotube Arrays on Silicon", *IEEE transactions on nanotechnology*, 5(5), 23.

288. Yokomichi, H., Sakai, F., Ichihara, M., and Kishimoto, N., (2002), "Carbon nanotubes synthesized by thermal chemical vapor deposition using $M(NO_3)_n$ .mH_2O as catalyst", *Physica B*, 323:311.

289. Yu , W. H., Fei, G. T., Chen, X. M., Xue, F. H., Xu, X. J., (2006), "Influence of defects on the ordering degree of nanopores made from anodic aluminum oxide" *Physics Letters A*, 350, 392.

290. Yu Ch en-Un, Hu Chi-Chang, Bai Allen, Yang Yong-Feng (2007), "Pore-size dependence of AAO films on surface roughness of Al-1050 sheets controlled by

electro polishing coupled with fractional factorial design." *Surface & Coatings Technology*, 201, 7259.

291. Yu, W. H., Fei, G. T., Chen, X. M., Xue, F. H., Xu, X. J., **(2006)**, "Influence of defects on the ordering degree of nanopores made from anodic aluminum oxide", *Physics Letters A*, 350, 392

292. Yuan, Z.H., Huang H, Dang HY, Cao JE, Hu BH, Fan SS. **(2001)** *Applied Physics Letters* 783127

293. Xia, Z.H., Lou, J. and Curtin, W.A., **(2008)**, "A multiscale experiment on the tribological behavior of aligned carbon nanotube/ceramic composites", *Scripta Materialia*, 58, 223

294. Zhang, L., Cho, H. S., Li, F., Metzger, R. M. and Doyle, W. D., **(1998)**, "Cellular growth of highly ordered porous anodic films on aluminium", *J. Mater. Sci. Lett.*, 17, 291.

295. Zhao, X., **(2004)**, "Smallest Carbon Nanotube is 3 Å in diameter", *Phys. Rev. Lett.*, 92,125502.

296. Zhou, H.Y., Qu, S.C. Wang, Z.G., Liang, L.Y., Cheng, B.C., Liu, J.P. , Peng, W.Q., **(2006)**, "Preparation and AFM characterization of self-ordered porous alumina films on semi-insulated gas substrate", *Materials Science in Semiconductor Processing*, 9, 337.

297. Zhu L.B., **(2006)**, Hess DW, Wong CP. Monitoring carbon nanotube growth by formation of nanotube stacks and investigation of the diffusion controlled kinetics", *J Phys Chem B*, 110(11), 5445.

298. Zhu W., Bower C, Zhou O, Kochanski G, Jin S., **(1999)**, "Large current density from carbon nanotube field emitters", *Appl. Phys. Lett.*, 75, 873.

299. Zhu, S., Su, C.-H., Cochrane, J.C., Lehoczky, S., Cui, Y., Burger, A., **(2002)**, "Growth orientation of carbon nanotubes by thermal chemical vapor deposition", *Journal of Crystal Growth*, 234, 584.

300. Zhu, Y.T., Narayan, J., Hirth, J.P., Mahajan, S., Wu, X.L. and Liao, X.Z., **(2009)**, "Formation of single and multiple deformation twins in nanocrystalline fcc metals", *Acta Materialia*, 57 (2009) 3763–3770.